Self-Assembled Nanoelectronic Networks with Tunable Molecule-Nanoparticle Ratios: Experiment, Modeling, and Applications

by

Anusha Venkataraman
B. Tech., Jawaharlal Nehru Technological University Hyderabad, 2012
M. Tech., Jawaharlal Nehru Technological University Hyderabad, 2014

A Dissertation Submitted in Partial Fulfillment
of the Requirements for the Degree of

DOCTOR OF PHILOSOPHY

in the Department of Electrical and Computer Engineering

University of Victoria

Supervisory Committee

Self-Assembled Nanoelectronic Networks with Tunable Molecule-Nanoparticle Ratios: Experiment, Modeling, and Applications

by

Anusha Venkataraman

B. Tech., Jawaharlal Nehru Technological University Hyderabad, 2012

M. Tech., Jawaharlal Nehru Technological University Hyderabad, 2014

Supervisory Committee

Dr. Chris Papadopoulos, Department of Electrical and Computer Engineering

Supervisor

Dr. Reuven Gordon, Department of Electrical and Computer Engineering

Departmental Member

Dr. Frank C. J. M. van Veggel, Department of Chemistry

Outside Member

Abstract

Supervisory Committee

Dr. Chris Papadopoulos, Department of Electrical and Computer Engineering
Supervisor

Dr. Reuven Gordon, Department of Electrical and Computer Engineering
Departmental Member

Dr. Frank C. J. M. van Veggel, Department of Chemistry
Outside Member

Replacing electronic components with molecule-sized analogs or hybrids is often seen as a promising alternative to further miniaturization of conventional electronics in the effort to achieve functional nanoscale circuit elements. In this thesis, electronic transport through self-assembled networks with tunable thiolated (alkane(di)thiol and benzenedithiol) molecule-to-colloidal gold (Au) nanoparticle ratios (1:5–50:1) is studied using a combination of broad area and scanning probe microscope-based measurements. The electronic transport paths through the network can be altered by adjusting the (di)thiol molecule–gold nanoparticle ratio and/or type of molecules in the network. Resistance can be controllably tuned by several orders of magnitude (~10^5 to 10^{11} ohms for the Au-thiolated structures studied). Two-terminal current–voltage (*I-V*) measurements of the Au-thiolated networks display linear behavior at low bias. High bias measurements in case of benzenedithiol networks show nonlinear negative differential resistance (NDR) and hysteresis behavior for different benzenedithiol concentrations, which can be attributed to a combination of field-assisted tunneling and charge trapping occurring in the nanoscale networks. Circuit simulations that account for different network morphologies, tunable via molecule-to-nanoparticle ratio, and defects show good agreement with the experiment and provide a guide to engineer network properties using different molecules. In addition, electronic transport properties of nanoscale networks, which are composed of Au metal clusters interconnected with thiolated molecules (benzene/alkanedithiol) and connected in linear chains and branched extended networks, are examined via first-principles density functional theory-based simulations. Calculated *I-V* characteristics of the metal-molecular networks exhibited nonlinearities and rectification with NDR peaks that became more pronounced with increasing chain length. The transmission spectra of the linear chains and branched networks showed an increase in the number and width of transmission peaks near the Fermi energy, as the structures were extended, indicating enhanced transmission. Peak-to-valley current NDR ratios as large as ~ 500 and rectification ratios of ~ 10 (0.25 V) were shown for linear and branched circuit elements, respectively, illustrating how charge transport through molecular-scale devices could be controlled with precision by modifying the structure and geometry of molecule-nanoparticle networks. These experimental and simulation results are utilized to propose molecular-scale circuits in applications such as memory, switching, and hardware security. The metal nanoparticle molecular electronic networks presented in this thesis provide an avenue for engineering electronics at the molecular level.

Table of Contents

List of Tables

List of Figures

List of Abbreviations

Abbreviation	Meaning
ACS	American chemical society
AFM	Atomic force microscope
AM1	Austin model 1
CNT	Carbon nanotube
CMOS	Complementary metal-oxide-semiconductor
DOS	Density of states
DFT	Density-functional theory
DNP	Double numerical basis set with polarization
FET	Field effect transistor
GAA	Gate-all-around
GGA	Generalized gradient approximation
HOMO	Highest occupied molecular orbital
KS	Kohn-Sham
LB	Langmuir-Blodgett
LDA	Local density approximation
LDOS	Local density of states
LSDA	Local spin density approximation
LUMO	Lowest unoccupied molecular orbital
MCBJ	Mechanically controlled break junctions
MTJ	Multiple-tunnel junctions
NIST	National Institute of Standards and Technology
NDR	Negative differential resistance
NEGF	Non-equilibrium green’s function
PBE	Perdew, Burke, and Erzenhof
PW_{SCF}	Plane-wave self-consistent field
DZP	Polarized double-zeta
PDOS	Projected density of states
RAM	Random access memory
RS	Resistive switching
STM	Scanning tunneling microscope
SAM	Self-assembled monolayer
SCF	Self-consistent field method

SET	Single electron transistor
SWCNT	Single-walled CNT
TEM	Transmission electron micrograph
UHF	Unrestricted Hartree-Fock
VNL	Virtual Nanolab
VOC	Volatile organic compounds

Acknowledgments

I express my deep sense of gratitude and reverence to my supervisor, Dr. Chris Papadopoulos, for his guidance and support throughout my program of study. He has inspired me to become an independent researcher and helped me realize the power of critical reasoning.

I am thankful to my supervisory committee members, Dr. Reuven Gordon and Dr. Frank C. J. M. van Veggel, for providing valuable suggestions.

Special thanks to my friends and fellow researchers at the Nanoscale Research Laboratory: Po, Ebere, Tristan, and Raju, for their help and support.

Finally, my deep and sincere gratitude to my family for their continuous and unparalleled love, help and support. Understanding me best as a Ph.D. herself, my mom has been my pillar of strength despite the long distance between us. I am grateful to Srinath (my husband), Shriyaan (my son), and Varsha (my sister) for their love, support, and encouragement that helped me get through my program in the most positive way.

Dedication

Dedicated to

The God Almighty

and

My Beloved Family

Chapter 1 Introduction

1.1. Background and Motivation

1.1.1 Introduction to Nanotechnology and Nanoelectronics

Nanotechnology refers to the study of materials and devices at the scale of 100 nanometers and less [1]. In 1959, Richard Feynman first discussed the idea of manipulating properties of materials and devices composed of nanometer-sized building blocks [2]. Since then, tremendous efforts are being made to understand the mechanical, chemical, and electrical properties at the nanoscale that would help in fabricating devices of that size [1], [3]. In the past few decades, with the invention of the scanning tunneling microscope (STM) [4], [5] and atomic force microscope (AFM) [6], a great progress has occurred in this field, both in theoretical and experimental research [7–10]. Materials exhibit different behavior at the nanoscale level as compared to their behavior at the macroscopic level. Properties such as melting point, fluorescence, electrical conductivity, magnetic permeability, and chemical reactivity change as a function of the size of the particle [1]. Research indicates that control of matter at the nanoscale is the key to fabrication of smaller electronic devices with capabilities like faster computing, better diagnostics, etc. [10–13].

The urge to reduce the size of devices led to the introduction of Moore's law in 1965 [14]. According to this law, the total number of transistors per integrated circuit doubles every two years. As a result, an increasing number of transistors have been scaled down in size and packed in a given area over the years (Figure 1.1 (a-b)). This rapid growth in the number of transistors per integrated circuit is mainly correlated with the persistent dimensional and functional scaling of complementary metal-oxide-semiconductor (CMOS) integrated circuits. On the design side, 14 nm and 10 nm tri-gate field effect transistors (FETs) are being manufactured, where a gate surrounds the three sides of the horizontal fin-shaped channel to control the flow of current (Figure 1.1 (c)).

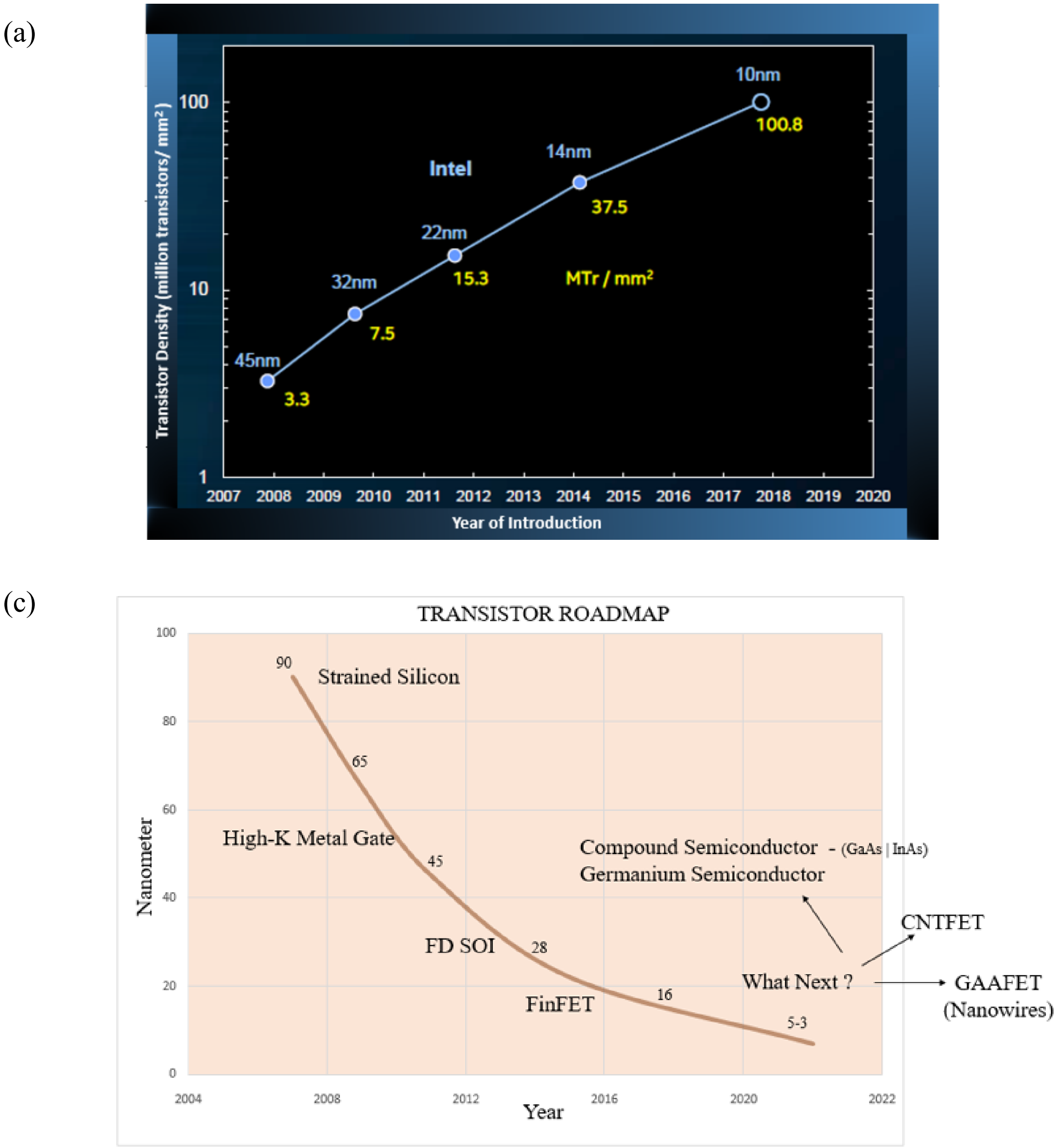

(c)

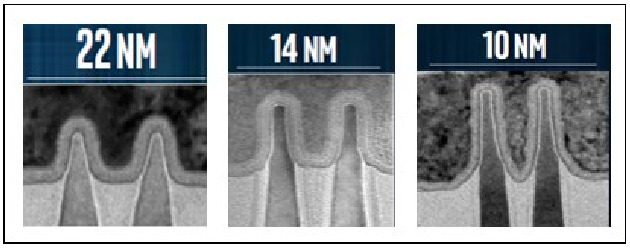

Figure 1.1: (a-b) Transistor density and feature size of integrated circuits *vs*. year of introduction. (b) FinFET technology from Intel with increased fin height to improve the current drive (Adapted from Intel.com; solid state technology-semiconductor-digest.com:2020).

However, owing to various material, physical, power, and technological limitations, engineers are facing challenges that significantly slow down/prevent CMOS transistors from being scaled down further [15], [16]. Examples of some of these challenges include pushing the ultimate limits of optical lithographic processes to develop photoresists and appropriate mask materials, and to provide resolution below the wavelength of light [17]. Additionally, during CMOS scaling, it is essential to shrink the gate dielectric thickness in order to maintain the required electric field. As the oxide layer is scaled down, quantum mechanical tunneling leads to an increase in the gate leakage current that can damage the dielectric [18], [19]. Moreover, the reduction in the channel length during CMOS scaling also leads to leakage currents [20]. Likewise, an increase in the number of transistors per unit area leads to higher thermal dissipation and increased power consumption, thereby leading to higher fabrication and production costs [18–21].

To address these challenges, various alternate information processing, data-storage, and other device technologies that extend the functionality of the CMOS platform are being explored (Figure 1.2) [18], [22]. For example, nanoparticle networks have gained interest in applications such memory, neuromorphic computing, and random number generation [7–13].

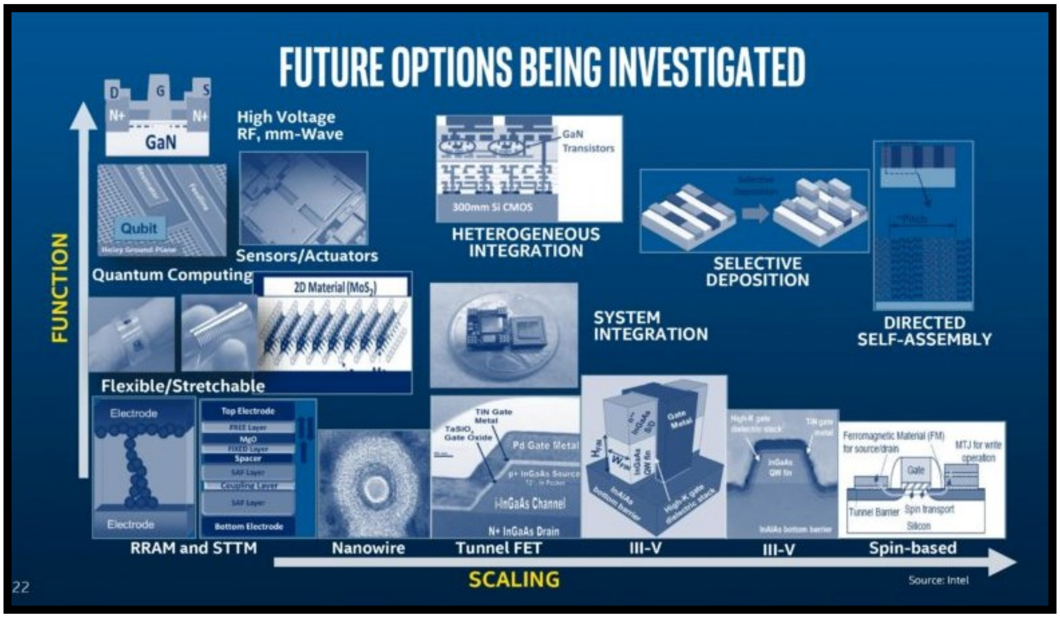
FUTURE OPTIONS BEING INVESTIGATED

Figure 1.2: Schematic showing the various possibilities for device technologies (5nm and beyond) that extend the functionality of the CMOS platform (Adapted from Intel.com*)

Currently, there is a need for memory technologies that offer higher density with fast read/write speeds of synchronous random-access memory (RAM) and non-volatile flash memory with an ability of data storage when the device is turned off. Technologies that explore basic memory mechanisms like chemical and phase changes, and charge trapping are gaining widespread popularity [23], [24]. Examples of emerging memory devices include ovonic unified memory (or phase change memory) that utilizes the rapid reversible phase change effect seen in some materials under the influence of electric current pulses [25], [26]. Here, data storage capabilities are due to a thermally induced phase change between amorphous and polycrystalline states in a thin film of chalcogenide alloy (Figure 1.3 (a)). This phase change results in variations in the material resistivity.

Alternatively, nano-floating gate memory devices that are fabricated by using controlled gold nanoparticle/polyelectrolyte composite layers and PMMA insulating polymers are also gaining widespread interest [27]. Here, these devices have shown good data retention and large memory windows of about 34 V, exhibiting memory properties that can potentially be retained for more than one year. An example architecture of a nano-floating gate memory device is shown in Figure 1.3 (b).

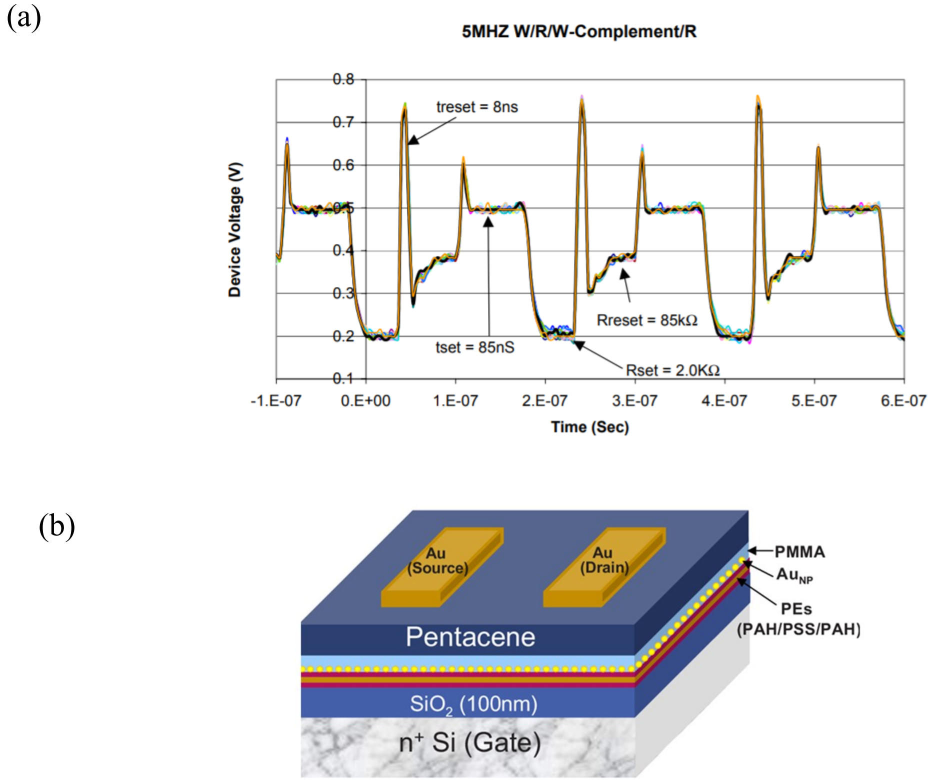

Figure 1.3: (a) Oscilloscope traces of the cycling characteristics of the ovonic unified memory cell during repetitive write/read/write-complement/read cycling (Adapted from [25]). (b) Schematic of the device architecture consisting of a bottom gate and the top contact organic transistor-based non-volatile memory devices. These devices consist of a charge trapping layer made of a controlled AuNP/polymer composite material and a PMMA organic tunneling layer (Adapted from [27]).

Additionally, a single-electron memory device made up of a multiple-tunnel junctions (MTJ) consisting of a series of small islands was demonstrated [28]. Here, flow of electrons into the MTJ is blocked due to the energy barrier created by the charging energy of the island. In single-electron memory devices, one bit of information is stored by one electron [29], [30]. Molecular memories which utilize individual molecules as building blocks of memory cells have also gained significant interest [31], [32]. For example, electronically programmable memory devices made up of molecular self-assembled monolayers (SAM) have shown that the memory devices work by storing a high or low conductivity state. On application of a voltage pulse, the low conductivity state is changed (written) to a high conductivity state that represents a stored bit [32].

Various logic-based devices like resonant tunneling diodes (RTD) [33], single electron transistors [34], carbon nanotube (CNT) based-FETs [35] [36] and molecular devices [37] are also being explored. RTD are typically a sandwich structure, made up of two thin layers of high-band-gap material acting as source and drain, which is surrounded by a thin layer of low-band-gap material. An RTD is characterized by an NDR region in the $I-V$ curve which facilitates its use in various circuit applications. One example includes a molecular-scale latch which provides signal restoration by managing interactions among a pair of molecular RTDs [38].

Single-electron charging effects based on Coulomb blockade are being widely investigated [39], [40]. Single-electron devices consist of tunnel barriers which are junctions that control the motion of each electron individually. The island associated with a tunnel barrier should be small enough for a single electron added to the island to cause a significant should voltage increase [41]. One example of single electron device is the single electron transistor (SET) [42]. A SET has three terminals and consists of a small island i.e., dot made of a semiconductor or metal, in which electrons can be confined. SET works on the principle of Coulomb blockade where the gate terminal controls the number of electrons on the dot. The energy that must be added or removed from the dot depends on the dot's size and the number of electrons that are already present in the dot.

CNT based-FETs are also being explored for future device applications [43]. CNTs are long, hollow cylindrical tubule structures made of graphite sheets (a.k.a. graphene), with diameters ranging from below 1 nm to 10 s of nm [44]. In one study, an enhancement-mode p-type FET was built with a single CNT in which the gate consisted of an aluminum wire over a negative Al_2O_3 layer (only a few nanometers thick) that lies beneath a single CNT acting as a conducting channel. Figure 1.4 shows the schematic and *I-V* characteristics of a CNT FET exhibiting switching for different gate voltages.

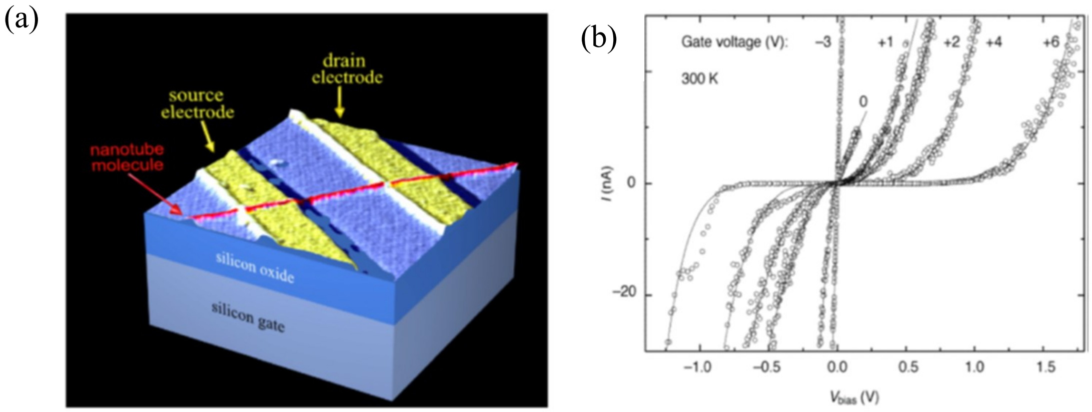

Figure 1.4: (a) Schematic illustration of the initial CNTFET demonstration. The transistor can be turned on by applying a gate voltage to the silicon substrate (back gate) that induces carriers into the nanotube channel bridging the source and drain electrodes. Adapted from [45]. (b) *I-V* characteristics of CNTFET showing switching between ohmic and nonlinear behaviors at different gate voltages. Adapted from [43].

Various studies have reported the use of molecules to build logic devices such as programmable molecular switches [46], rectifiers [47][48], etc. In one study, tunneling junctions with linear alkanes sandwiched between metal electrodes were developed where the molecule (consisting of an electron donor, a bridge, and an acceptor, and extended between two electrodes) showed rectifying behavior [49].

With the invention of new technologies like molecular electronics and quantum cellular automata [50], there is a growing need for the development of new system architectures that support their applications. As the scaling of semiconductor-based devices continues, new paradigms for system architecture that are based on bottom-up fabrication methods involving molecules or atoms as the device building blocks are gaining widespread interest [51–54]. Examples include the 3D integration of various technologies, memory-based molecular computers that are built by using molecular architectures, intelligently-assembled nanodevices based on defect-tolerant architecture, and quantum devices based on quantum computing architectures [18], [55]. For example, with the inclusion of new technologies, the electrical characteristics of a single gate FET can be enhanced by employing new device architectures forming structures like FinFETs, and gate-all-around (GAA) FETs that include nanowire FETs and the nanosheet FETs. FinFETs are made up of 3D structures that rise above the substrate and resemble a fin [56].

These fins represent the source and the drain terminals where the gate wraps around the fin, enabling it to interface with three side of the fin or channel. This architecture enables the ability to include more volume as compared to a traditional planar transistor (with the same area). Additionally, when the device is in the 'OFF' state, there is just minor amount of current that could leak through the body. FinFETs have shown to use lower threshold voltages leading to better performance and lower power dissipation. However, as the fin width in a FinFET approaches 5nm, various shortcomings associated with the channel width are reported. An alternate to solve this issue is based on using GAA FETs, in which the gate is placed on all sides of the channel. For example, a nanosheet GAA FET consists of horizontally stacked nanosheets made using alternating layers of silicon and silicon germanium, patterned/etched into sheets (Figure 1.5).

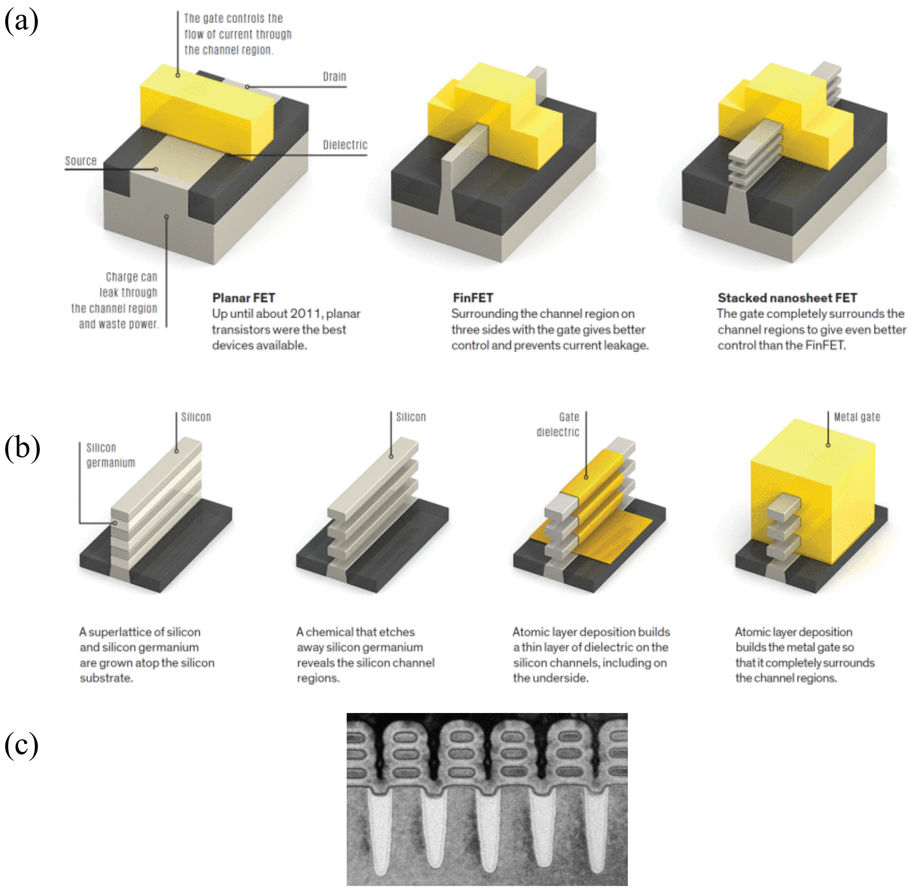

Figure 1.5: (a) Schematic of planar FET, FINFET and stacked nanosheet FET (b) Step-by-step representation of creating a nanosheet transistor utilizing atomic layer deposition techniques. (c) Microscopic images of stacked nanosheet FETs. Adapted from [57].

Finally, neuromorphic and quantum processing systems are paving the way for the next generation of artificial intelligence [58–60]. Quantum neuromorphic computing aims to physically implement neural networks in brain inspired quantum hardware in which the computers can potentially use data to learn, adapt, and think. Quantum computers can store information in the form of quantum bits, commonly referred as qubits that can exist in two different information states at the same time, and can process complex calculations at very high speeds. On the other hand, neuromorphic computing aims to complement the classic von Neumann architecture. Recently, researchers revealed the ability of Intel’s neuromorphic research chip, named Loihi, that could learn and recognize hazardous chemicals in the presence of significant noise and occlusion [58].

1.1.2 Molecular Electronics

Molecular electronics is a branch of nanotechnology that deals with the engineering of materials and electronic devices at the molecular scale [54], [61–63]. It provides an alternate approach to shrinking electronic circuits further. Since the typical size of molecules is between 1 and 10 nm, a higher packing density of these molecules can be seen in various devices which could offer advantages like higher efficiency, lower cost and lower power dissipation [64]. The challenges faced by CMOS technology scaling such as increased leakage currents, higher thermal dissipation and increased power consumption, could potentially be overcome using molecular as the active components of the circuits. Molecular electronic structures and devices are built using specific number of molecules that are made to assemble forming complex structures like molecular wires etc. Utilization of various molecules to fabricate electronic devices like molecular transistors [65], rectifiers [47], sensors [66], integrated circuits [67], etc. allows the control of device properties at the molecular level.

Evolutions in the field of molecular electronics can be traced back to the 1970s, where the conductivity measurements through monolayers of cadmium salts of fatty acids employing the Langmuir-Blodgett (LB) technique were reported [68]. Results from this work showed an exponential decrease in conductivity with respect to layer thickness. Figure 1.6 (a) shows the plot of logarithm of current density versus *(vs.)* the applied voltage for monolayers of thickness varying from 18-22. Later in 1974, a pioneering work by Aviram and Ratner explained the possibility of a molecular rectifier [47] (Figure 1.6 (b)). In their work, they proposed a donor π-system and an acceptor π-system linked together by a σ -bonded tunneling bridge. Phenomenon of a unidirectional electrical conduction system was demonstrated based on alignment of the highest occupied molecular orbital (HOMO) and lowest unoccupied molecular orbital (LUMO) levels. The σ –bonded electron system acted as an insulating barrier between the donor and the acceptor groups. With the invention of the STM and AFM in the 1980s [4], [6], further progress in theoretical and experimental research of molecular electronics could take place.

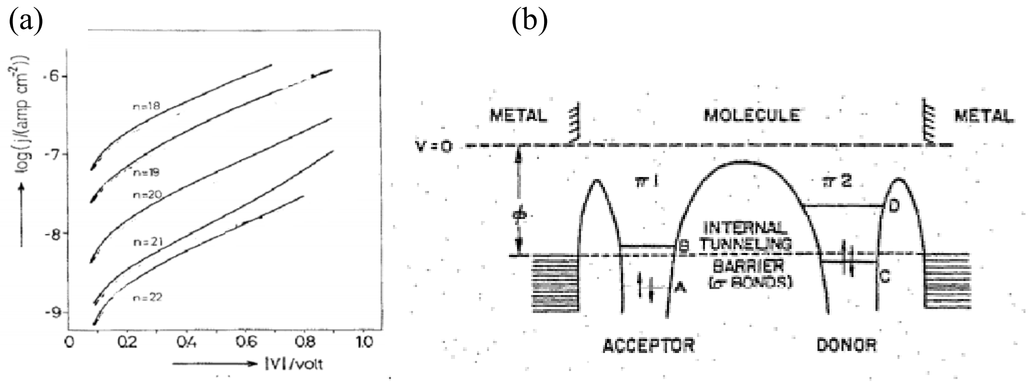

Figure 1.6: (a) Logarithm of current density (j) *vs.* the applied voltage (V) for monolayers of cadmium salts of fatty acids of thickness varying from n= 18-22 (Adapted from [68]). (b) Energy *vs.* distance of the molecular rectifier device. Here, B and D are the electron affinity levels and A and C the HOMO levels of the donor and acceptor (Adapted from [47]).

The understanding of flow of electrons towards and through single molecules integrated between metallic electrodes is an important aspect in the field of molecular electronics. Molecules attached to metal electrodes forming a metal-molecule-metal junction offer a potential alternative and/or complement the conventional semiconductor electronics [69–71]. Recent developments in this field have led to a widespread popularity in study and manufacturing of molecular electronic devices based on top-down (ex. lithographic techniques) and/or bottom-up (ex. self-assembly techniques) approaches. A commonly known method of creating a single-molecular junction is based on the mechanically controlled break junctions (MCBJ technique) [72], [73]. In one of early works using this technique, the electrical properties of 1, 4-benzenedithiol, self-assembled between two gold electrodes were investigated [52]. In MCBJ technique, nanogaps are created by stretching a metal wire, glued onto a substrate, until it narrows and then breaks leading to tip-like formation. Post this; molecules can be incorporated in this gap, formed between the metal electrodes as shown in Figure 1.7 (a-b). Figure 1.7 (c) shows the typical current-voltage and conductance-voltage characteristics. The use of MCBJ techniques have helped in the possibility of formation of small contacts with a tunable nanometer-sized gap where desired nanostructures can be trapped and tested electrically [52].

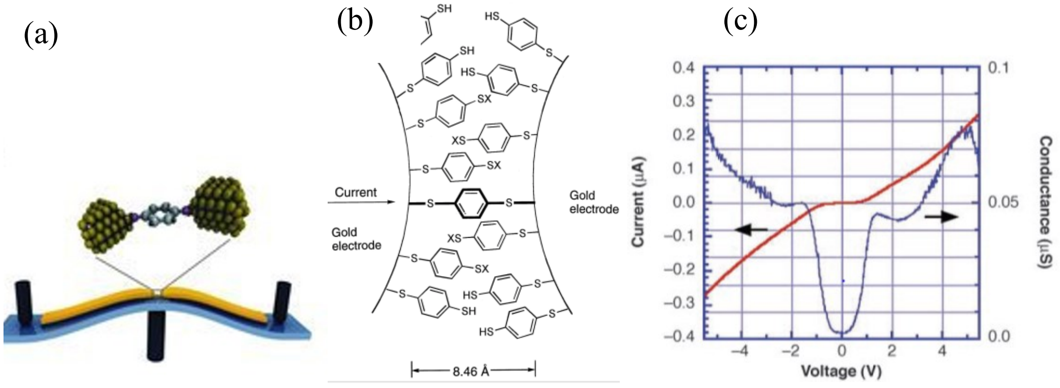

Figure 1.7: Schematic of (a) Formation of a single-molecular junction using MCBJ technique. Here a three-point adjustable bending mechanism is used to stretch the metal wire until it breaks to produce a nanogap where desired molecules are inserted (Adapted from [73]). (b) A benzene-1,4-dithiolate SAM between two gold electrodes formed using MCBJ technique. (c) Typical *I(V)* and *G(V)* characteristics (Adapted from [52]).

Another favored approach to fabrication of these molecular junctions is using SAM techniques [74]. SAMs are films formed due to spontaneous assembly of organic molecules, in particular thiolated molecules [ex. alkane(di)thiols] in solution or gas phases onto any curved or planar solid surfaces [74], as seen in Figure 1.8. Alkane(di)thiols (due to the presence of a sulfanyl group [–SH]), have strong affinity to various metals like gold [75–77], silver [76], etc. Due to this, such films are widely studied in this field.

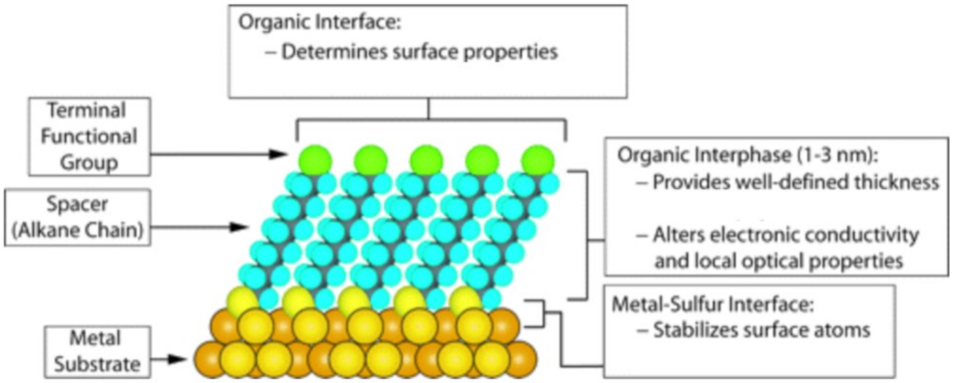

Figure 1.8: Illustration of SAM of alkanethiolates on a gold surface (Adapted from [74]).

Studies have shown that variations in the type of alkane(di)thiol molecules and/or the molecular weight can alter the properties of the films formed [69], [74]. For example, with an increase in length of dithiol linkers, the conductivity of close-packed layers or films (Figure 1.9 (a)) of dithiol molecule-covered nanoparticles (formed by alternating layer-by-layer assembly of gold nanoparticles and dithiols) decreased [74], [78]. Alternatively, when two colloidal gold nanoparticles were joined by an organic dithiol molecule, forming a dimer based nanoparticle molecular junction, the conductance through the dimer varies depending on the degree of molecular orbital delocalization [75], [79]. Here, a dimer structure was made of two colloidal gold nanoparticles bridged by a dithiol organic molecule as shown in Figure 1.9 (b). It was observed that the electrical conduction is higher in the case of a fully conjugated molecule [i.e. 4,4’-biphenyldithiol (BPD)], as compared to the case where localizing groups [(i.e. bis-(4-mercaptophenyl)-ether (BPE), where the conjugation is broken at the centre by an oxygen atom; and 1,4-benzenedimethanethiol (BDMT), where the conjugation is broken near the contacts by a methylene group] were added to the conjugated molecule [79].

(b)

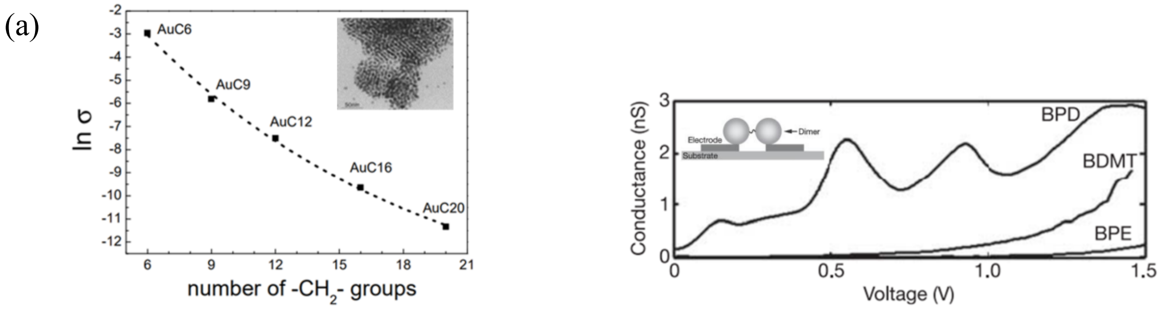

Figure 1.9: (a) Plot showing a decrease in conductivity of Au-nanoparticle/alkylenedithiol films with an increase in the chain length of linkers. Inset shows an example of nanoparticle–molecular systems consisting of bulk films with very large number of molecules (Adapted from [75]) and (b) Plot showing the variations in the conductance of a dimer molecule depending on the degree of molecular orbital delocalization. Inset shows an example of nanoparticle oligomers with single molecules (Adapted from [79]).

Experimental studies involving molecules are supported by different computational quantum mechanical modeling techniques that are considered as an important tool for the development of molecular electronics [80], [81]. Various computational methods using concepts of semi-empirical and density-functional theory (DFT) approximations with Boltzmann transport equation [82], non-equilibrium Green's function (NEGF) method [83], plane waves, and Landauer-Buttiker [84] approximations etc., are being utilized to simulate electronic structural and transport properties of metal-dithiol molecular junctions. It is predicted that charge transfer from metal to molecule occurs due to the interfacial interaction resulting in the change in the electrostatic potential in the molecule, which changes the molecular levels [85]. The interaction between a molecule's frontier orbitals, i.e., the orbitals closest to the HOMO and LUMO gap, and the states of the metal contacts determine the energy and character of the system's molecular orbitals that are typically responsible for electronic transport [85–89]. Study of transport properties of such systems (schematic shown in Figure 1.10) using different theoretical methods has gained tremendous interest recently [80], [87], [89], [90].

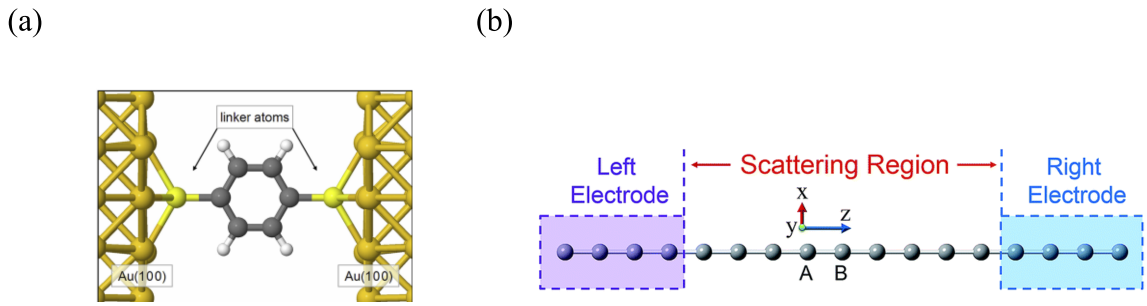

Figure 1.10: (a) Schematic of a (a) metal–molecule-metal junction (Adapted from [53]). (b) A technique used to calculate the electron transport through molecular structures (Adapted from [83]).

Molecular electronic devices have shown a potential to be used in different applications like sensors, FETs, robotics, health based diagnostic tools, etc. [36], [66], [91–93]. Due to their smaller sizes, they can be integrated as three-dimensional layers that would help in reducing the overall size of the device without compromising on the overall efficiency. Existing experimental work mainly focusses on studying the properties of metal-molecule-metal junctions made up of bulk films [78], [94] or with very few molecules [79]. Here, the variations and control of electrical characteristics of the above described junctions is mainly based on the use of different types/chain length of molecules (ex. saturated or π-conjugated molecules). Alternative techniques of varying the properties of these molecular networks is needed for further development in this field. Similarly, majority of the existing computational research on such junctions is mainly focused on understanding the properties of individual molecules bridging bulk metallic electrodes. In order to plan for the realization of large-scale molecular integrated networks, alternative designs may be required, as the use of some of the existing design arrangements may lead to increased computational resources hindering the development in this area. Similarly, there is also a need to advance from modelling single molecule based junctions to modeling molecular networks that would help in building future molecular electronic circuits.

Motivated by existing work on metal-molecule-metal junctions made up of bulk films (consisting of many molecules) or with very few molecules, as discussed above, the current study focuses on understanding the electronic transport in self-assembled nanoscale networks with tunable molecule-nanoparticle ratios in the intermediate regime (Figure 1.11a). This work is focused on progressing from the existing studies done on metal-molecular junctions towards designing molecular electronic circuits based on different network morphologies using inexpensive self-assembly techniques. It includes the details of associated fabrication methodologies used in the formation of nanoscale networks, understanding different electronic properties using various analysis, characterization and computational modeling techniques.

Here, properties of self-assembled metal-molecular networks in the intermediate regime are experimentally tuned by adjusting the gold nanoparticle to molecule ratio and/or type of molecule in the network. This leads to different circuit configurations with tunable electrical conductance, which would provide a potential pathway for realizing a wide range of applications. A combination of broad area and SPM-based measurements are used for understanding the electrical behavior of self-assembled gold nanoparticle-molecular networks that can be interpreted in terms of different network morphologies. Circuit simulation-using LTspice, provides a guide for tuning electronic properties of these networks. In addition, the effect of defects in the networks are taken into consideration in circuit modeling, i.e., by assigning certain variables with extremely high resistance, to achieve more precise simulations. By using molecules as basic components in the circuit, these structures can be treated as a unit cell and be repeated to build larger networks thereby, closely approaching a model of large-scale molecular integrated circuit. From computational modeling's perspective, which involves the use of different DFT and semi-empirical approximations, this work includes modeling nanoscale networks of varying sizes (for example, linear chains, a three-terminal network forming a Y-shaped network, a H-shaped, a ring-shaped and a diamond-shaped network) using thiolate molecules that are interconnected with metal clusters. Results from simulations on supercomputers using both bulk electrodes and single metal atoms as electrodes illustrate how different extended molecular networks and systems may help in controlling the electrical properties over larger distances. These results are analysed for potential device applications for memory, switching, logic circuits, and for random key generation that can be used in hardware security applications. A schematic representation of the proposed work is presented in Figure 1.11 (b).

(a)

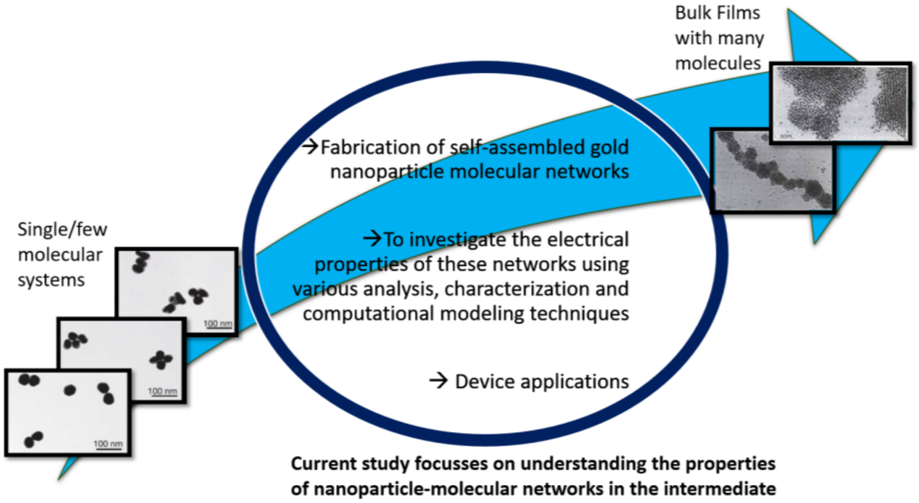

Current study focusses on understanding the properties of nanoparticle-molecular networks in the intermediate and bulk regime

(b)

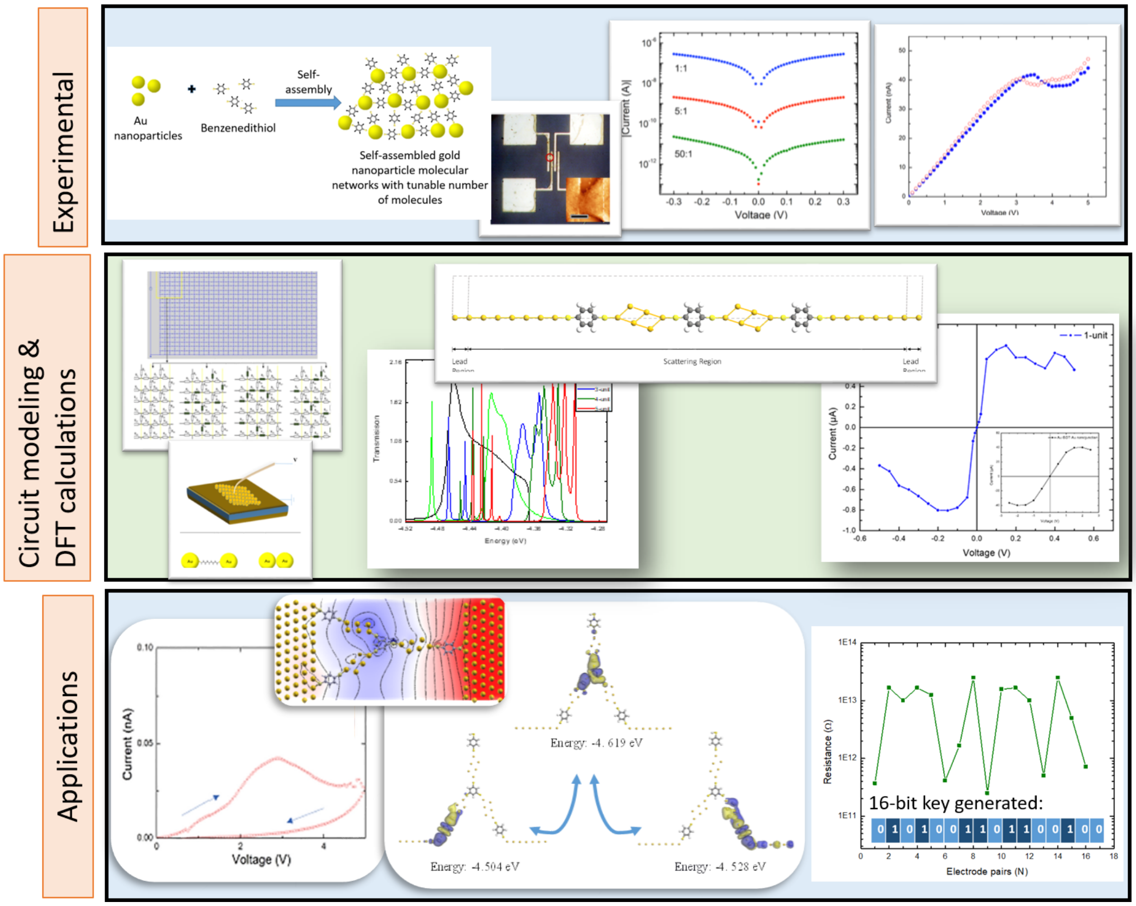

Figure 1.11: (a) Existing work on metal-molecule-metal junctions is mainly focussed on studies with very few molecules (dimers, trimers, etc. shown on left) or with many molecules (bulk films shown on right). Focus of the current work is in the intermediate region with tunable molecule-nanoparticle ratios. (b) A schematic representation of results from the current work [95][96] [97].

1.2 Overview of Thesis and Contributions

This thesis presents the study of electronic transport in nanoscale networks with tunable molecule-nanoparticle ratios. The outline of this thesis is as follows:

After the current chapter on general introduction to nanotechnology and molecular electronics, chapter 2 gives details of fabrication, various characterization, and analysis techniques used to fabricate and analyse the properties of self-assembled nanoscale networks with tunable molecule-gold nanoparticle ratios. Chapter 3 focusses on the experimental results obtained, with details associated to the obtained tunable electrical properties, based on various linear and non-linear *I-V* characteristics obtained at low- and high-bias measurements. This chapter also covers the simulation results of different metal-molecular networks using LTspice circuit modeling, which was used to compliment the experimental results. Chapter 4 is devoted to a brief description of the computational modeling tools and methods used to understand the electronic properties of gold nanoparticle molecular electronic networks, followed by the results obtained from various *ab-initio* calculations for understanding the electronic structure, transmission, and *I-V* properties of the modeled networks. Chapter 5 focusses on potential applications from the experimental and computational simulation results obtained in this work. An overall summary of this work, conclusions, and details of future work are presented in Chapter 6. Appendix A-F has details of scripts used for computational modeling and calculations, and Appendix G has additional details of Hamming distance metric tests, and the National Institute of Standards and Technology (NIST) tests to support the results presented in Chapter 5.

- **Contributions**

Journal articles

1. A. Venkataraman *et al.*, "Negative Differential Resistance and Hysteresis in Self-Assembled Nanoscale Networks with Tunable Molecule-to-Nanoparticle Ratios," *Physica Status Solidi (b)*, **vol. 257**, (6), pp. 2000019, 2020 [96].
2. A. Venkataraman *et al.*, "Carbon Nanotube Assembly and Integration for Applications," *Nanoscale Research Letters*, **vol. 14**, (1), pp. 220-220, 2019. [44] .
3. A. Venkataraman, P. Zhang and C. Papadopoulos, "Electronic transport in metal-molecular nanoelectronic networks: A density functional theory study," *AIP Advances*, **vol. 9**, (3), pp. 35122-035122-12, 2019 [95].
4. P. Zhang, A. Venkataraman and C. Papadopoulos, "Self-assembled gold nanoparticle-molecular electronic networks," *Physica Status Solidi (b)*, **vol. 254**, (9), pp. 1700061, 2017 [120].
5. Emadi, E.V., Venkataraman, A., Zaborniak, T.S.M., Zhang, P. & Papadopoulos, C., "Nanoelectronic circuit elements based on nanoscale metal-molecular networks", *Journal of Computational Electronics, 2021* (under revisions).
6. Emadi, E.V., Venkataraman, A, & Papadopoulos, C., "Nanoscale self-assembly: concepts, applications, and challenges", *Nanotechnology,* (submitted).
7. Venkataraman, A., Emadi, E.V. & Papadopoulos, C., "Hardware security using self-assembled nanoelectronic networks", in *Small* (to be submitted).

Conferences:

1. Venkataraman, A., Emadi, E.V. & Papadopoulos, C., "Random key generation using metal-molecular networks", in *American Chemical Society (ACS) Spring Meeting*, 2021 [97].
2. Emadi, E.V., Venkataraman, A., & Papadopoulos, C., "Nanoelectronic circuit elements based on nanoscale metal-molecular networks", in *American Chemical Society (ACS) Spring Meeting*, 2021 [99].
3. Zaborniak, T.S.M., Venkataraman, A., Emadi, E.V.& Papadopoulos, C., "Electronic Transport in Gold Nanoparticle-Molecular Networks", in *Jamie Cassels Undergraduate Research Awards (JCURA) Research Fair*, 2019.
4. Venkataraman, A., Zhang, P. & Papadopoulos, C., "Transport Properties of Metal Nanoparticle-Molecular Electronic Networks", in *Pacific Centre for Advanced Materials and Microstructures (PCAMM)*, 2017.

Chapter 2 Self-Assembled Nanoscale Networks with Tunable Molecule - Gold Nanoparticle Ratios

Fabrication of nanoscale networks was based on the self-assembly of thiolated molecules and colloidal gold nanoparticles using a potentially inexpensive solution-based technique. Here, by adjusting the gold nanoparticle to molecule ratio and/or type of molecule in the network, a directed self-assembly process to effect different circuit configurations results in tunable electrical conductance. This solution-based technique shows promise for designing molecular electronic circuits based on different network morphologies.

2.1 Motivation and Background

2.1.1 Self-Assembled Monolayers

Mulvaney and Giersig's work first reported the stabilization of gold nanoparticles with thiols of varying chain lengths [100]. Here, citrate- and alkanethiol-stabilized gold colloids were electrophoretically deposited onto carbon coated copper grids, leading to the formation of ordered monolayers (Figure 2.1). The core-to-core inter-particle spacing was influenced by the size of the alkane chains on the stabilizers used in the sol preparation.

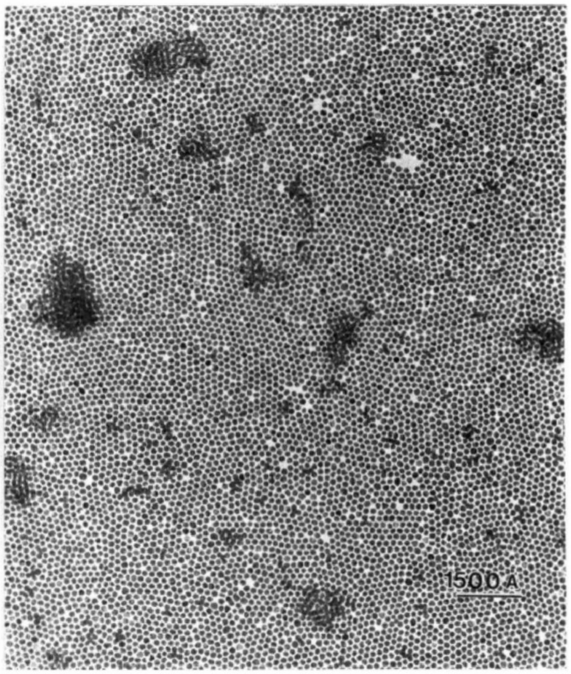

Figure 2.1: Electron micrograph image showing a 2D gold colloid monolayer deposited onto carbon coated copper grids by electrophoresis (Adapted from [100]).

Later, Brust *et al.* reported the facile synthesis of thermally stable and air-stable, dodecanethiol-stabilized nanoparticles of controlled size for the first time, using a two-phase liquid system that utilized the techniques of thiol self-assembly and ion-pair extraction [78]. In this synthesis, particles having average core diameters in the range of 1.3 nm were produced when a gold salt (hydrogen tetrachloroaurate) was reduced by sodium borohydride in the presence of a thiol molecule (Figure 2.2a). Electron micrograph images of the specimens showed the quality of the material to be polydisperse with a higher percentage of cuboctahedral and icosahedral structures (Figure 2.2b-c). This method excluding the use of a thiol could also be used to prepare wine-red colloidal solutions of gold particles diameters in the range of 8 nm [101].

Additionally, by adding dithiols in small quantities to the wine-red gold sols prepared in toluene (in the absence of a thiol) showed the formation of chains and globular supramolecular structures (Figure 2.2d).

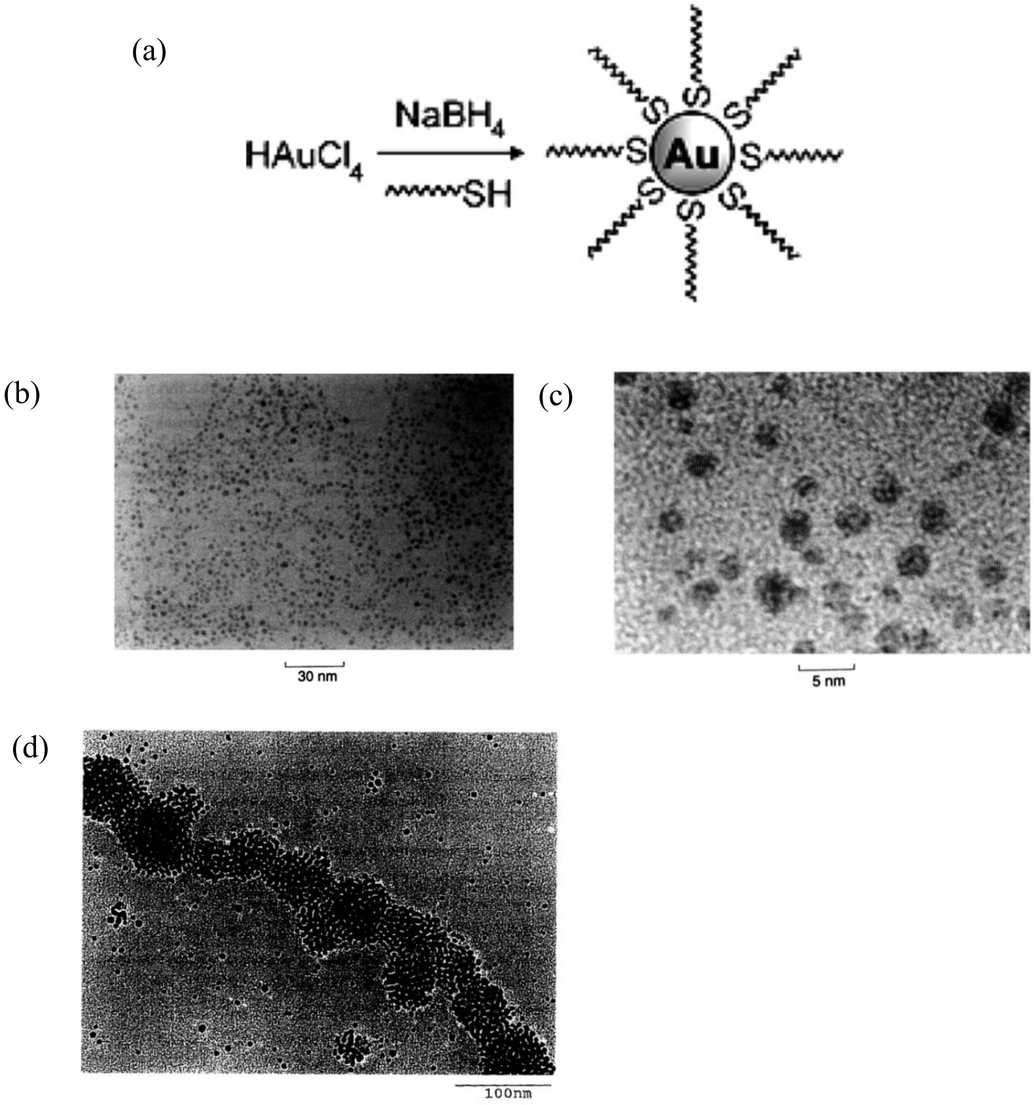

Figure 2.2: (a) Schematic of the formation of Monolayer-Protected Clusters using the Brust−Schiffrin method (Adapted from [102]). (b-c) Transmission electron micrograph (TEM) of thiol derivatized gold nanoparticles and (d) TEM image of gold nanoparticles prepared on treatment of 1,9- nonanedithiol (Adapted from [78], [101]).

Subsequently, various studies have reported modifications to this classic method of synthesizing monolayer-protected clusters using different type of thiols [103], [104] and different metals such as Ag, Cu, Pt, etc. [105], [106]. For example, Weisbecker *et al.* proposed a complementary method of producing SAMs of alkanethiolates via adsorption of alkanethiols onto the surfaces of gold colloids in aqueous dispersions [107]. This study used aliphatic thiols with the structure $HS(CH_2)_nR$, where 'R' refers to the functional group representing a variety of neutral and acidic functionalities. The functionalized gold colloids benefiting from the ability to tailor their surface properties using SAMs, have shown interesting applications in the field of biosensors and catalysis.

2.1.2 Nanoparticle Oligomers

Various studies report the controlled self-assembly of nanoparticles to produce nanoparticle oligomers (dimers, trimers, etc.). These nanoparticle oligomers are used in numerous applications in different research fields, such as plasmonics, chemical catalysis, bio-medical sciences etc. One of the challenges of fabrication of self-assembled nanoparticle clusters relies on the ability to control the interactions between nanoparticles in the colloidal solution, allowing for controlled self-assembly while avoiding bulk aggregates. Bar-Joseph *et al.* developed a procedure for synthesizing a dimer structure, consisting of two colloidal gold particles connected by three different dithiolated short organic molecules (Figure 2.3a) [79]. Here, a solution of dithiolated molecules was mixed with a gold colloid that was stabilized using the conventional citrate method [108]. It was reported that the thiols on the bridging molecule form stable Au–S bonds by displacing the citrate anions. Based on the number of molecules that bind to a colloidal particle, dimers; trimers; tetramers; and higher oligomers were formed (Figure 2.3 b-e). For example, dimer structures were formed when the concentration of the molecule *vs*. the colloidal gold particles was kept to be 1:10 (that resulted in the presence of fewer molecules as compared to the gol particles). Centrifuging was used to separate dimers from other monomeric or oligomeric particles. The corresponding nanoparticle-molecule-nanoparticle junction was used to study the electronic transport properties.

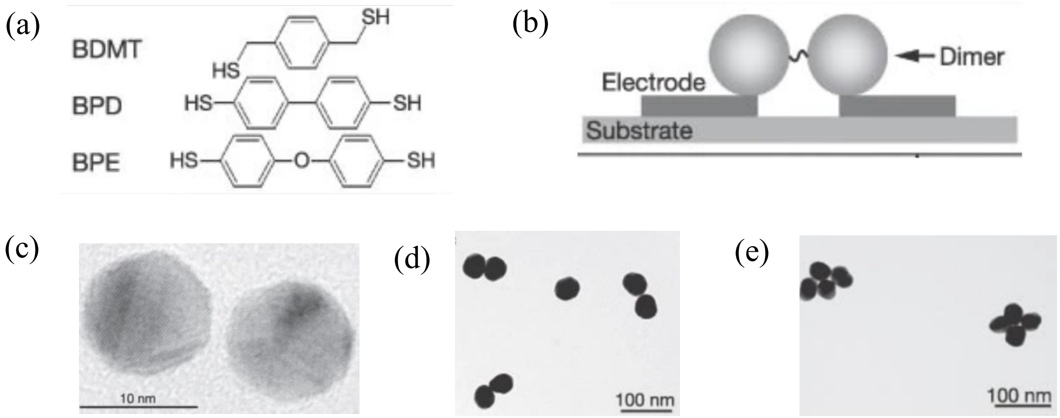

Figure 2.3: (a) Structures of dithiolated short organic molecules used in the preparation of nanoparticle oligomers. (b) Schematic of colloidal dimeric device (c) TEM image of a dimer formed using 10-nm colloidal gold particles, (d-e) TEM images of dimer and tetramer structures formed using 50-nm colloidal gold particles (Adapted from [79]).

An important aspect of building electronic devices on the molecular level that can potentially support the miniaturization of integrated circuits into the atomic scale depends on the ability to tune the electrical properties of the nanoparticle-molecular networks. The existing work on structures made up of gold nanoparticles and (di)thiol molecules represent two extreme cases based on the fabrication techniques used. In the first case, it either focusses on the formation of bulk films consisting of close-packed layers of molecule-covered nanoparticles (with many molecules in the network). Whereas, in the second case, focus is on the formation of well-defined molecular junctions with very single/very few molecules to produce nanoparticle oligomers (dimers, trimers, etc.). For bulk films, the conductance-measuring techniques involve measuring groups of tens of molecules and averaging them. On the other hand, the conductance-measuring techniques used in single-molecule-measurements give a well characterized value of molecular conductance. The main goal of this study is to understand the electronic properties of self-assembled nanoscale networks with tunable molecule-nanoparticle ratios in the intermediate regime, that falls between the properties of networks having particles that are fully covered by molecules (bulk films), and networks with few molecules interconnecting the nanoparticles (dimers, trimers, etc.) (Figure 2.4). The number of molecules interconnecting the colloidal gold particles can be controlled by varying the ratio of $N_{\text{molecules}}$: $N_{\text{particles}}$ during the fabrication process. In addition, the current study also focuses on understanding the effect of changing the type of molecule in the network and their corresponding variations in the electronic transport properties. The solution-based fabrication approach presented below shows the ability of directed self-assembly to create electronic networks with tunable building blocks to harness the unique electronic properties of next-generation molecular circuits.

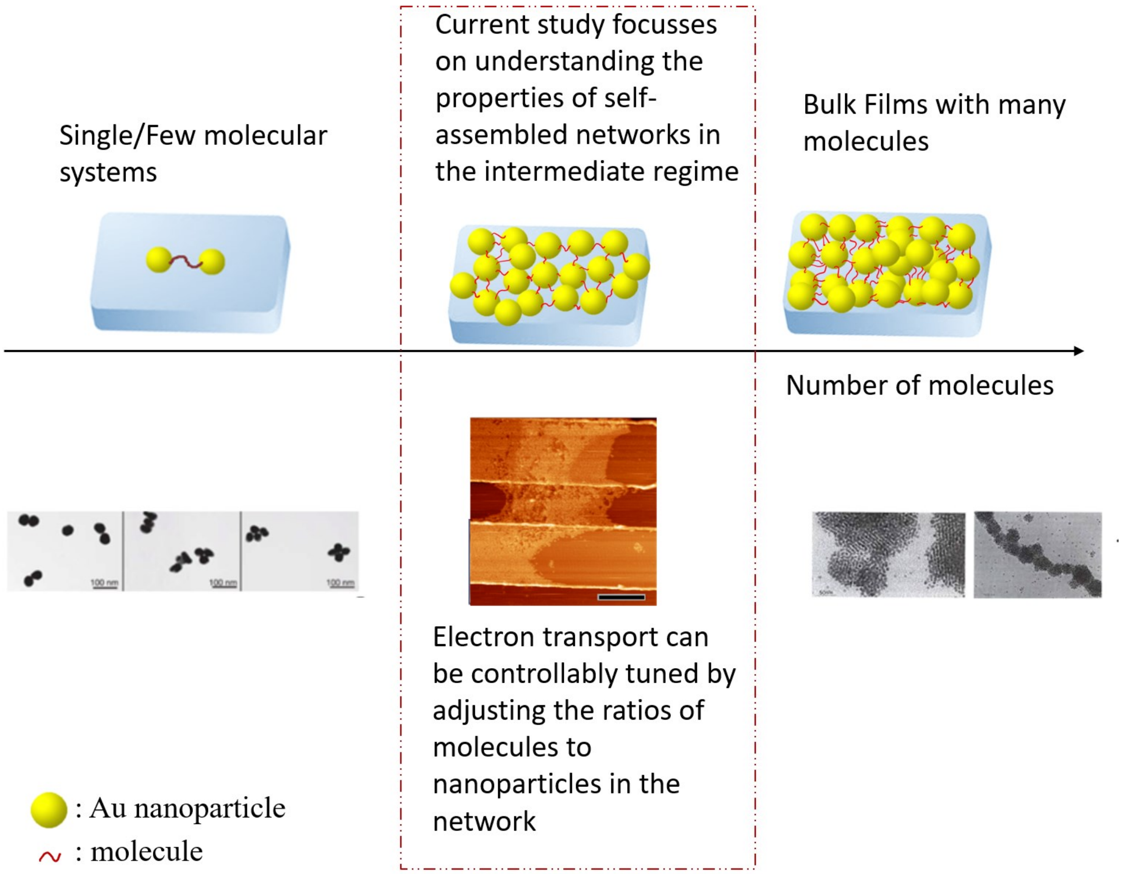

Figure 2.4: Existing work on metal-molecule-metal junctions is mainly focussed on studies with very few molecules (left) or with many molecules as compared to the number of particles (right) [75], [79]. Focus of the current work (center) is in the intermediate region with tunable molecule-nanoparticle ratios.

2.2 Fabrication Results

Nanoscale networks were fabricated based on the self-assembly of thiolated molecules and colloidal gold nanoparticles. Thiolated alkane molecules were used in the networks due to their relatively simple structure and extensively studied individual molecular properties. The synthesis procedure was based on methods described by Weisbecker *et al.* [107] and Dadosh *et al.* [79] with some modifications [120]. In our fabrication method, we control the number of molecular connections in the network by changing the ratio of the concentration of colloidal gold nanoparticles *vs.* the (di)thiol molecules. Additionally, we also change the type of molecule in the network and study the different network morphologies.

2.2.1 Recipe Details: Fabrication of Tunable Self-Assembled Gold Nanoparticle-Molecular Networks

30 nm citrate-stabilized colloidal gold nanoparticles; 1,4-benzenedithiol; 1, 6-hexanedithiol; 1, 9-nonanedithiol; 1-octanethiol and 1-hexanethiol were used in the fabrication of self-assembled gold nanoparticle-molecular networks. Deionized water and pure ethanol were used as solvents. Figure 2.5a shows a pictorial representation of the fabrication procedure followed.

The synthesis procedure involved varying the molecular concentrations in the gold nanoparticle–molecular networks to produce networks with different N_{molecule}:N_{particle} ratios (where N_{molecule} is the number of thiol/dithiol molecules and N_{particle} is the number of colloidal gold particles), in order to control the number and distribution of molecular connections in the resulting networks. For example, in order to achieve an $\mathrm{N_{molecule}}$:$\mathrm{N_{particle}}$ ratio of 1:1, a stock solution of molecules was first prepared in pure ethanol (1.5 x 10^{-4} M). This solution was diluted further in ethanol and stirred for about 5 min resulting in a concentration of 1.5 x 10^{-9} M. Next, colloidal gold suspension was centrifuged at 9.8 x 10^{3} g for 5 min, after which the supernatant was discarded. The deposit was resuspended in 1 mM NaOH solution. This centrifuging/resuspension procedure was repeated twice more resulting in a concentrated colloidal gold suspension (1.5 x 10^{-9} M) in NaOH. The colloidal gold suspension was then mixed with an equal volume of molecule solution and incubated at 4°C for 24 hours. For different $N_{molecule}$:$N_{particle}$ ratios, we repeated the above synthesis procedure using a modified concentration of molecular solution. After incubation, one or two 1 μL drops from the resultant suspension of colloidal gold particles and molecules were deposited on the substrates (that were first cleaned with acetone, isopropanol, and deionized water, dried using nitrogen gas), and allowed to dry under ambient conditions in order to form self-assembled Au-molecular networked films before proceeding with structural characterization.

The substrates consisted of an array of photolithographically patterned interdigitated gold electrodes with a thin adhesion layer on a silicon wafer substrate coated with a 100 nm layer of silicon dioxide. The gold electrodes on the substrates were ~35 nm thick, on top of a 5 nm thick Ti layer. The gaps between electrodes were in the range of 1-2.5 μm. Two-terminal current vs. voltage (*I-V)* measurements were performed on these substrates in a probe station connected to a semiconductor characterization system (see Chapter 3 for more detail), The steps involved in the fabrication process are shown in Figure 2.5b.

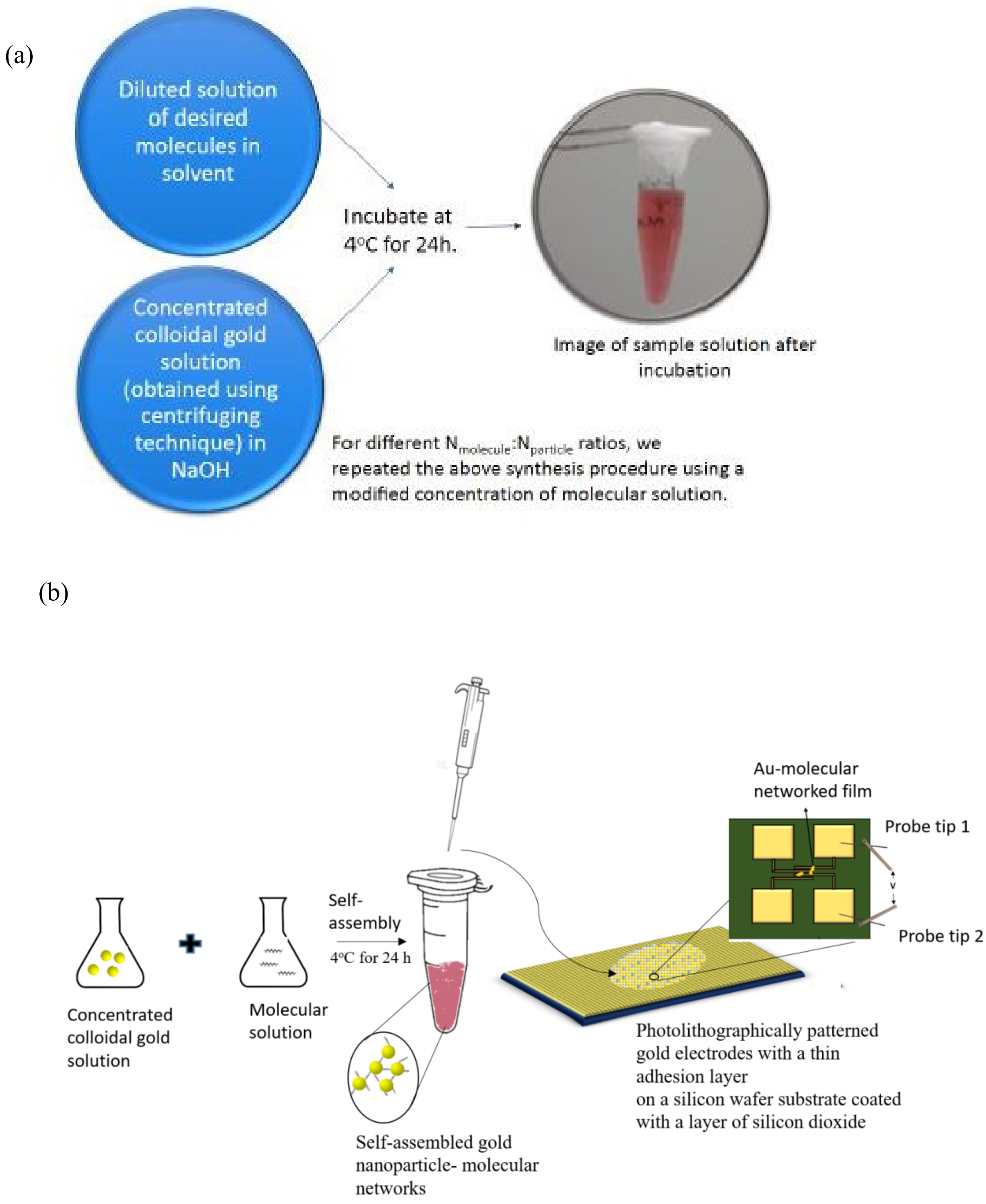

Figure 2.5: (a) Steps involved in the fabrication procedure. (b) Diagrammatic representation of steps involved in the fabrication and electrical characterization of the self-assembled Au-molecular networked films.

In order to study the effect variations in N_{molecule}: N_{particle} ratios, the above synthesis procedure was repeated using a modified concentration of molecular solution. Overall, in this work, results from the following ratios of N_{molecule}: N_{particle} were studied in great detail: 1:1, 5:1, and 50:1. For comparison, control samples were fabricated without any molecules, by mixing equal quantities of colloidal gold solution with ethanol.

In addition, to study the effect of type of molecule in the network, we fabricated several samples using different type of molecules (ex: benzenedithiol, nonanedithiol, hexanedithiol, hexanethiol, and octanethiol). For example, to fabricate gold-benzenedithiol networks, solutions of benzenedithiol in ethanol (at different ratios) were prepared and mixed with desired amount of colloidal gold solution in NaOH.

This recipe leads to the formation of metal-molecular networks with tunable electrical properties based on the type of molecule and/or $\mathrm{N}_{\text{molecule}}$: $\mathrm{N}_{\text{particle}}$ ratios, used in the network. With minor modifications in terms of the nanoparticle/ molecular concentrations used, the same recipe can also be used to fabricate networks with other types of molecules (ex: molecules other than benzenedithiol/ alkane(di)thiols), and using different sizes of gold nanoparticles (2 nm, 10 nm, 30 nm, etc.).

2.3 Structural Characterization and Analysis

2.3.1 AFM and Optical Microscopy

The morphology of the networked films was studied by using an Olympus BXFM optical microscope and Nanonics MultiView 1000™ AFM with pulled glass fiber tips

(10 nm nominal diameter) using intermittent contact mode. An AFM scan measures the three-dimensional topography of a sample by monitoring the inter-atomic forces acting between a scanning probe and the atoms on the surface of the sample. Figure 2.6 shows a schematic view of an AFM that consists of the following components:

- A sharp tip or a probe mounted on a cantilever
- Photodiode and laser that sense the deflection of the cantilever
- A feedback control system that can monitor and control the cantilever deflections
- A scanning system that can move the mounted sample with respect to the tip, and a computer that converts the acquired data into a 3D image. AFM scanners are made from piezoelectric material, which expands and contracts proportionally to an applied voltage.

AFM can be operated in many ways such as in tapping mode (also called as the intermittent contact mode), or in non-contact mode, or in contact mode. In this work, the AFM in intermittent contact mode is used for topography imaging. Briefly, the working principle is described as follows: the probe (or the tip) is made to oscillate near or at its natural frequency, touching the sample surface at every oscillation, without the tip sticking to the sample surface. At each oscillation, the tip experiences attractive and repulsive forces that cause the amplitude to vary. The deflection sensor measures the deflection or the variations of the cantilever from its reference amplitude. The feedback controller maintains constant amplitude of oscillation (based on a pre-determined value) of the cantilever. During this oscillation, when the tip approaches the sample surface, van der Waals forces, and electrostatic forces etc. (i.e., the long-range attractive forces) become dominant and the tip is pulled closer to the sample surface until it is in contact with the surface. Post this, repulsive forces start dominating and deflect the probe tip. In order to maintain the tip's amplitude of oscillation at the pre-determined value, the sample stage moves in the vertical direction. A deflection sensor monitors the cantilever deflections. Then, this data is sent to a computer that converts it into a 3D image. The structures of the networks formed was studied further using AFM image analysis software: WSxM, a freeware SPM software based on MS-Windows [109].

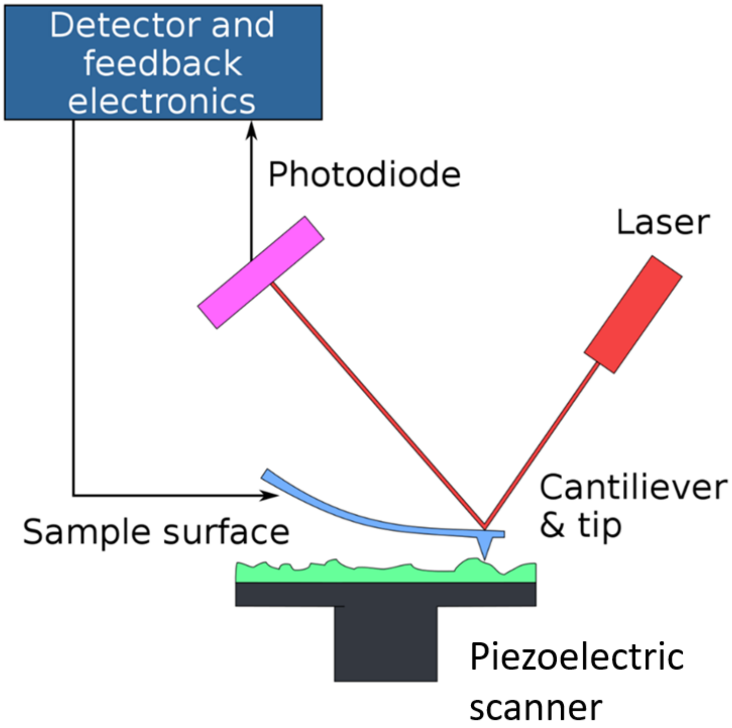

Figure 2.6: Schematic representation of various parts of an AFM system.

In this work, the electrical conductivity of samples is also probed locally, using conducting-tip AFM probes (pulled fibers covered by a chromium/gold coating, ~30 nm nominal diameter with a nominal cantilever length of 600 μm and spring constant equal to 10 N/m). Further details about the use of conducting-tip AFM are provided in Chapter 3. All measurements are obtained at room temperature.

2.3.2 Structural Characterization Results of Self-Assembled Nanoelectronic Networks with Tunable Molecule-Nanoparticle Ratios

Several samples containing 30 nm Au nanoparticle-molecular network solutions with tunable electrical properties were fabricated for structural characterization. Tunability was achieved by either varying the type of molecule in the network (i.e., by using one of the following: nonanedithiol, benzenedithiol, hexanedithiol, hexanethiol, and octanethiol) and/or, by varying the N_{molecule}: N_{particle} ratios of 1:5, 1:1, 5:1, and 50:1.

Figure 2.7 shows microscopic images of a typical networked film of colloidal gold particles and nonanedithiol molecules (N_{molecule}: N_{particle} ratio of 5:1) formed via directed self-assembly, and deposited between interdigitated electrodes on SiO_2/Si substrates. The optical microscopic image shows the networked film appears as a thick deposit (in yellowish gold color, indicated by a circle) that bridges the fingers of the gold electrodes. Further observations from AFM images support the evidence of how the dithiol molecules can act as linkers between gold nanoparticles during self-assembly.

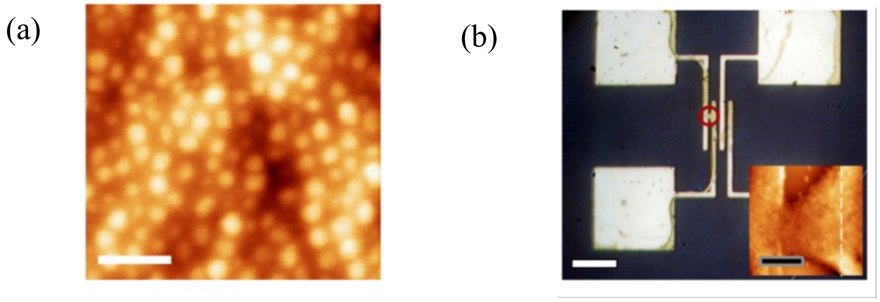

Figure 2.7: Microscope images of gold nanoparticle–nonanedithiol structures N_{NDT}: N_{particle} = 5:1. (a) AFM image of typical networked particle film self-assembled on SiO_2 substrate (scale bar equals 100 nm). (b) Optical microscope image of patterned gold electrodes after deposition of nanoparticle–molecular network from solution (scale bar equals 20mm). Inset shows corresponding AFM image of encircled region with network film bridging two electrodes (scale bar equals 1 mm). Effective dimensions for electrical characterization were estimated from the narrowest portion of the film deposits.

Similar observations were found in samples with networked film of colloidal gold particles and benzenedithiol molecules at N_{molecule}: N_{particle} ratio of 1:1, 5:1 and 50:1. Figure 2.8 shows microscopic images of a typical networked film of colloidal gold particles and benzenedithiol molecules (N_{molecule}: N_{particle} ratio of 1:1) formed via directed self-assembly, and deposited between interdigitated electrodes on SiO_2/Si substrates.

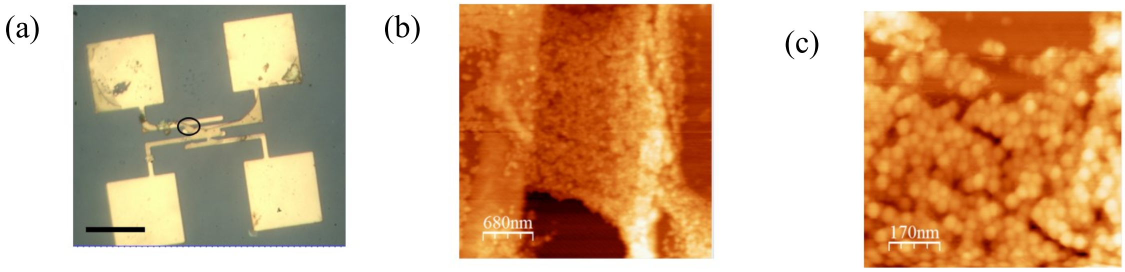

Figure 2.8: (a) Optical microscope image of patterned gold electrodes after deposition of gold nanoparticle-benzenedithiol network (N_{BDT}: N_{particle} = 5:1) from solution (scale bar equals 20 µm). (b) AFM image of encircled region in (a) showing gold nanoparticle-molecular film bridging gold electrodes (scale bar equals 3 µm). (c) Zoom-in AFM of networks (scale bar equals 1 µm; 100 nm in inset).

As an example, the microscopic images of a networked film of colloidal gold particles and benzenedithiol molecules at N_{molecule}: N_{particle} ratio of 5:1 (Figure 2.9).

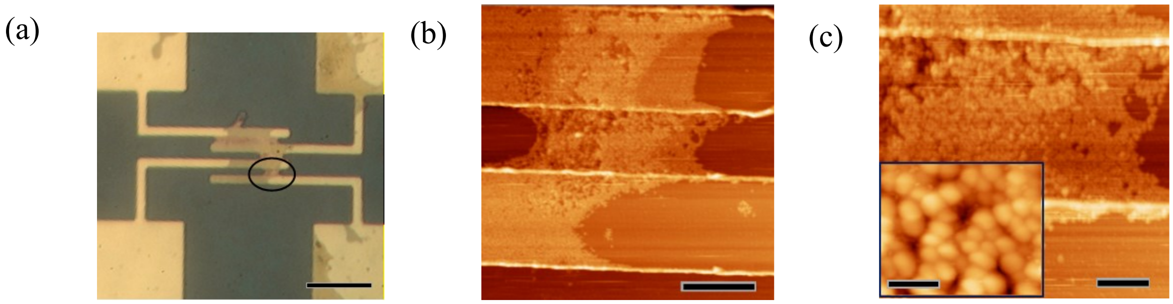

Figure 2.9: (a) Optical microscope image of patterned gold electrodes after deposition of gold nanoparticle-benzenedithiol network (N_{BDT}: N_{particle} = 5:1) from solution (scale bar equals 15 μm). (b) AFM image of encircled region in (a) showing gold nanoparticle-molecular film bridging gold electrodes (scale bar equals 3 μm). (c) Zoom-in AFM of networks (scale bar equals 1 μm; 100 nm in inset).

Figure 2.10 shows the microscopic images of a networked film of colloidal gold particles and benzenedithiol molecules at N_{molecule}: N_{particle} ratio of 50:1. Similar to the networks formed with N_{molecule}: N_{particle} ratio of 1:1, and 5:1, the 50:1 ratio sample also showed clear network formations after the deposition of suspensions of colloidal gold particles and thiolated molecules on the substrates. However, one difference to note is the colour of the networked film observed in the 50:1 ratio sample, which showed blue/black deposits between the electrode fingers as opposed to golden coloured networks formed in the 1:1 and 5:1 sample. One reason for this could be the presence of higher number of molecules in the network, as compared to the number of colloidal gold particles.

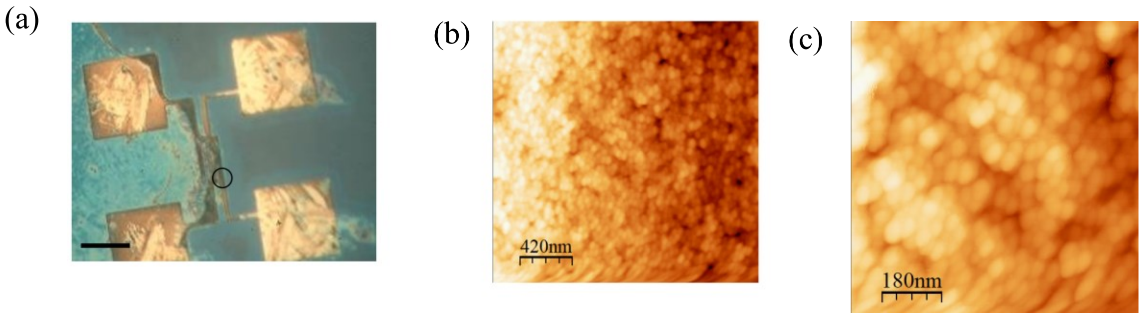

Figure 2.10: (a) Optical microscope image of patterned gold electrodes after deposition of gold nanoparticle-benzenedithiol network (N_{BDT}: $N_{\mathrm{particle}} = 50:1$) from solution (scale bar equals 15 μm). (b) AFM image of encircled region in (a) showing gold nanoparticle-molecular film bridging gold electrodes (scale bar equals 3 μm). (c) Zoom-in AFM of networks (scale bar equals 1 μm; 100 nm in inset).

2.3.2.1. AFM Image Processing: Height Analysis

The two-dimensional profiles (or cross sections) were used to measure the distance and height of the structures formed. AFM measurements of 30 nm colloidal gold nanoparticle dimers and larger oligomers observed after depositing suspensions based on different molecules confirmed the individual gold particle height as approximately 30 nm. This value corresponds to the diameter of colloidal gold used in this work. In addition to dimers and larger oligomers, large networked films were also observed on the substrates, either between the electrodes or on the large area of the gold film. (Figure 2.11).

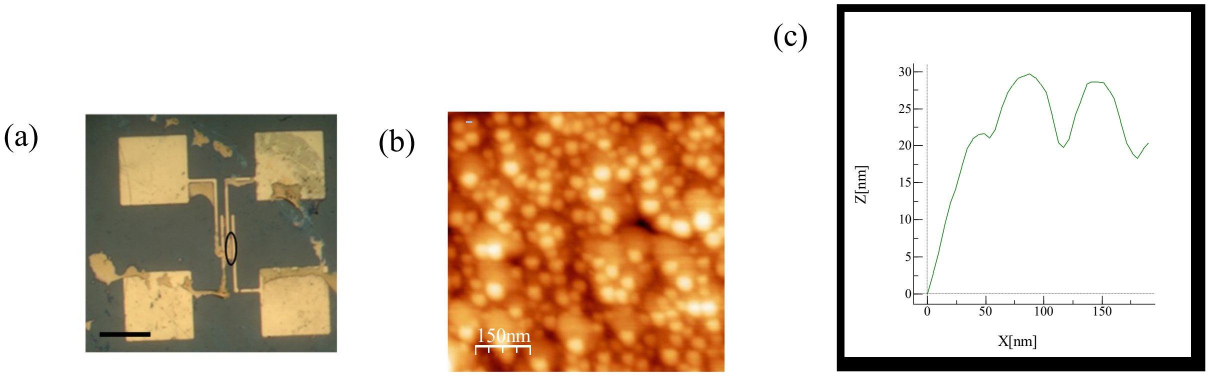

Figure 2.11: (a) Optical microscope image of patterned gold electrodes after deposition of gold nanoparticle-benzenedithiol network from solution with N_{BDT}: N_{particle} = 5:1 (scale bar equals 15 µm). (b) AFM image of encircled region in (a) showing gold nanoparticle-molecular film bridging gold electrodes. (c) AFM cross-sectional profile shows the gold particle height as approximately 30 nm, corresponding to the colloidal gold diameter. Blue line represents the area selected for height analysis.

In some cases, the network was composed of multiple layers (2or 3 layers thick) of colloidal gold nanoparticles, as seen in Figure 2.12. In this example, the cross-sectional analysis of the AFM image showed the particle height to be about 180 nm in some areas, indicating that the network is composed of multiple layers (in this case, approximately five-six layers) of colloidal gold nanoparticles.

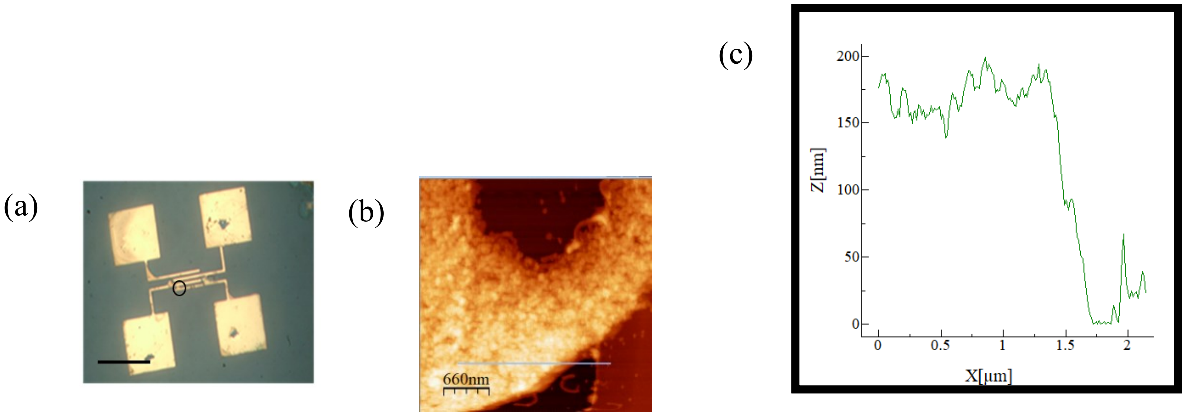

Figure 2.12: (a) Optical microscope image of patterned gold electrodes after deposition of gold nanoparticle-benzenedithiol network from solution with N_{BDT}: N_{particle} = 5:1. (scale bar equals 20 µm) (b) AFM image of encircled region in (a) showing gold nanoparticle-molecular film bridging gold electrodes. (c) AFM cross-sectional profile shows the gold particle height as approximately 180 nm in some areas, corresponding to multilayers of colloidal gold nanoparticles. Green line represents the area selected for height analysis.

2.3.2.2 Defects

Previous work on SAMs has shown that the homogeneity and nature of defects in the self-assembled structures, can be considered detrimental or advantageous to applications and device assembly [110]. The appearance of defects could be due to both intrinsic and external factors. The external factors contributing to defects include dirt or contamination on the substrate, purity of the solutions used during fabrication and, defects introduced due to handling/issues during the experiment [111]. On the other hand, internal factors contributing to the defect formation include, defects due to the thermodynamics of formation. For example, previous work on thiol SAMs on gold, has shown to exhibit etch pits (or vacancy islands), possibly due to the extraction of adatoms from the substrate and formation of adatom-adsorbate moieties [112]. Alternatively, defects can be regions where the molecules are not well organized, i.e., regions where hydrocarbon chains are not fully extended, or have a different tilt (α). High-quality SAMs are critical for many applications in the field of molecular electronics. For example, metallization of the thiol SAMs is often needed to build different types of devices. However, during metallization from the gas phase, SAM defects lead to the diffusion of metal adatoms, thereby connecting the deposited metal layer with the substrate, and leading to inefficient systems [113]. Additionally, substrate-induced defects dramatically increase the oxidation rate of the alkanethiolate molecules (to form sulfonates) [114]. In terms of advantages, defects can be utilized to build nanocontacts and to prepare small metallic nanoclusters by confined growth at defects. Additionally, the charge transfer through SAMs is also influenced by the defects. For example, in one study, the presence of defects, offered an alternative path to charge transfer. It was reported that electron transfer occurred mainly through defects, and the charge transfer was hindered when the defect density was reduced [113].

In this work, defects, loose packing, and clustering of particles was evident in various samples. Figure 2.13 (a-c) shows an example of cracks/holes in the network film of gold nanoparticle-benzenedithiol network from solution with N_{BDT}: N_{particle} = 1:1. Figure 2.13 (d-e) shows loose packing in the gold nanoparticle networks.

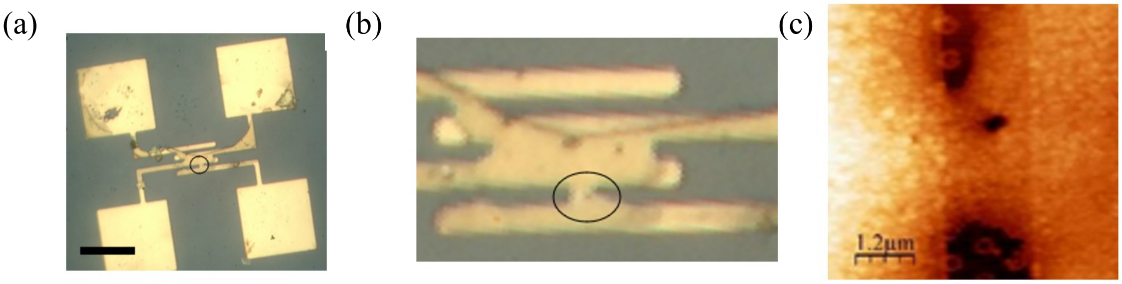

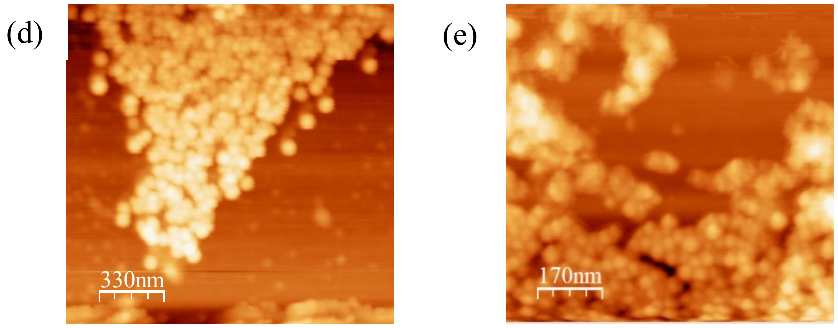

Figure 2.13: (a) Optical microscope image of patterned gold electrodes after deposition of gold nanoparticle-benzenedithiol network from solution with N_{BDT}: N_{particle} = 1:1. (scale bar equals 20 μm) (b) Zoom-in of the optical image of encircled region in (a) showing gold nanoparticle-molecular film bridging gold electrodes. (c) AFM image of network shown in the encircled region (a), showing a defect in the network. (d) AFM image of gold nanoparticle network from solution with N_{BDT}: N_{particle} = 1:1. (e) AFM image of gold nanoparticle network from solution made without molecules and deposited on SiO_2 substrate. Loose packing and defects are likely caused by the lack of strong particle coupling due to absence of thiolated molecules.

In order to investigate the source of defects/loose packing, we closely examined the structure of such samples via AFM. The defects in the networks fabricated in this work, could be due to impurities in the thiol molecule used, or due to impurities in the surface, or due to variations and restructuring of the underlying gold surface. Additionally, it was seen that networks showed loose packing in samples containing small number of molecules. Essentially the molecular "glue" that largely guides the directed self-assembly process of the network circuits is missing in this case, leading to lack of strong particle coupling due to absence of thiolated molecules. This leads to higher resistance due to decreased availability of electron paths to traverse the network. We noticed similar features (defects/ loose packing) when thiols were used in the fabrication of the gold-molecular networks, instead of dithiols. From the optical and AFM characterizations, it appears that a ratio of molecules to nanoparticles of between 1:1 and 5:1 is needed to achieve well-connected molecular electronic networks. This conclusion is further supported using the electrical characterization results that are presented in Chapter 3 of this work.

In conclusion, nanoscale networks based on the self-assembly of thiolated molecules and colloidal gold nanoparticles were fabricated and their structural characteristics were studied as a function of the number, and type of molecular connections. By modifying the N_{molecule}: N_{particle} ratio during the synthesis, this technique allows for the formation of metal-molecular networks with varying number of molecules, whose number falls in the intermediate range between the networks representing bulk films, and nanoparticle dimers. Changes in the network topology was observed by varying the concentration of (di)thiol molecules, and/or the type of (di)thiol molecules used in the synthesis. The ability to tune the network properties using the solution-based approach described in this work, displays the ability of directed self-assembly for engineering molecular circuits.

Chapter 3 Electrical Characteristics of Metal-Molecular Nanoelectronic Networks

3.1 Experimental Setup

Current-voltage (*I-V*) data was obtained by electrical measurements using a Janis probe station, which was configured with an electrical characterization system (Keithley 4200 semiconductor characterization system). Figure 3.1 shows a schematic of the probe station setup.

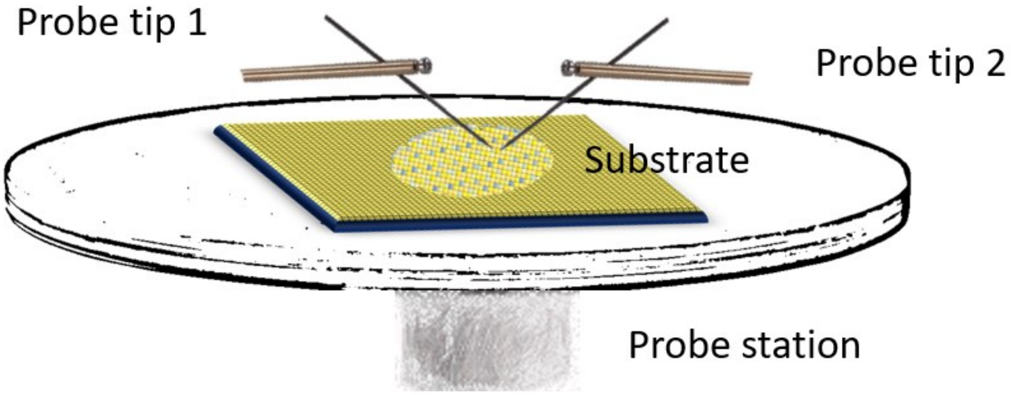

Figure 3.1: Schematic representation of the probe station setup.

The two-terminal *I-V* measurements are carried on the sample substrates with self-assembled gold-molecular network films that are formed between the interdigitated electrodes. The sample substrate is loaded into the probe station containing tungsten probes. An optical microscope is connected to the probe station that enables clear visualization of the probe tips, and helps in precise placement of the two tips at the desired location on the sample substrate. In addition, the optical microscope is also connected to a computer screen, which serves as an alternative platform to locate a desired area of the sample. The two probes apply a programmed voltage sweep on the selected electrodes and the current response data is recorded using the Keithley 4200 semiconductor characterization system.

All the measurement were conducted at room temperature and recorded in the Keithley Source-Measure Unit. The low-bias *I–V* measurements were done by setting the voltage across the two terminals to sweep from -0.3 V to +0.3 V with a step size of 0.01 V. In some cases, the voltage across the two terminals was set to sweep from -0.5 V to +0.5 V with a step size of 0.025 V. On the other hand, all the high bias *I–V* measurements were done by setting the voltage across the two terminals to sweep from -5 V to +5 V with a step size of 0.1 V. For samples showing nonlinear *I-V* characteristics at high bias, the samples were tested for potential hysteretic behavior by sweeping the voltage from 0 to +5V, and then back to 0 V; and 0 to -5 V and then back to 0 V.

3.2 Substrates

Substrates for two-terminal *I–V* measurements consisted of photolithographically patterned interdigitated gold electrodes with a thin adhesion layer on a silicon wafer substrate coated with a 100 nm layer of silicon dioxide. The gold electrodes were ~40 nm thick, on top of a 5 nm thick Ti layer. The gaps between electrodes were in the range of 1-2.5 μm. Two-types of substrates, namely 4-pad and 8-pad, were majorly used for *I-V* measurements. Figure 3.2 shows examples of the device architecture with multiple electrode pairs.

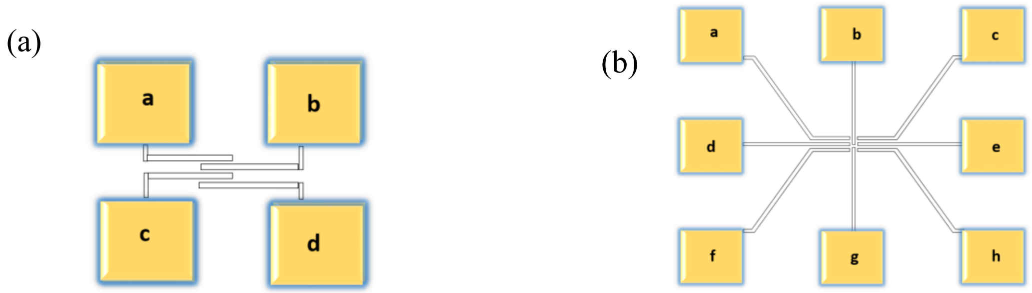

Figure 3.2: Schematic of the device architecture showing multiple electrode pairs (a) 4-pad substrates indicated by alphabets a-d (b) 8-pad substrates indicated by letters a-h.

3.3 Results and Discussions

Study of thiolated molecules (1,4 benzenedithiol; 1,3,5 benzenetrithiol; 1, 8-octanedithiol; 1, 6-hexanedithiol; and 1, 9- nonanedithiol) with colloidal gold is considered to be of increasing importance in the field of molecular electronics [69], [74], [78], [107]. In this work, several samples were fabricated for electrical characterization by using different dithiol/thiol molecules (based on benzene, hexane, octane, and nonane), and by using different N_{molecule}: N_{particle} ratios. This section shows the low and high bias I–V curves of various gold nanoparticle- molecular network samples that show variations in the network resistance by tuning the number/type of molecules in the network.

3.3.1 Tunable Electrical Properties of Alkane(di)thiol-30 nm Gold Nanoparticle Networks

3.3.1.1 Linear *I-V* characteristics obtained at low-bias measurements

<u>Nonanedithiol-Gold Nanoparticle Networks</u>

The low-bias current–voltage (*I–V*) plots of gold nanoparticle network samples formed with nonanedithiol for an N_{NDT}:N_{particle} ratio of 1:1, 5:1 and 50:1 showed significant amount of current whose magnitude varies between μA and pA, as the ratio of N_{NDT}:N_{particle} is varied. Most of the *I-V* curves showed linear behaviour in the low-bias regime, which could be explained using the simplified Simmons equation that was derived to model the tunneling current density though a trapezoidal barrier in a low bias range [63]:

$$J = J_0 \, e^{-\beta d} \tag{3-1}$$

Where 'J' is the tunneling current density that flows through the barrier (in units of A cm^{-2}); 'β' is the tunneling decay constant (in Å^{-1}); 'd' is the barrier width (in Å); 'V' is the applied bias (in V); 'J_0' is the hypothetical current density (in A cm^{-2}) that flows across the junctions when 'd' is zero. Simmons's equation illustrates that as the barrier thickness increases, often corresponding to the larger molecular length in the molecular junctions, the tunneling current shows an exponential decrease.

In addition, weak non-linearity was seen in some samples, which had higher number of molecules in the network, as compared to the gold nanoparticles. This observation is consistent with previous work using alkane molecules [115] (Figure 3.3).

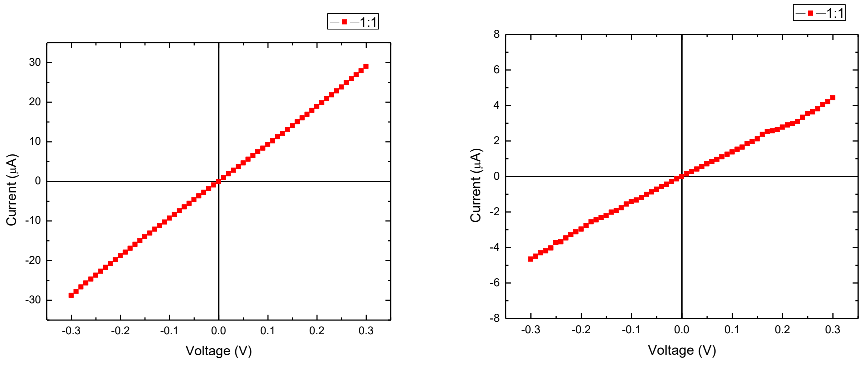

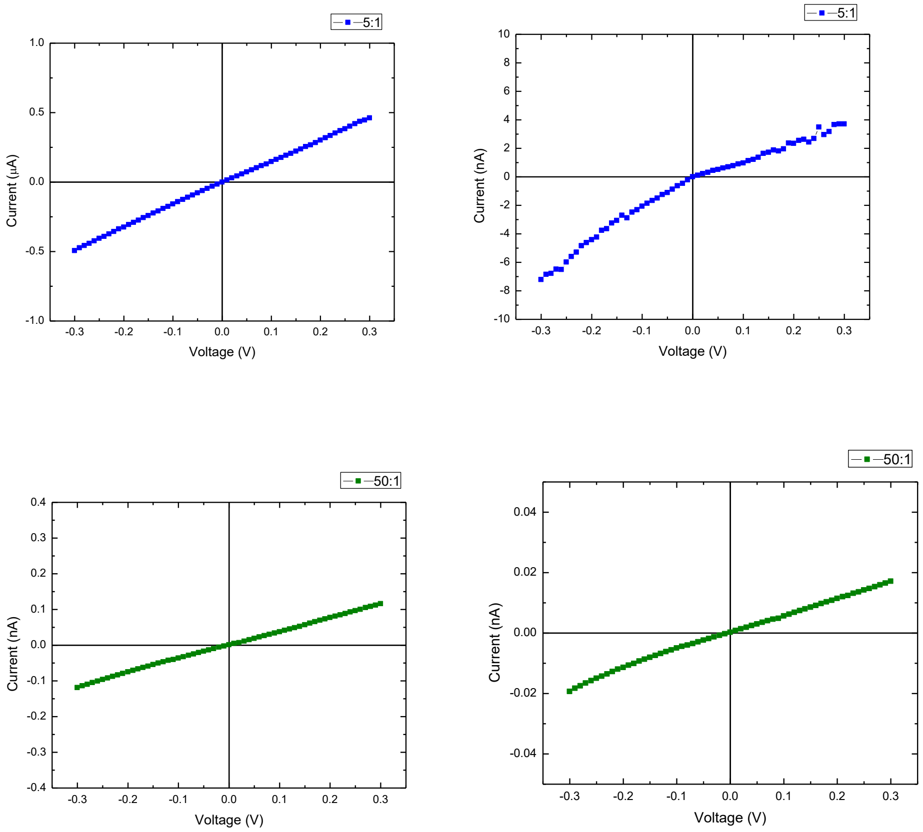

Figure 3.3: Plots of current *vs.* voltage for different molecule to nanoparticle ratios of nonanedithiol network samples: 1:1 (red), 5:1 (blue), and 50:1 (green).

Overall, on comparing the *I*-*V* curves of samples with different N_{NDT}:N_{particle} ratios with approximately equal film length to width dimensions, it was observed that the current was typically in the μA range for 1:1 samples, whereas the current decreased to the nA range for 5:1 network samples and further decreased to ~pA for 50:1 ratio samples (Figure 3.4). These results show that the measured current depends on the number of molecules in the network, i.e., the current decreases with an increase in the number of molecules, agreeing with the length-dependence regulation described by Simmons model [63]. In other words, an increase in the network resistance was observed with an increase in the percentage of molecules in the network.

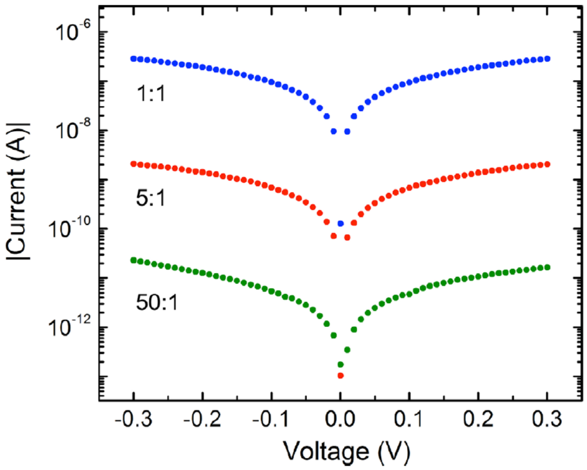

Figure 3.4: Semi-logarithmic plots of magnitude of current *vs.* voltage for different molecule to nanoparticle ratios of nonanedithiol network samples: 1:1 (blue), 5:1 (red), and 50:1 (green). All sample film length to width dimension ratios for data shown are approximately equal.

Hexanedithiol-Gold Nanoparticle Networks

The low-bias current–voltage (*I*–*V*) plots of gold nanoparticle network samples formed with hexanedithiol for an N_{HDT}:N_{particle} ratio of 1:1, 5:1 and 50:1 showed significant amount of current, whose magnitude varies as the ratio of N_{HDT}:N_{particle} is varied. Most of the *I-V* curves showed linear behaviour, a characteristic similar to the results seen in the low-bias regime of the nonanedithiol network samples. As an example, *I-V* plots of N_{HDT}:N_{particle} ratio of 1:1, and 5:1 are shown in Figure 3.5 below.

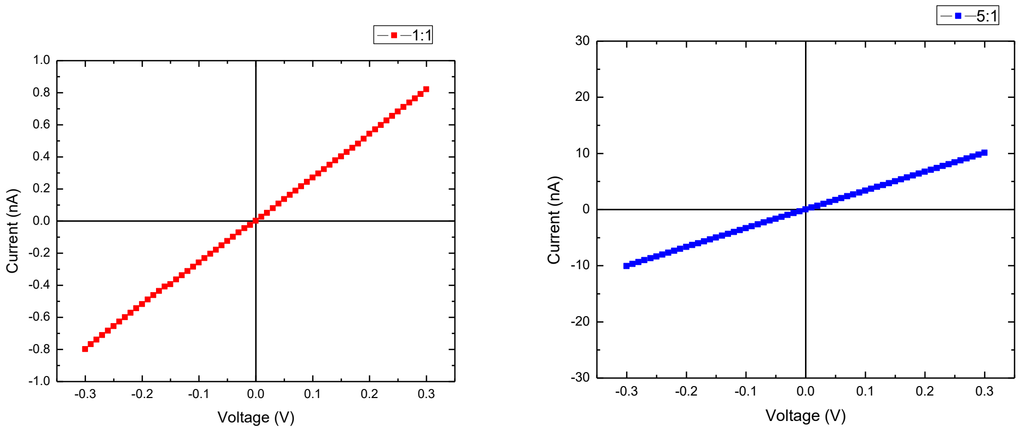

Figure 3.5: Plots of current *vs.* voltage for different molecule to nanoparticle ratios of hexanedithiol network samples: 1:1 (red) and 5:1 (blue).

Octanethiol-Gold Nanoparticle Networks

As expected, the alkanethiols network samples showed larger resistances than the sample networks with alkanedithiols [115], [116]. The low-bias current–voltage (*I*–*V*) plots of gold nanoparticle network samples formed with octanethiol for an N_{OT}:N_{particle} ratio of 1:1 and 5:1 show significant amount of current, whose magnitude varies as the ratio of N_{OT}:N_{particle} is varied. Most of the *I-V* curves showed linear behaviour. Some of the 50:1 ratio samples showed slight non-linearity. (Figure 3.6).

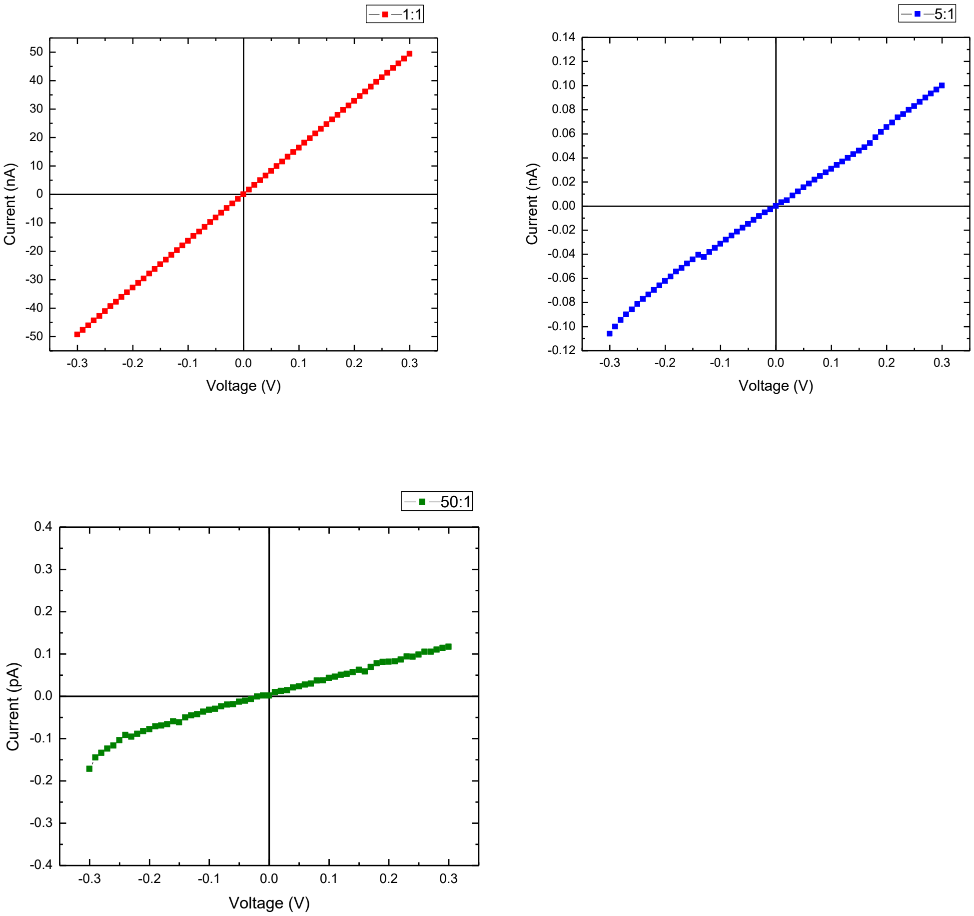

Figure 3.6: Plots of current *vs.* voltage for different molecule to nanoparticle ratios of octanethiol network samples: 1:1 (red), 5:1 (blue), and 50:1 (green).

Figure 3.7a shows the *I–V* curves of gold nanoparticle molecular networks for different molecules. The highest currents were observed for hexanedithiol network samples, whereas nonanedithiol network samples had currents that were several orders of magnitude smaller. In other words, as the chain length of the molecules (nominally 9.5A for hexanedithiol; and 13Å for nonanedithiol) in the network increases the current decreases. This result is consistent with the previous work that shows that the conductance of alkanedithiol/ thiol molecules decreases exponentially with increasing number of methyl units [116–118]. Lastly, compared to dithiols, much lower currents for thiol molecules such as octanethiol and hexanethiol were observed, and this behavior can be attributed to the higher resistance for the S/Au bond formed for the thiol samples as compared to the S/Au bond for the dithiol network samples (Figure 3.7b). In addition, in case of networks formed with alkanethiols, as only one end of the molecule is strongly coupled to gold, it leads to a larger overall network resistance.

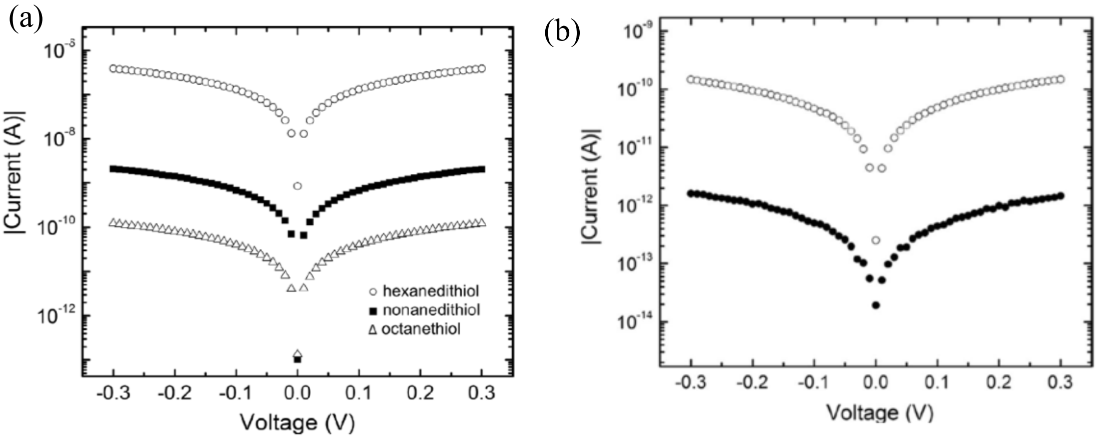

Figure 3.7: Semi-logarithmic plots of magnitude of current *vs.* voltage for (a) gold nanoparticle–molecular network samples (5:1) containing different molecules: hexanedithiol (open circles), nonanedithiol (solid squares), and octanethiol (open triangles). (b) gold nanoparticle–molecular network samples (1:1) containing hexanethiol (solid circles) and hexanedithiol (open circles) illustrating roughly two orders of magnitude decrease in current for thiol *vs.* dithiol networks. Sample film length to width dimension ratios for data shown within each plot were approximately equal.

3.3.1.2 Circuit Modeling using LTspice

Observations from Conducting-tip AFM

In order to probe the nanoparticle-molecular networks locally, conducting-tip AFM in contact mode was used with a small bias voltage (10-50 mV) applied to the tip relative to the substrate (Figure 3.8a). The materials to be probed were deposited on a thin gold film substrate that was connected to ground potential. Conductance of the sample was obtained when the tip was lowered on the gold film. This technique allows us to examine electron transport through the networks in the vertical direction (typically two or three monolayers thick) between the AFM tip and substrate. By probing different locations of gold nanoparticle-dithiol network film samples, two distinct resistance ranges, i.e., either kΩ or MΩ were observed. This implies the existence of two types of connections between neighboring particles in the network (Figure 3.8b): In the first type of connection, a molecule bridges gold nanoparticles, whereas, in the second type of connection, particles are directly touching each other. When the vertical region between the conducting tip and gold substrate is interconnected by molecules, the resistance is larger compared to regions made up of only close-packed gold particles (in this case, determined by the contact resistance between neighboring nanoparticles).

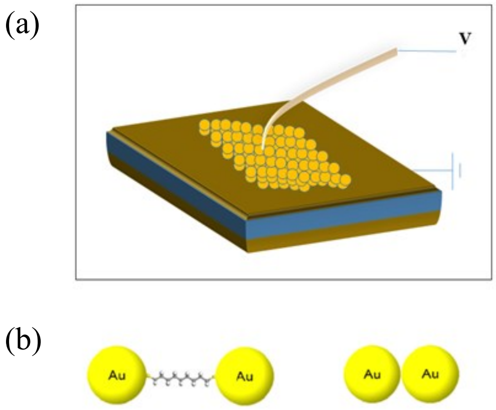

Figure 3.8: (a) Schematic of conducting-tip AFM measurement setup used to probe nanoparticle-molecular networks by applying small bias voltage applied to the tip (coated with thin film of gold) relative to the thin film gold substrate held at ground potential. (b) Representation (not to scale) of two possible particle connections within the network: gold nanoparticles are bridged by a molecule (left), or are in direct contact with each other (right).

The variations in resistance found using conducting-tip AFM can be used to model the network's structure: Figure 3.9a shows an idealized network morphology wherein all particles are connected via molecules. However, extrapolating from the conducting tip AFM data, the topology of the network would in general consist of both molecular contacts and direct gold-gold contacts (Figure 3.9b). In order to study the effect of different configurations on electronic transport through the nanoparticle-molecular networks LTspice, a SPICE simulation tool for electronic circuits by Linear Technology Corporation was used to implement a circuit model of the networks as described below.

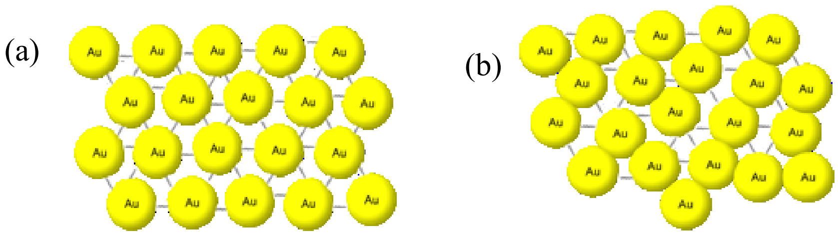

Figure 3.9: Schematic (not to scale) of possible configurations within self-assembled gold nanoparticle-molecular networks. (a) Neighboring gold nanoparticles are bridged by molecules. (b) In addition to gold-molecular connections, gold-gold connections exist for nanoparticles in direct contact with each other.

First structures are abstracted such as those in Figure 3.9 into a general network of interconnected resistors. For this purpose, a close-packed lattice with each particle having six nearest neighbors was considered and each particle in the network is converted into a lattice of resistors representing the inter-particle electrical connections as shown in Figure 3.10a. This basic element is used to create larger network circuits as shown in Figure 3.10(b-c): A building block of 36 resistors (yellow box), represented by unique variables R_1 to R_{36}, is the unit cell for the circuit. The network is then created by repeating the unit cell as per the desired dimensions obtained from microscopy data. It was assumed that the gold-gold nanoparticle contacts within the network have a resistance equal to the quantized value of 12907 Ω. In order to vary the number of gold-molecule connections *vs.* gold-gold particle contacts, a Python script (see Appendix D) using the function "random.shuffle" that is based on the Mersenne Twister pseudorandom number generator was used. The random variable generator assigns a resistor in the unit cell to be one of two values – either the quantized inter-particle contact resistance or the appropriate molecule's resistance (using values based on previous work) [79], [119]. Thus for different configurations the resistor values are randomized within the unit cell. Figure 3.10(d-f) show example random configurations found in this manner for a network containing 25% molecular connections. The resistance of the network was calculated five times (i.e., five random configurations) for each percentage in order to emulate the experimental relation between network resistance and the percentage of molecules in the network statistically.

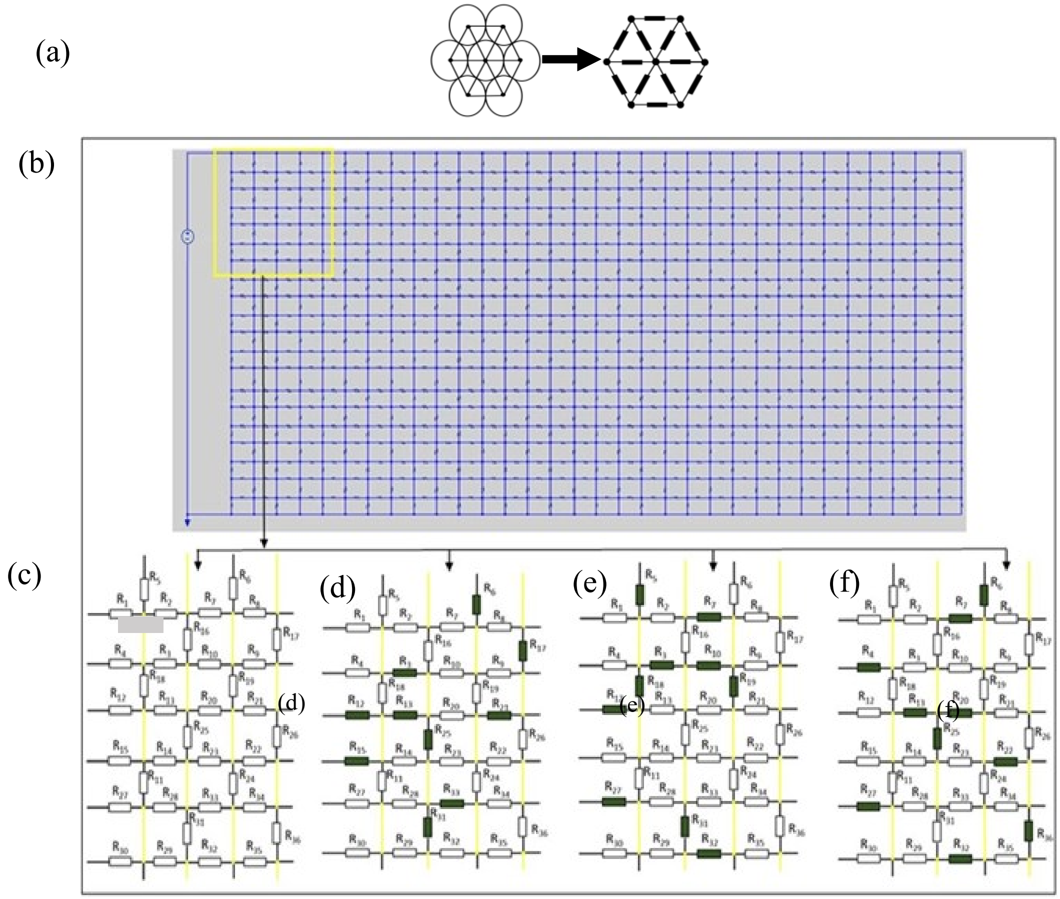

Figure 3.10: (a) Abstraction of particle connections into interconnected resistors. Particle with six nearest neighbors (left) is converted into resistor circuit elements (right). (b) Example resistor network (length: 330 nm, width: 1000 nm) construction for circuit simulations. Top and bottom connections are considered bulk electrode contacts to the network with a resistance of 0.55 Ω. Yellow highlighted box represents the unit cell (building block of the circuit network). (c) Unit cell close-up showing 36 resistor variable positions. The yellow lines represent nanoparticles, each with six nearest neighbor connections. Each resistor is assigned one of the two possible values, i.e., either gold-gold nanoparticle contact resistance or molecule resistance. (d-f) Randomized unit cell configurations corresponding to 25% molecular connections (molecules – dark, gold-gold nanoparticle contacts – white).

Figure 3.11 shows circuit simulation results for a nonanedithiol network with dimensions of length and width both equal to 500 nm. The calculated resistances ranged from approximately 10 kΩ (for all gold particles in the network) to almost 1 GΩ (for all contacts between particles equal to the resistance of nonanedithiol, which was set to 10^9 Ω). There is a transition or threshold region, typically around 50% of molecular connections, where the different resistor circuit configurations also display more dispersion in the calculated resistances due to random variations in network morphology.

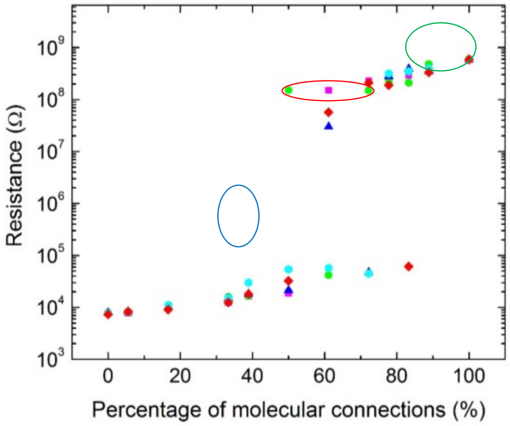

Figure 3.11: Circuit simulation results for a 500 nm by 500 nm network. Semi-log plot of gold nanoparticle-nonanedithiol network resistance *vs.* percentage of molecular connections in circuit. Colored symbols correspond to five simulation trials. Overlap of experimental resistance data with simulated results for 5:1 (red circle) and 50:1 (green circle) ratio samples shown. 1:1 ratio sample data (blue circle) shown lying outside of simulated values.

Compared to the experimental data the spice circuit model showed good agreement for samples with molecule to nanoparticle ratios greater than 1:1 (i.e., 5:1, and 50:1). For example, the measured resistance for 5:1 nonanedithiol network samples in Figure 3.11, fall near 50–70% of molecular connections in the network, with 50:1 sample resistance data located near 100% molecular connections, as expected. Similar agreement with experimental data was found for simulations of networks containing hexanedithiol molecules (molecule resistance set to 10^7 Ω). However, we consistently found that samples with N_{molecule}:N_{particle} ratios of 1:1 had measured resistances that were somewhat greater than the simulated values, regardless of molecule type or network dimensions. Further electrical measurements on samples with network ratios of 1:5 exacerbated this behavior and lastly, samples made without any molecules (0% molecular connections) showed the worst agreement with circuit simulations. In order to investigate the source of this behavior we examined the structure of such samples via AFM (additional details in Chapter 2), and noticed that loose packing and defects may be the source of the higher resistance observed for networks containing smaller amounts of molecules. Other factors that could affect circuit simulation accuracy include parasitic contact resistances, in addition to the fact that we assume a monolayer network in our model (with single molecule interconnections) whereas in reality that networked films are often 2 or 3 layers thick (and may also contain multiple molecule interconnections between two particles). Although there are uncertainties in the circuit simulation, our circuit spice modelling is consistent with the measured data over a wide range of experimental conditions and can be used to guide the design of self-assembled molecular electronic circuits based on different nanoparticles/molecules and network configurations.

3.3.2 Tunable Electrical Properties of Benzenedthiol-30 nm Gold Nanoparticle Networks

Building on results shown in Section 3.3., in this section, the low- and high-bias electrical properties of gold nanoparticle networks with benzenedithiol are presented.

3.3.2.1 Linear *I-V* characteristics obtained at low-bias measurements

Figure 3.12 shows low-bias current-voltage (*I-V*) plots of gold nanoparticle-benzenedithiol networked films with N_{BDT}: N_{particle} ratios of 1:5, 1:1, 5:1 and 50:1. The highest currents (in μA range) were observed for 1:1 ratio samples, followed by currents in the nA range for the 5:1 ratio samples, and the current further decreased to the pA range for 50:1 ratio samples. Current decreased with an increase in the percentage of molecules in the network, and conversely for resistance, as observed previously for alkanedithiols molecules [120]. The simplified version of the Simmons equation detailed in Section 3.3.1 could be used to explain the linear low-bias characteristic seen in the samples with benzenedithiol. Similar to the case of alkanedithiols, weak nonlinearities were also observed, in some cases, especially in samples with higher percentage of benzenedithiol connections. Samples consisting solely of colloidal gold nanoparticles (the control samples) also displayed linear *I-V* characteristics, in most cases.

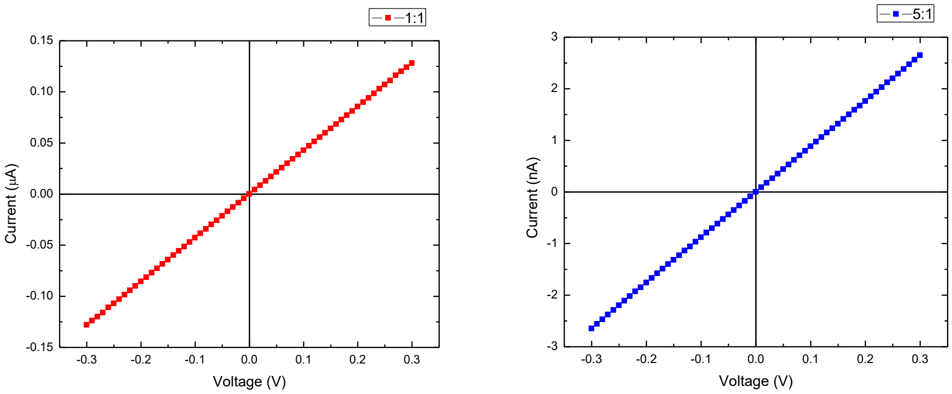

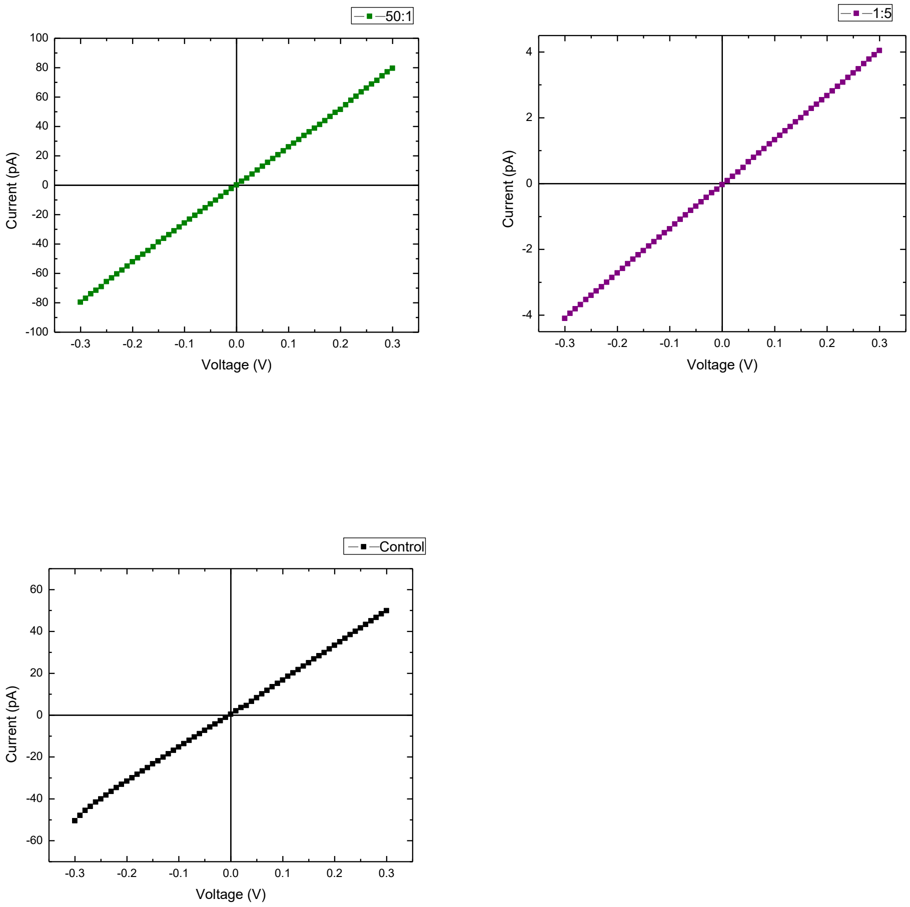

Figure 3.12: Plots of current *vs.* voltage for different molecule to nanoparticle ratios of benzenedithiol network samples: 1:1 (red), 5:1 (blue), 50:1 (green), 1:5 (purple), and control (black).

Figure 3.13 shows a comparison of the *I-V* curves of samples with different N_{BDT}:N_{particle} ratios with approximately equal film length to width dimensions, where the measured current depends on the number of molecules in the network, i.e., the current decreases with an increase in the number of molecules.

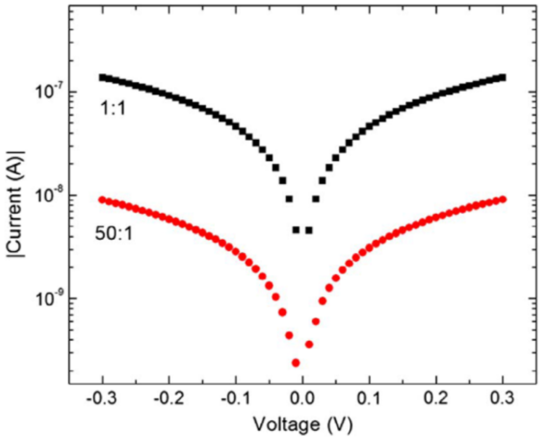

Figure 3.13: Semi-logarithmic plots of magnitude of current *vs.* voltage for different molecule to nanoparticle ratios of benzenedithiol network samples: 1:1 (black), and 50:1 (red). All sample film length to width dimension ratios for data shown are approximately equal.

Low-bias measurements made on the same set of electrode pairs more than once showed good repeatability and stability for all the samples. As an example, in Figure 3.14, the repeatability in the *I-V* characteristics is shown for various benzenedithiol samples, indicating the reproducibility and stability in the measured data over a period of time.

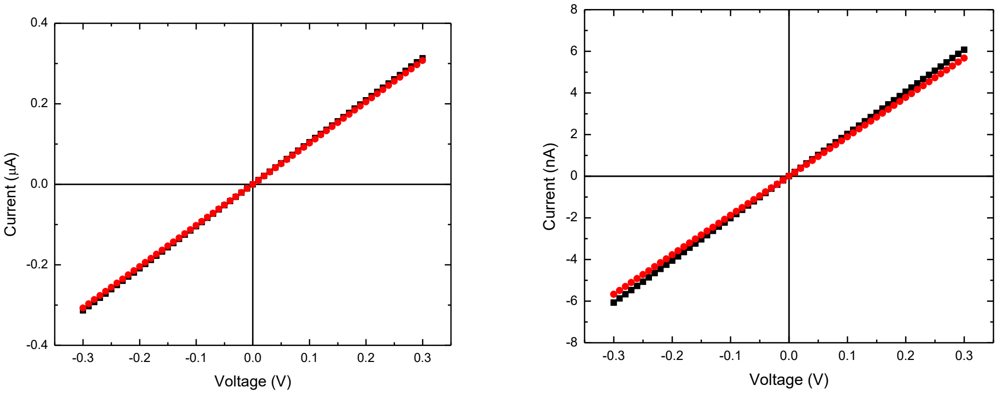

Figure 3.14: Plots of current *vs.* voltage for different molecule to nanoparticle ratios of benzenedithiol network samples: (a) 1:1, and (b) 5:1 measured in 2018 (red) and 2019 (black).

3.2.2.2 Circuit Modeling using LTspice

Results from local conducting-tip AFM as described above showed that gold nanoparticle–molecular samples with tunable organic/inorganic building block ratios, as described here display distinct resistance ranges that can be described by the type of connection being probed. For direct gold–gold particle connections, the resistance was found to be much lower than the gold particle–molecule connections [121]. These variations in resistance values were used to develop a linear resistor circuit model of the network's structure (similar to a method described in Section 3.3.1 above) to analyze the low-bias behavior of our samples. In addition, our learnings from the circuit simulations results for alkanedithiol network samples (as discussed in Section 3.3.1), showed some disagreements with the experimental and the simulated results. It was mentioned that, one of the reasons for this could be defects, which were not considered during the simulations.

Therefore, to simulate the benzenedithiol networks using LTspice, we also considered defects in the circuit model. The modified circuit comprised of a network of gold nanoparticle–benzenedithiol connections, gold–gold nanoparticle contacts and defects, each having unique resistance values, with their positions determined by a randomizing algorithm.

For example, a 500 nm long by 500 nm wide network, created by repeating a 36-resistor unit cell as per the desired dimensions, was built for simulating our networks. The circuit model used for our simulations is shown in Figure 3.15 (a-b). The random variable generator assigns all the resistors in the unit cell to be one of three values: either the quantized inter-particle contact resistance (12907 Ω), the benzenedithiol molecule resistance (1 MΩ), or the defect resistance (1 x 10^{15} Ω), depending on the desired molecule: gold nanoparticle concentration as well as the desired percentage of defects, as shown by the configurations in Figure 3.15 (c-d). For example, a network having 50% molecular connections and no defects would be such that 18 resistor values out of the unit cell, would be set to the benzenedithiol molecule resistance, 1 MΩ, and 18 resistor values would be set to the gold-gold inter-particle contact resistance. Similarly, for a network with 50% molecular connections, and 30% defects, 11 resistors were set to defect resistance, and 12 resistors were set to the benzenedithiol molecule resistance, and the rest of the resistors were set to gold-gold inter-particle contact resistance. Simulations were generally repeated 3 to 5 times with the resistor values within the unit cell being randomized each time for the desired molecule: gold nanoparticle and defect ratio.

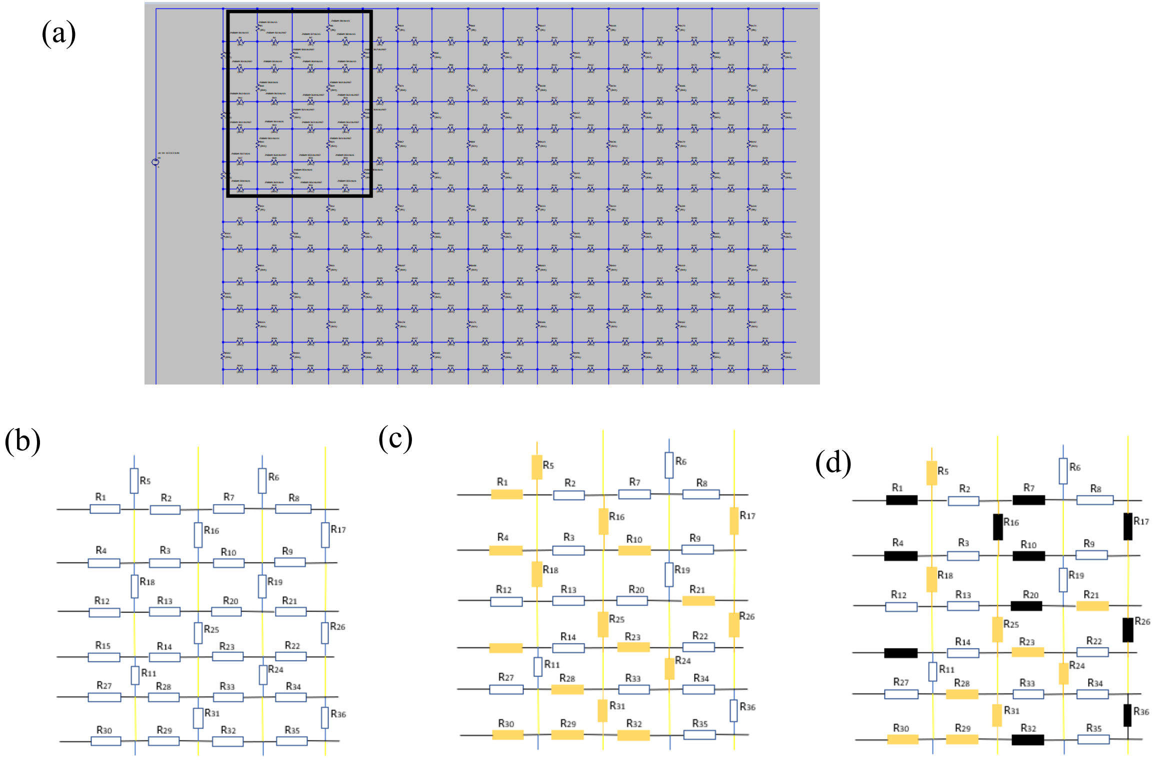

Figure 3.15: (a) Resistor network (length: 500 nm, width: 500 nm) used for circuit simulations. Black highlighted box represents the unit cell (building block of the circuit network). (b) Unit cell

close-up showing 36 resistor variable positions. The yellow lines represent nanoparticles, each with six nearest neighbour connections. Each resistor is assigned one of three possible values, i.e., either the gold-gold nanoparticle contact resistance or the molecule resistance, or the defect resistance. (c) Randomized unit cell configurations corresponding to 50% molecular and 0 defect connections. (d) Randomized unit cell configurations corresponding to 50% molecular connections, and 30% defects (molecules- white, gold-gold nanoparticle contacts- gold, defects- black).

Figure 3.16 shows results of low bias circuit simulation with resistance ranges from about 80 kΩ (no molecules in the network) to a few MΩ (all molecular contacts in the network). The resistance is seen to increase with an increase in the concentration of benzenedithiol molecules, in agreement with experimental data. For example, circuit simulation data showed an order of magnitude increase in resistance for greater than 30-40% molecular contacts in the network. Adding point defects (>30%) also generally improved agreement with the observed low-bias *I-V* characteristic, consistent with observations via AFM imaging.

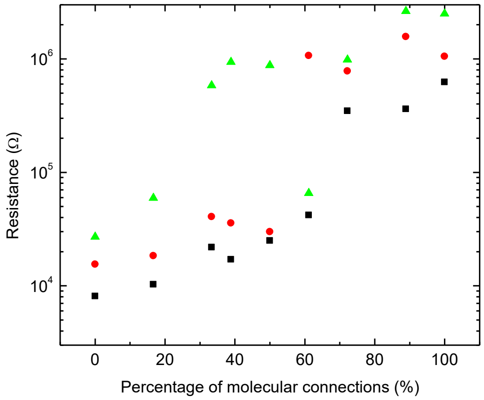

Figure 3.16: Low-bias linear circuit simulation results for a 500 by 500 nm network: Semi-log plot of gold nanoparticle–benzenedithiol network resistance *vs.* percentage of molecular connections in circuit. Simulated resistance values with no defects (black squares), 30% defects (red circles) or 50% defects (green triangles) are also shown.

3.2.2.3 Non-linear I-V characteristics seen at high-bias measurements

In contrast to the low-bias linear *I-V* characteristics shown above, several gold nanoparticle-benzenedithiol network ratios showed strong nonlinearities in their *I-V* characteristics as bias voltage was increased, a behaviour which is consistent for π-conjugated molecules [122]. NDR peaks of differing widths and peak-to-valley ratios from ~ 1.05 to 1.5 were found to typically occur near 3–4 V in our studies, becoming more prevalent as the number of molecules in the networks increased with the critical N_{BDT}:N_{particle} ratio near 5:1. Figure 3.17 shows an evolution of *I-V* characteristics as a function of N_{BDT}:N_{particle} ratio (control sample consists of gold nanoparticles only) showing increase in nonlinearity and NDR appearance near 5:1.

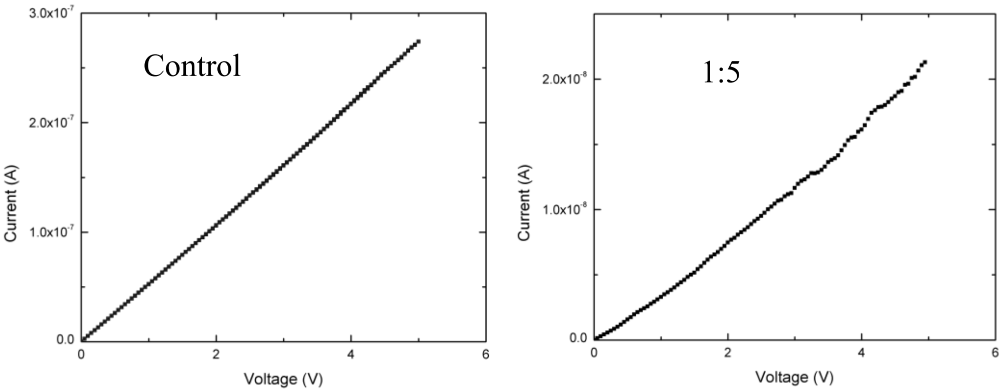

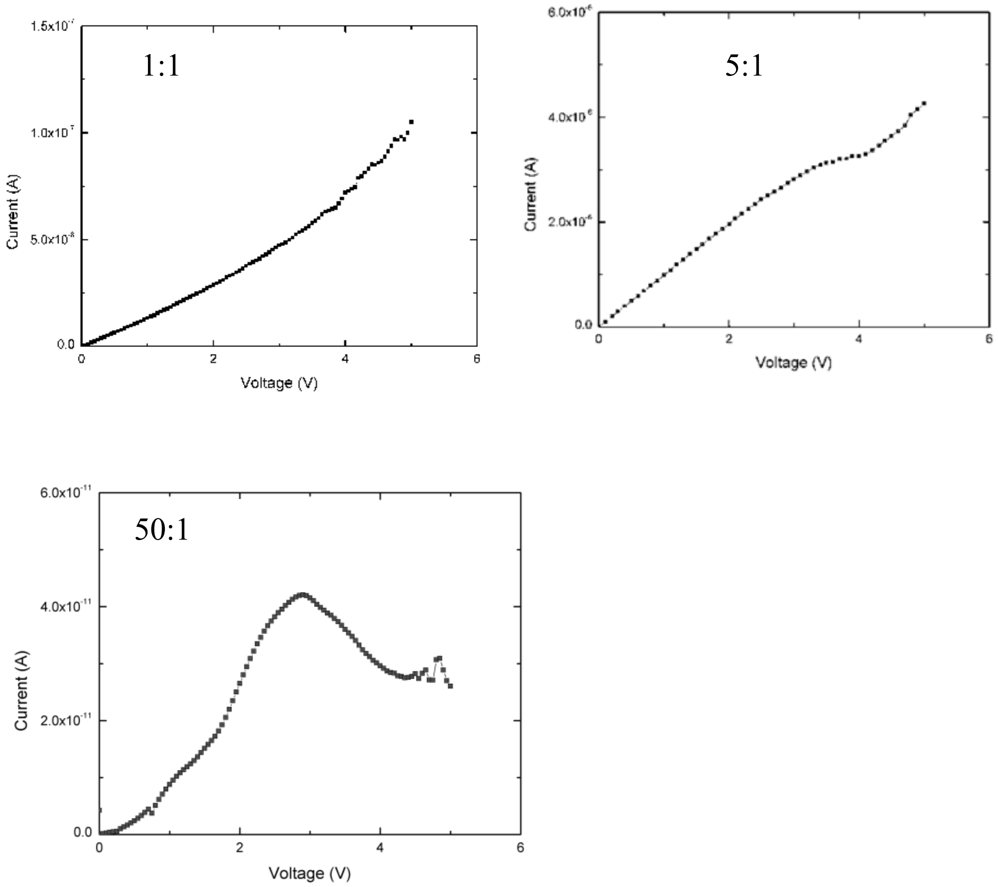

Figure 3.17: Evolution of *I-V* characteristics as a function of N_{BDT}:$N_{particle}$ ratio (control sample consists of gold nanoparticles only) showing increase in nonlinearity and NDR appearance near 5:1. A peak-to-valley ratio of approximately 1.52 is seen for the 50:1 network sample.

NDR behaviour was very evidently seen in samples with higher percentage of molecular connections with N_{BDT}:$N_{particle}$ ratio of 50:1 as voltage is increased up to 5 V (Figure 3.18).

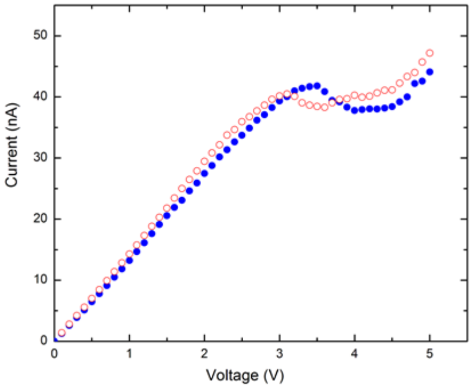

Figure 3.18: *I-V* plots of 50:1 networks showing NDR for different sample sweeps with peak-to-valley ratios of approximately 1.1 (solid dots) and 1.06 (open dots).

In addition to NDR, we also observed hysteresis in samples that displayed nonlinear *I-V* characteristics: Figure 3.19 shows the cyclic nonlinear *I-V* characteristics of a 5:1 network samples, exhibiting hysteretic behaviour, when voltage is swept from 0 to 5 V and then back to 0 V. In the forward sweep direction, the current increases gradually as the voltage is increased from 0 to about 2 V. Beyond 2 V, the current begins to increase more rapidly with increasing voltage. In the reverse direction, the current does not retrace the forward-sweep for voltages between approximately 1.5 and 4 V. Similar behavior was observed for 50:1 samples.

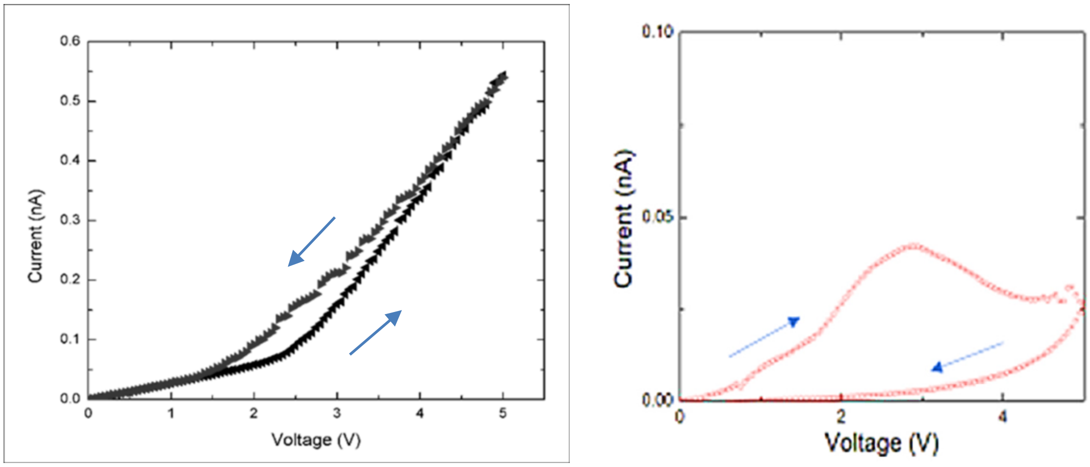

Figure 3.19: Nonlinear *I-V* characteristics of a 5:1 gold nanoparticle-benzenedithiol network samples showing hysteresis for forward and reverse sweep directions (as indicated by arrows).

Similar to the low-bias measurements, repeatability in *I-V* characteristics was observed when high-bias measurements were made more than once on the same set of electrode pairs. As an example, in Figure 3.20, the repeatability in the *I-V* characteristics is shown for a 5:1 benzenedithiol network sample. The NDR peak maintained its repeatability after two sweeps in the forward (from 0 V to 5 V) and backward (from 5 V to 0 V) directions. The variation in the current during the first and second voltage sweeping could be attributed to heating of the sample during the two sweeping cycles.

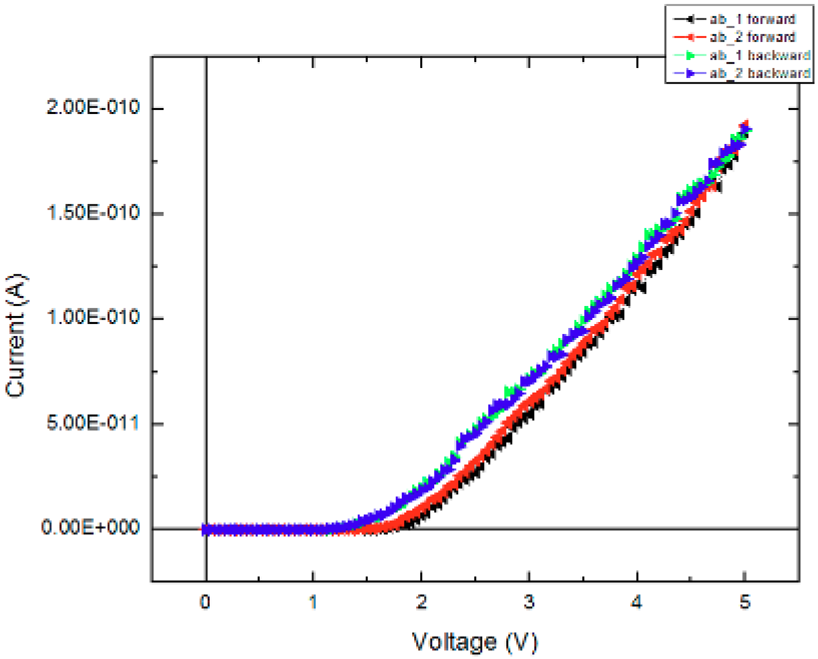

Figure 3.20: Nonlinear *I-V* characteristics of a 5:1 gold nanoparticle-benzenedithiol network samples showing hysteresis for forward (from 0 V to 5 V) and backward (from 5 V to 0 V) sweep directions.

A possible model that explains the nonlinear *I-V* characteristics at larger biases for networks containing a higher percentage of molecules can be based on tunneling transport and charge trapping [123–126]. In the high-bias regime, the simplified Simmon's equation discussed above does not hold and hence a modified Simmon's model [127] provides a description of the relationship between tunneling current and the magnitude of applied bias in molecular systems. At higher biases (above ≈1 V), a transition to field-assisted Fowler-Nordheim tunneling can be used to explain the observed increase in current shown in the *I–V* curve of Figure. 3.18a. The tunneling mechanism coupled with field-assisted charge trapping/emission in metal–molecular interfaces [128], [129] such as the gold nanoparticle–benzenedithiol networks also provides a plausible explanation for the observed NDR and hysteresis. For example, a change in tunneling barriers at ≈3–4 V could be caused by charge capture due to the reactions/defects becoming active in the networks at higher biases, which inhibits further injection of charge through the junction and in turn causes a decrease in current. The opposite process, i.e., charge carrier emission, would then leads to hysteretic behavior upon cycling voltage sweeps.

Another possible explanation for the observed NDR could be resonant tunneling between molecular orbitals and the metal delocalized states, thereby leading to a conduction peak followed by a decrease in the tunneling current for charge carrier energies that are off-resonance at higher biases [130]. In addition, single-electron charging effects and Coulomb blockade could also lead to NDR and hysteretic behavior [131][132], although these may be less likely for the 30 nm gold particles used in this study. The coupling and conformation of benzenedithiol particularly at larger biases may also alter the observed *I–V* characteristics and in particular lead to nonlinearities and/or asymmetry

[133][134]. Lastly, the effect of structural disorder [135] and metal nanogaps [136] in the network could play important roles in charge transport that warrant further investigation

3.4 Conclusions

In summary, gold nanoparticle–molecular networks with varying concentrations of molecular connections were fabricated using a directed self-assembly process. The two-terminal electronic transport measurements on the resulting samples showed variations in the electrical properties of the networks depending on the concentration and the type of molecular connections. By using different ratios of molecules to nanoparticles in the network, the electron transport could be controllably tuned over a broad range from electrical circuits consisting of just a few molecular connections to almost fully connected molecular networks. At low biases, an increase in the network resistance was observed with an increase in the percentage of molecules in the network. Circuit simulations modeling the networks at low bias as a combination of interconnected resistors with resistance values were determined by the concentration of molecules, gold contacts and defects, agreed well with experiment, which demonstrates a reliable mean to design molecular electronic network properties. At high biases, the networks showed nonlinearities, in particular NDR and hysteresis that could be explained by a combination of as tunneling transport and charge trapping. These nonlinear properties depend on the molecule to nanoparticle ratios used in the fabrication process, and by applying different bias voltages; electron transport properties of the networks could be controllably tuned. The solution-based fabrication approach presented shows the ability of directed self-assembly to create electronic networks with tunable building blocks to harness the unique electronic properties of next-generation molecular circuits, with potential applications in sensing, memory devices, switches, and molecular integrated circuits.

Chapter 4 Modeling the Electronic Properties of Gold Nanoparticle Molecular Electronic Networks

4.1 Basic Theory

4.1.1 The Schrodinger equation

Quantum mechanics is the branch of physics that provides a description of the properties of nature at the scale of atoms, electrons, and other subatomic particles [137]. In order to describe the properties of a collection of atoms within a system such as an isolated molecule or a crystal, knowledge about the energy of these atoms in stationary conditions, and also when these atoms are in motion is critical. To understand about where an atom is, one needs to have an idea of where its nucleus is and where its electrons are. Quantum mechanics helps in finding solutions to these questions by dividing them into two parts as per the Born–Oppenheimer approximation, that states that the motion of electrons and the motion of nucleus in molecules can be separated [138]. First, we consider the atomic nuclei as fixed, and find solutions to equations that describe the electron motion, that results in knowing about the lowest energy configuration (or the ground state of electrons, 'E'). Consider that there are 'M' nuclei at positions r_1, r_2, …r_M. The ground state energy as a function of the positions of these nuclei is given by:

$$\mathbf{E(r_1, r_{2,\dots} r_m)} \qquad \textbf{(4-1)}$$

In quantum mechanics, the state of a system at any given time can be completely described by its wavefunction, 'ψ', which is obtained by solving the Schrodinger equation. Many physical properties of a given system can be determined once the wave function is known. The simplest form of the Schrodinger equation, i.e. the time-independent Schrodinger equation is given by;

$$\boldsymbol{H\varphi = E\varphi} \tag{4-2}$$

Where ‘H’ is the Hamiltonian operator, ‘E’ is the ground state energy of the electrons and $'\varphi'$ is the electronic wavefunction, which is a set of solutions, or eigenstates, of the Hamiltonian.

Solving the Schrodinger equation for a single body-system is less complicated, however it becomes extremely challenging to obtain a solution to this equation when a many-body system (consisting of many electrons) is involved. For such a system, a more complex form of the Schrodinger equation is given by:

$$\left[\frac{\mathbf{h}^2}{\mathbf{2m}} \sum_{i\ 1}^{\mathbf{N}} \boldsymbol{\nabla}_{\mathbf{i}}^2 + \sum_{\mathbf{i}1}^{\mathbf{N}} \mathbf{V}(\mathbf{r}_{\mathbf{i}}) + \sum_{\mathbf{i}\quad 1}^{\mathbf{N}} \sum_{\mathbf{j}<\mathbf{1}} \mathbf{U}(\mathbf{r}_{\mathbf{i}}, \mathbf{r}_{\mathbf{j}})\right] \boldsymbol{\Psi} = \mathbf{E}\boldsymbol{\Psi} \tag{4-3}$$

Where ‘h’ is the Plank’s constant, ‘m’ is the mass of the electron. The first term inside the bracket represents the kinetic energy of each electron, the second term represents the interaction energy between each electron and the collection of atomic nuclei, and the last term defines the interaction energy between different electrons. $'\varphi'$ represents the electronic wave function, which is a function of each of the spatial coordinates of each of the ‘N’ electrons. By approximating φ (the full wave function) as a product of individual electron wave functions we get;

$$\varphi = \varphi 1\,(r)\,\varphi 2(r)\ldots.\,\varphi N(r) \tag{4-4}$$

Obtaining information about larger systems such as atoms, molecules and various solids becomes difficult when considering the Hamiltonian term defining the electron–electron interactions. The individual electron wave functions cannot be calculated without simultaneously considering the individual electron wave functions associated with the rest of the electrons. In addition, the wave function for any particular set of coordinates cannot be directly predicted and it depends on the probability that the ‘N’ electrons are at a particular set of coordinates given by r_1, r_2, .. r_n.The density of electrons at a particular position in space, ‘n(r)’, written in terms of the individual electron wave functions is given as:

$$\mathbf{n(r) = 2 \sum_i \Psi_i^*(r)\,\psi_i(r)} \tag{4-5}$$

Where ‘n(r)’ is the electron density, the factor 2 is associated with the electron spin, as defined by the Pauli Exclusion Principle (which states that each individual electron wave function can be occupied by two separate electrons provided they have different spins) [138]. The summation goes over all the individual electron wave functions that are occupied by electrons. Based on this, the term inside the summation is defined as the probability that an electron in individual wave function $'\,\psi_i(r)$’ is located at position r. $'\Psi_i^*(r)$’ represents its complex conjugate. It becomes extremely challenging to obtain a solution to this equation when a many-body system (consisting of many electrons) is involved [137],[138]. To overcome the challenge of many-electron problem, various theoretical methods such as the Hartee-Fock method [139], Wigner and Seitz method [140], DFT method [138], Monte Carlo[141], methods were introduced.

4.1.2 Density Functional Theory

One of the commonly used approach to investigate the electronic structure of many-body systems is based on DFT theories and calculations [142–144]. In simple words, a DFT calculation takes the electron density (a function of the position coordinate, r) as an input and outputs a number (an energy). DFT calculation heavily rely on a set of equations given by Kohn and Hohenberg [145], and Kohn and Sham [146].

The first set of equations given by Kohn and Hohenberg provided a rationale for choosing electron density to calculate the ground-state energy of a system. A ground state wavefunction is a unique functional of the ground state density. It is stated that there is a one to one mapping between the ground-state electron density, the external potential, and the ground-state wave function. However, these equations fail to give further information and the associated solutions to the unique functional. In mid-1960s, Kohn and Sham gave a modified version of these equations. Here, additional details about the unique functional and its association with the electron density were clearly defined. With these equations, the many-body problem was divided into equivalent set of self-consistent single-body equations. The energy functional was given by:

$$\mathbf{E}[\{\boldsymbol{\psi}_{\mathbf{i}}\}\mathbf{J} = \mathbf{E}_{\mathbf{known}}[\{\boldsymbol{\psi}_{\mathbf{i}}\}] + \mathbf{E}_{\mathbf{XC}}[\{\boldsymbol{\psi}_{\mathbf{i}}\}] \qquad \textbf{(4-6)}$$

Where '$\mathrm{E}_{\mathrm{known}}[\{\psi_{\mathrm{i}}\}]$' is a set of known information that is given by:

$$E_{\mathrm{known}}[\{\psi_i\}] = \frac{h^2}{m}\sum_i \int \psi_i^* \ \nabla^2\psi_i \, d^3r + \int V(r)n(r)\, d^3r$$

$$+\frac{e^2}{2}\iint \frac{n(r)n(r')}{|r \quad r'|} d^3r \ d^3r' + E_{\mathrm{ion}}$$

The terms on the right describe the electron kinetic energies, the Coulomb interactions between the electrons and the nuclei, the Coulomb interactions between pairs of electrons, and the Coulomb interactions between pairs of nuclei. $E_{XC}[\{\psi_i\}]$ represents the complete energy functional (i.e. the exchange–correlation functional) that includes all the quantum mechanical effects that are not a part of $E_{\mathrm{known}}[\{\psi_i\}]$ term. Therefore, the Kohn–Sham equations that involves only a single electron is given by:

$$\left[\frac{\mathbf{h^2}}{\mathbf{2m}}\boldsymbol{\nabla}^{\mathbf{2}} + \mathbf{V(r)} + \mathbf{V_H(r)} + \mathbf{V_{XC}(r)}\right] \ \boldsymbol{\psi}_{\mathbf{i}}\mathbf{(r)} = \boldsymbol{\varepsilon}_{\mathbf{i}}\, \boldsymbol{\psi}_{\mathbf{i}}\ \mathbf{(r)} \qquad \textbf{(4-7)}$$

Here, 'V(r)' denotes the interaction between an electron and the collection of atomic nuclei; 'V_H (r)' defines the Hartree potential that describes the Coulomb repulsion between the electron being considered in one of the Kohn–Sham equations and the total electron density defined by all electrons in the problem. 'V_{XC}' represents the functional derivative of the exchange–correlation energy. Solving the Kohn-Sham (KS) equations involves an iterative approach that is summarized below:

1. Choose an initial value for n(r) that represents the electron density
2. Solve for the single-particle wave function ψ_i (r) by substituting the n(r) term (chosen in the first step) in the Kohn–Sham equations.
3. Calculate the new electron density [nks (r)] defined by the Kohn–Sham single particle wave functions from step 2.
4. Compare n(r) and [nks (r)].

5. If the two values are same, then this is the ground-state electron density. Otherwise, the trial electron density (from step 1) must be updated and then the above steps are repeated until both the values for electron density match.

KS's equations are solved self-consistently to get the ground state density of the interacting system, provided that there is some knowledge of the exchange–correlation functional. For this, various models are introduced that approximate the exchange correlation functional. Examples of these models include the local spin density approximation (LSDA), where a solid is considered as being similar to the homogeneous electron gas, and thus $V_{xc}(r)$ of the solid is considered to be approximately same as that of the homogeneous electron gas [147]. However, in case of inhomogeneous systems such as atoms and molecules, this model fails to give accurate results. For inhomogeneous systems, functional based on generalized gradient approximation (GGA) [147] or local density approximation (LDA) are considered to give results with better accuracy. LDA is regarded as a model involving very simple approximations and its implementation has been a remarkable success. However, LDA has the disadvantage that some physical and chemical properties are not estimated accurately. On the other hand, with GGA functional, the exchange correlation is considered not only as a functional of the density but also of the magnitude of gradient of the density [138].

4.1.3 Hartree-Fock method

An alternate technique to find the solution to the solution to Schrodinger equation for atoms with more than one electron was obtained by using a self-consistent method given initially described by Hartee. The focus of this method was to understand the motion of an electron under the influence of the potential of the nucleus and other surrounding electrons. However, the wavefunction in this method was not anti-symmetrized, which led to some drawbacks. An improvised version of this method, known as the Hartee-Fock method [139], was introduced later, which solved the initial drawbacks. This method also called as the self-consistent field method (SCF), is used for determination of the wavefunction and the energy of many-body systems in a stationary state. Here, wavefunctions are optimized in order to get the lowest possible energy of the system (also called the ground-state energy). In this method, the orbitals that suit for a Slater determinant wave function are optimized rather than the wavefunction. The Hartee-Fock calculation method is also an iterative procedure that is very similar to the iterative method used to solve the Kohn–Sham equations within a DFT calculation [138].

4.1.4 Quantum transport

The study of electron transport through molecules is an important aspect in realizing the practical application of molecular electronics [1]. Analysis of transport properties of metal-molecular junctions using various state-of-art computational tools allows for realistic evaluation of properties of molecular systems [2, 3].

Understanding the details of transport at nanoscale involves the use of various techniques, models and approximations. Study of transport properties of such systems using different theoretical methods has gained tremendous interest recently [80], [89], [148]. Calculations based on plane waves [149], NEGF [83] and Landauer-Buttiker formalization [84] are considered as some of the useful computational methodologies for the study of electronic transport properties. One of the techniques to calculate to charge transport across a junction is using DFT plane wave basis sets and Landauer-Buttiker approach [84]. Here, the test system consists of a scattering region bridged between semi-infinite left and right leads (Figure 4.1).

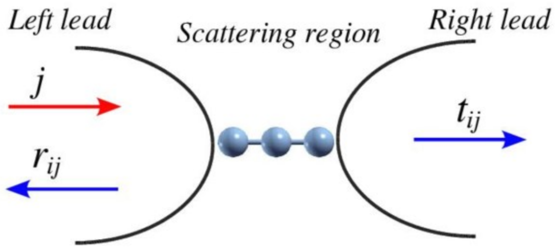

Figure 4.1: Schematic of system consists of a scattering region bridged between semi-infinite left and right leads.

First, the reflection ‘r_{ii}’ and transmission ‘t_{ij}’ amplitudes for electron waves ‘j’ propagating from the left to the right are calculated. Initially, the ground state DFT calculations for solving the KS wave functions and finding the self-consistent energies are performed using pseudo-potentials and exchange-correlation functionals. Based on this the total transmission at Fermi energy:

$$T(E_F)= \sum_{ij} |t_{ij}(E_F)|^2 \qquad (4\text{-}8)$$

is obtained which determines the ballistic conductance of the system using the Landauer-Buttiker formula;

$$G= (e^2/h)\, T(E_F) \qquad (4\text{-}9)$$

Total current of the junction can be calculated computationally using the Landauer approximation [150], represented mathematically as follows:

$$I = \frac{2e}{h} \int \boldsymbol{M(E)\, T(E)[f_L(E) - f_R(E)]}\mathrm{dE} \qquad \textbf{(4-10)}$$

where ‘I’ represents the electric current, ‘e’ represents the electric charge, ‘h’ is Planck’s constant, M(E) is the number of channels, T(E) is the transmission, f_L (E) and f_R (E) are the Fermi functions of the left and right leads.

Another commonly used techniques of understanding charge transport in metal-molecule-metal junction is based on the principle of DFT-NEGF [83]. Briefly, this technique uses a setup with a molecule sandwiched between two semi-infinite leads as shown in Figure 4.2. The NEGF method, a modification to the mesoscopic transport theory developed by Landauer, includes the effects of inelastic (electron-phonon) scattering and electron-electron interactions under non-equilibrium conditions (under an applied bias), and gives a more general approach for solving the transport problem [83].

Figure 4.2: Schematic of a device setup for calculation charge transport using NEGF principles.

The NEGF method of solving for electronic systems’ transport basically entails the calculation and integration of the Green’s functions with respect to the energy and wave vectors, to obtain the density matrix of the electronic system (Piccinin, 2006). The NEGF formalism, combined self-consistently with DFT (DFT-NEGF) is the most ubiquitous method of modelling electronic transport at the nanoscale [83]. The DFT is first used to obtain the Hamiltonian and electronic structure for the scattering region and then the NEGF is used to solve for the charge density, transmission and current of the molecular system. After solving the ground state problem using DFT, the Green's function of the central region is computed. The Green's function at energy E is given by [83]:

$$\mathbf{G(E) = [(E+i\eta)S-H-\Sigma_L-\Sigma_R]^{-1}} \tag{4.11}$$

where H and S are the Hamiltonian and overlap matrix for the scattering region as determined by DFT, η is a positive infinitesimal and $\Sigma_{L,R}$ are self-energies that account for the effect of the left and right electrodes on the scattering region. Following this, the new charge density and potential are calculated. The charge or electronic density is obtained as:

$$\boldsymbol{\rho = \frac{1}{2\pi} \int_{-\infty}^{\infty} [f(E, \mu_L)\, G\Gamma_L G^{\dagger} + f(E,\ \mu_R)\, G\, \Gamma_R G^{\dagger})] dE} \tag{4.12}$$

where $\mu_{L,R}$ are the electrochemical potentials of the electrodes and $f(E, \mu)$ is the Fermi-Dirac function that describes the population for a given energy. The electronic density obtained from Green's function is used in a subsequent DFT step, and the calculation is repeated until self-consistency between DFT and NEGF is attained. The transmission function can be obtained from Green's function as:

$$\mathbf{T(E) = Tr\ (\Gamma_L G \Gamma_R G^{\dagger})} \tag{4.13}$$

Finally, the current can be obtained using the Landauer-Büttiker formula as:

$$\boldsymbol{I = \frac{2e}{h} \int_{\mu_L}^{\mu_R} T(E) dE = \frac{2e}{h} \int_{\mu_L}^{\mu_R} (\,Tr\ (\Gamma_L G \Gamma_R G^{\dagger})\ dE} \tag{4.14}$$

4.2 Details of Computational Modeling Tools and Methods used in this work

Different structures were studied by combining various thiolate molecules (1,4 benzenedithiol, 1,3,5 benzenetrithiol, 1, 8-octanedithiol and 1, 6-hexanedithiol) with Au metal atoms, which are of increasing importance in the field of molecular electronics.[151–154] The electronic and transport properties of metal-molecular networks were studied using various software packages. The electronic structure properties of metal-molecular nanojunctions and networks, was studied using the Accelrys Materials Studio's DFT package (DMol^3) [155] based on first principles electronic structure calculations. For the transport calculations, all the metal-molecular networks were designed in Virtual Nanolab (VNL) [156]. The electron transport properties of these networks was studied using the Quantum Espresso package based on DFT and plane wave basis sets.[157] In addition, SIESTA, was used to perform equilibrium electronic structure calculations on the molecular networks and generate information about their electronic density of states (DOS) and molecular orbitals [148]; while the TranSIESTA module of the SIESTA-4.0 and 4.1 versions, which is based on the DFT-NEGF formalism, in conjunction with a tight-binding transport code, TBTrans, was used to compute electronic transport properties, such as the transmission spectra, transmission eigenvalues*, I-V* characteristics of the networks under an applied finite bias. For visualizing the generated electronic structure information from the SIESTA package, XCrySDen [158], a molecular structure visualization program, was used to display molecular orbital isosurface of the nanoscale networks.

4.2.1 DMol^3

DMol^3 is a software package, which uses DFT to calculate the electronic properties of molecules, clusters, surfaces and crystalline solid materials from first principles. It uses a set of numerical functions on atomic basis set which are obtained from solving the DFT equations for individual atoms. All Au-molecular structures were built using optimized molecules and optimized planar parallelogram-shaped Au metal clusters containing 6 atoms (henceforth referred as Au_6), which is one of the commonly used stable configurations of Au_6 cluster [70], [107] [Figure 4.3(a-b)]. We had 7 Au atoms on either side of the structures that correspond to lead extensions for the transport calculations. After optimization, we obtained Au-S bond length of 2.3 Å; and bond lengths between Au atoms in the Au_6 cluster ranged from 2.5 Å to 3 Å; similar to previous work [159], [160]. Distance between Au atoms in in the lead extensions was chosen to be 2.5 Å in accordance to other studies [160], [161]. Au-molecular linear chains of different lengths are defined by the number of cluster units they contain, as shown in [Figure 4.3(c-e)]. These were modeled into a Y-, H- and diamond shaped multi-terminal networks by adding 1, 3, 5 benzenetrithiol as shown in Figure 4.3 (f-i).

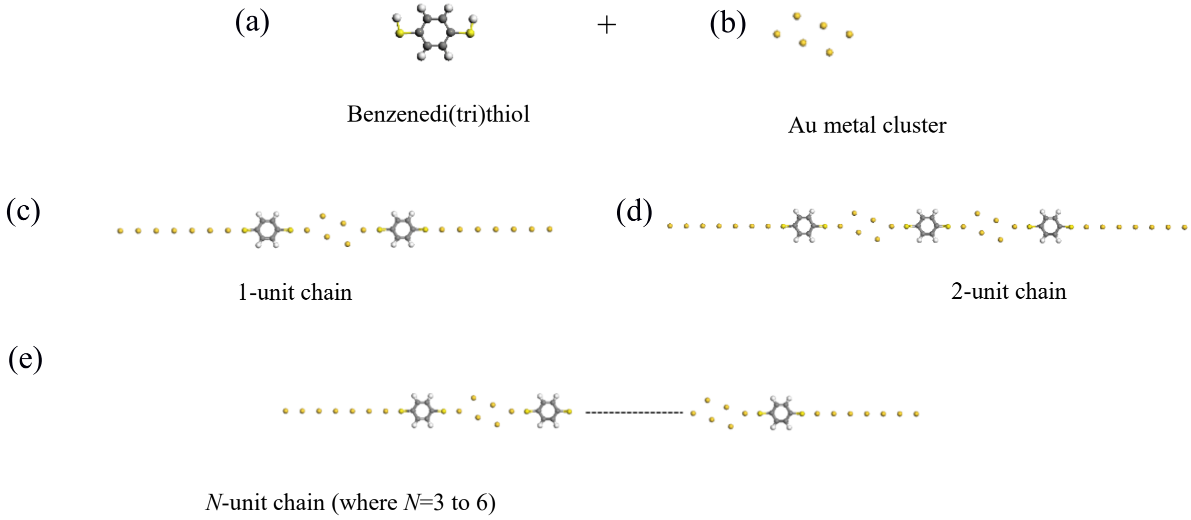

Benzenedi(tri)thiol

Au metal cluster

1-unit chain

2-unit chain

N-unit chain (where *N*=3 to 6)

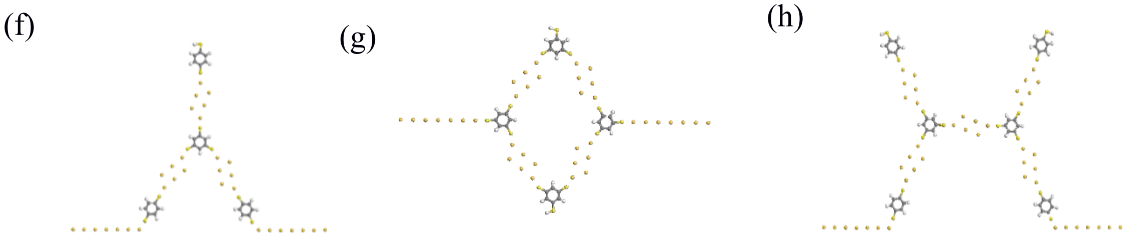

Y-shaped network

Diamond-shaped network

H-shaped network

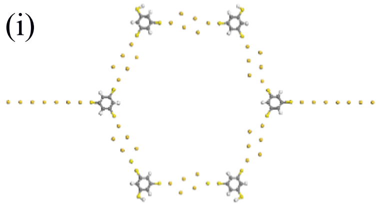

Ring-shaped network

Figure 4.3: GGA PW91 optimized building blocks and starting structures for (a-e) Benzenedithiol-Au cluster chains of various lengths and (f-i) Optimized benzenedi(tri)thiol-Au Y-/diamond-/H-shaped networks. The approximate values of bond lengths for all the structures are as follows; Au-S: 2.3 Å, Au-Au: 2.5 Å to 3 Å, C-C: 1.4 Å, C-H: 1.08 Å and S-C: 1.78 Å. Here, golden color denotes Au metal atoms and yellow, white and grey colors denote sulfur, hydrogen and carbon atoms, respectively.

Within DMol^3, GGA model by Perdew and Wang (PW91) was used for all DFT calculations [162]. The double numerical basis set with polarization (DNP) was used, which is comparable in size and quality to one of the most frequently used Gaussian basis sets; 6-31 G** [142], [163–165]. For the geometry optimization of isolated molecules, and the resulting extended Au-molecular chains and networks, tolerances were set to at least 1×10^{-5} for self-consistent field and a smearing of 0.005 Ha was used. The isosurface value for all molecular orbital plots shown was 0.003.

4.3.3 Quantum Espresso

Quantum Espresso stands for quantum open source package for electronic structure, simulation and optimization [84]. This package uses DFT, plane wave basis sets and pseudopotentials for the electronic structural and charge transport calculations. For the transport calculations using Quantum Espresso package, we used a unit cell approach and had extended the optimized structures by attaching metallic electrodes on either side, thereby resembling a lead-conductor (scattering)-lead configuration. An example of a unit cell that was used to calculate electron transport in a 2-unit benzenedithiol-Au_6 linear chain is shown in Figure 4.4. In order to avoid spurious interactions between the periodic repetitions of the structures, sufficient height of the unit cell in vertical direction was incorporated to accommodate a vacuum layer for all the structures [90].

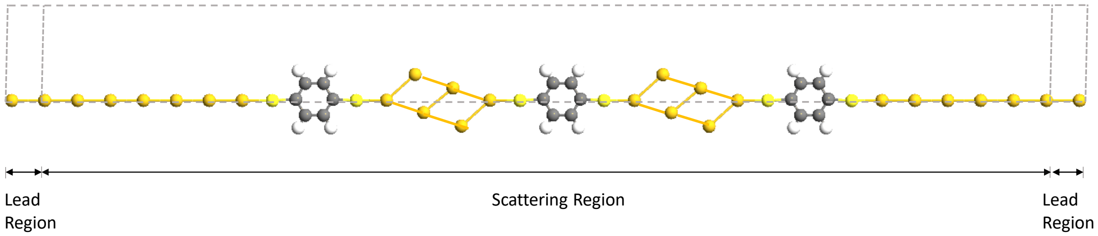

Figure 4.4: Ball–stick representation of the lead-scattering-lead region that was used to calculate the electron transport in a 2-unit benzenedithiol-Au_6 linear chain. Dotted lines represent the tetragonal unit cell for this structure with dimensions of ~9.5 A in the vertical direction. Here, the single atom Au leads were attached on the ends on either side of the scattering regions. The golden color denotes Au metal atoms and yellow, white and grey colors denote sulfur, hydrogen and carbon atoms, respectively.

Plane-Wave Self-Consistent Field (PW_{SCF}) code [84], [166] was used for all ground state DFT calculations. The formalism is based on the Hohenberg-Kohn theorem, where the ground-state energy of any system can be expressed as the ground state single-particle density. The transmission calculations were implemented using the PW_{COND} code using a scattering-based approach [90], [149]. The kinetic energy cut-off for wavefuctions was set to 25 Ry. For charge density, the values ranged from 200 Ry to 300 Ry. The Methfessel-Paxton first-order spreading[166] was used with a smearing value of 0.01 Ry for all the calculations and the momentum space was sampled using Monkhorst-Pack mesh. Distance between Au atoms in in the lead extensions was chosen to be 2.5 Å in accordance to other studies [160], [161]. Here, transmission spectrum corresponds to the sum of all the channels contributing in the networks' transmission.

4.3.4 Siesta/Transiesta

DFT-NEGF-based, TranSIESTA and TBtrans were used in this work for computing the electron transport properties and *I-V* characteristics of the molecular systems studied under an applied bias.

The TranSIESTA method is based on the NEGF technique that has been interfaced with the SIESTA electronic structure package in such a way that the density matrix of the system is calculated self-consistently when the system is subject to an external bias. In the typical TranSIESTA calculation setup, a molecular system is coupled to two electrodes with different electrochemical potentials. The program uses SIESTA to obtain the Hamiltonian in a localized basis set, and the Hamiltonian, *H* is separated into left electrode, contact region, and right electrode. The electrode Hamiltonians are obtained from separate bulk calculations, whereas the Hamiltonian of the contact region is calculated self-consistently. The *trans* part calculates the non-equilibrium density matrix, *D*, from *H*, using a nonequilibrium Green's function (NEGF) technique [148].

The TBtrans code is a tight-binding transport code based on the non-equilibrium Green's function method. It is primarily implemented for the support of TranSiesta (DFT+NEGF) as a backend for calculating electron transport, interpolated *I-V* curves, and transmission eigenvalues etc., for self-consistent DFT software under an applied bias [148, 151].

For the transport calculations, the system was divided into three regions, namely; the scattering region, which included linear or branched chains of interconnected thiolated molecules and gold clusters plus five layers of gold atoms on each side to serve as the electrode extension or screening region; the semi-infinite (bulk-like) left electrode; and the semi-infinite (bulk-like) right electrode, as shown in Figure 4.5 (a-c).

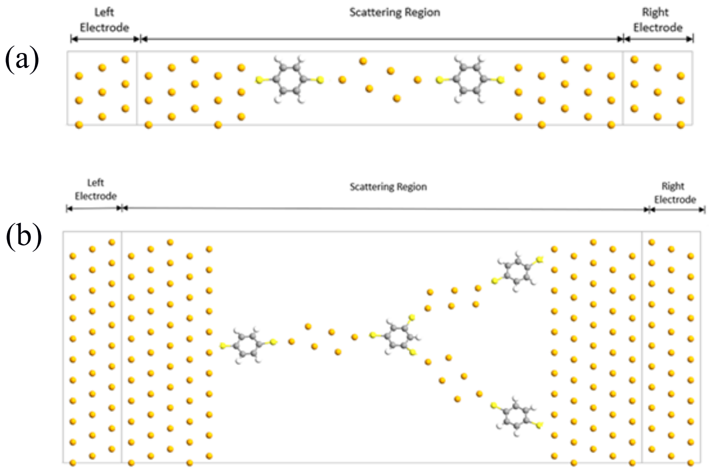

(c)

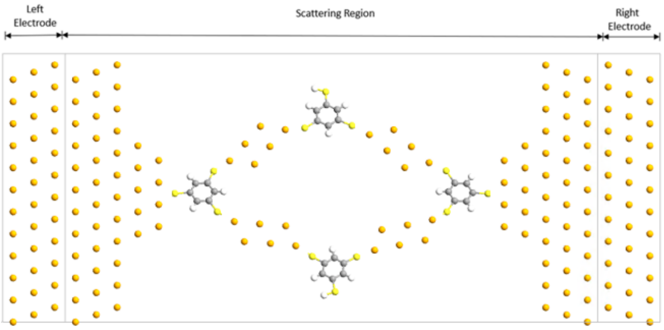

Figure 4.5: Benzenedithiol-Au_6 linear chains and branched networks of various lengths. (a) 1-unit chain (b) Y-shaped network, (c) Diamond-shaped network. Here, golden, yellow, white, and grey colors denote gold, sulfur, hydrogen and carbon atoms, respectively. In addition to the networks, the central scattering region also contains a transition region from the left and right electrodes, whose size was chosen to balance accuracy and computational time.

The transport properties of the molecular networks were calculated by setting bias voltages between the electrodes. Troullier-Martin norm-conserving pseudopotentials [167] were used to replace the core electrons. The basis set used for KS orbitals expansions for the scattering region and electrodes, was the polarized double-zeta (DZP). The exchange correlation functional [146] for transport calculations was the GGA parameterized by Perdew, Burke and Erzenhof (PBE) [168]. The mesh density was chosen such that the energy of plane waves was less than 200 Ry. For generating the transmission functions of the linear chains, Y-shaped network, and diamond-shaped network, the number of energy points in the energy range, -3.0 to +3.0 eV, of the computed transmission function was 2000, 500, and 300, respectively. For generating the *I-Vs.*, the density matrix mixing weight value for the self-consistent field cycle was 0.003 and the density matrix tolerance values ranged between 1.0×10^{-3} and 1.0×10^{-5}. The projected density of states (PDOS) information of the isolated molecular networks comprising of the scattering region without the electrode extensions, and the total DOS information of the molecular networks comprising of the entire scattering region, were generated by performing SIESTA calculations on the scattering region with the range of atoms corresponding to the isolated molecular networks and entire scattering region, respectively, specified in all cases. For generating the PDOS and local density of states (LDOS) information, the density matrix mixing weight value for the self-consistent field cycle was 0.01, and the broadening parameter used for plotting the PDOS was 0.01 eV. For generating molecular orbitals, the LDOS at energies corresponding to peaks in the projected DOS plots, were visualized as isosurfaces, with isovalue, 0.0002.

4.3 Results and Discussions

4.3.1 Energy levels and molecular orbital distribution

The molecular orbitals, in particular the frontier molecular orbitals, called HOMO and LUMO play an important role in determining electronic properties of the network [142].Various studies indicate that charge transport through a molecular system depends on the degree of molecular orbital delocalization and the metal-molecular junction geometry.[86], [87], [89] In Table 4.1, selected frontier orbitals of a 4-and 5-unit benzenedithiol-Au_6 chains are shown.

Table 4-1: Frontier orbitals of benzenedithiol-Au$_6$ 4- and 5- unit chain optimized using DFT-GGA PW91.

Orbital	**4- unit benzenedithiol-Au$_6$ chain**	**5- unit benzenedithiol-Au$_6$ chain**
HOMO	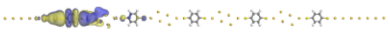 HOMO, Energy: -4.471 eV	 HOMO, Energy: -4.454 eV
HOMO-1	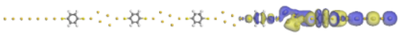 HOMO-1, Energy: -4.490 eV	 HOMO-1, Energy: -4.467 eV
HOMO-2	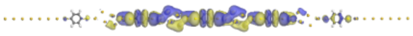 HOMO-2, Energy: -4.518 eV	 HOMO-2, Energy: -4.500 eV
HOMO-3	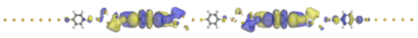 HOMO-3: -4.524 eV	 HOMO-3, Energy: -4.504 eV
LUMO	 LUMO, Energy: -4.312 eV	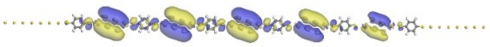 LUMO, Energy: -4.295 eV
LUMO+1	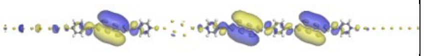 LUMO+1, Energy: -4.309 eV	 LUMO+1, Energy: -4.293 eV
LUMO+2	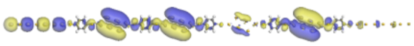 LUMO+2, Energy: -4.306 eV	 LUMO+2, Energy: -4.290 eV
LUMO+3	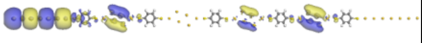 LUMO+3, Energy: -3.304 eV	 LUMO+3, Energy: -4.288 eV

It was observed that a large number of molecular orbitals that are closer in energies combine and/or overlap with each other leading to formation of potential delocalized band-like conduction pathways. For example, HOMO-1, HOMO-2 and HOMO-3 are energetically close to each other and can contribute to charge transport by means of electron hopping from one orbital to another. This behavior becomes more significant as the chain length of the structures consisting of organic molecules increases, a trend consistent with previous work [169].

As the charge transport is mainly influenced by the position of the frontier orbitals, in Figure 4.6, HOMO/LUMO positions with respect to number of units in the benzenedithiol-Au_6 chains are shown.

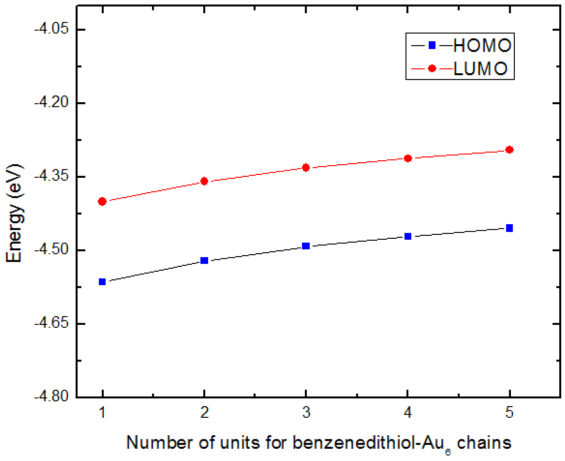

Figure 4.6: HOMO and LUMO position *vs.* number of units for benzenedithiol-Au_6 chains optimized with DFT-GGA PW91 approximations.

A HOMO-LUMO gap of 3.517 eV was obtained for an isolated benzenedithiol molecule which is comparable to previous work (~3.53 eV) [170], [171]. For Au_6 metal cluster, a very small HOMO-LUMO gap of about 0.001 Å was obtained. In case of Au_6-benzenedithiol molecular chains, a decrease in the frontier orbital gap as a function of chain length (0.164 eV for 1-unit chain and 0.159 eV for a 5-unit chain) was observed, as compared to the isolated benzenedithiol molecule. This decrease in the HUMO-LUMO gap with increase in the length of the chains, lowers the barrier for electron to transport through the molecule; indicating enhanced possibility of charge transport as these networks are extended [169]. In Figure 4.7, the electronic DOS plots for 1- and 5-unit benzenedithiol-Au_6 chains are shown.

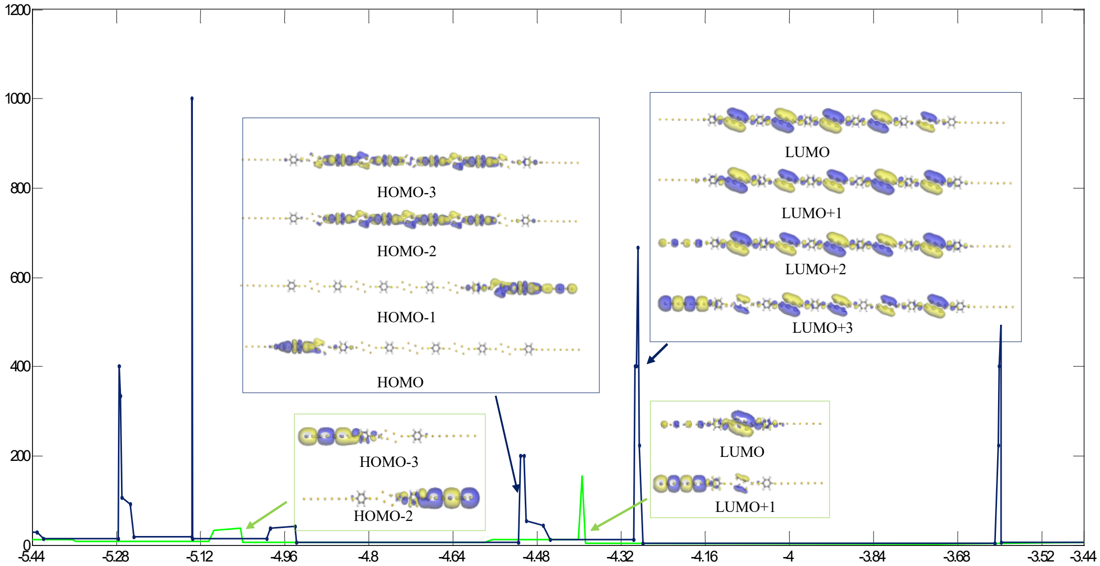

Figure 4.7: DOS plots of benzenedithiol-Au_6 1- and 5-unit chains calculated using DFT-GGA PW91 approximations. Frontier orbitals of a 1- and 5-unit chain corresponding to peaks in the DOS plots near Fermi energy are also included.

Each peak in this plot is the result of energetically close molecular orbitals overlapping or combing together. The 5-unit structure shows a significant increase/broadening of the DOS as compared to the 1-unit structure, due to overlapping of a number of discrete orbitals with similar energies (ex: HOMO-1: -4.467 eV, HOMO-2: -4.500 eV and HOMO-3: -4.504 eV; LUMO: -4.295 eV, LUMO+1: -4.293 eV, LUMO+2: -4.290 eV and LUMO+3: -4.288 eV), indicating an enhanced transmission as the chain length of the structures increases. For the energies within the HOMO–LUMO gap (from -4.454 eV to -4.293 eV), the DOS peaks are negligible due to absence of any orbital states contributing to the overall transmission. On the other hand, the 1-unit structure shows very few DOS peaks due to lower number of energetically close molecular orbitals (ex: HOMO-2: -5.039 eV and HOMO-3: -5.043 eV; LUMO: -4.400 eV, LUMO+1: -4.394 eV and LUMO+2: -4.387 eV).

For comparison with the benzenedithiol-Au_6 chains, the frontier orbitals of alkane chains; hexanedithiol-Au_6 and octanedithiol-Au_6 linear chains were also studied. Table 4. 2 shows selected orbitals of hexanedithiol-Au_6 4-unit linear chains.

Table 4-2: Frontier orbitals of hexanedithiol-Au_6 4-unit chain optimized using DFT-GGA PW91.

HOMO	**LUMO**
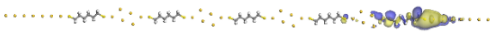 HOMO, Energy: -4.688 eV	 LUMO, Energy: -4.276 eV
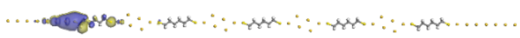 HOMO-1, Energy: -4.688 eV	 LUMO+1, Energy: -4.276 eV
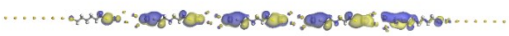 HOMO-2, Energy: -4.715 eV	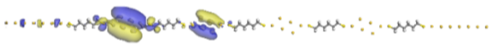 LUMO+2, Energy: -4.274 eV

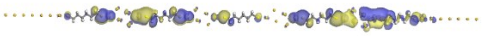 HOMO-3, Energy: -4.716 eV	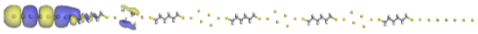 LUMO+3, Energy: -4.258 eV

The orbitals of hexanedithiol-Au_6 4.unit linear chains are localized and do not extend throughout the chain (for example, HOMO-1, HOMO-2 and LUMO+2 to LUMO+3) causing difficulty for electrons to pass along the entire network.[154], [172] Similar results were observed for octanedithiol based structures in which the orbitals were mainly localized around the metal cluster leading to lower charge transport pathways. HOMO-LUMO gaps of 4.715 eV and 4.803 eV for hexanedithiol and octanedithiol molecules were obtained, which are comparable with previous work (~4.32 eV for hexanedithiol and ~5 eV for octanedithiol) [87], [171]. Similar to the benzenedithiol-Au_6 chains, in case of Au_6-hexane/octanedithiol chains of varying lengths, a decrease in the HOMO-LUMO gap as a function of chain length (0.447 eV for a 1-unit and 0.437 eV for a 5-unit Au_6-hexanedithiol chain; and 0.522 eV for a 1-unit and 0.491 eV for a 5-unit Au-octanedithiol chain) was observed, as compared to the respective isolated hexane/octanedithiol molecules. Since benzenedithiol is known to be more conductive than hexane/octanedithiol molecules; which belong to alkane family, it can be understood that these would lead to reduced charge transport due to their wider HOMO-LUMO gaps.[87], [88], [173]. The frontier orbitals of multi-terminal networks such as a Y- and H-shaped networks; are shown in Table 4.3.

Table 4-3: Frontier orbitals of Y- and H-shaped networks optimized using DFT-GGA PW91.

Y-shaped network		H-shaped network	
HOMO	LUMO	HOMO	LUMO
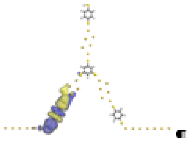 HOMO, Energy: -4.504 eV	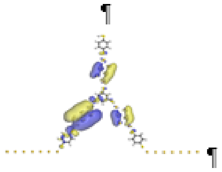 LUMO, Energy: -4.321 eV	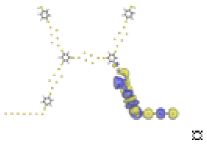 HOMO, Energy: -4.241 eV	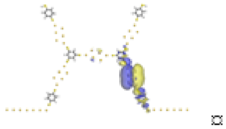 LUMO, Energy: -4.068 eV
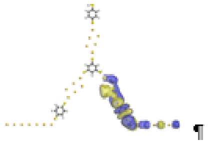 HOMO-1, Energy: -4.528 eV	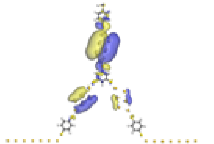 LUMO+1, Energy: -4.299 eV	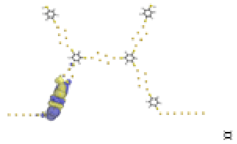 HOMO-1, Energy: -4.268 eV	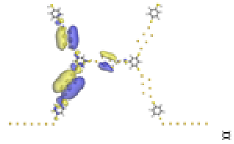 LUMO+1, Energy: -4.052 eV
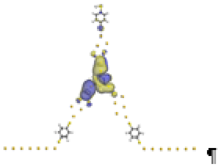 HOMO-2, Energy: -4.619 eV	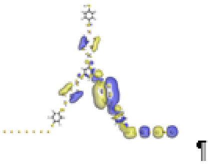 LUMO+2, Energy: -4.294 eV	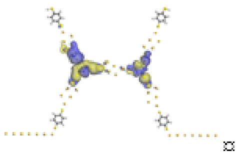 HOMO-2, Energy: -4.369 eV	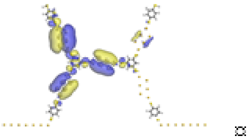 LUMO+2, Energy: -4.043 eV
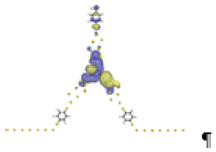 HOMO-3, Energy: -4.647 eV	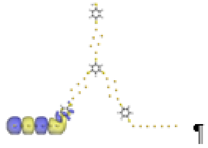 LUMO+3, Energy: -4.285 eV	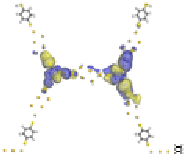 HOMO-3, Energy: -4.370 eV	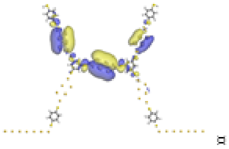 LUMO+3, Energy: -4.041 eV

For the Y-shaped network, we observed that the orbitals around the HOMO-LUMO gap are well-delocalized and/or overlap with other orbitals in the same energy range (ex: HOMO, HOMO-1 to HOMO-3). In addition, at different energies, orbital delocalization seems to shift from one arm/branch of this structure to another. For example, orbitals are mainly delocalized in the left branch (HOMO), which are then shifted to right branch (HOMO-1) and then to the central region (in HOMO-2 and HOMO-3). In the case of a H-shaped network where the orbitals closet to HOMO-LUMO gap show good delocalization, overlap to form a transport pathway.

4.3.2 Transmission and *I-V* characteristics

Understanding of various properties associated with the metal-molecular junction geometries is essential for analysis of the electron transport mechanisms. The transmission properties in metal-molecular networks are analyzed based on simulations of electron-transmission spectra for linear chains and bigger networks. The transmission coefficient T(E) is a property of the entire system shown which includes the leads, the molecule and the contact between the leads and the molecule.

In Figure 4.8, the transmission spectra of 1- and 5-unit benzenedithiol-Au_6 linear chains are shown.

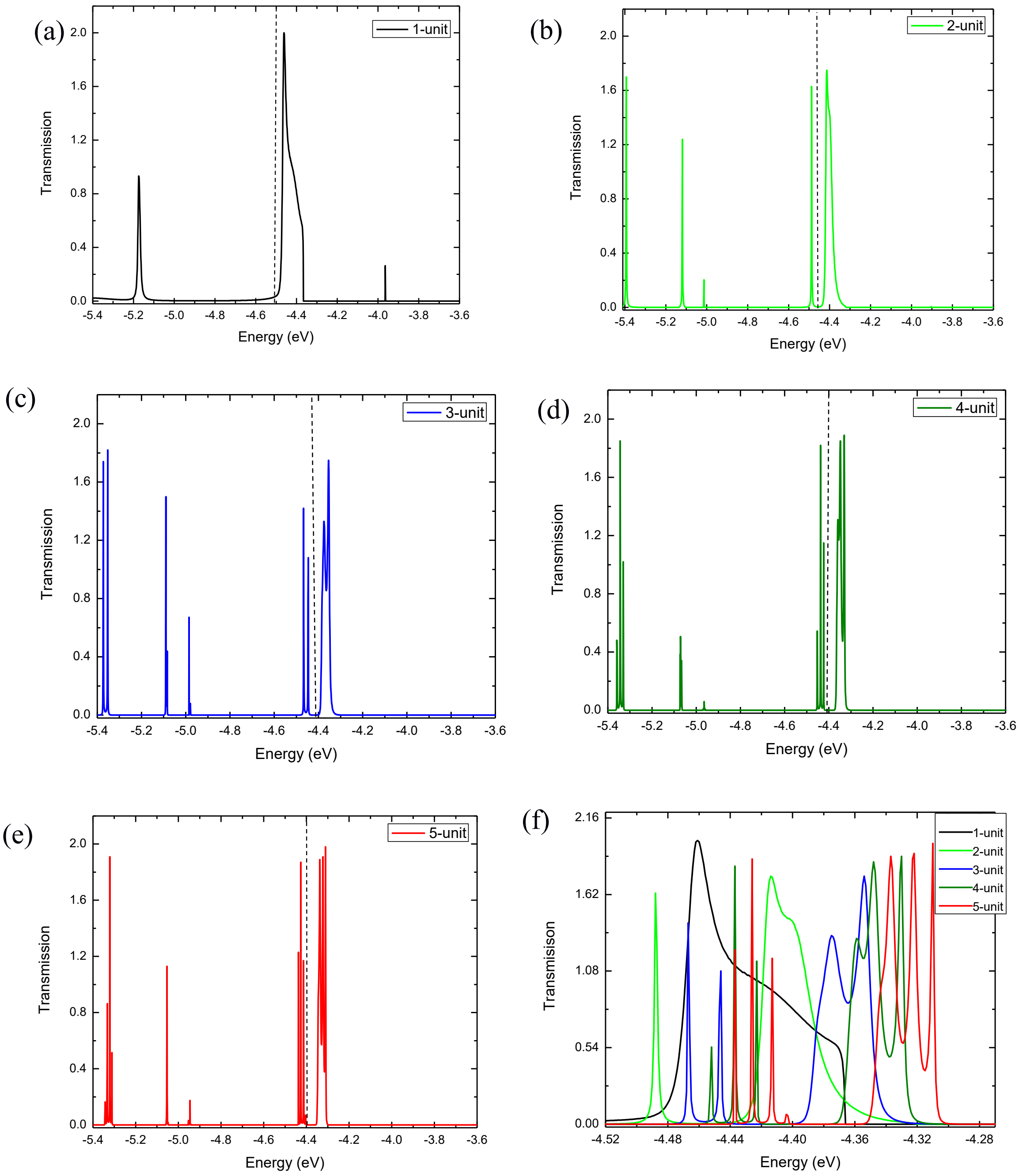

Figure 4.8: Electron transmission with respect to scattering energy calculated with DFT-GGA approximations for Au_6-benzenedithiol linear chains of varying lengths (a) 1-unit, (b) 2-unit, (c) 3-unit, (d) 4-unit and (e) 5-unit. Dotted line in each plot represents Fermi energy. (f) Magnified view of transmission spectra near the Fermi energies for 1-5 unit Au_6-benzenedithiol linear chains.

Presence of multiple transmission channels may be attributed to overlapping of a number of discrete orbitals which enhance the transmission. In case of benzenedithiol-Au_6 linear chains of varying lengths, an increase/broadening of the number of transmission peaks near the Fermi energy was observed with an increase in chain length, indicating enhanced transmission as these chains are extended. This behaviour can be seen clearly in the transmission spectra of 2-5 unit linear chains magnified near the approximate value of Fermi energy of these structures. In case of a 1-unit linear chain, a single broad peak near the Fermi energy is observed that may be due to the small size of the overall benzenedithiol-Au_6 structure which contains only a single molecule between two metal clusters.

Focussing on the 3-unit Au_6-benzenedithiol linear chain as an example, Figure 4.9 shows approximate correlation of the transmission peaks with the corresponding frontier orbitals. The peaks in transmission arise due to the orbitals that become more closely spaced/overlap with each other. Thin peaks near the HOMO (-4.491 eV), HOMO-1 (-4.505 eV) arise due to the overlap of these orbitals. Post this, there seems to be very low/no transmission which can be associated to lack of states/orbitals in the leads which couple with the states/orbitals of the Au_6-benzenedithiol chain in the central region. Transmission peaks are once again observed near HOMO-4 (-4.970 eV) and HOMO-5 (-4.973 eV). Overlap of the LUMO orbitals i.e. LUMO (-4.331 eV), LUMO+1 (-4.327 eV), LUMO+2 (-4.323 eV), LUMO+3 (-4.322 eV), contributes to the wide peak in transmission. Overall, similar results were observed for other Au_6-benzenedithiol linear chains which showed an increase in broadening of the transmission peaks as the length of the chains are extended.

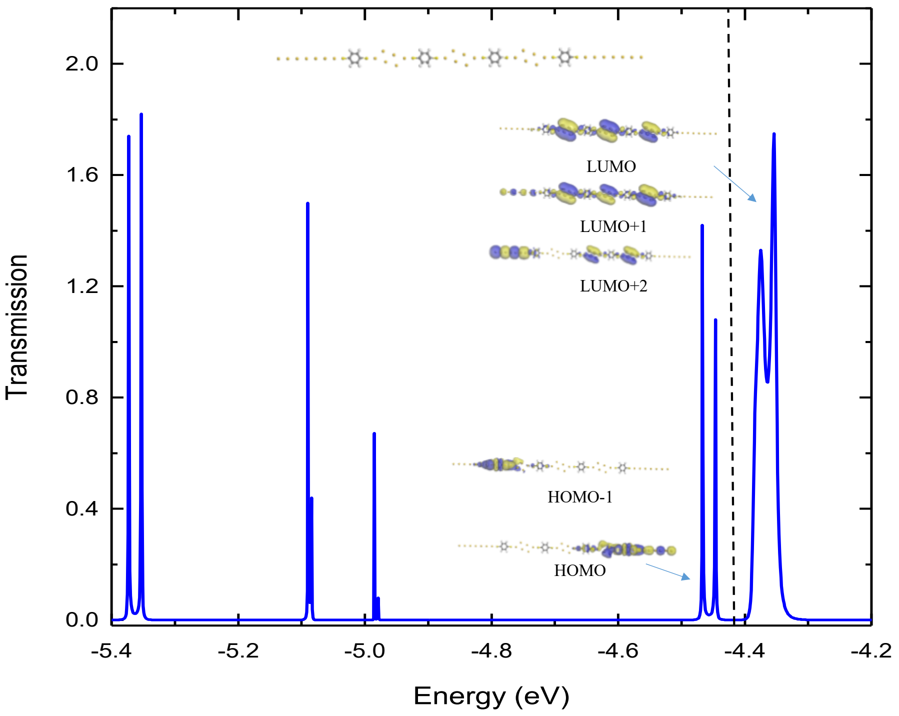

Figure 4.9: Electron transmission with respect to scattering energy calculated with DFT-GGA approximations for a 3-unit Au_6-benzenedithiol linear chain. Dotted line represents the Fermi energy. The structure used in the scattering region and selected orbital isosurfaces corresponding to peaks in transmission are also shown.

Similarly, on approximating the transmission peaks obtained for a 2-unit Au-benzenedithiol network to the corresponding frontier orbitals near the HOMO-LUMO gap that lead to peaks in the DOS spectra (shown in Figure 4.10), the following were observed: The peaks in transmission arise due to the orbitals that become more closely spaced/overlap with each other. Thin peak in transmission near the HOMO (-4.521 eV), HOMO-1 (-4.539), HOMO-2 (-4.573 eV) arise due to the overlap of these orbitals. Post this, there seems to be very low/no transmission which can be associated to lack of states/orbitals in the leads which couple with the states/orbitals of the Au-benzenedithiol network in the central region. Transmission peaks are once again observed near HOMO-3 (-4.996 eV), HOMO-4 (-5.001 eV), HOMO-5 (-5.047 eV), HOMO-6 (-5.059 eV). In this structure, the LUMO orbitals are mainly localized to the metal clusters yielding lower contributions to the transmission as seen at LUMO (-4.359 eV), LUMO+1 (-4.353 eV), LUMO+2 (-4.352 eV), LUMO+3 (-4.340 eV). Overall, this behavior becomes increasingly significant as the chain length of the network increases, thereby showing an increase in the number of peaks.

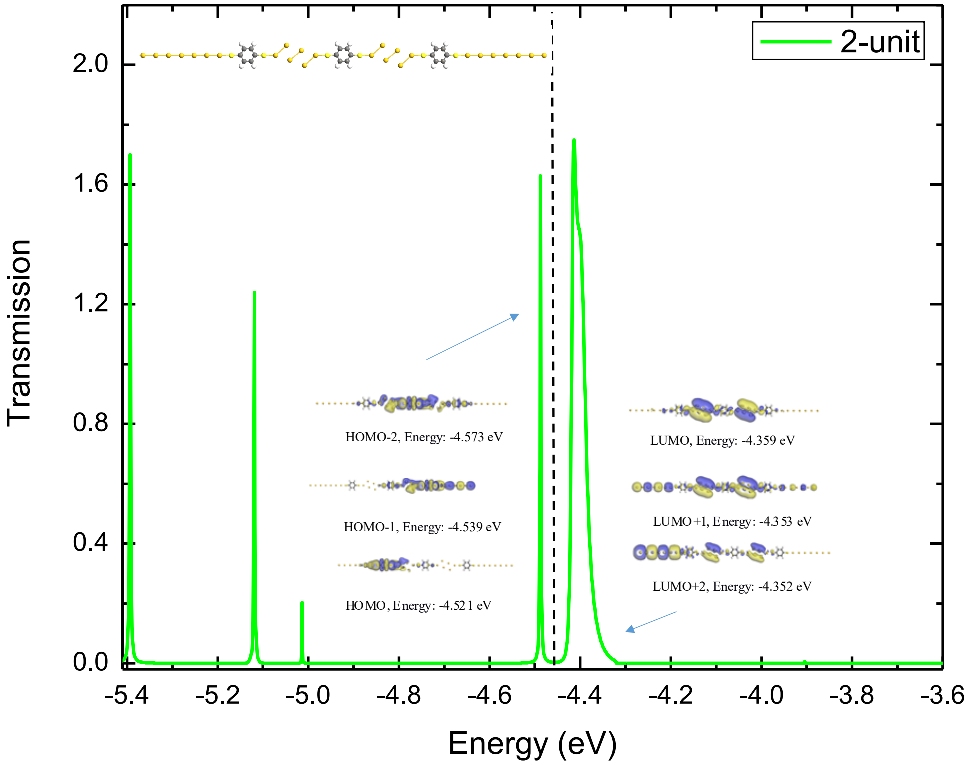

Figure 4.10: Electron transmission with respect to scattering energy calculated with DFT-GGA approximations for a 2-unit Au-benzenedithiol linear chain. Dotted line represents the Fermi energy. The structure used in the scattering region and selected orbital isosurface corresponding to peaks in transmission are also shown.

In comparison, lower number of transmission peaks close to the Fermi energy, that contribute in charge transport through the structure were seen in case of Au_6-hexanedithiol chains of varying lengths. By examining the transmission spectra for a 3-unit Au_6-

hexanedithiol linear chain as an example in Figure 4.11, it was observed that these results support the earlier explanation regarding reduced transmission in case of alkane chains due to wider HOMO-LUMO gaps as compared to benzenedithiol-Au_6 chains. Very low transmission may be attributed to most of the orbitals being localized around the metal atoms and/or insufficient overlapping. Similar results were seen in Au_6-octanedithiol chains of varying lengths.

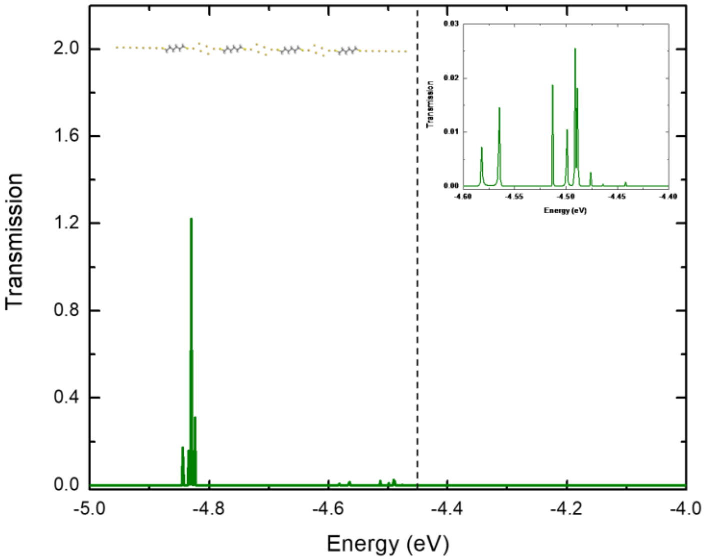

Figure 4.11: Electron transmission with respect to scattering energy calculated with DFT-GGA approximations for a 3-unit Au_6-hexanedithiol linear chain. Dotted line represents the Fermi energy. Inset shows magnified view of transmission near the Fermi energy. The structure used in the scattering region is also shown.

Similarly, as the linear chains were extended to multi-terminal networks representing a Y-, H-, diamond-shaped networks, the overall transmission near seemed to increase near the Fermi energy as the size of the networks was increased (for example, in case of a Y-, H-shaped networks). In comparison, for a diamond-shaped network, low transmission near the Fermi energy could be due to the structure forming a closed loop with less pathways for electron transmission. The transmission plots for each of these networks are shown below in Figure 4.12.

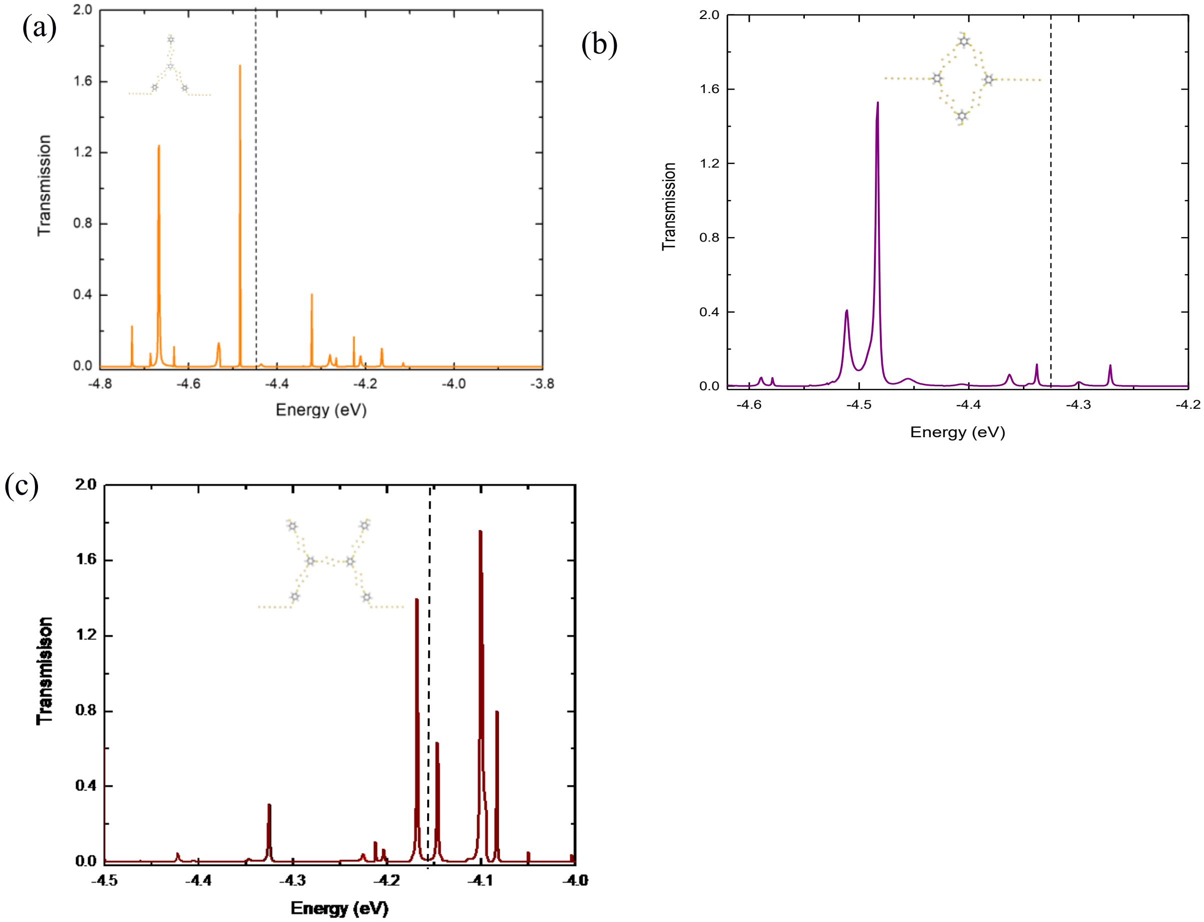

Figure 4.12: Electron transmission with respect to scattering energy calculated with DFT-GGA approximations for a (a) Y-, (b) diamond- and (c) H-shaped network. Dotted line represents the Fermi energy. The structure used in the scattering region is also shown.

Looking at the transmission spectra of a diamond-shaped network in detail, as shown in Figure 4.13. The peaks in transmission arise due to the orbitals that become more closely spaced/overlap with each other. A broad transmission peak is seen due to the overlap of the HOMO orbitals; HOMO (-4.485 eV), HOMO-1 (-4.520 eV), HOMO-2 (-4.554 eV), HOMO-3 (-4.556 eV) and HOMO-4 (-4.602 eV) that are similar in energy.

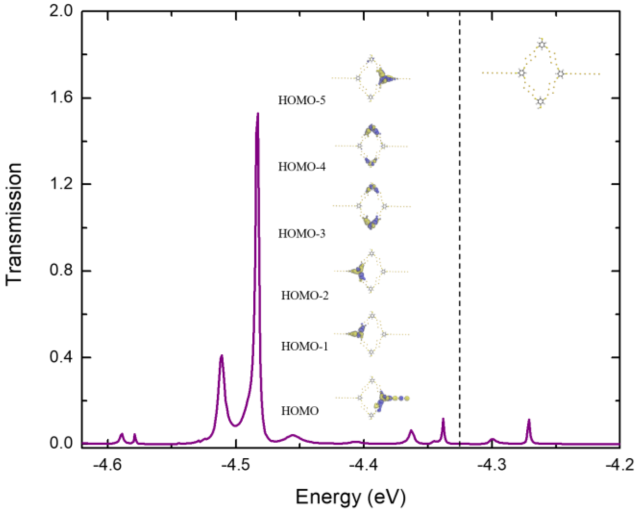

Figure 4.13: Electron transmission with respect to scattering energy calculated with DFT-GGA approximations for diamond-shaped network. Dotted line represents the Fermi energy. The structure used in the scattering region and selected orbital isosurfaces corresponding to peaks in transmission are also shown.

These results illustrate how different extended molecular networks and systems may help in controlling the transmission over larger distances. To further probe the electronic and transport properties of the molecular networks, we calculated their transmission spectra and *I-V* characteristics by attaching bulk electrodes on either side of the scattering region (see Figure 4.5). Figure 4.14 shows the transmission spectra of 1- and 3-unit benzenedithiol-Au_6 linear chains. The peaks in the transmission spectra likely correspond to delocalized molecular orbitals forming conduction channels for charge carriers through the chains: The transmission peaks below the fermi energy level likely correspond to delocalized molecular orbitals (e.g. HOMO, HOMO-1 etc.), which overlap with each other and extend across the entire linear chain, thereby providing effective conduction pathways; conversely, the presence of fewer transmission peaks above the fermi energy level can be attributed to the presence of localized molecular orbitals at higher energies (LUMO, LUMO+1 etc.), thereby resulting in a significant reduction of the transmission coefficient transmission coefficient [174].

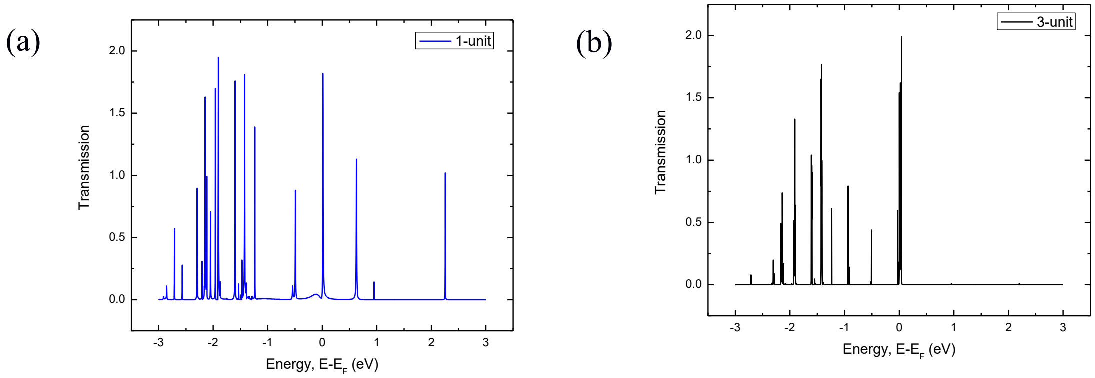

Figure 4.14: Electron transmission with respect to energy for benzenedithiol-Au$_6$ linear chains of varying lengths (a) 1-unit and (b) 3-unit.

The calculated current-voltage (*I-V*) characteristics of the linear chains are plotted in Figure 4.15 (a-d). Nonlinear *I-V* characteristics with NDR are observed as bias magnitude is increased. NDR effects are seen to be more pronounced with increasing length of the linear chains, as illustrated in Figure 4.15e, which shows a plot of the peak-to-valley current ratio (PVCR) against the length of the linear chains. The plot shows a rapid rise in PVCR as the linear chains are extended, from just over 1 to greater than 500, for 1- through 4-unit chains, respectively. This behavior can be correlated to the number of accessible orbitals at higher energies as the chains are extended, consistent with the transmission spectra of Figure 4.14, and similar to previous work on different length molecular structures [95], [175]. As a comparison, the *I-V* characteristics of a metal-molecule-metal junction comprising of a BDT molecule sandwiched between symmetric bulk gold electrodes is shown in Figure 4.15a (inset). The measured current was found to be in the µA range with less pronounced nonlinearity/NDR peaks, which is comparable to previous work [89], [176].

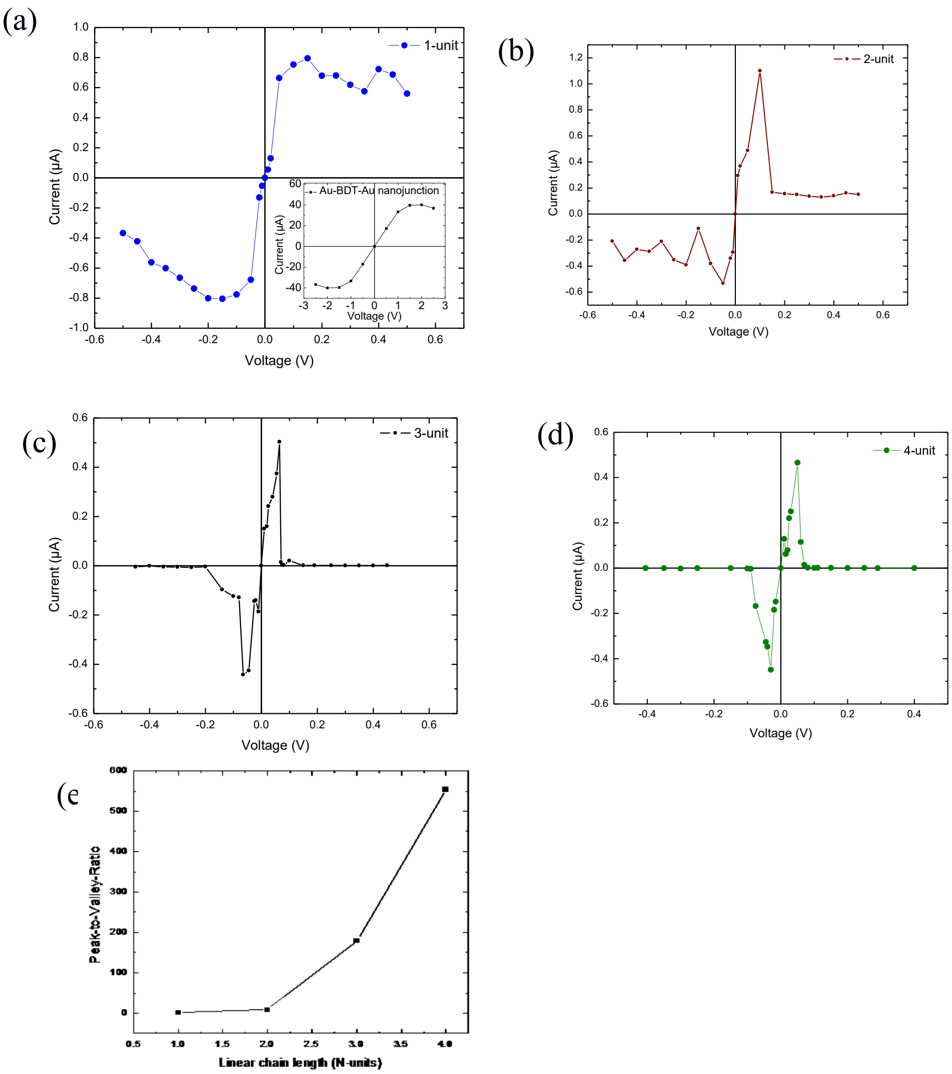

Figure 4.15: *I-V* characteristics of benzenedithiol-Au$_6$ linear chains of various lengths (a) 1-unit, inset –*I-V* characteristics of Au-BDT-Au junction (b) 2-unit, (c) 3-unit, (d) 4-unit and (e) Peak-to-valley current ratio vs linear chain length of benzenedithiol-Au$_6$ linear chains.

Differential conductance *vs.* bias voltage plots of different length linear chains exhibit asymmetric, nonlinear behavior with significant fluctuations between some bias points as expected from the NDR behavior in the *I-V* characteristics. In addition, as chain length increases these fluctuations appear to become more pronounced. The transmission spectra of Y- and diamond-shaped networks are shown in Figure 4.16. The broad peaks observed in the transmission spectra of both networks are likely due to a larger number of available overlapping molecular orbitals which together form conduction pathways for electron transport. These observations are very similar to the results obtained using Quantum espresso package with linear chain of electrodes.

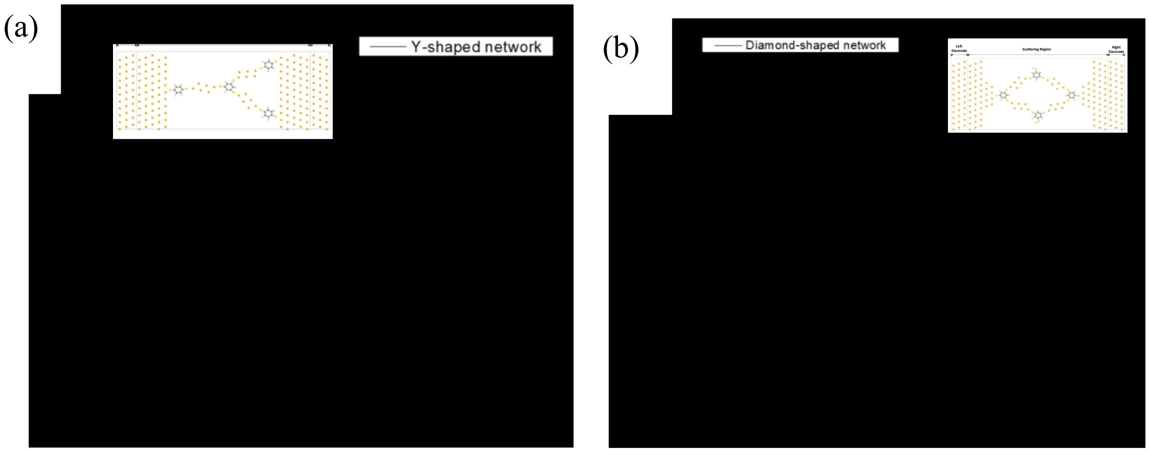

Figure 4.16: Electron transmission with respect to energy for a (a) Y-, and (b) Diamond-shaped network.

The Y-structure exhibits an asymmetric, nonlinear *I-V* characteristic with rectifying behavior and NDR in combination over the operating voltage range (Figure 4.17a). The Y-shaped network's *I-V* curve contains a distinct NDR peak near +0.05 V with a peak-to-valley ratio of 2.3 and a significant rectification ratio that reaches 10.6 (0.25 V). On the other hand, the diamond-shaped structure exhibits non-ohmic I-V behavior (Figure 4.17b) with sharp NDR features near +0.1 V and – 0.05 V and large PVCRs on the order of 200.

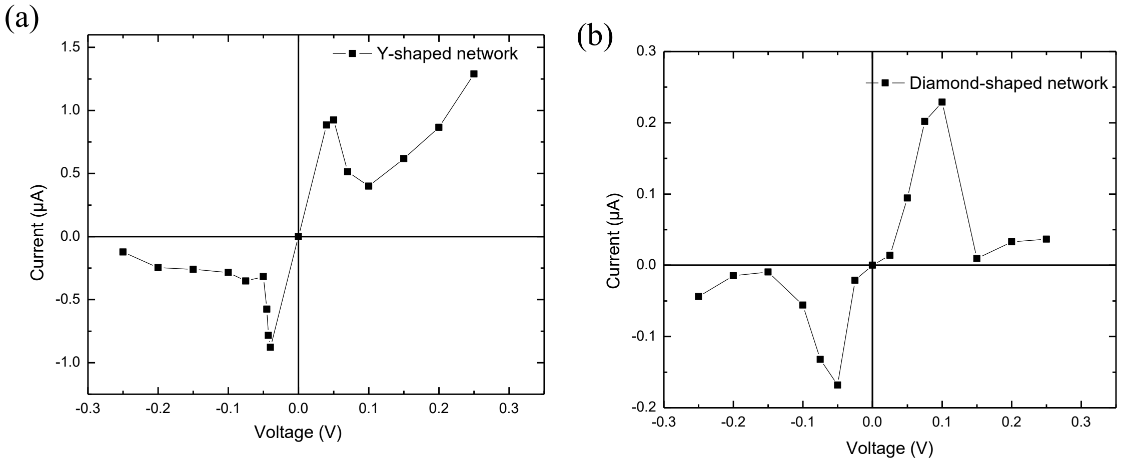

Figure 4.17: *I-V* characteristics and of (a) benzenedithiol-Au_6 Y-shaped network. (b) benzenedithiol-Au_6 diamond-shaped network.

To gain further insight into the charge transport characteristics, in Figure 4.18 we compare calculated voltage drops for a 1-unit linear chain and Y-shaped network: As expected for the symmetric linear chain in Figure 4.18a, the voltage drop is essentially a mirror image upon switching polarity for a given magnitude of applied bias. In contrast, the Y-structure in Figure 4.18b shows a distinct difference in the potential drop depending on the sign of applied bias with an electrostatic barrier or pinning apparent near the intersection of the three branches. This asymmetry likely leads to the observed rectifying *I-V* characteristic of Figure 4.17a, which, along with its simultaneous NDR, is reminiscent of an Esaki diode, or perhaps the metal-molecular analog of an interband resonant tunneling diode [177]. In addition, quantum interference [178] or ratcheting effects [179]could contribute to the observed Y-structure *I-V* characteristic and provide avenues for tuning behavior in different device applications.

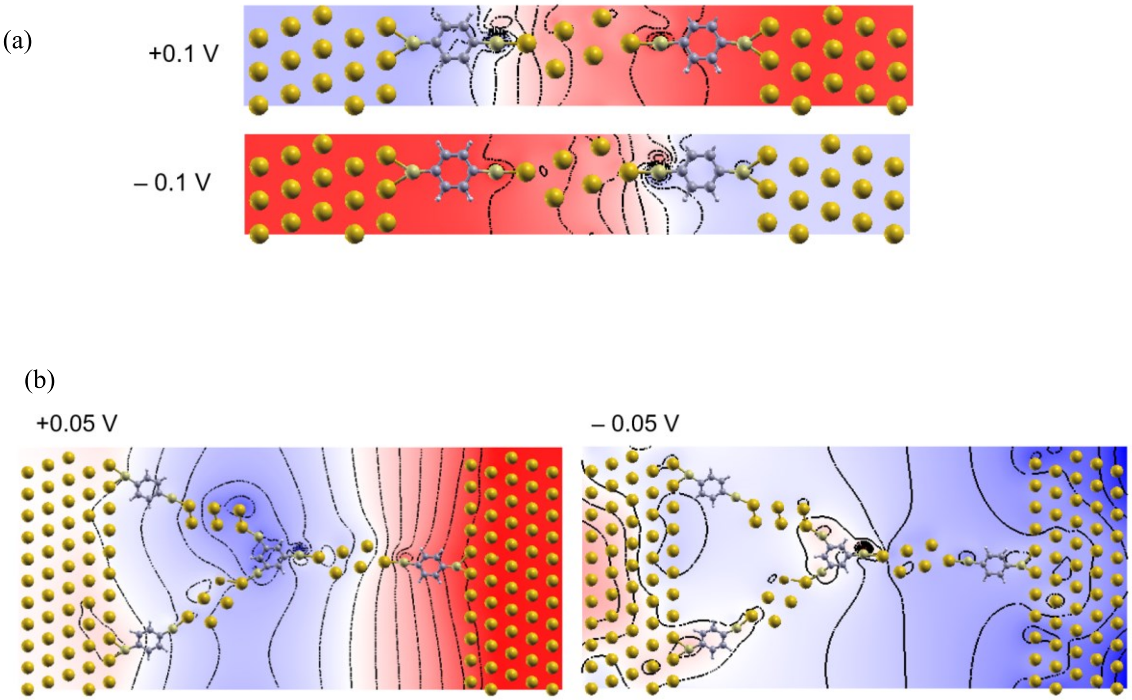

Figure 4.18: Potential drop in scattering region between electrodes for (a) 1-unit benzenedithiol-Au$_6$ linear chain, and (b) Y-shaped benzenedithiol-Au$_6$ network. Applied bias is indicated near each image.

The observed NDR and non-ohmic *I-V* behaviors in the branched networks are likely due to tunneling effects and bias-induced energy level alignment/misalignment of the molecular orbitals with the Fermi level of the metallic electrodes. The differential conductance *vs.* bias voltage plots of both branched structures exhibit asymmetric, nonlinear behavior with fluctuations in differential conductance values between bias voltage points. Observed differential conductance fluctuations in nanostructures have been attributed to complex quantum mechanical phenomena like electron-electron interactions [180][181] and tunneling effects [180][182] in other works. The three-terminal metal-molecular Y- and diamond-shaped structures thus represent unique possibilities for device functionality in novel logic/switching, signal processing and memory nanoelectronic circuit elements.

Comparisons with Experimental Results:

From the experimental results, NDR peaks of differing widths and peak-to-valley ratios from ~ 1.05 to 1.5 were found to typically occur near 3–4 V in our studies, becoming more prevalent as the number of molecules in the networks increased with the critical $N_{\mathrm{BDT}}:N_{\mathrm{particle}}$ ratio near 5:1. Figure 3.17 (Chapter 3) shows an evolution of *I-V* characteristics as a function of $\mathrm{N}_{\mathrm{BDT}}:\mathrm{N}_{\mathrm{particle}}$ ratio showing increase in nonlinearity and NDR appearance near 5:1. A peak-to-valley ratio of approximately 1.52 is seen for the 50:1 network sample. The computational results show a similar trend for NDR effects that are seen to be more pronounced with increasing length of the linear chains. Nonlinear *I-V* characteristics with NDR are observed as bias magnitude is increased. Figure 4.15e, shows a plot of the peak-to-valley current ratio (PVCR) vs. the length of the linear chains. The plot shows a rapid rise in PVCR as the linear chains are extended, from just over 1 to greater than 500, for 1- through 4-unit chains, respectively.

Our computational and experimental results complement each other and illustrate how the transmission through molecular-scale devices could potentially be controlled with precision by modifying the number of molecules (or the chain length) in the hybrid organic-inorganic molecule-nanoparticle networks.

4.4 Conclusions

In conclusion, several types of metal-molecular nanojunctions and networks with thiolated molecule-metallic clusters were modeled using DFT approximations. Analysis of the corresponding optimized geometries, molecular orbital spatial distributions, HOMO-LUMO gaps, DOS peaks, transmission and the *I-V* spectra facilitate the understanding of electronic characteristics and charge transport properties of such molecular networks. A decrease in HOMO-LUMO gap is observed due to the inclusion of the metal cluster in the formation of various metal-molecule nanojunctions. Size of the networks played a significant role on the HOMO-LUMO gaps, energy level distributions, as well as on the electron transport. Detailed examination of the molecular orbitals and transport spectrums of systems composed of benzenedi(tri)thiol-metal networks, showed delocalized frontier orbitals, a decrease in the HOMO-LUMO gap and an increase in the number of transmission peaks near fermi energy with an increase in the chain length, indicating enhanced transmission. On the other hand, for systems composed of alkanedithiol molecules, significant localization to the metallic clusters was observed along with decrease in the height of transmission peaks, indicating increased barrier to electron transport. Calculated *I-V* characteristics of the metal-molecular networks exhibited nonlinearities and rectification with negative differential resistance (NDR) peaks that became more pronounced with increasing chain length. A significant overlap of the energetically close delocalized molecular orbitals near the Fermi energy was observed, which likely combine and contribute to electron transport. The transmission spectra of the linear chains and branched networks showed an increase in the number and width of transmission peaks near the Fermi energy, as the structures were extended, indicating enhanced transmission. Peak-to-valley current NDR ratios as large as ~ 500 and rectification ratios of ~ 10 (0.25 V) were shown for linear and branched circuit elements, respectively, illustrating how charge transport through molecular-scale devices could be controlled with precision by modifying the structure and geometry of molecule-nanoparticle networks. Based on these results and phenomena observed in the metal-molecular networks, potential applications for these systems in future nanoelectronic circuits abound: Future work on larger networks, consisting of different metal particle/molecule combinations and geometries, could provide a rich framework for exploring applications of metal-molecular networks in nanoelectronic devices such as nanoscale molecular memory, logic circuits and switches.

Chapter 5 Potential Applications

The metal-molecular networks studied in this work provide several possibilities for applications in nanoelectronics and hardware security. Some of these applications are detailed below.

5.1 Switching, logic and memory based applications

- **Introduction**

Nanostructures, such as, organic molecular electronic components, carbon nanotubes, and quantum dots can rapidly assemble into complex circuitry that show potential use in applications such as memory and logic devices. Recently, great progress has been made in the fabrication of non-volatile memory devices based on metallic nanoparticles [183][184]. For example, gold nanoparticles are used as charge trapping elements in non-volatile memory devices due to their unique properties such as chemical stability, and ease of synthesis [184].

There is a great demand for floating gate flash memory devices that uses a type of non-volatile memory technology. However, floating-gate based flash memory devices suffer from issues such as limits in continuous device scaling due to increasing cell-to-cell interference. Researchers are currently working on developing flash memory devices with discrete semiconducting or metallic charge trapping layers, examples include, nano-floating gate memory devices, silicon-oxide-nitride-oxide-silicon devices, nanocrystal flash memory devices, etc. (Figure 5.1). Briefly, the operation of a non-volatile memory device is as follows: the non-volatile memory devices have charge storage (or trapping) layers where the charge carriers are stored. The flash memory cell consist of a floating gate in which the electrons are stored (via programming operations) and moved back to the substrate (via erasing operations). The threshold voltage (V_{th}) of the device can be influenced by the channel conductance that in turn depends on whether the charge carriers are stored in the floating gate or not. The measure of drain current (I_d) gives the information the programmed and erased states of the flash memory devices which is denoted by "1" an d"0" states, respectively. Each flash memory cell can retain 1 bit (or more) information as a "0" or a "1" state. Flash memory devices based on metallic or semiconducting nanocrystals or nanoparticles offer advantages over the other types of flash memory devices as the trap levels and trap sites can be effectively tuned by adjusting the work function and dimensions of the nanocrystals. For example, figure 5.1 (c-d) shows an organic transistor-based nanofloating gate memory device that used thin HfO_2 tunnelling dielectric layer for charge injection as well as data retention. The gold nanoparticles synthesized were adsorbed on the LbL assembled polyelectrolyte layer (PAH/PSS/PAH) via electrostatic interaction, and PMMA was used as the tunnelling dielectric layer. This device showed a very large memory window (~34 V) and reasonable data retention properties. Alternatively, another type of non-volatile random-access memory called as the phase change memory utilizes the rapid reversible phase change effect seen in some materials under the influence of electric current pulses [25], [26]. Here, data storage capabilities are due to a thermally induced phase change between amorphous and polycrystalline states in a thin film of chalcogenide alloy. This phase change results in variations in the material resistivity.

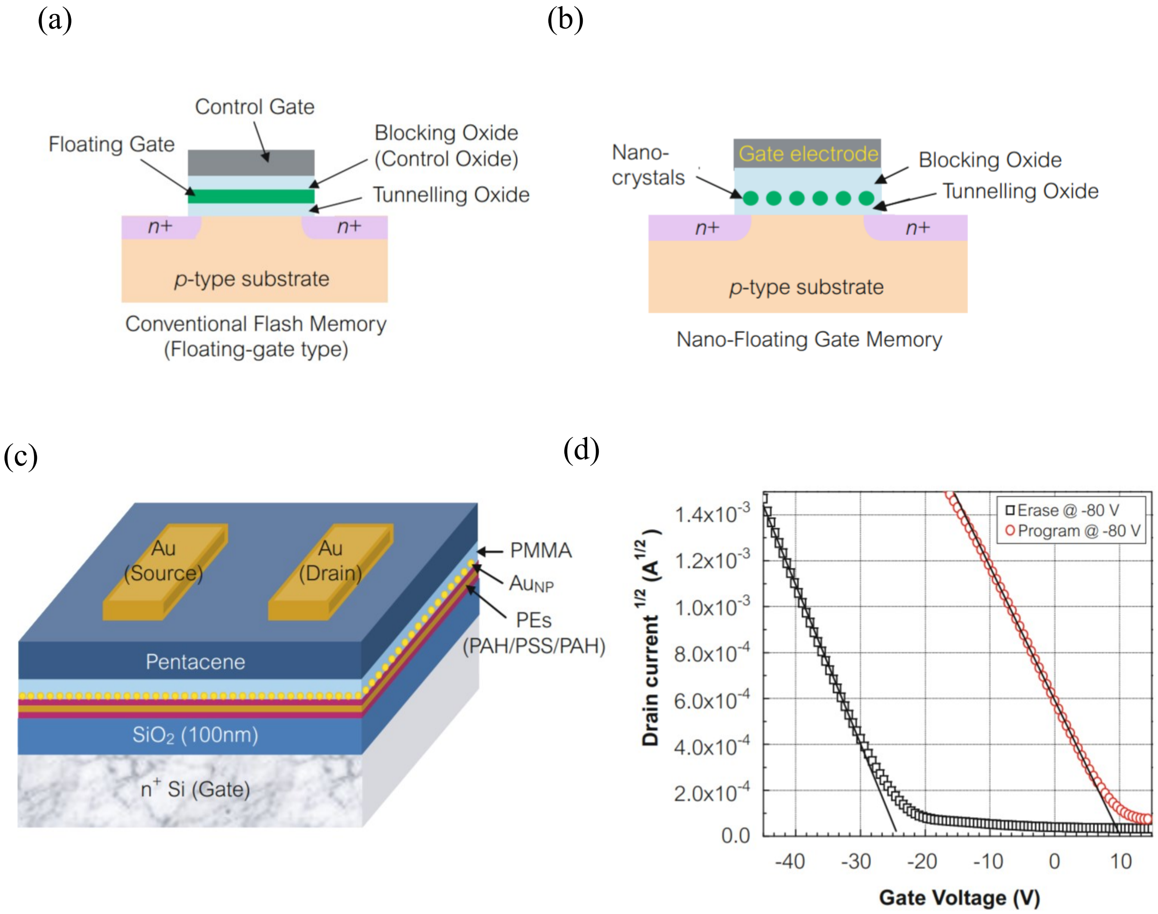

Figure 5.1: Schematic device structure of (a) conventional non-volatile flash memory devices and (b) Nano-floating gate charge trapping flash memory devices. (c) Schematic of a bottom-gate and top-contact structured organic transistor-based nano-floating gate memory device and (d) Erase/Program characteristics of the memory device. Adapted from [184], [185]

On the other hand, there has been a great interest in electron devices utilizing quantum interference, in applications such as switching and logic [186]. For example, logical circuitry based on electron waveguides consists of branching electron waveguides (resembling a Y-branch switch) that switches an incoming current between two drain leads. This device under the influence of an electric field, shows a nonlinear digital response function, exhibiting a standardized signal level, and it shows features comparable to CMOS devices (when the Y-branch switches are connected to each other) [187]. Figure 5.2 (a) shows an example of a Y-branch switch whose functioning is analogous to the optical digital switch. Under the influence of an electric field perpendicular to a branching waveguide, electrons from the source can be forced to enter the drain with highest electrostatic potential. When two Y-branches are connected to each other, an inverter device can be implemented (Figure 5.2 (b)). When the gate voltage (V_G) is high, the upper Y branch connects V_a to V_{DD} and the lower Y branch connects V_{out} to ground. Similar to a CMOS device, current flows through the gate of a Y-branch inverter only during switching. Alternatively, NAND and NOR gates can also be implemented using these Y-branch networks.

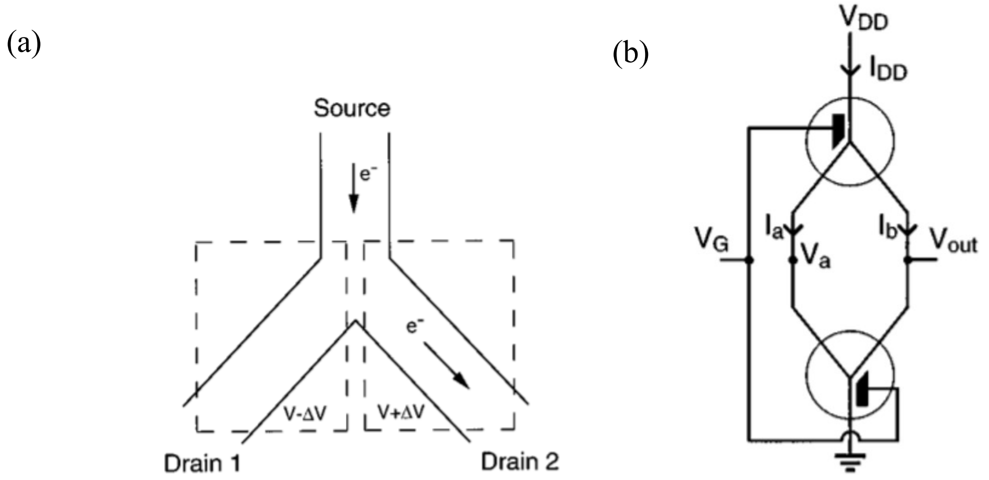

Figure 5.2: Schematic of a (a) Y-branch switch in which the current from the source is transmitted into the drain (with higher electrostatic potential) under the influence of an electric field and (b) Y-branch inverter created by joining two Y-branches that ensure that no current flows except during switching. Adapted from [187].

Another type of non-volatile memory device known as the memristor is regarded as a promising candidate for next generation devices with applications in bio-inspired computing systems [188] and neuromorphic computing [189], [190].

Researchers have demonstrated memristive phenomena in various materials such as amorphous silicon, carbon, polymer-nanoparticle composites, etc. [191][192]. Unlike the conventional resistor that has a fixed resistance, a memristor shows voltage-dependent resistance. The memristor consists on a variable resistor whose value is based on the amount of current that has circulated through it, i.e., on its previous history; a concept that leads to interesting behaviour such as hysteresis and non-linear effects.

The concept of resistive switching influences the behaviour of the memristor and non-volatile resistive random-access memories (RRAM) devices. Resistive switching (RS) is a reversible and non-volatile variation in the resistance after the application of a pulsed voltage/current stimulus [193]. In devices showing RS, multilevel memory states are observed in addition to the "on" and "off" states. By measuring the remnant resistance state i.e., read operation that is observed after pulsing i.e., write operation in a loop where increasing positive pulses are applied up to a maximum value, then the amplitude is decreased, then the polarity is reversed until a negative maximum is reached, to finally return back to zero. As an example, Figure 5.3 (a) shows the resistance (R_D)- voltage (or *R-V*) hysteresis switching loops. R_D values for the interface at electrode D as a function of pulsing voltage strength applied between electrodes A and D that exhibits two well defined states, termed as the high H and low L resistance states, in addition to the two rapid transitions through a multitude of stable intermediate states.

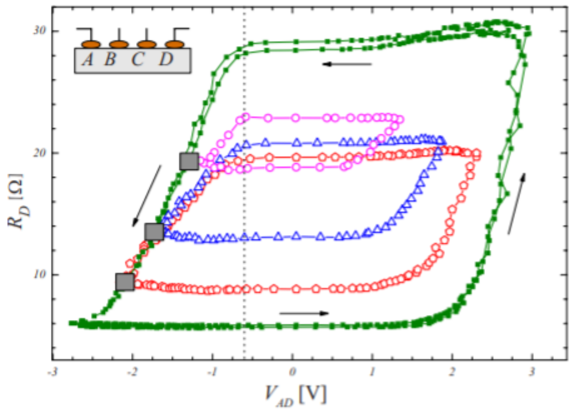

Figure 5.3: *R-V* hysteresis switching loops showing the non-volatile resistance (after the pulse) that is plotted as a function of voltage-pulse intensity along a full cycle. Adapted from [193].

By organizing individual memristors into high-density crossbar arrays, there is a possibility of creating a power-efficient solution for information storage and processing in the next-generation devices [194]. Recently, a memristor crossbar arrays with a 2-nm feature size was shown where the memristors in the arrays switch with tens of nanoamperes electric current with nonlinear behaviour. The electrodes of memristor crossbar arrays could be made of metal nanostructures, CNTs, dopant nanowires, graphene nanoribbons, etc. In one example, memristor crossbar array was created by depositing a 7-nm switching layer on a polished nanofin chip. This was bonded to another chip with the two nanofin arrays orthogonal to each other (Figure 5.4). Each device in the array was programmed as either the on or off state.

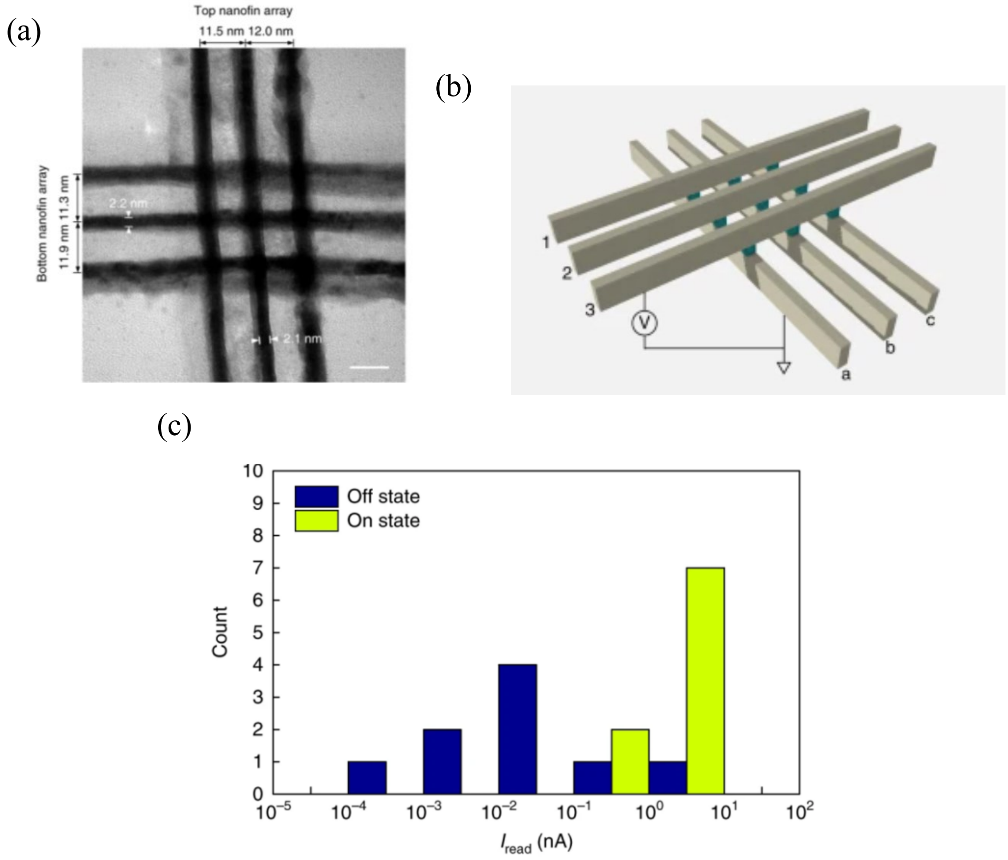

Figure 5.4: TEM image of a 3 × 3 memristor crossbar array. (b) Schematic of the programming technique used for devices in the array. Here, a voltage bias is applied to the top electrode of a selected cell, while keeping the bottom electrode grounded and the remaining unselected electrodes floating. While programming, the nine devices in the 3x3 array are selected in sequence without disturbing their neighbours. The top electrodes are labelled as 1, 2 and 4, while the bottom electrodes are labeled as a, b, c. (c) A histogram showing the read current at −1 V for the on and off states of all nine devices. Adapted from [194].

There has been significant progress in research being conducted for future electronic devices using molecules including transistors [90], rectifiers [47] and optoelectronic switches [51]. Bottom-up nanofabrication approaches offer a broad range of possibilities for the design and construction of functional nanostructured materials [15], [16] and various structures and devices with metal-molecular junctions formed by linking thiolated molecules to metal electrodes using techniques such as self-assembly [195–197] have been demonstrated [198]. Structured metal nanoparticle arrays are model systems for granular materials and they showcase a wide variety of electronic properties, which include metal–insulator transitions, catalytic surfaces, energy conversion devices, sensors, computing networks [61], [67], [197], [199], [200] or even information storage platforms [201]. By controlling and tuning the arrangements and properties of the particles, the resultant networks can be used as model systems for various molecular-level applications in electronics [84], [202]. In this work, various nanoscale networks were modeled and their electron transport properties were investigated under an applied bias including linear chains and branched molecular networks (Y- and diamond- shaped) of various sizes. Our results suggest potential development of future nanoelectronic circuit elements based on nanoscale metal-molecular networks.

- **Results:**
  - **Molecular orbitals of potential switching elements**

Analogous to electron waveguide devices [203], such as the Y-branch switch, [186] we illustrate a potential switching element in Figure 5.5(a) based on the Au_6-benzenedi(tri)thiol Y-shaped network: In this configuration a lateral electric field (e.g., via a gate electrode) is used to deflect an incoming current between the two arms or drain leads of the Y-branch structure. In case of the Y-shaped molecular network, this switching occurs between different molecular orbitals that are similar in energy but in different arms. It has also been shown that such switching is possible by applying a potential difference between the drain arms, i.e., without external gates, allowing gain and potentially THz operation.[187] One can also consider using our structures to create larger molecular networks. For example, a ring-shaped network could be implemented by using two Y-shaped networks linked to each other via a Au_6 cluster and could be used as a two terminal molecular network device as shown in Figure 5.5 (b).

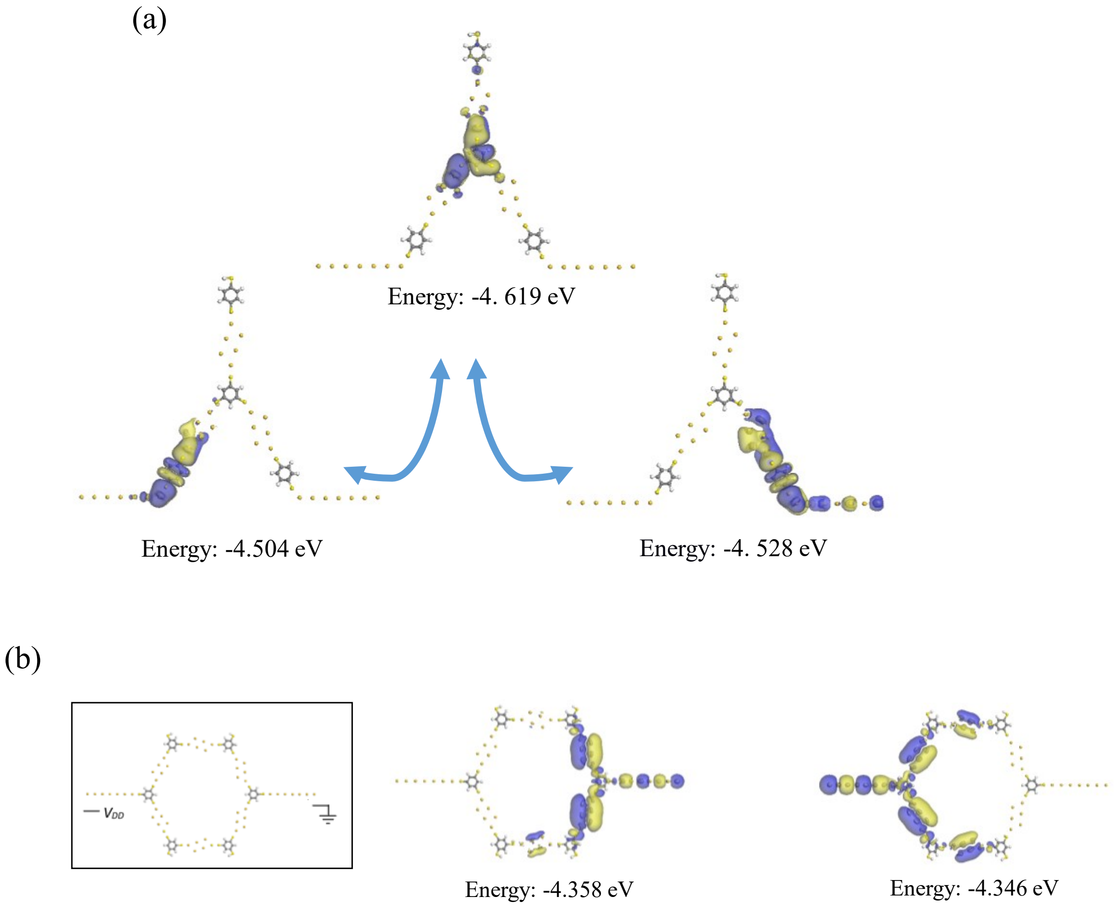

Figure 5.5: Switching elements based on various Au_6-benzenedi(tri)thiol networks. (a) Y-shaped switching element in which application of a lateral electric field effects switching of the incoming current between the different branches (orbital energies indicated). (b) A first-order implementation of a two terminal ring-shaped molecular network device.

Y-branches can be used to implement logic functions, such as NAND and NOR, for different biasing configurations [187]. Similar applications could also be realized by using these networks as building blocks and extending to multi-terminal networks representing a type of molecular integrated circuit. In Figure 5.6, we show two Y-shaped networks coupled to each other via a benzenedithiol molecule that can operate as an inverter. In addition, all these networks can also be used as continuous pathways for signals or information transfer from one arm to another.

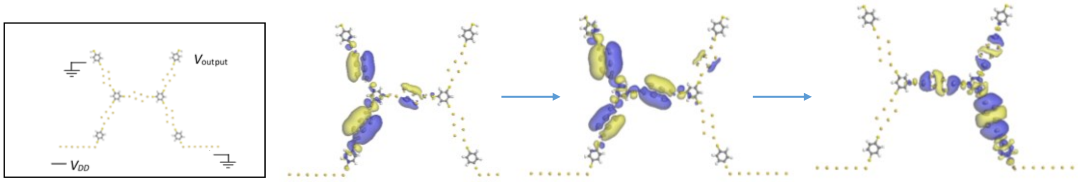

Energy: -4.274 eV Energy: -4.035 eV Energy: -3.662 eV

Figure 5.6: A first-order implementation of a logical inverter with a H-shaped molecular network. Simulation results show example where for low gate voltage output is V_{DD} (on left), whereas switching to a higher energy orbital gives output as ground (on right).

○ *I-V* plots supporting the potential device applications

DFT calculations on the metal-molecular networks of varying lengths showed nonlinear *I-V* characteristics with NDR as bias magnitude is increased. NDR effects are seen to become more pronounced with increasing length of the linear chains, as illustrated in Figure 4.15.

As an example, the *I-V* plots of 1- and 4-unit benzenedithiol-Au_6 linear chains, and Y- and diamond-shaped networks is shown once again in Figure 5.7. Resonant tunneling mechanisms [204], bias induced alignment of the molecular orbitals [205] and weak molecule-electrode coupling [206] have also been identified as possible sources of NDR in molecular systems connected to metallic electrodes, with the unique hybrid metal-molecular networks containing gold clusters studied here possibly amplifying these effects.

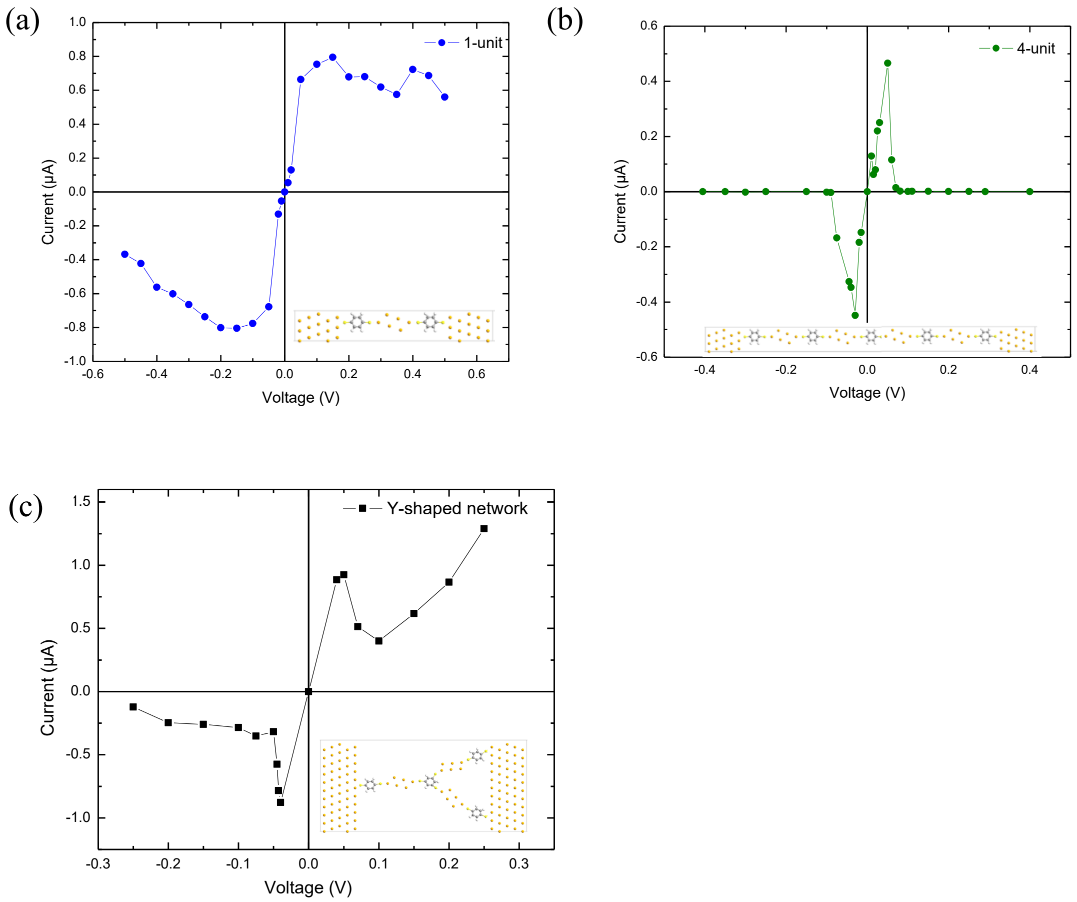

Figure 5.7: *I-V* characteristics of benzenedithiol-Au$_6$ linear chains of various lengths (a) 1-unit (b) 4-unit. *I-V* characteristics of corresponding branched benzenedithiol-Au$_6$ networks (c) Y-shaped network. The corresponding structures are shown as insets.

The asymmetry in the Y-structure likely leads to the observed rectifying *I-V* characteristic [99], which, along with its simultaneous NDR, is reminiscent of an Esaki diode, or perhaps the metal-molecular analog of an interband resonant tunneling diode [177]. In addition, quantum interference [178] or ratcheting effects [179] could contribute to the observed Y-structure *I-V* characteristic and provide avenues for tuning behavior in different device applications. These molecular networks show potential applicability in nanoelectronic circuits by harnessing observed NDR effects for future design of molecular diodes [207], high density memory and logic devices [207], and analog-to-digital converters [208]. Potential switching behavior, as seen from the molecular orbital visualizations, could also account for some of the nonlinearities in the *I-V* characteristics of the branched networks.

Similarly, results obtained from experimental work (see Chapter 3) on electronic transport through self-assembled nanoscale networks with tunable organic/inorganic building blocks showed NDR and hysteresis behavior for different molecular concentrations. The nonlinearities seen in the current-voltage characteristics at larger biases were explained to be due to tunnelling transport and charge trapping.

The solution-based fabrication approach presented in this work shows the ability of directed self-assembly to create electronic networks with tunable building blocks to harness the unique electronic properties of next generation molecular circuits. These results show promising ability of the electronic circuitry mimicked by molecules for realizing memory devices in the modern era of computing systems, which can store an ocean of information accessible by an electronic circuit/device. Fabrication of devices made of inorganic, and organic molecules, either in self-assembled monolayers or built from crossbar arrays of nanowires sandwiching molecules has shown great potential for the realization of molecular memory devices [209][194]. Memory devices built from crossbar arrays of nanowires were reported to act as on/off switches. In such systems, at one voltage, the electrical resistance through the molecules decreases, turning the switch “on”; while at other voltages, the switch is “off”. Engineering miniaturization and flexibility into future devices is crucial for applications in wearable electronics, biometrics, medical and healthcare applications. However, several obstacles still exist that need to be addressed. In particular, future experimental and characterization work focussed on choosing suitable electrodes and materials required for lower power consumption, higher scalability, faster writing/erasing, repeatable throughput, easy device fabrication and cost reliability is necessary. Further, work on metal nanoparticle-molecular networks involving extended circuit simulations/nanostructure modelling and further electrical and structural characterization experiments, along with fabrication using other classes of molecules/nanoparticles and deposition techniques would provide a pathway for the design of sensors, memory devices, switches and molecular integrated circuits for applications including computing and hardware security. These molecular networks show potential applicability in nanoelectronic circuits by harnessing observed NDR effects and rectification for future design of molecular diodes [55], high density memory and logic devices [55], and analog-to-digital converters [56]. The three-terminal metal-molecular Y- and diamond-shaped structures thus represent unique possibilities for device functionality in novel logic/switching, signal processing (amplification, oscillators) and memory nanoelectronic circuit elements.

5.2 Random Key Generation for Hardware Security Applications

In this application, nanoscale electronic circuits composed of molecules and colloidal nanoparticles are being investigated for information and hardware security applications by utilizing device level physical randomness and imperfections induced during fabrication [97].

- **Introduction**

Various nanoelectronic devices based on graphene, carbon nanotubes, quantum dots and colloidal nanoparticles, are currently being explored for use in information and hardware security solutions [15], [157], [210]. Nanoscale electronic circuits composed of molecules were at first, developed as a potential alternative to the CMOS technology in order to overcome the device scaling limitations [51], [61], [201]. These molecular electronic circuits exhibit novel behaviours such as ease of fabrication, miniscule form factors, low cost, and high degree of tunability; enabling their utilization in potentially advanced and strong security primitives and applications [61], [67], [200].

Conventional security primitives are majorly based on various mathematical or algorithmic protocols. For example, pseudorandom number generators are commonly used to generate encryption keys that enable the management of confidential information. However, these are commonly non-random in nature and the generated cryptographic keys are vulnerable to physical attacks [211]. To overcome some of these challenges, various device level hardware security based methodologies are being investigated that focus on achieving security and safeguarding data by utilizing physical randomness and device imperfections induced during fabrication. Examples include, use of hardware-based true random number generators (TRNG) that utilize thermal noise to generate random outputs [157], [197]; and cryptographic key generation based on physically unclonable functions (PUFs) from intrinsic physical imperfections [4], [211].

Majority of the cryptographic primitives aim to generate unique keys that are used to authenticate the required information and prevent security threats [69]. For example, silicon based PUFs utilize process-variation-induced local device mismatches like random dopant fluctuation that arise from stochastic atomic variations. These PUFs could be easily affected by noise due to supply voltage and temperature variations that could lead to data tampering, counterfeiting and information leakage [7]. A potential replacement for creating security primitives is using functional nanomaterials, which are regarded to be more robust and less susceptible to physical attacks as compared to the CMOS based security primitives [16], [199]. These materials exhibit structural disorders due to fabrication processes, or internal defects that can be considered for generating physical randomness.

Specifically, properties of devices such as memristors, carbon nanotubes, nanowires, and quantum dots can be tuned to a great extent for various security primitives[15], [157], [162], [210]. These devices can be used in applications such as generating PUFs, TRNGs, anti-counterfeit measures and resilience against tampering. Various studies proposed the use of metallic nanoparticles, with unique optical properties, to be useful in generating PUFs that can serve as tamper-evident sensors and nanofingerprints for anti-counterfeit applications [15], [90]. PUFs generated using self assembled CNTs integrated into metallic meshes or trenches on a substrate are regarded as promising candidates for future security devices due to their advantages such as chemical stability, superlative electronic properties, and solution-processability [7]. By tuning the inherent imperfections by varying the dimensions of the trenches, an unclonable electronic random structure could be generated.

Alternatively, replacing CNTs with self-assembled gold nanoparticle networks also shows a potential for use in generating random encryption keys. Previous work on self-assembled networks have shown interesting behaviour such as negative differential resistance (NDR) [96], [212], hysteresis [96], rectification [213], and switching phenomenon [214]. In addition, network mismatches from self-assembly, irreproducible atomic variations that lead to random metal-molecular connections, further support the network's capabilities of generating random encryption keys [7].

In this application, presented are the self-assembled metal-molecular networks formed between interdigitated electrodes on SiO_2/Si substrates on patterned silicon substrates, showing random connections between the gold electrodes that are utilized for generating arrays of random bits, which could be used as encryption keys. The substrates contain multiple electrode pairs, due to which predicting the dynamics of the self-assembled network formed between these electrode pairs is impossible. Modifications observed in the properties of these networks based on the variations in network assembly leading to unique current–voltage (*I*–*V*) profiles, prove useful for their application in the field of information security.

- **Results**
    - **Self-assembled colloidal gold nanoparticle molecular networks**

Presented below are the results of random key generation using networks of self-assembled colloidal gold particles interconnected with tunable ratios of thiolated molecules, formed between interdigitated electrodes. The intrinsic physical randomness and imperfections induced during fabrication are utilized to generate arrays of binary bits, which can be used as encryption keys; a schematic of random bit generation is shown in Figure 5.9.

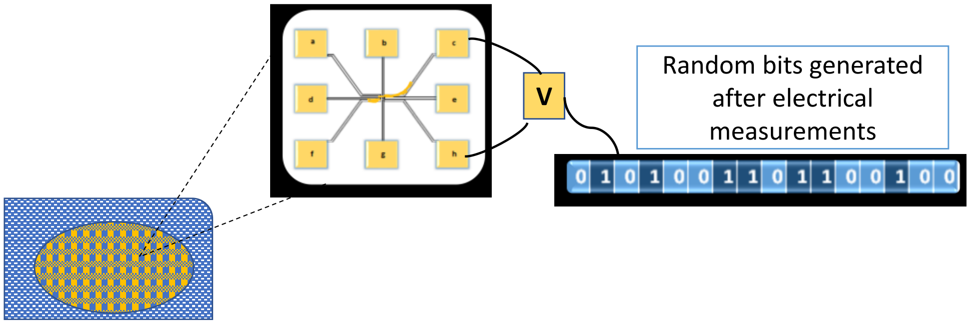

Figure 5.9: A schematic of random key generation procedure used in this work.

The substrates contain multiple electrode pairs, due to which predicting the dynamics of the self-assembled network formed between these electrode pairs is impossible. Figure 5.10a shows an intermittent contact mode AFM image of the networked films consisting of colloidal gold particles and molecules, depicting the dithiol molecules acting as linkers between gold nanoparticles during the directed self-assembly process. Figure 5.10b shows an optical microscope image of the gold nanoparticle-molecular network self-assembled between portions of the interdigitated contacts on SiO_2/Si substrates. Figure 5.10c shows a schematic of the device architecture showing multiple electrode pairs that can be probed for two-terminal electrical characterization.

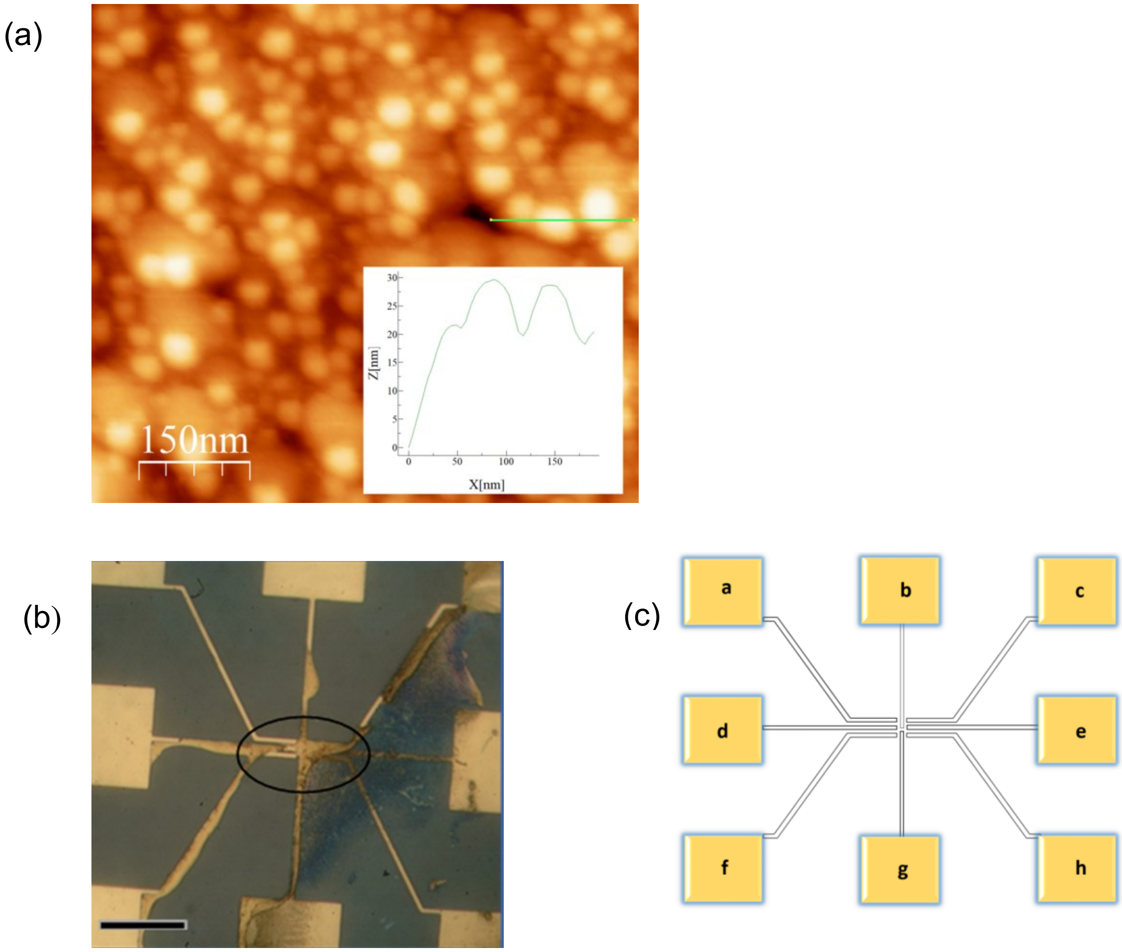

Figure 5.10: (a) AFM image of typical self-assembled networked films formed on SiO_2/Si substrate (scale bar equals 100 nm). (b) Optical microscope image of patterned gold electrodes after deposition of gold nanoparticle-hexanedithiol network from solution ($N_{HDT}:N_{particle} = 5:1$, scale bar equals 15 µm). (c) Schematic of the device architecture showing multiple electrode pairs indicated by alphabets a-h.

The dynamics of self-assembly lead to device level physical randomness and imperfections induced during fabrication. This leads to unique properties of the self-assembled networks resulting in variations in the measured resistance when different electrode pairs are probed electrically.

○ *I-V* characteristics supporting the random key generation

The *I–V* curves measured for different electrode pairs, and the corresponding resistance profile showed variations in their relative shape and in the values of current obtained when different pair of electrodes are measured. This random variation depends on the size of the network film formed between the electrodes, type of molecules used in the network, and also on the ratio of N_{molecule}:N_{particle}. To generate arrays of binary bits, we compare the adjacent resistances plotted as a function of the electrode pair number (N). For a certain electrode pair, if the measured resistance is greater than the resistance of the next pair, an integer value of "1" is assigned to this pair. On the contrary, a value of "0" is assigned. The generated array of binary keys can span to various lengths based on the number of electrode pairs measured for each sample. Our work resulted in keys of varying lengths: 8-, 16-, 32-, 64-bits, 100-bits and so-on; based on the number of electrode pairs measured. As an example, the resistance profiles and the corresponding 16- digit binary bits generated by using linear *I-V* data for gold nanoparticle–benzenedithiol networked films with N_{BDT}:N_{particle} ratio of 5:1 are shown in Figure 5.11.

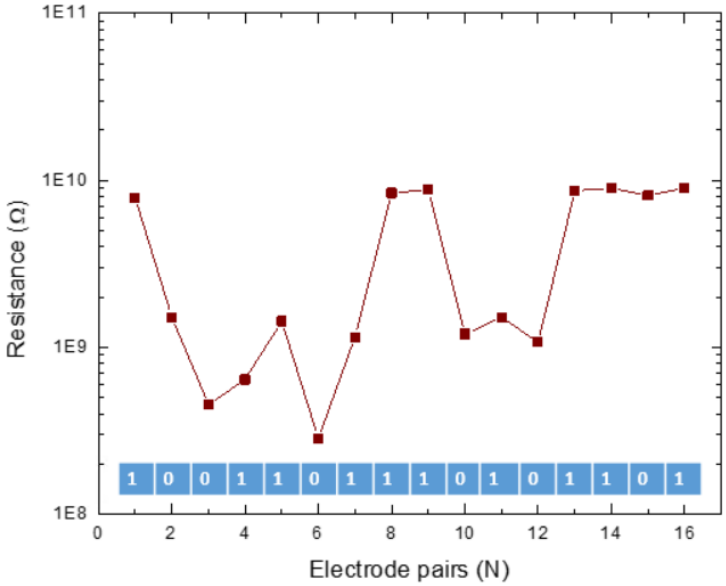

Figure 5.11: Resistance profiles built by calculating resistance values for different electrode pairs measured for N_{BDT}: N_{particle} ratio of 5:1. Insets show the 16-bit random keys generated by comparing the values of adjacent resistances.

Alternatively, an example of and a 100-bit key generated by using linear and non-linear *I-V* data for gold nanoparticle–nonanedithiol networked films with N_{NDT}:N_{particle} ratio of 1:1 is shown in Figure 5.12. he following bit stream, comprising of a 100-bit key was generated by comparing the adjacent resistances:

0111010110110101110101011100011001111011001010110010010110011011110010111001010001111010101001010101.

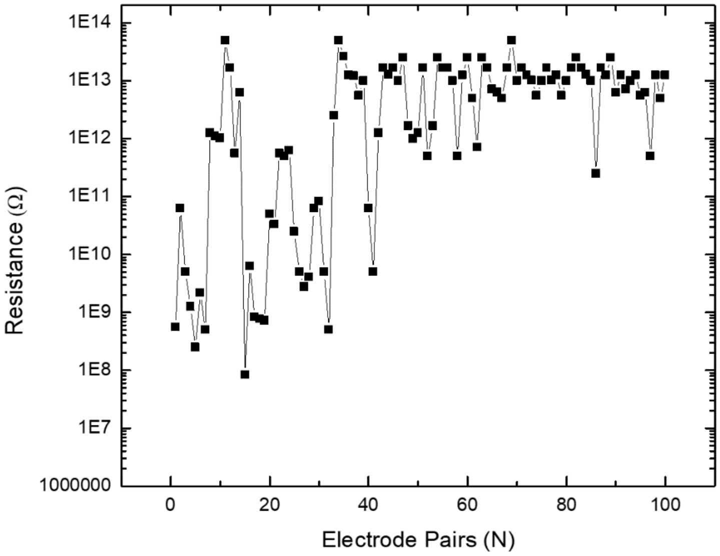

Figure 5.12: Resistance profiles built by calculating resistance values for different electrode pairs measured for N_{NDT}: N_{particle} ratio of 1:1.

The randomness of the generated bits was evaluated using the following testing methodologies: NIST statistical randomness test suite [215], and the Hamming distance metric [116], [118]. Details of the randomness tests are given in Appendix G.

Results from Hamming distance metric tests gave a normalized Hamming distance value very close to 0.5. Previous work in this field suggests that a inter-Hamming distance of 0.5 or closer indicates that the two keys are random, uncorrelated and unclonable [98], [119]. On the other hand, results from the NIST statistical randomness tests (frequency monobit and the cumulative sums test) gave a p-value > 0.01 (see Appendix G). Based on these tests, it can be concluded that the generated keys are random, and unclonable.

To complement the experimental results, circuit simulations using LTspice were used to generate keys of varying lengths. Circuit simulations were performed using a technique described in Chapter 3. The circuit model used for our simulations is shown in

Figure 5.12a. The random variable generator assigns all the resistors in the unit cell to be one of three values: either the quantized inter-particle contact resistance, the molecule resistance, or the defect resistance, depending on the desired molecule: gold nanoparticle concentration as well as the desired percentage of defects, as shown by the configurations in Figure 5.12b.

The networks were probed at different locations using eight electrodes (indicated by letters A-H in Figure 5.12 (a) to simulate the electrical measurements being conducted experimentally on the metal-molecular networks deposited on 8-pad substrates. The simulated resistance of the molecular networks typically varied between electrode pairs and these variations in resistance values were used to generate arrays of random bits which could be applicable as security keys. The bit streams could also be extended to form longer, more secure keys by combining smaller bit streams together.

(a)

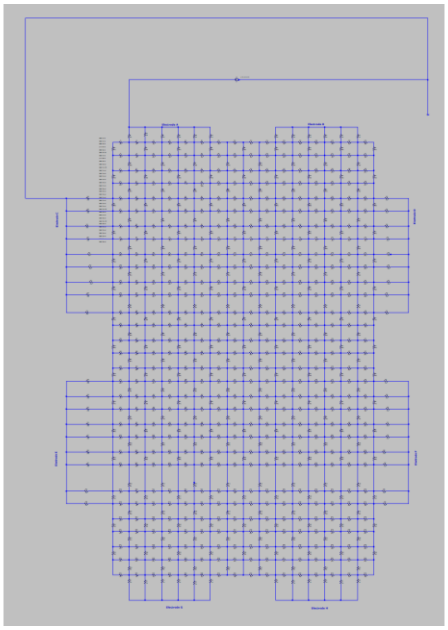

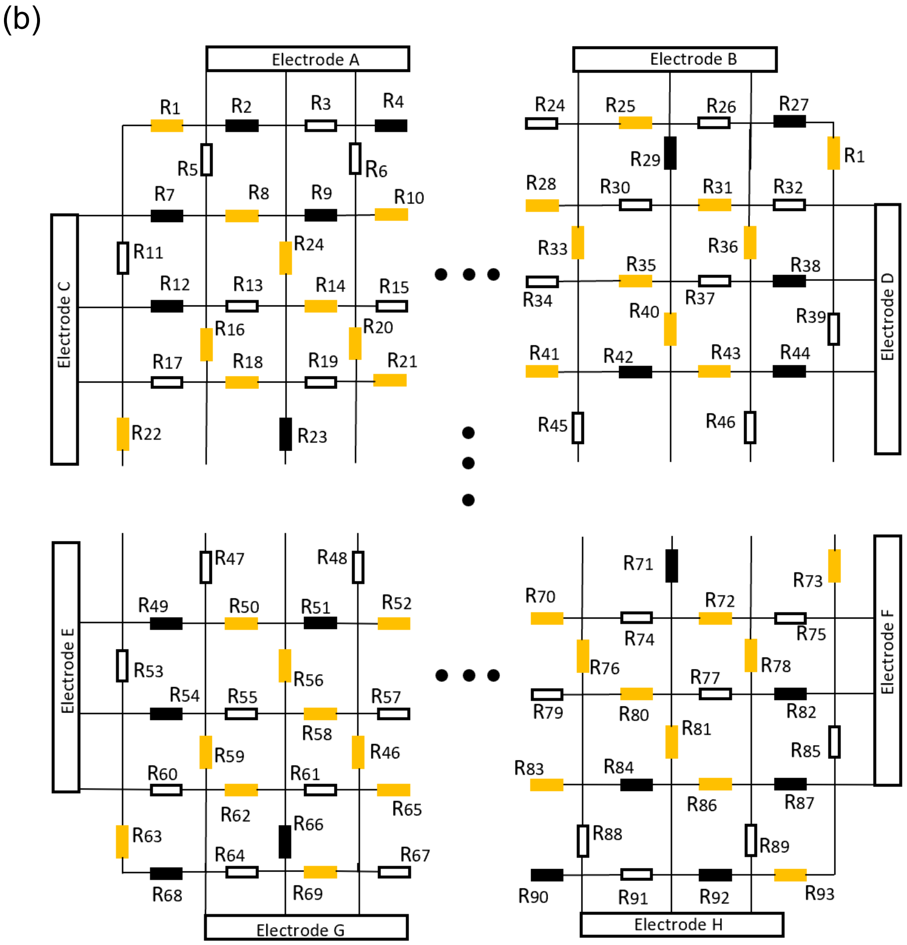

Figure 5.12: (a) Resistor network (length: 500 nm, width: 500 nm) used for circuit simulations. (b) Schematic of the resistor and electrode network used for LTspice circuit simulations. Each resistor is assigned one of three possible values, i.e. either the gold-gold nanoparticle contact resistance (in gold) or the molecule resistance (in white), or the defect resistance (in black).

Figure 5.13 shows the results of low-bias circuit simulations with resistances in the MΩ range. The resistance profiles shown correspond to networks comprised of all molecular contacts with no defects, and 33% molecular contacts with 50% defects, respectively. 27-bit key generated by comparing the resistance values between adjacent electrode pairs.

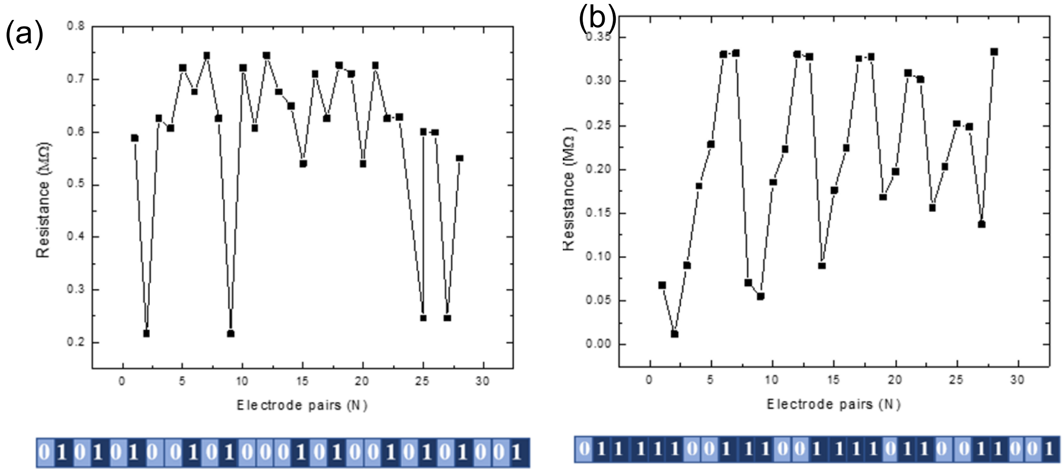

Figure 5.13: Low-bias linear circuit simulation results for a 500 by 500 nm network: Resistance profiles built by calculating resistance value at V = 0.5 V between different electrode pairs of molecular networks with (a) molecule: gold nanoparticle, R_{mol}: R_{gold} ratio of 18:0 (no defects) and (b) R_{mol}: R_{gold} ratio of 6:12 (50% defects).

Similar to the experimental results, the generated arrays of bits via circuit simulations also passed different randomness tests that are a part of NIST test suits and the Hamming algorithm-based randomness tests. These results as shown in table Appendix G.

The intrinsic physical randomness and imperfections induced during fabrication are utilized to generate arrays of binary bits, which can be used as encryption keys. The two-terminal electronic transport measurements on these organic-inorganic networks showed variations in the resistance of the network when different electrode pairs were probed. The solution-based fabrication approach presented shows the ability to generate arrays of random binary bits that prove useful for various application in the field of information security. Modifications observed in the properties of these networks based on the variations in network assembly leading to unique current–voltage (*I*–*V*) profiles, prove useful for their application in the field of information security. In addition to the two-terminal *I-V* measurements, our work could also be extended to further understand the properties of these networks by measuring voltage with respect to time between two contacts. Random spikes in voltage vs. time due to random connections forming between particles under an applied voltage can potentially be observed that would prove useful for device applications. These molecular electronic networks combine ease of fabrication with a broad choice of network building blocks, enabling their utilization in hardware security.

Chapter 6 Conclusions and Future Work

6.1 Conclusions

This work presents the results of electronic transport through self-assembled networks consisting of colloidal gold nanoparticles interconnected with tunable ratios of thiolated alkane molecules. The number of molecules in these self-assembled networks lies between networks having a huge number of molecules (bulk films), and networks with few molecules interconnecting the nanoparticles (dimers, trimers, etc.).

AFM images showed several gold nanoparticle-thiolated interconnections, revealing the formation of potential metal-molecular networks. On measuring the two-terminal electrical characteristics of these networks, linear *I-V* curves with currents ranging from µA to pA were observed at low bias. This variation was proved to be due to the different ratios of N_{mol}: $N_{particle}$, and/or the type of of molecule used during the fabrication. On the other hand, at larger biases, NDR and hysteresis behavior were observed for different molecular concentrations due to a combination of field-assisted tunneling and charge trapping occurring in the nanoscale networks. Results from conducting tip AFM showed distinct resistance ranges, i.e., either kΩ or MΩ, when different locations of gold nanoparticle-dithiol network film samples were probed, indicating the presence of two types of connections between neighboring particles in the network. Observations from LTspice circuit simulations accounting for different network morphologies that include different types of connections and defects in the network, agreed well with the measured experimental data.

Computational quantum mechanical modeling using DFT simulations was used to study the electronic transport properties of nanoscale networks composed Au metal clusters interconnected with thiolated molecules (1,4-benzenedithiol and 1,3,5-benzenetrithiol), connected in linear chains and branched (Y-, diamond-shaped) extended networks. Molecular orbital calculations showed that the HOMO-LUMO gaps of linear chains decreased with length, indicating decreased barrier to electron transport. Calculated *I-V* characteristics of these networks exhibited nonlinearities and rectification with NDR peaks that became more pronounced with increasing chain length. The transmission spectra of the structures studied indicated an increase in the number/width of transmission peaks near the Fermi energy, as the structures were extended, indicating enhanced transmission. Transmission spectra were also in good agreement with associated peaks in electronic DOS. By modifying the structure and geometry of molecule-nanoparticle networks, charge transport through molecular-scale devices could be tuned. Results showed the possibility of realizing several applications such as random key generation for hardware security applications, potential switching, memories, and inverting based applications of these networks.

These self-assembled networks show a promising pathway in the fabrication of large scale molecular electronic networks with tunable properties based on the type/number of molecules in the network.

6.2 Future Work

6.2.1 Experimental work

- **Fabrication and characterization of Au nanoparticle- thiolated molecular networks**

The properties of gold nanoparticles are tunable by changing their size, and shape [216], [217]. This work uses 30 nm colloidal gold for the fabrication of self-assembled gold nanoparticle networks with tunable molecule-nanoparticle ratios. Observing the properties of nanoparticle-molecular networks fabricated using different sized Au nanoparticles, from smaller than 10 nm to over 100 nm in diameter, (ex: 10 nm, 2 nm, etc.) would lead to the development of networks with tailored electronic properties for different applications.

As a preliminary step, several samples with 10 nm Au nanoparticle-nonanedithiol network solutions with tunable electrical properties were fabricated for structural characterization using a method described in Chapter 2. Tunability was achieved by varying the $N_{molecule}$: $N_{particle}$ ratios of 1:5, 1:1, 5:1 and 50:1. Optically, networked films observed on the substrates, either between the electrodes or on the large area of gold film, were lighter in appearance as compared to thick gold deposits observed in case of 30 nm Au-molecular network samples (Figure 6.1). Similar to the samples with 30 nm Au-molecular network solutions, results from AFM measurements of 10 nm colloidal showed the presence of gold nanoparticle dimers and larger oligomers after depositing suspension based on nonanedithiol that confirmed the individual gold particle height as approximately 10 nm, corresponding to the colloidal gold diameter.

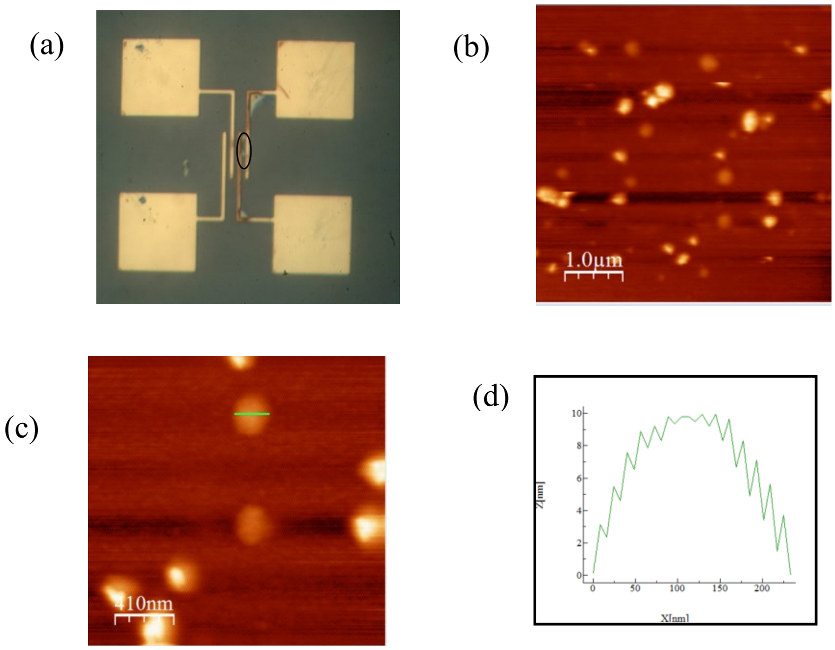

Figure 6.1: (a) Optical microscope image of patterned gold electrodes after deposition of 10 nm gold nanoparticle-nonanedithiol network from solution with N_{NDT}: N_{particle} = 1:1. (b) AFM image of encircled region in (a) showing gold nanoparticle-molecular film bridging gold electrodes. (c) Zoom-in AFM image of network shown in (b). (d) AFM cross-sectional profile shows the gold particle height as approximately 10 nm in some areas, corresponding to diameter of the colloidal gold nanoparticles. Green lines represent the area selected for height analysis.

Alternatively, the nanoparticle-molecular networks can also be fabricated using a two-phase liquid-liquid system that would yield thiol-capped Au nanoparticles. The synthesis procedure was based on a method described by Burst *et al.* [78] with some modifications.

Decanethiol-capped Au nanoparticles were synthesized in toluene using the following procedure. 15 mL of a 0.03 mol/L aqueous solution of hydrogen tetrachloroaurate is mixed with 40 mL of a 0.05 mol/L solution of tetraoctylammonium bromide in toluene. The two-phase mixture is vigorously stirred until all the tetrachloroaurate is transferred into the organic layer. At this point, the aqueous layer will become colorless. The aqueous phase is removed and 0.103 mL decanethiol was added to the organic phase. 12.5 mL of a 0.4 mol/L freshly prepared aqueous solution of sodium borohydride is slowly added with vigorous stirring over the course of 10 sec. The solution is stirred for 3 hours, post which the organic phase is separated which is dark brown in color. This toluene and gold nanoparticle solution will then be evaporated to ~5 mL in a rotary evaporator and then mixed with 200 mL ethanol to remove excess thiol. This mixture is stored in a freezer (~-18°C) for 4 hours, and then the dark brown precipitate is removed from ethanol top solution. The remaining product (precipitated colloid) will be centrifuged at ~9000 rpm for 10 minutes. The crude product is once again dissolved in 5 mL toluene and centrifuged with 200 mL ethanol. The final solution will be deposited on the substrates (substrates were first cleaned with acetone, isopropanol, and deionized water and dried using nitrogen gas) and allowed to dry under ambient conditions in order to form self-assembled films before proceeding with characterization. Figure 6.2 shows AFM images of the networked films that were observed on the substrates after depositing suspensions of decanethiol-capped gold nanoparticle solutions. AFM measurements confirmed the gold particle height to be between 2-8 nm, in most cases.

(a)

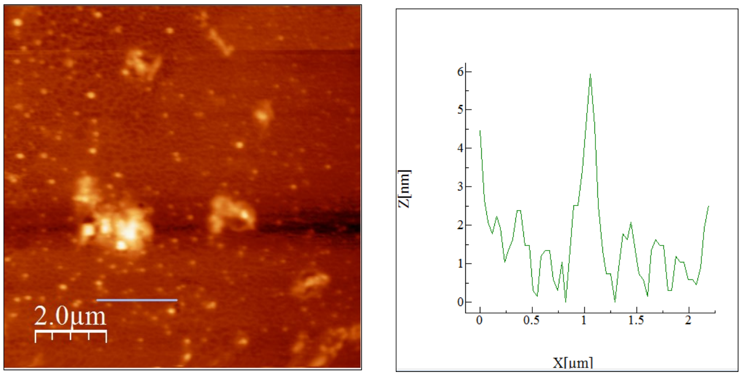

(b)

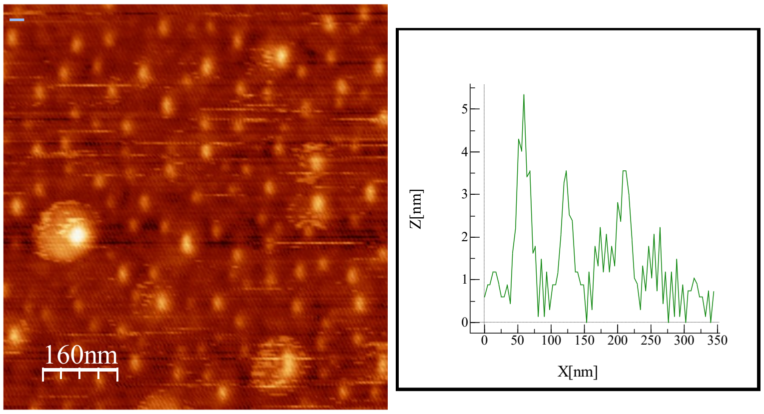

Figure 6.2 (a-b): AFM images and the corresponding height analysis of thiol capped gold nanoparticle networked films at different locations. Blue and green lines represent the area selected for height analysis.

Linear current-voltage plots were measured on selected areas on the decanethiol gold nanoparticle networked films with typical range of currents being ~10^{-11} A to 10^{-12} A (Figure 6.3). The low currents could be attributed to the use of a long chain thiol molecule, which has only one end that has the capability to be attached to gold nanoparticles.

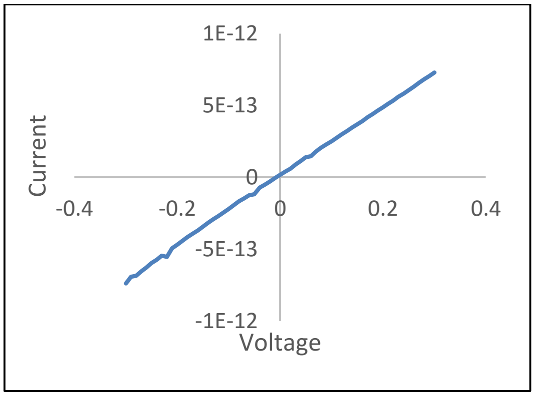

Figure 6.3: Plot of magnitude of current *vs.* voltage for gold nanoparticle–decanethiol network sample.

Future work includes further electrical analysis of the samples fabricated using different sized Au nanoparticles, and observing their characteristics using AFM measurements. The influence of change in particle size on the conductance properties of the network can also be explored.

Additionally, the observed NDR and hysteresis properties of the 30 nm Au-molecular nanoparticle networks can be further explored for device applications such as in sensors and memristive devices. Recently, the *I–V* characteristic of a two-terminal single nanowire Au–Ti/TiO2/Ti–Au as a promising RRAM device were investigated [218]. Results showed switching behaviour under vacuum conditions and the hysteresis loops exhibited a NDR region that could be overcome at higher applied bias due to oxygen vacancies. The *I–V* hysteresis with distinct voltage thresholds was used in SET/RESET operations in the RRAM devices. The metal-molecular networks fabricated in this work can be characterised under vacuum and high bias conditions to potentially utilize them in similar applications. Additionally, the metal-molecular networks can be tested as FETs. The substrate could be used as a gate contact, which can potentially be used to show switching behavior.

Results from this thesis also indicate the influence of structural disorders (present in the metal nanoparticle networks) on the electronic transport. The impact of structural disorders in various $N_{molecle}$:$N_{particle}$ ratio samples can be further tested for single electron charging effects and Coulomb blockade phenomenon that could also lead to NDR and hysteretic behavior [32,45]. Although we believe that the single electron charging effects and Coulomb blockade is less likely for the 30 nm gold particles, we could understand the influence of structural disorders, NDR and hysteresis using 10 nm or smaller sized colloidal gold nanoparticles.

Additionally, the use of other type of molecules (ex. amines, other thiols/dithiols not included in this work, etc.) with different lengths, could lead to variations in the conductance of the network. Understanding the relation between the molecule's conductance and length would enable the development of networks with tailored properties for different applications.

Many experimental groups have studied the structural morphology of mixed SAMs as each type of alkane(di)thiol molecule in the mixed SAMs confers the nanoparticles with a certain set of properties [219][220]. Mixing a pure, single-molecule based SAMs with another molecule leads to the formation of mixed molecular networks [221]. Recently, the role of surface topography in the performance of molecular-scale electronic devices was investigated in junctions formed with mixed SAMs. Here, systematic dilution of single-component, long n-alkanethiolate (n-hexadecane-thiolate; denoted as SC_{16}) SAM with another short n-alkanethiol (SC_n where n = 14, 12, 10, 8) lead to the formation of a mixed SAMs with variations in total disorders/pits in the structure (Figure 6.4). It will be interesting to investigate the properties of metal-molecular networks made of varying chain lengths of thiols/dithiol molecules and their influence on the charge transport behaviors of the network formed.

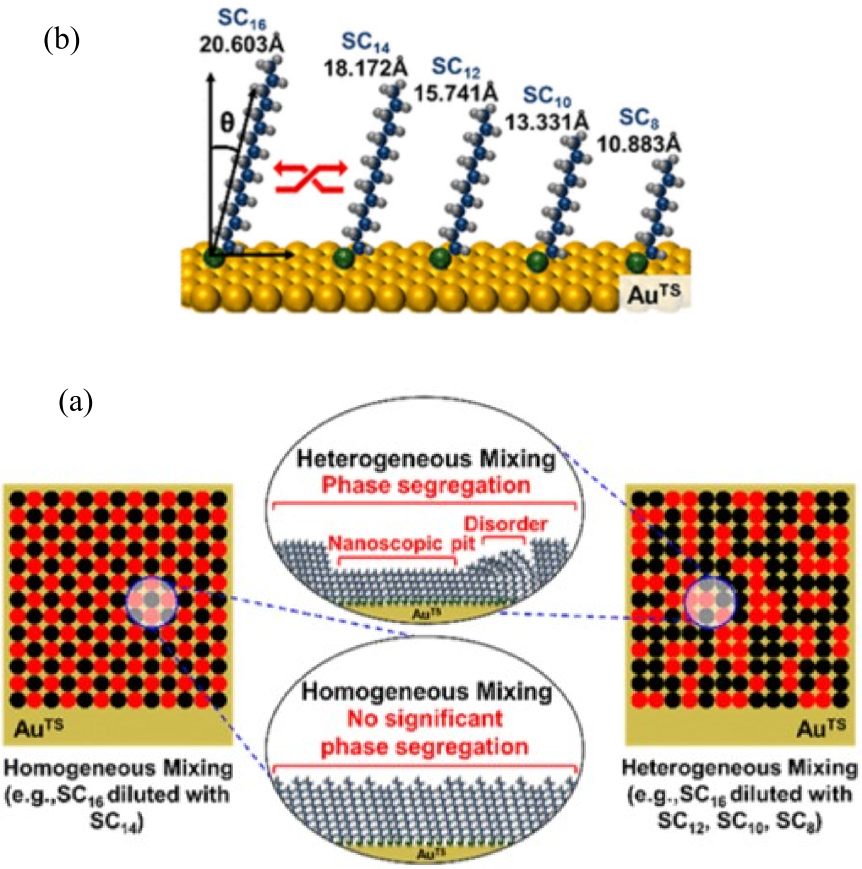

Figure 6.4: Schematic showing the (a) mixing two *n*-alkanethiolates on template-stripped gold (Au^{TS}) and (b) mixed SAMs formed with n-alkanethiols of similar (homogeneous mixing) and different (heterogeneous mixing) lengths. Adapted from [222].

Besides gold, dithiol molecules can also form covalent bond with other metals such as Ag, Cu, Pt, Sn etc. [74]. Thus, using other types of metallic particles in the fabrication is another interesting topic as an extension of this study.

- **Fabrication of Au nanoparticle networks based on different nanostructures**

Alternatively, studies have reported the use of graphene/ CNTs/ doped graphene-carbon nanotubes and attaching them to gold nanoparticles for different applications [223][224]. For example, in one study, a novel three dimensional (3D) networks based on nitrogen doped graphene-carbon nanotubes attaching with gold nanoparticles was shown to exhibit glucose sensing properties (Figure 6.5) [224].

Figure 6.5: Schematic illustration of preparation of N-GR-CNTs/Au nanoparticles nanohybrid. Adapted from [224].

Our in-solution fabrication method can be utilized (with some modifications in the recipe) to fabricate such hybrid structures. Additionally, molecular electronic devices with tunable properties can be formed by covalently bridging a gap in a single-walled CNT (SWCNTs) with an electrically functional molecule [225], [226]. This combination of using dithiol molecules and or using CNTs in designing molecular electronic devices shows a great potential in future electronics [44]. In addition, CNTs have also been tested to create a unclonable electronic random structure to create cryptographic keys that can be a used to provide significantly higher level of security as compared to the conventional binary-bit architecture with the same key size [227]. A schematic of generation of random bits based on two-dimensional (2D) CNT arrays is shown in (Figure 6.6a). A combination of most of the above applications includes the use of CNTs in wearable electronics consisting of many memory units, capacitors, transistors and logic circuits, etc. [228] (Figure 6.6b).

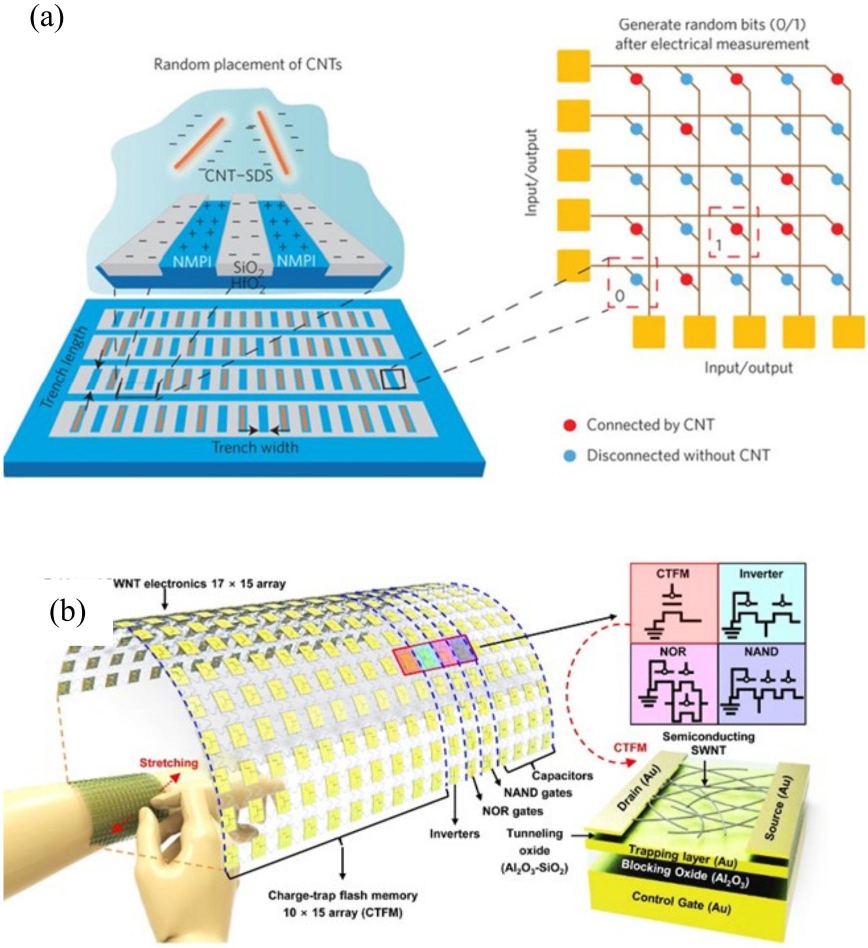

Figure 6.6: (a) Schematic of a randomly connected 2D nanotube array that can be used as a crossbar switch. Here, CNTs self-assemble in the HfO2 trenches with width of 70–300 nm. Adapted from [227]. (b) Schematic of an s-SWCNT-based wearable array of electronic devices, consisting of memory units, capacitors and logic circuits that can be integrated into different circuits for day-to-day applications. Adapted from [228].

Lastly, in addition to new fabrication experiments and result analysis of metal-molecular networks with different types of molecules and/or using gold nanoparticles of various sizes, a possible extension of the current study would be to understand the variations in the properties of currently fabricated metal-molecular network properties, under the influence of varying conditions such as temperature, light and under vacuum.

These conditions can prove useful in the realization of future molecular electronic circuits for various device applications.

6.2.2 Computational simulations

- **Electron Transport Calculations of Larger Networks**

Based on the results explained in Chapter 4, the metal-molecular electronic network analysis could be further extended to larger networks (ring-, H-shaped) as shown in Figure 6.7a-b below. Additionally, by considering these structures as unit cells, larger networks could be built and simulated by repeating the unit cell structure to desired dimensions (Figure 6.7c). Potential transport of electrons from one branch to another in these networks may predict switching or inverting behavior that could be used in designing future molecular integrated circuits in a large scale.

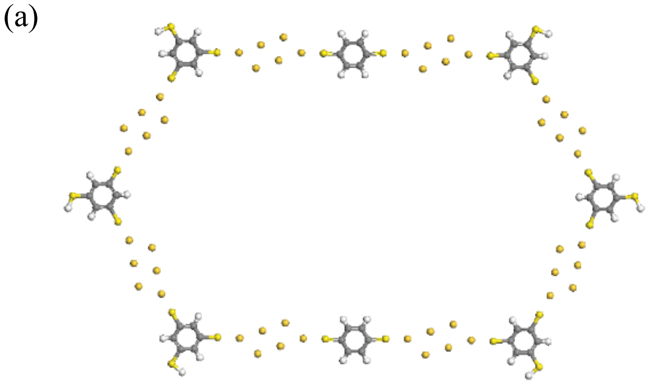

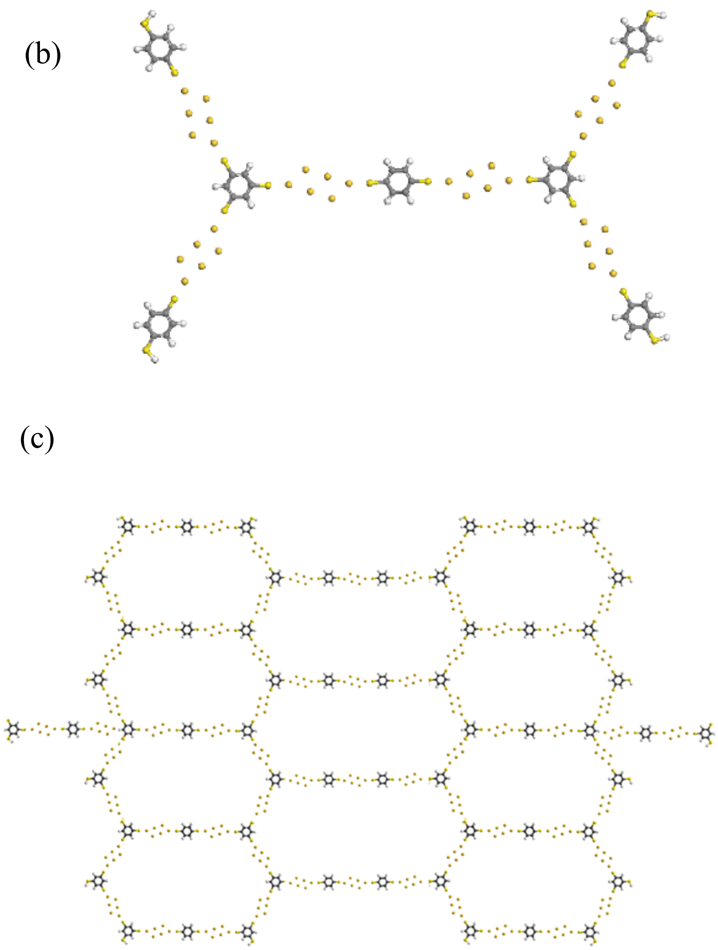

Figure 6.7: Schematic of extended metal-molecular networks (a) Ring- and (b) H-shaped networks (c) A larger network formed by repeating the ring- and H-shaped networks to desired dimensions.

In recent years, many researchers have investigated the electronic characteristics of 2-terminal nanojunctions [163], [229]. Understanding the transport mechanism in multi-terminal molecular junctions is very critical for applications in the field of molecular electronics [230]. For example, in one study the inclusion of additional two terminals (leading to a four-terminal setup) showed pronounced NDR, as compared to the results obtained from two-terminal measurements on the same device. (Figure 6.8). Here, the four-terminal device was made of an organic molecule [9, 10-Bis((2’-para-mercaptophenyl)-ethinyl)-anthracene] connected via thiol bridges to four gold nanowires. Our larger networks (such as Y-branch, H-shaped networks) could also be tested as multi-terminal networks for switching, memory or other applications.

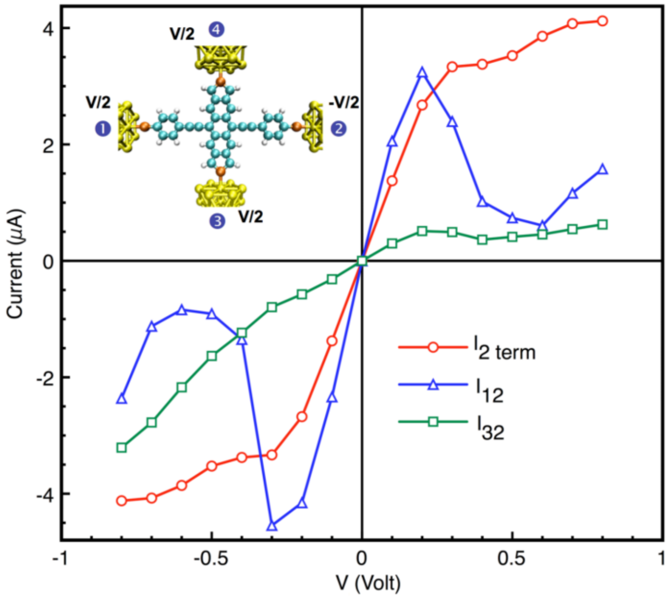

Figure 6.8: *I-V* characteristics of the four-terminal molecular device. The inset shows the bias geometry of the four-terminal system, and the atoms are shown in yellow (gold), S (red), C (cyan) and H (gray), respectively. The red curve represents the *I-V* results obtained from a two-terminal measurement between terminals 1 and 2. On the other hand, blue and green curves show the *I-V* results obtained from four-terminal measurement. Adapted from [230].

- **Modeling of Metal-Molecular Networks using metals other than gold**

Various computational simulations of Au-molecular networks modeled in this work have shown promising results with a possibility of realizing different device-based applications in the field of molecular electronics. Similar calculations could be done using other types of molecules (ex. graphene), which is of increasing importance in the field of molecular electronics. In one study [231], the electron transport properties of graphene nanoribbons that were connected to Au electrodes via different number of thiol groups at two sides showed significant rectification of graphene nanoribbons (the average rectification ratio reaches 8.4 in the bias range from -1.0 to 1.0 V). It was reported that the rectification property of such a structure can be understood to be associated with the narrow band gap under negative bias.

Computational modeling results presented in this thesis exhibited nonlinearities and rectification with NDR peaks that became more pronounced with increasing chain length (see Chapter 4). It would be interesting to study the electronic properties of similar metal-molecular networks that are built by replacing the Au clusters with graphene molecules. An example of a 1-unit chain built using C_{16} graphene flakes is shown in Figure 6.9.

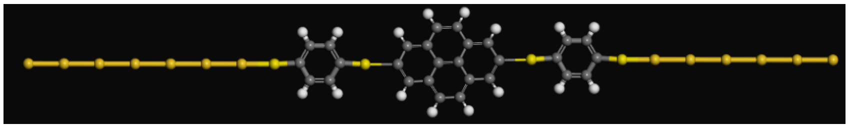

Figure 6.9: Schematic of a 1-unit linear chain built using C_{16} graphene nanoflake.

Similar calculations could be done using other types of metals like Al [232], [233], Cu [234], etc. which are of increasing importance in the field of molecular electronics.

6.3 Future applications

- **Sensors (vapour and biosensors)**

Studies have shown that controlling the physical and chemical properties of self-assembled metal-nanoparticle/organic films have potential uses chemiresistor-type or microgravimetric gas sensors. One study reported that the conductivity and vapor-sensing properties of alkanedithiol-interlinked gold nanoparticle films depends on the alkylene chain length. Briefly, gold nanoparticles self-assembled on a thin film using different organic linkers (like dodecanethiol, nonanedithiol, benzenethiol, 4-chlorobenzenethiol, 4-bromobenzenethiol, 4-(trifluoromethyl) benzenethiol, 4-hydroxybenzenethiol, and 4-aminobenzenethiol, benzenedimethanethiol, etc.) have a potential use as vapor sensors.[66], [235] When these films are dosed with vapors of toluene, 1-propanol, 2-methyl-4-pentanone, water, etc. a fast fully reversible increase in resistance was measured.[66], [235] As an example, Figure 6.10 shows the response of self-assembled Au nanoparticle-nonanedithiol films when exposed to vapors such as water, toluene, carbon monoxide and ammonia. The possibility of fast response, reversibility and the high sensitivity to volatile organic compounds (VOCs) make noble metal nanoparticle composite films promising materials for sensor applications. [66], [235], [236].

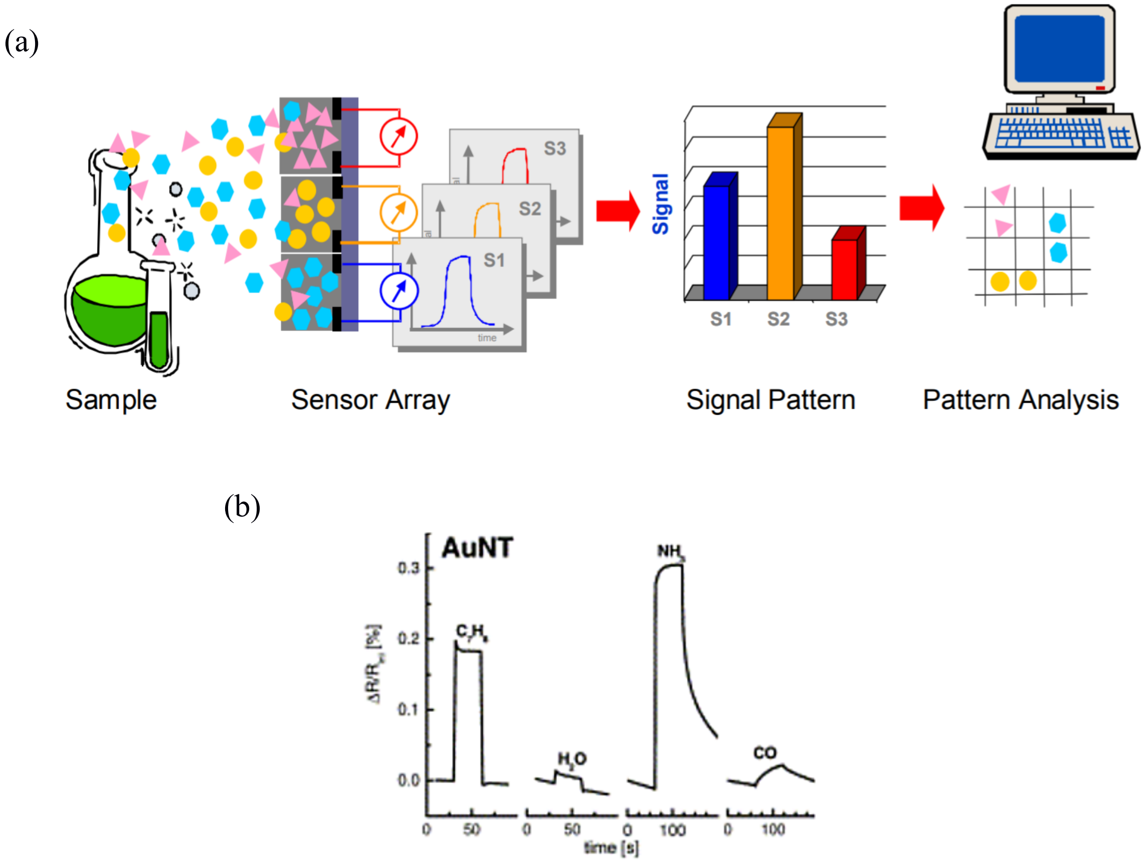

Figure 6.10: (a) A schematic showing the steps involved in the use of metal-nanopartice/organic films as vapour sensors. (b) Relative change in resistance with time plots of Au-nonanedithiol based vapor sensors to exposure with 400 ppm of toluene (C7H8), water (H_2O), ammonia (NH_3), and carbon monoxide (CO) [200], [237].

The sensing response is based on the variations in resistance of the network that occur when organic vapors are absorbed. Similar kind of devices with tunable properties can be fabricated using metal-molecular networks fabricated in this work.

Additionally, a promising approach for non-invasive and safe screening, diagnosis, and follow-up of disease conditions relies on the detection of VOCs in exhaled breath [238]. Here, gold nanoparticles are synthesized in a technique where dodecyl amine was added with thiol ligands like chlorobenzenemethanethiol etc. In this case, silver electrodes were used with copper as a base metal. Layer-by-layer (LbL) film was deposited by immersing the electrodes alternately in a GNP solution with a linker solution containing hexadecanedithiol in toluene. These samples were then exposed to VOCs/breath samples from subjects and analysis was done using special software's (Figure 6.11).

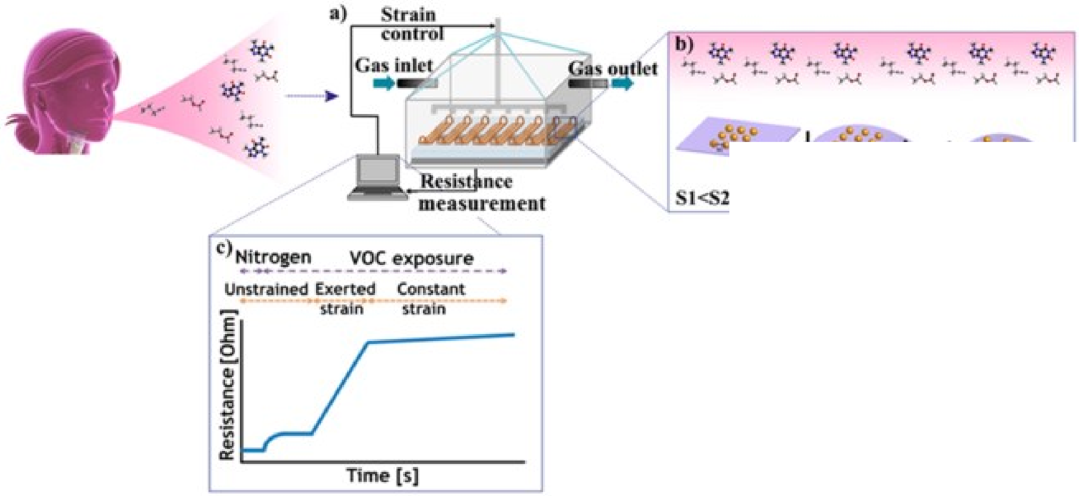

Figure 6.11: (a) Schematic of a sensing chamber that allows the exposure of multiple sensors to a controlled VOC environment (b) The sensors are strained in multiple bending steps; at each increment of increasing strain, the nanoparticle film morphology is affected, leading to unique responses to the VOCs present. (c) Sensor resistance is measured during sensor bending and analyte exposure, allowing the collection of multiple bending-related features. Adapted from [236].

Using the synthesis procedure described in Section 6.2.1, samples can be fabricated and exposed to VOC related vapors. The variations in resistance obtained when samples are exposed to clean air *vs.* VOC vapors can be recorded. One can begin by testing the vapor sensing properties of long alkane chains, aromatic rings using the samples already available in our lab. Data from these samples can be used for the realization of various sensors for health-based applications.

- **Nanoelectronic Networks**

The in-solution fabrication method used in this work can be used to build a nanocell device [239][240]. Typically, a nanocell is a device with molecular computing capabilities that consist of molecules and metal clusters that assemble into a programmable electronic device. Figure 6.12 shows an example of a nanocell that consists of molecules interconnected with metallic clusters, prepared lithographically. The yellow contacts are addressable externally. The molecules interconnecting the clusters are ~2-nm long, and the sizes of the clusters (green) are very similar in diameter to the length of the molecules. For the realization of a programmable device, molecules (with special features such as ability to show NDR, etc.) can be interconnected using metallic clusters. The programming on a nanocell is done by applying high or low bias voltage on the nanocell's contacts until it functions as target logic device.

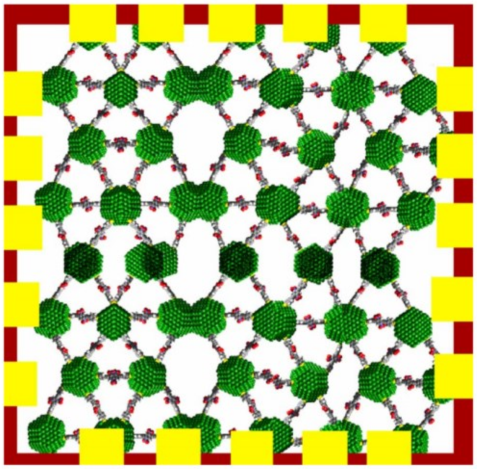

Figure 6.12: Schematic representation of a nanocell, consisting of a network of molecules and metallic clusters.

- **Optical/photonic devices**

Gold nanoparticles have numerous applications in nanophotonics, due to their interesting optical properties, depending on the particle size, and shape [241][242]. They absorb and scatter light that results in different colours ranging from red to blue to black, and finally to clear and colorless due to the phenomenon of surface plasmon resonance, in which conduction electrons on the surface of the nanoparticle oscillate in resonance with incident light. Due to the ability of gold nanoparticles to interact strongly with visible light, they are regarded as good candidates for labelling applications in cancer management [243]. Here, gold nanoparticles are targeted and accumulated at the site of interest, they enable visualization of the region of interest due to their optical scattering properties, and these nanoparticles can then be detected using photo-thermal imaging or dark field microscopy. It will be interesting to investigate the optical properties of the gold nanoparticle-molecular networks fabricated in this study, and understand their use in such applications. Replacing thiols with biocompatible molecules in the networks might also prove useful in different bio-applications. In addition, the tunability in network's optical properties that might be observed by varying the size/type in molecule in our networks can also be explored.

Outlook and Summary:

The solution-based approach presented as part of this PhD thesis, shows the ability of directed self-assembly to create electronic networks with tunable electronic for next-generation molecular electronic circuits. The two-terminal electronic transport measurements on the self-assembled gold nanoparticle–molecular networks with varying concentrations of molecular connections, samples showed tunable electrical properties of the networks depending on the concentration of molecular connections. At low biases, an increase in the network resistance was observed with an increase in the percentage of molecules in the network. At high biases, the networks showed nonlinearities, in particular NDR and hysteresis that could be explained by a combination of as tunneling transport and charge trapping. These nonlinear properties depend on the molecule-to-nanoparticle ratios used in the fabrication process, and by applying different bias voltages, electron transport properties of the networks could be controllably tuned. Results from circuit simulations, and DFT modeling agreed well with the experiment. These self-assembled nanoscale molecular electronic networks provide an avenue for engineering electronics at the molecular level by using superstructures of different organic molecules and topologies.

Some of the potential ideas for further progress in this field are listed below:

- Future work on metal nanoparticle–molecular networks involving extended circuit simulations/nanostructure modeling would provide a pathway for the design of sensors, memory devices, switches, and molecular integrated circuits for applications including computing and hardware security.

- New electrical and structural characterization experiments, that include the fabrication of metal-molecular networks using other classes of molecules and/or using different sized metal nanoparticles would help in understanding the variations in network properties based on the size of nanoparticle, and/or the type of molecule used in the network.
- Further understanding of the various principles contributing in electron transport schemes including, effect of voltage drops across different regions in the networks, effects such as Coulomb blockade, influence of changing the size of colloidal gold nanoparticles and/or change in the type of dithiol/thiol molecule in the fabrication process is necessary.
- Future work on larger and multi-terminal networks, consisting of different metal particle/molecule combinations and geometries, could provide a rich framework for exploring applications of metal-molecular networks in nanoelectronic devices.

References:

[1] C. Binns, *Introduction to nanoscience and nanotechnology*. Hoboken, N.J: Wiley, 2010.

[2] R. P. Feynman, “There’s plenty of room at the bottom,” *California Institute of Technology Journal of Engineering and Science*, vol. 4, no. 4, pp. 23–36, 1960.

[3] S. M. Lindsay, *Introduction to nanoscience*. Oxford: Oxford University Press.

[4] C. Herder, M.-D. Yu, F. Koushanfar, and S. Devadas, “Physical Unclonable Functions and Applications: A Tutorial,” *Proceedings of the IEEE*, vol. 102, no. 8, pp. 1126–1141, 2014.

[5] G. Binnig, H. Rohrer, C. Gerber, and E. Weibel, “Tunneling through a controllable vacuum gap,” *Applied Physics Letters*, vol. 40, no. 2, pp. 178–180, 1982.

[6] G. Binnig, C. Quate, and C. Gerber, “Atomic force microscope,” *Physical review letters*, vol. 56, no. 9, pp. 930–933, 1986.

[7] Z. Hu, J. M. M. L. Comeras, H. Park, J. Tang, A. Afzali, G. S. Tulevski, J. B. Hannon, M. Liehr, and S.-J. Han, “Physically Unclonable Cryptographic Primitives using Self-Assembled Carbon Nanotubes,” *Nature Nanotechnology*, vol. 11, no. 6, pp. 559–565, 2016.

[8] N. Agraït, A. L. Yeyati, and J. M. van Ruitenbeek, “Quantum properties of atomic-sized conductors,” *Physics Reports*, vol. 377, no. 2, pp. 81–279.

[9] J. Gimzewski and R. Möller, “Transition from the tunneling regime to point contact studied using scanning tunneling microscopy,” *Physical review. B, Condensed matter*, vol. 36, no. 2, pp. 1284–1287, 1987.

[10] D. Joh, L. Sun, M. Stangl, A. Al Zaki, S. Murty, P. Santoiemma, J. Davis, B. Baumann, M. Alonso-Basanta, D. Bhang, G. Kao, A. Tsourkas, and J. Dorsey, “Selective Targeting of Brain Tumors with Gold Nanoparticle-Induced Radiosensitization,” *Plos One*, vol. 8, no. 4, p. e62425, 2013.

[11] S. Jain, D. Hirst, and J. O’Sullivan, “Gold nanoparticles as novel agents for cancer therapy,” *British Journal of Radiology*, vol. 85, no. 1010, pp. 101–113, 2012.

[12] W. A. Goddard, *Handbook of nanoscience, engineering, and technology*, 3rd ed. Boca Raton, FL: CRC Press, 2012.

[13] J. Yang, D. Strukov, and D. Stewart, “Memristive devices for computing,” *Nature Nanotechnology*, vol. 8, no. 1, pp. 13–24, 2013.

[14] M. G.E., “Cramming more components onto integrated circuits,” *Electronics*, vol. 38, pp. 114–117, 1965.

[15] A. F. Smith, P. Patton, and S. E. Skrabalak, “Plasmonic Nanoparticles as a Physically Unclonable Function for Responsive Anti-Counterfeit Nanofingerprints,” *Advanced Functional Materials*, vol. 26, no. 9, pp. 1315–1321, 2016.

[16] H. Tanaka, M. Akai-Kasaya, A. TermehYousefi, L. Hong, L. Fu, H. Tamukoh, D. Tanaka, T. Asai, and T. Ogawa, “A molecular neuromorphic network device consisting of single-walled carbon nanotubes complexed with polyoxometalate,” *Nature Communications*, vol. 9, no. 1, pp. 2693–7, 2018.

[17] J. Dong, J. Liu, G. Kang, J. Xie, and Y. Wang, “Pushing the resolution of photolithography down to 15nm by surface plasmon interference,” *Scientific reports*, vol. 4, no. 1, pp. 5618–5618, 2014.

[18] J. A. Hutchby, G. I. Bourianoff, V. V. Zhirnov, and J. E. Brewer, “Extending the road beyond CMOS,” *IEEE circuits and devices magazine*, vol. 18, no. 2, pp. 28–41, 2002.

[19] N. Z. Haron and S. Hamdioui, “Why is CMOS scaling coming to an END?,” 2008, pp. 98–103.

[20] M. Liu, M. Cai, and Y. Taur, “Scaling Limit of CMOS Supply Voltage from Noise Margin Considerations,” 2006, pp. 287–289.

[21] A. Kanduri, A. M. Rahmani, P. Liljeberg, A. Hemani, A. Jantsch, and H. Tenhunen, “A Perspective on Dark Silicon,” Cham: Springer International Publishing, 2017, pp. 3–20.

[22] T. I. of Electrical and E. E. (IEEE), “International Roadmap for Deviices and Systems.” 2020.

[23] Y.-H. Peng, F. Liu, R. Jin, K.-L. Wei, G. Du, J.-F. Kang, and X.-Y. Liu, “Impact of Quantum Confinement and Coulomb Blockade on the retention of nanocrystals based charge trapping memory,” 2012, pp. 1–3.

[24] A. Bhattacharyya, *Silicon based unified memory devices and technology*. Boca Raton: CRC Press, Taylor & Francis Group, CRC Press is an imprint of the Taylor & Francis Group, an informa business, 2017.

[25] M. Gill, T. Lowrey, and J. Park, “Ovonic unified memory - a high-performance nonvolatile memory technology for stand-alone memory and embedded applications,” 2002, vol. 2, pp. 158–446.

[26] L. Bo, S. Zhi-Tang, Z. Ting, F. Song-Lin, and G. Fu-Xi, “Novel material for nonvolatile ovonic unified memory (OUM)–Ag11In12Te26Sb51 phase change semiconductor,” *Chinese physics (Beijing, China)*, vol. 13, no. 7, pp. 1167–1170, 2004.

[27] S.-J. Kim, Y.-S. Park, S.-H. Lyu, and J.-S. Lee, “Nonvolatile nano-floating gate memory devices based on pentacene semiconductors and organic tunneling insulator layers,” *Applied physics letters*, vol. 96, no. 3, pp. 033302–033302–3, 2010.

[28] R. Chen and K. Likharev, “Multiple-junction single-electron transistors for digital applications,” *Applied physics letters*, vol. 72, no. 1, pp. 61–63, 1998.

[29] K. Nakazato, R. Blaikie, and H. Ahmed, “Single Electron Memory,” *Journal of applied physics*, vol. 75, no. 10, pp. 5123–5134, 1994.

[30] L. Guo, E. Leobandung, and S. Chou, “A Silicon Single-Electron Transistor Memory Operating at Room Temperature,” *Science (American Association for the Advancement of Science)*, vol. 275, no. 5300, pp. 649–651, 1997.

[31] J. Berg, S. Bengtsson, and P. Lundgren, “Can molecular resonant tunneling diodes be used for local refresh of DRAM memory cells?,” *Solid-state electronics*, vol. 44, no. 12, pp. 2247–2252, 2000.

[32] M. Reed, J. Chen, A. Rawlett, D. Price, and J. Tour, “Molecular random access memory cell,” *Applied physics letters*, vol. 78, no. 23, pp. 3735–3737, 2001.

[33] N. Jin, S.-Y. Chung, R. M. Heyns, P. R. Berger, R. Yu, P. E. Thompson, and S. L. Rommel, “Tri-state logic using vertically integrated Si-SiGe resonant interband

tunneling diodes with double NDR," *IEEE electron device letters*, vol. 25, no. 9, pp. 646–648, 2004.

[34] K. S. Makarenko, Z. Liu, M. P. de Jong, F. A. Zwanenburg, J. Huskens, and W. G. van der Wiel, "Single-Electron Transistors: Bottom-Up Single-Electron Transistors (Adv. Mater. 42/2017)," *Advanced materials (Weinheim)*, vol. 29, no. 42, p. n/a, 2017.

[35] V. Derycke, R. Martel, J. Appenzeller, and P. Avouris, "Carbon Nanotube Inter- and Intramolecular Logic Gates," *Nano letters*, vol. 1, no. 9, pp. 453–456, 2001.

[36] S. M. Khamis, R. A. Jones, A. T. C. Johnson, G. Preti, J. Kwak, and A. Gelperin, "DNA-decorated carbon nanotube-based FETs as ultrasensitive chemical sensors: Discrimination of homologues, structural isomers, and optical isomers," *AIP advances*, vol. 2, no. 2, pp. 22110–022110–11, 2012.

[37] J. Andréasson, U. Pischel, S. D. Straight, T. A. Moore, A. L. Moore, and D. Gust, "All-Photonic Multifunctional Molecular Logic Device," *Journal of the American Chemical Society*, vol. 133, no. 30, pp. 11641–11648, 2011.

[38] R. H. Mathews, J. P. Sage, T. C. L. G. Sollner, S. D. Calawa, C.-L. Chen, L. J. Mahoney, P. A. Maki, and K. M. Molvar, "A new RTD-FET logic family," *Proceedings of the IEEE*, vol. 87, no. 4, pp. 596–605, 1999.

[39] T. Mueller, J. Guettinger, D. Bischoff, S. Hellmueller, K. Ensslin, and T. Ihn, "Fast detection of single-charge tunneling to a graphene quantum dot in a multi-level regime," *Applied physics letters*, vol. 101, no. 1, p. 12104, 2012.

[40] S. Bouvron, R. Maurand, A. Graf, P. Erler, L. Gragnaniello, M. Skripnik, D. Wiedmann, C. Engesser, C. Nef, W. Fu, C. Schonenberger, F. Pauly, and M. Fonin, "Charge transport in a single molecule transistor probed by scanning tunneling microscopy," *Nanoscale*, vol. 10, no. 3, pp. 1487–1493, 2018.

[41] J. Huang, M. Momenzadeh, and F. Lombardi, "An Overview of Nanoscale Devices and Circuits," *IEEE design & test of computers*, vol. 24, no. 4, pp. 304–311, 2007.

[42] R. Patel, Y. Agrawal, and R. Parekh, "Single-electron transistor: review in perspective of theory, modelling, design and fabrication," *Microsystem technologies : sensors, actuators, systems integration*, vol. 27, no. 5, pp. 1863–1875, 2021.

[43] C. Dekker, S. J. Tans, and A. R. M. Verschueren, "Room-temperature transistor based on a single carbon nanotube," *Nature (London)*, vol. 393, no. 6680, pp. 49–52, 1998.

[44] A. Venkataraman, E. V. Amadi, Y. Chen, and C. Papadopoulos, "Carbon Nanotube Assembly and Integration for Applications," *Nanoscale research letters*, vol. 14, no. 1, pp. 220–220, 2019.

[45] P. L. McEuen, "Nanotechnology Carbon-based electronics," *Nature (London)*, vol. 393, no. 6680, pp. 15–17, 1998.

[46] T. Huang, J. Zhao, M. Peng, A. Popov, S. Yang, L. Dunsch, and H. Petek, "A Molecular Switch Based on Current-Driven Rotation of an Encapsulated Cluster within a Fullerene Cage," *Nano Letters*, vol. 11, no. 12, pp. 5327–5332, 2011.

[47] A. Aviram and M. A. Ratner, "Molecular rectifiers," *Chemical Physics Letters*, vol. 29, no. 2, pp. 277–283, 1974.

[48] A. Batra, P. Darancet, Q. Chen, J. Meisner, J. Widawsky, J. Neaton, C. Nuckolls, and L. Venkataraman, “Tuning Rectification in Single-Molecular Diodes,” *Nano Letters*, vol. 13, no. 12, pp. 6233–6237, 2013.

[49] A. Flood, J. Stoddart, D. Steuerman, and Heath, “Whence Molecular Electronics?,” *Science (American Association for the Advancement of Science)*, vol. 306, no. 5704, pp. 2055–2056, 2004.

[50] T. N. Sasamal, A. K. Singh, A. Mohan, and S. (Online service), *Quantum-Dot Cellular Automata Based Digital Logic Circuits: A Design Perspective*, 1st 2020. ed., vol. 879. Singapore: Springer Singapore, 2020.

[51] M. R. Stan, P. D. Franzon, S. C. Goldstein, J. C. Lach, and M. M. Ziegler, “Molecular electronics: from devices and interconnect to circuits and architecture,” *Proceedings of the IEEE*, vol. 91, no. 11, pp. 1940–1957, 2003.

[52] M. A. Reed, C. Zhou, C. J. Muller, T. P. Burgin, and J. M. Tour, “Conductance of a Molecular Junction,” *Science*, vol. 278, no. 5336, pp. 252–254, 1997.

[53] W. Kamiński, R. Topolnicki, P. Hapala, P. Jelínek, and R. Kucharczyk, “Tuning the conductance of benzene-based single-molecule junctions,” *Organic Electronics*, vol. 34, pp. 254–261, 2016.

[54] G. Cuniberti, G. Fagas, and K. Richter, *Introducing molecular electronics*, 1. Aufl., vol. 680.;680; New York;Berlin;: Springer, 2005.

[55] J. R. Heath, P. J. Kuekes, G. S. Snider, and R. S. Williams, “A Defect-Tolerant Computer Architecture: Opportunities for Nanotechnology,” *Science (American Association for the Advancement of Science)*, vol. 280, no. 5370, pp. 1716–1721, 1998.

[56] T. S. Perry, “The father of FinFets: Chenming Hu took transistors into the third dimension to save Moore’s Law,” *IEEE spectrum*, vol. 57, no. 5. pp. 46–51, 2020.

[57] P. Ye, T. Ernst, and M. V. Khare, “The last silicon transistor: Nanosheet devices could be the final evolutionary step for Moore’s Law,” *IEEE spectrum*, vol. 56, no. 8. pp. 30–35, 2019.

[58] N. Imam and T. A. Cleland, “Rapid online learning and robust recall in a neuromorphic olfactory circuit,” *Nature machine intelligence*, vol. 2, no. 3, pp. 181–191.

[59] E. Prati, “Quantum neuromorphic hardware for quantum artificial intelligence,” *Journal of physics. Conference series*, vol. 880, no. 1, p. 12018, 2017.

[60] D. Marković and J. Grollier, “Quantum neuromorphic computing,” *Applied physics letters*, vol. 117, no. 15, 2020.

[61] M. Ratner, “A brief history of molecular electronics,” *Nature Nanotechnology*, vol. 8, no. 6, pp. 378–381, 2013.

[62] C. Mirkin and M. Ratner, “Molecular Electronics,” *Annual Review of Physical Chemistry*, vol. 43, no. 1, pp. 719–754, 1992.

[63] D. Xiang, W. Xiaolong, J. Chuancheng, L. Takhee, and G. Xuefeng, "Molecular-Scale Electronics: From Concept to Function," Chemical Reviews, vol. 116, (7), pp. 4318-4440, 2016.

[64] J. C. Cuevas and E. Scheer, *Molecular electronics: an introduction to theory and experiment: World Scientific series in nanoscience and nanotechnology v. 1*. GB: World Scientific Pub Co Pte, 2010.

[65] K. Sotthewes, V. Geskin, R. Heimbuch, A. Kumar, and H. J. W. Zandvliet, “Research Update: Molecular electronics: The single-molecule switch and transistor,” *APL Materials*, vol. 2, no. 1, pp. 10701–010701–11, 2014.

[66] Y. Daskal, R. Dittrich, J. Walter, and Y. Joseph, “Chemiresistor Sensors Based on Gold Nanoparticle Composites,” *Procedia Engineering*, vol. 120, pp. 799–802, 2015.

[67] S. V. Aradhya and L. Venkataraman, “Single-molecule junctions beyond electronic transport,” *Nature nanotechnology*, vol. 8, no. 6, pp. 399–410, 2013.

[68] B. Mann and H. Kuhn, “Tunneling through Fatty Acid Salt Monolayers,” *Journal of Applied Physics*, vol. 42, no. 11, pp. 4398–4405, 1971.

[69] A. Zabet-Khosousi and A. Dhirani, "Charge Transport in Nanoparticle Assemblies," Chemical Reviews, vol. 108, (10), pp. 4072-4124, 2008.

[70] A. Deka and R. C. Deka, “A density functional study on equilibrium geometries, stabilities and electronic properties of Au5Li binary clusters,” *Applied Nanoscience*, vol. 2, no. 3, pp. 359–364, 2012.

[71] A. Zabet-KhosousI, Y. Suganuma, K. Lopata, P. Trudeau, A. Dhirani, B. Statt, "Influence of linker molecules on charge transport through self-assembled single-nanoparticle devices," Physical Review Letters, vol. 94, (9), pp. 096801.1-096801.4, 2005.

[72] L. Wang, L. Wang, L. Zhang, and D. Xiang, “Advance of Mechanically Controllable Break Junction for Molecular Electronics,” *Topics in Current Chemistry*, vol. 375, no. 3, 2017.

[73] D. Xiang, H. Jeong, T. Lee, and D. Mayer, “Mechanically Controllable Break Junctions for Molecular Electronics,” *Advanced materials (Weinheim)*, vol. 25, no. 35, pp. 4845–4867, 2013.

[74] J. Love, L. Estroff, J. Kriebel, R. Nuzzo, and G. Whitesides, “Self-assembled monolayers of thiolates on metals as a form of nanotechnology,” *Chemical Reviews*, vol. 105, no. 4, pp. 1103–1169, 2005.

[75] M. Brust, D. Bethell, D. Schiffrin, and C. Kiely, “Novel Gold-Dithiol Nano-Networks with Nonmetallic Electronic Properties,” *Advanced Materials*, vol. 7, no. 9, pp. 795–795, 1995.

[76] P. Laibinis, M. Fox, J. Folkers, and G. Whitesides, “Comparisions of Self-Assembled Monoloayers of Silver and Gold- Mixed Monolayers Derived from HS(Ch2)21x and HS(Ch2)10y (x, y = ch3, Ch2OhH),” *Langmuir*, vol. 7, no. 12, pp. 3167–3173, 1991.

[77] D. Leff, P. Ohara, J. Heath, and W. Gelbart, “Thermodynamic Control of Gold Nanocrystal Size - Experiment and Theory,” *Journal of the American Chemical Society*, vol. 99, no. 18, pp. 7036–7041, 1995.

[78] M. Brust, M. Walker, D. Bethell, D. J. Schiffrin, and R. Whyman, “Synthesis of thiol-derivatised gold nanoparticles in a two-phase Liquid?Liquid system,” *Journal of the Chemical Society, Chemical Communications*, no. 7, p. 801, 1994.

[79] T. Dadosh, Y. Gordin, R. Krahne, I. Khivrich, D. Mahalu, V. Frydman, J. Sperling, A. Yacoby, and I. Bar-Joseph, “Measurement of the conductance of single conjugated molecules,” *Nature*, vol. 436, no. 7051, pp. 677–680, 2005.

[80] J. Taylor, H. Guo, and J. Wang, “Ab initio modeling of quantum transport properties of molecular electronic devices,” *Physical Review B*, vol. 63, no. 24, p. 245407, 2001.

[81] K. S. Thygesen and K. W. Jacobsen, “Molecular transport calculations with Wannier functions,” *Chemical Physics*, vol. 319, no. 1, pp. 111–125, 2005.

[82] T. Scheidemantel, C. Ambrosch-Draxl, T. Thonhauser, J. Badding, and J. Sofo, “Transport coefficients from first-principles calculations,” *P*, vol. 68, no. 12, 2003.

[83] S. Datta, Electronic transport in mesoscopic systems. 3, (Cambridge University Press: Cambridge, UK;New Yor, 1954).

[84] R. Landauer, Spatial variation of currents and fields due to localized scatterers in metallic conduction. IBM Journal of Research and Development 32, 306–316 (1988).

[85] Y. Xue, S. Datta, and M. A. Ratner, “Charge transfer and ‘band lineup’ in molecular electronic devices: A chemical and numerical interpretation,” *The Journal of Chemical Physics*, vol. 115, no. 9, pp. 4292–4299, 2001.

[86] P. A. Derosa and J. M. Seminario, “Electron transport through single molecules: Scattering treatment using density functional and green function theories,” *The Journal of Physical Chemistry B*, vol. 105, no. 2, pp. 471–481, 2001.

[87] Z. Ning, J. Chen, S. Hou, J. Zhang, Z. Liang, J. Zhang, and R. Han, “First-principles calculation of the transport properties of molecular wires between Au clusters under equilibrium,” *Physical Review B*, vol. 72, no. 15, 2005.

[88] J. M. Seminario and L. Yan, “Ab initio Analysis of Electron Currents in Thioalkanes,” *International Journal of Quantum Chemistry*, vol. 102, no. 5, pp. 711–723, 2005.

[89] K. Stokbro, J. Taylor, M. Brandbyge, J.-L. Mozos, and P. Ordejon, “Theoretical study of the nonlinear conductance of Di-thiol benzene coupled to Au (111) surfaces via thiol and thiolate bonds,” *Computational Materials Science*, vol. 27, no. 1, pp. 151–160, 2003.

[90] V. Prasad, S. Lukose, P. Agarwal, and L. Prasad, “Role of Nanomaterials for Forensic Investigation and Latent Fingerprinting—A Review,” *Journal of forensic sciences*, vol. 65, no. 1, pp. 26–36, 2020.

[91] J. Wang, “Can Man-Made Nanomachines Compete with Nature Biomotors?,” *ACS Nano*, vol. 3, no. 1, pp. 4–9, 2009.

[92] L. Rastogi, A. J. Kora, and A. J, “Highly stable, protein capped gold nanoparticles as effective drug delivery vehicles for amino-glycosidic antibiotics,” *Materials Science & Engineering C*, vol. 32, no. 6, pp. 1571–1577, 2012.

[93] H. Mizuta, H.-O. Müller, K. Tsukagoshi, D. Williams, Z. Durrani, A. Irvine, G. Evans, S. Amakawa, K. Nakazato, and H. Ahmed, “Nanoscale Coulomb blockade memory and logic devices,” *Nanotechnology*, vol. 12, no. 2, pp. 155–159, 2001.

[94] M. Brust, D. Bethell, C. Kiely, and D. Schiffrin, “Self-assembled gold nanoparticle thin films with nonmetallic optical and electronic properties,” *Langmuir*, vol. 14, no. 19, pp. 5425–5429, 1998.

[95] A. Venkataraman, P. Zhang, and C. Papadopoulos, “Electronic transport in metal-molecular nanoelectronic networks: A density functional theory study,” *American Institute of Physics Advances*, vol. 9, no. 3, p. 035122, 2019.

[96] A. Venkataraman, E. V. Amadi, T. S. M. Zaborniak, P. Zhang, and C. Papadopoulos, “Negative Differential Resistance and Hysteresis in Self-Assembled Nanoscale Networks with Tunable Molecule-to-Nanoparticle Ratios,” *physica status solidi (b)*, vol. 257, no. 6, p. 2000019, 2020.

[97] A. Venkataraman, E. V. Amadi, and C. Papadopoulos, “Random key generation using self-assembled nanoparticle-molecular networks,” in *American Chemical Society*, 2021.

[98] E. Burzurí, D. Granados, and E. M. Pérez, “Physically Unclonable Functions Based on Single-Walled Carbon Nanotubes: A Scalable and Inexpensive Method toward Unique Identifiers,” *ACS Applied Nano Materials*, vol. 2, no. 4, pp. 1796–1801, 2019.

[99] E. V. Amadi, A. Venkataraman, and C. Papadopoulos, “Nanoelectronic circuit elements based on nanoscale metal-molecular networks,” in *American Chemical Society*, 2021.

[100] M. Giersig and P. Mulvaney, “Preparation of ordered colloid monolayers by electrophoretic deposition,” *Langmuir*, vol. 9, no. 12, pp. 3408–3413, 1993.

[101] D. Bethell, “From monolayers to nanostructured materials: an organic chemist’s view of self-assembly,” vol. 409, no. 1, pp. 137–143.

[102] L. Sun, R. M. Crooks, and V. Chechik, “Preparation of polycyclodextrin hollow spheres by templating gold nanoparticles,” *Chem. Commun.*, no. 4, pp. 359–360, 2001.

[103] A. C. Templeton, W. P. Wuelfing, and R. W. Murray, “Monolayer-Protected Cluster Molecules,” *Accounts of chemical research*, vol. 33, no. 1, pp. 27–36, 2000.

[104] M. J. Hostetler, J. E. Wingate, C.-J. Zhong, J. E. Harris, R. W. Vachet, M. R. Clark, J. D. Londono, S. J. Green, J. J. Stokes, G. D. Wignall, G. L. Glish, M. D. Porter, N. D. Evans, and R. W. Murray, “Alkanethiolate Gold Cluster Molecules with Core Diameters from 1.5 to 5.2 nm: Core and Monolayer Properties as a Function of Core Size,” *Langmuir*, vol. 14, no. 1, pp. 17–30, 1998.

[105] E. Foresti, G. Fracasso, M. Lanzi, I. G. Lesci, L. Paganin, T. Zuccheri, and N. Roveri, “New Thiophene Monolayer-Protected Copper Nanoparticles: Synthesis and Chemical-Physical Characterization,” *Journal of nanomaterials*, vol. 2008, pp. 1–6, 2008.

[106] S. Sun, D. Gebauer, and H. Coelfen, “A solvothermal method for synthesizing monolayer protected amorphous calcium carbonate clusters,” *Chemical communications (Cambridge, England)*, vol. 52, no. 43, pp. 7036–7038, 2016.

[107] A. Deka and R. C. Deka, “Structural and electronic properties of stable Aun (n=2–13) clusters: A density functional study,” *Journal of Molecular Structure: THEOCHEM*, vol. 870, no. 1–3, pp. 83–93, 2008.

[108] K. C. Grabar, K. J. Allison, B. E. Baker, R. M. Bright, K. R. Brown, R. G. Freeman, A. P. Fox, C. D. Keating, M. D. Musick, and M. J. Natan, “Two-Dimensional Arrays of Colloidal Gold Particles: A Flexible Approach to Macroscopic Metal Surfaces,” *Langmuir*, vol. 12, no. 10, pp. 2353–2361, 1996.

[109] I. Horcas, R. Fernández, J. M. Gómez-Rodríguez, J. Colchero, J. Gómez-Herrero, and A. M. Baro, “WSXM: a software for scanning probe microscopy and a tool for nanotechnology,” vol. 78, no. 1, pp. 13705–13705.

[110] D. A. Patel, A. M. Weller, R. B. Chevalier, C. A. Karos, and E. C. Landis, “Ordering and defects in self-assembled monolayers on nanoporous gold,” vol. 387, pp. 503–512.

[111] D. A. Patel, A. M. Weller, R. B. Chevalier, C. A. Karos, and E. C. Landis, “Ordering and defects in self-assembled monolayers on nanoporous gold,” vol. 387, pp. 503–512.

[112] Y. Tang, J. Yan, F. Zhu, C. Sun, and B. Mao, “Comparative Electrochemical Scanning Tunneling Microscopy Study of Nonionic Fluorosurfactant Zonyl FSN Self-Assembled Monolayers on Au(111) and Au(100): A Potential-Induced Structural Transition,” vol. 27, no. 3, pp. 943–947.

[113] C. Vericat, M. E. Vela, and R. C. Salvarezza, “Self-assembled monolayers of alkanethiols on Au(111) : surface structures, defects and dynamics,” vol. 7, no. 18, pp. 3258–3268.

[114] M.-T. Lee, C.-C. Hsueh, M. S. Freund, and G. S. Ferguson, “Air Oxidation of Self-Assembled Monolayers on Polycrystalline Gold: The Role of the Gold Substrate,” vol. 14, no. 22, pp. 6419–6423.

[115] C. Chu, J.-S. Na, and G. N. Parsons, “Conductivity in Alkylamine/Gold and Alkanethiol/Gold Molecular Junctions Measured in Molecule/Nanoparticle/Molecule Bridges and Conducting Probe Structures,” vol. 129, no. 8, pp. 2287–2296.

[116] W. N. Waggener, *Pulse code modulation techniques: with applications in communications and data recording*. New York: Van Nostrand Reinhold, 1995.

[117] J. M. Seminario, A. G. Zacarias, and J. M. Tour, “Theoretical study of a molecular resonant tunneling diode,” *Journal of American Chemical Society*, vol. 122, no. 13, pp. 3015–3020, 2000.

[118] Z. Hu, J. M. M. L. Comeras, H. Park, J. Tang, A. Afzali, G. S. Tulevski, J. B. Hannon, M. Liehr, and S.-J. Han, “Physically unclonable cryptographic primitives using self-assembled carbon nanotubes,” *Nature nanotechnology*, vol. 11, no. 6, pp. 559–565, 2016.

[119] H. Chen, M. Song, Z. Guo, R. Li, Q. Zou, S. Luo, S. Zhang, Q. Luo, J. Hong, and L. You, “Highly Secure Physically Unclonable Cryptographic Primitives Based on Interfacial Magnetic Anisotropy,” *Nano letters*, vol. 18, no. 11, pp. 7211–7216, 2018.

[120] P. Zhang, A. Venkataraman, and C. Papadopoulos, “Self-assembled gold nanoparticle-molecular electronic networks,” *Physica Status Solidi B*, vol. 254, no. 9, p. 1700061, May 2017.

[121] Xiao, Xu, and N. J. Tao, “Measurement of Single Molecule Conductance: Benzenedithiol and Benzenedimethanethiol,” *Nano Lett.*, vol. 4, no. 2, pp. 267–271, 2004.

[122] Y. Zhang, X. Qiu, P. Gordiichuk, S. Soni, T. L. Krijger, A. Herrmann, and R. C. Chiechi, “Mechanically and Electrically Robust Self-Assembled Monolayers for Large-Area Tunneling Junctions,” vol. 121, no. 27, pp. 14920–14928.

[123] J. Zheng, J. Zhang, Z. Wang, L. Zhong, Y. Sun, Z. Liang, Y. Li, L. Jiang, X. Chen, and L. Chi, “Programmable Negative Differential Resistance Effects Based on Self-Assembled Au@PPy Core-Shell Nanoparticle Arrays,” *Adv. Mater.*, vol. 30, no. 35, p. 1802731, Aug. 2018.

[124] T. Zhang, D. Guérin, F. Alibart, D. Vuillaume, K. Lmimouni, S. Lenfant, A. Yassin, M. Oçafrain, P. Blanchard, and J. Roncali, "Negative Differential Resistance, Memory, and Reconfigurable Logic Functions Based on Monolayer Devices Derived from Gold Nanoparticles Functionalized with Electropolymerizable TEDOT Units," *J. Phys. Chem. C*, vol. 121, no. 18, pp. 10131–10139, May 2017.

[125] T. Lee, W. Wang, and M. A. Reed, "Mechanism of Electron Conduction in Self-Assembled Alkanethiol Monolayer Devices," *Ann. N.Y. Acad. Sci.*, vol. 1006, no. 1, pp. 21–35, 2003.

[126] A. Vilan, "Analyzing Molecular Current-Voltage Characteristics with the Simmons Tunneling Model: Scaling and Linearization," *J. Phys. Chem. C*, vol. 111, no. 11, pp. 4431–4444, 2007.

[127] J. G. Simmons, "Generalized Formula for the Electric Tunnel Effect between Similar Electrodes Separated by a Thin Insulating Film," vol. 34, no. 6, pp. 1793–1803.

[128] J. G. Simmons and R. R. Verderber, "New Conduction and Reversible Memory Phenomena in Thin Insulating Films," vol. 301, no. 1464, pp. 77–102.

[129] N. S. H. Pagnia, "Bistable switching in electroformed metal–insulator–metal devices."

[130] N. Crivillers, M. Paradinas, M. Mas-Torrent, S. T. Bromley, C. Rovira, C. Ocal, and J. Veciana, "Negative differential resistance (NDR) in similar molecules with distinct redox behaviour," vol. 47, no. 16, pp. 4664–4666.

[131] W.-H. Zhu, G.-H. Ding, and B. Dong, "Negative differential conductance and hysteretic current switching of benzene molecular junction in a transverse electric field," vol. 25, no. 46, pp. 465202–465202.

[132] T. T. T. Huong, K. Matsumoto, M. Moriya, H. Shimada, Y. Kimura, A. Hirano-Iwata, and Y. Mizugaki, "Gate-tuned negative differential resistance observed at room temperature in an array of gold nanoparticles," vol. 123, no. 4, pp. 1–5.

[133] S. Kaneko, Y. Nakamura, R. Matsushita, S. Marqués-González, and M. Kiguchi, "Simultaneous measurement of electrical conductance and thermopower of single benzenedithiol molecular junctions," vol. 8, no. 6, p. 65201.

[134] Y. Kim, T. Pietsch, A. Erbe, W. Belzig, and E. Scheer, "Benzenedithiol: A Broad-Range Single-Channel Molecular Conductor," vol. 11, no. 9, pp. 3734–3738.

[135] R. Parthasarathy, X. Lin, and H. Jaeger, "Electronic transport in metal nanocrystal arrays: The effect of structural disorder on scaling behavior," vol. 87, no. 18.

[136] Y. Naitoh, M. Horikawa, H. Abe, and T. Shimizu, "Resistance switch employing a simple metal nanogap junction," vol. 17, no. 22, pp. 5669–5674.

[137] K. Gottfried, *Quantum Mechanics: Fundamentals*, vol. 1. Boulder: Chapman and Hall/CRC, 2018.

[138] D. S. Sholl and J. A. Steckel, *Density functional theory: a practical introduction*, 1. Aufl. Hoboken, N.J: Wiley, 2009.

[139] C. Froese Fischer, "General Hartree-Fock program," *Computer physics communications*, vol. 43, no. 3, pp. 355–365, 1987.

[140] E. Wigner and F. Seitz, "On the Constitution of Metallic Sodium," *Physical review*, vol. 43, no. 10, pp. 804–810, 1933.

[141] J. S. Reese, S. Raimondeau, and D. G. Vlachos, “Monte Carlo Algorithms for Complex Surface Reaction Mechanisms: Efficiency and Accuracy,” *Journal of computational physics*, vol. 173, no. 1, pp. 302–321, 2001.

[142] A. Deka and R. C. Deka, “A density functional study on equilibrium geometries, stabilities and electronic properties of Au5Li binary clusters,” *Applied Nanoscience*, vol. 2, no. 3, pp. 359–364, 2012.

[143] A. Deka and R. C. Deka, “Structural and electronic properties of stable Aun (n=2–13) clusters: A density functional study,” *Journal of Molecular Structure: Theochem*, vol. 870, no. 1–3, pp. 83–93, 2008.

[144] S. H. Yang, D. A. Drabold, J. B. Adams, and A. Sachdev, “First-principles local-orbital density-functional study of Al clusters,” *Physical Review B*, vol. 47, no. 3, p. 1567, 1993.

[145] P. Hohenberg and W. Kohn, “Inhomogeneous Electron Gas,” *Physical Review*, vol. 136, no. 3B, pp. B864–B871, Nov. 1964.

[146] W. Kohn and L. J. Sham, “Self-Consistent Equations Including Exchange and Correlation Effects,” *Physical Review*, vol. 140, no. 4A, pp. A1133–A1138, Nov. 1965.

[147] 1942 Richard M. Martin, *Electronic structure: basic theory and practical methods*, [Second]. New York, NY;Cambridge, United Kingdom;: Cambridge University Press, 2020.

[148] K. Stokbro, J. Taylor, M. Brandbyge, and P. Ordejon, “TranSIESTA: A Spice for Molecular Electronics,” *Annals of the New York Academy of Sciences*, vol. 1006, no. 1, pp. 212–226, 2003.

[149] H. Joon Choi and J. Ihm, “Ab initio pseudopotential method for the calculation of conductance in quantum wires,” *Physical Review B*, vol. 59, no. 3, pp. 2267–2275, Jan. 1999.

[150] R. Landauer, “Spatial variation of currents and fields due to localized scatterers in metallic conduction,” *IBM Journal of Research and Development*, vol. 32, no. 3, pp. 306–316, 1988.

[151] N. Papior, N. Lorente, T. Frederiksen, A. García and M. Brandbyge, "Improvements on non-equilibrium and transport Green function techniques: The next-generation transiesta," Computer Physics Communications, vol. 212, pp. 8-24, 2017.

[152] P. J. Feibelman, “Sulfur adsorption near a step on Al,” *Phys. Rev. B*, vol. 49, no. 20, p. 14632, 1994.

[153] P. J. Feibelman, “Interaction between adsorbed chalcogen and Al atoms on Al (001),” *Phys. Rev. B*, vol. 38, no. 17, p. 12133, 1988.

[154] Z. Ning, J. Chen, S. Hou, J. Zhang, Z. Liang, J. Zhang, and R. Han, “First-principles calculation of the transport properties of molecular wires between Au clusters under equilibrium,” *Phys. Rev. B*, vol. 72, no. 15, p. 155403, 2005.

[155] B. Delley, “From molecules to solids with the DMol3 approach,” *The Journal of Chemical Physics*, vol. 113, no. 18, pp. 7756–7764, 2000.

[156] Q. 2017.2, “QuantumATK.” .

[157] W. A. Gaviria Rojas, J. J. McMorrow, M. L. Geier, Q. Tang, C. H. Kim, T. J. Marks, and M. C. Hersam, “Solution-Processed Carbon Nanotube True Random Number Generator,” *Nano Letters*, vol. 17, no. 8, pp. 4976–4981, 2017.

[158] A. Kokalj, “XCrySDen—a new program for displaying crystalline structures and electron densities,” *Journal of molecular graphics & modelling*, vol. 17, no. 3, pp. 176–179, 1999.

[159] H. Qian, W. Eckenhoff, Y. Zhu, T. Pintauer, and R. Jin, “Total Structure Determination of Thiolate-Protected Au-38 Nanoparticles,” *Journal of the American Chemical Society*, vol. 132, no. 24, pp. 8280–8280, 2010.

[160] B. Tollberg, X. Hu, L. Wang, and L. Xiao, “Structural study of gold clusters,” *Journal of Chemical Physics*, vol. 124, no. 11, pp. 114309–114309–10, 2006.

[161] C. Untiedt, A. Yanson, R. Grande, G. Rubio-Bollinger, N. Agrait, S. Vieira, and J. van Ruitenbeek, “Calibration of the length of a chain of single gold atoms,” *Physical Review B*, vol. 66, no. 8, 2002.

[162] H. Nili, G. C. Adam, B. Hoskins, M. Prezioso, J. Kim, M. R. Mahmoodi, F. M. Bayat, O. Kavehei, and D. B. Strukov, “Hardware-intrinsic security primitives enabled by analogue state and nonlinear conductance variations in integrated memristors,” *Nature Electronics*, vol. 1, no. 3, pp. 197–202, 2018.

[163] D. J. Henry, A. Varano, and I. Yarovsky, “Performance of numerical basis set DFT for aluminum clusters,” *The Journal of Physical Chemistry. A*, vol. 112, no. 40, pp. 9835–9844, 2008.

[164] N. A. Benedek, I. K. Snook, K. Latham, and I. Yarovsky, “Application of numerical basis sets to hydrogen bonded systems: a density functional theory study,” *The Journal of Chemical Physics*, vol. 122, no. 14, p. 144102, 2005.

[165] Y. Inada and H. Orita, “Efficiency of numerical basis sets for predicting the binding energies of hydrogen bonded complexes: Evidence of small basis set superposition error compared to Gaussian basis sets,” *Journal of Computational Chemistry*, vol. 29, no. 2, pp. 225–232, 2008.

[166] M. Methfessel and A. T. Paxton, “High-precision sampling for Brillouin-zone integration in metals,” *Physical Review B*, vol. 40, no. 6, pp. 3616–3621, Aug. 1989.

[167] N. Troullier and J. Martins, “Efficient pseudopotentials for plane-wave calculations,” *Physical review. B, Condensed matter*, vol. 43, no. 3, p. 1993—2006, Jan. 1991.

[168] J. Perdew, K. Burke, and M. Ernzerhof, “Generalized gradient approximation made simple (vol 77, pg 3865, 1996),” *Physical review letters*, vol. 78, no. 7, pp. 1396–1396, 1997.

[169] P. Zhang and C. Papadopoulos, “Electronic properties of metal-molecular nanojunctions and networks,” in *2015 IEEE Nanotechnology Materials and Devices Conference (NMDC)*, 2015, pp. 1–5.

[170] Xiao, Xu, and N. J. Tao, “Measurement of Single Molecule Conductance: Benzenedithiol and Benzenedimethanethiol,” *Nano letters*, vol. 4, no. 2, pp. 267–271, 2004.

[171] A. Gul, C. Bacaksiz, E. Unsal, B. Akbali, A. Tomak, H. M. Zareie, and H. Sahin, “Theoretical and experimental investigation of conjugation of 1,6-hexanedithiol on MoS2,” *Materials Research Express*, vol. 5, no. 3, p. 36415, 2018.

[172] R. Hoft, J. Liu, M. Cortie, and M. Ford, “Electron tunneling through alkanedithiol molecules,” in *Microelectronics, MEMS, and Nanotechnology*, 2005, pp. 603603–603603.

[173] X. Cui, A. Primak, X. Zarate, J. Tomfohr, O. Sankey, A. Moore, T. Moore, D. Gust, L. Nagahara, and S. Lindsay, “Changes in the electronic properties of a molecule when it is wired into a circuit,” *The Journal of Physical Chemistry B*, vol. 106, no. 34, pp. 8609–8614, 2002.

[174] H. Cheraghchi and K. Esfarjani, “Negative differential resistance in molecular junctions: Application to graphene ribbon junctions,” *Physical Review B*, vol. 78, no. 8, p. 085123, Aug. 2008.

[175] J. Fan, N. N. Gathitu, Y. Chang, and J. Zhang, “Effect of length on the position of negative differential resistance and realization of multifunction in fused oligothiophenes based molecular device,” *The Journal of chemical physics*, vol. 138, no. 7, pp. 74307–74307, 2013.

[176] D. Q. Andrews, R. Cohen, R. P. Van Duyne, and M. A. Ratner, “Single molecule electron transport junctions: Charging and geometric effects on conductance,” *The Journal of chemical physics*, vol. 125, no. 17, pp. 174718–174718, 2006.

[177] M. Sweeny and J. Xu, “Resonant Interband Tunnel-Diodes,” *Applied Physics Letters*, vol. 54, no. 6, pp. 546–548, 1989.

[178] T. Palm, L. Thylen, O. Nilsson, and C. Svensso, “Quantum Interference Devices and Field-Effect Transistors - A Switch Energy Comparison,” *Journal of Applied physics*, vol. 74, no. 1, pp. 687–694, 1993.

[179] A. Song, A. Lorke, A. Kriele, J. Kotthaus, W. Wegscheider, and M. Bichler, “Nonlinear electron transport in an asymmetric microjunction: A ballistic rectifier,” *Physical review letters*, vol. 80, no. 17, pp. 3831–3834, 1998.

[180] H. Mehrez, A. Wlasenko, B. Larade, J. Taylor, P. Grutter, and H. Guo, “I-V characteristics and differential conductance fluctuations of Au nanowires,” *Physical review. B*, vol. 65, no. 19.

[181] S. Alagha, S. E. Hernández, C. Blömers, T. Stoica, R. Calarco, and T. Schäpers, “Universal conductance fluctuations and localization effects in InN nanowires connected in parallel,” *Journal of applied physics*, vol. 108, no. 11, pp. 113704–113704–7, 2010.

[182] A. van Oudenaarden, M. H. Devoret, E. H. Visscher, Y. V. Nazarov, and J. E. Mooij, “Conductance fluctuations in a metallic wire interrupted by a tunnel junction,” *Physical review letters*, vol. 78, no. 18, pp. 3539–3542, 1997.

[183] J. Kim, D. Son, M. Lee, C. Song, J.-K. Song, J. H. Koo, D. J. Lee, H. J. Shim, J. H. Kim, M. Lee, T. Hyeon, and D.-H. Kim, “A wearable multiplexed silicon nonvolatile memory array using nanocrystal charge confinement,” *Science advances*, vol. 2, no. 1, pp. e1501101–e1501101, 2016.

[184] J.-S. Lee, “Recent progress in gold nanoparticle-based non-volatile memory devices,” *Gold Bulletin*, vol. 43, no. 3, pp. 189–199, 2010.

[185] S.-J. Kim, Y.-S. Park, S.-H. Lyu, and J.-S. Lee, “Nonvolatile nano-floating gate memory devices based on pentacene semiconductors and organic tunneling insulator layers,” *Applied physics letters*, vol. 96, no. 3, pp. 033302–033302–3, 2010.

[186] T. Palm, “Self-consistent calculations of an electron-wave Y-branch switch,” *Journal of Applied Physics*, vol. 74, no. 5, pp. 3551–3557, 1993.

[187] T. Palm and L. Thylen, “Designing logic functions using an electron waveguide Y-branch switch,” *Journal of Applied Physics*, vol. 79, no. 10, pp. 8076–8081, 1996.

[188] M. D. Pickett, G. Medeiros-Ribeiro, and R. S. Williams, “A scalable neuristor built with Mott memristors,” *Nature materials*, vol. 12, no. 2, pp. 114–117.

[189] P. M. Sheridan, F. Cai, C. Du, W. Ma, Z. Zhang, and W. D. Lu, “Sparse coding with memristor networks,” *Nature nanotechnology*, vol. 12, no. 8, pp. 784–789, 2017.

[190] N. D. Mathur, “The fourth circuit element,” *Nature (London)*, vol. 455, no. 7217, pp. E13–E13, 2008.

[191] S. H. Jo, T. Chang, I. Ebong, B. B. Bhadviya, P. Mazumder, and W. Lu, “Nanoscale Memristor Device as Synapse in Neuromorphic Systems,” *Nano letters*, vol. 10, no. 4, pp. 1297–1301, 2010.

[192] R. J. Tseng, J. Huang, J. Ouyang, R. B. Kaner, and Yang, “Polyaniline Nanofiber/Gold Nanoparticle Nonvolatile Memory,” *Nano letters*, vol. 5, no. 6, pp. 1077–1080, 2005.

[193] N. Ghenzi, M. J. Sánchez, F. Gomez-Marlasca, P. Levy, and M. J. Rozenberg, “Hysteresis switching loops in Ag-manganite memristive interfaces,” *Journal of applied physics*, vol. 107, no. 9, pp. 093719–093719–6, 2010.

[194] S. Pi, C. Li, H. Jiang, W. Xia, H. Xin, J. J. Yang, and Q. Xia, “Memristor crossbar arrays with 6-nm half-pitch and 2-nm critical dimension,” *Nature nanotechnology*, vol. 14, no. 1, pp. 35–39.

[195] M. Brust, D. Bethell, C. J. Kiely, and D. J. Schiffrin, “Self-assembled gold nanoparticle thin films with nonmetallic optical and electronic properties,” *Langmuir*, vol. 14, no. 19, pp. 5425–5429, 1998.

[196] A. Guttman, D. Mahalu, J. Sperling, E. Cohen-Hoshen, and I. Bar-Joseph, “Self-assembly of metallic double-dot single-electron device,” *Appl. Phys. Lett.*, vol. 99, no. 6, p. 063113, 2011.

[197] H. Jiang, D. Belkin, S. E. Savel’ev, S. Lin, Z. Wang, Y. Li, S. Joshi, R. Midya, C. Li, M. Rao, M. Barnell, Q. Wu, J. J. Yang, and Q. Xia, “A novel true random number generator based on a stochastic diffusive memristor,” *Nature Communications*, vol. 8, no. 1, pp. 882–9, 2017.

[198] V. B. Engelkes, J. M. Beebe, and C. D. Frisbie, “Length-dependent transport in molecular junctions based on SAMs of alkanethiols and alkanedithiols: effect of metal work function and applied bias on tunneling efficiency and contact resistance,” *J. Am. Chem. Soc.*, vol. 126, no. 43, pp. 14287–14296, 2004.

[199] G. S. Rose, J. Rajendran, N. McDonald, R. Karri, M. Potkonjak, and B. Wysocki, “Hardware security strategies exploiting nanoelectronic circuits,” in *18th Asia and South Pacific Design Automation Conference (ASP-DAC)*, 2013, pp. 368–372.

[200] Y. Joseph, I. Besnard, M. Rosenberger, B. Guse, H. Nothofer, J. Wessels, U. Wild, A. Knop-Gericke, D. Su, R. Schlogl, A. Yasuda, and T. Vossmeyer, “Self-assembled gold nanoparticle/alkanedithiol films: Preparation, electron microscopy, XPS-analysis, charge transport, and vapor-sensing properties,” *Journal of Physical Chemistry B*, vol. 107, no. 30, pp. 7406–7413, 2003.

[201] J. Knechtel, “Hardware Security For and Beyond CMOS Technology: An Overview on Fundamentals, Applications, and Challenges,” 2020, pp. 75–86.

[202] G. Sclauzero and A. Dal Corso, "Efficient DFT+U calculations of ballistic electron transport: Application to Au monatomic chains with a CO impurity," *Phys. Rev. B*, vol. 87, no. 8, 2013.

[203] R. Waser, *Nanoelectronics and information technology*. John Wiley & Sons, 2012.

[204] H. Wan, Y. Xu, and G. Zhou, "Dual conductance, negative differential resistance, and rectifying behavior in a molecular device modulated by side groups," *The Journal of chemical physics*, vol. 136, no. 18, pp. 184704–184704–6, 2012.

[205] J. Cornil, Y. Karzazi, and J. L. Brédas, "Negative Differential Resistance in Phenylene Ethynylene Oligomers," *Journal of the American Chemical Society*, vol. 124, no. 14, pp. 3516–3517, 2002.

[206] X. Shi, X. Zheng, Z. Dai, Y. Wang, and Z. Zeng, "Changes of Coupling between the Electrodes and the Molecule under External Bias Bring Negative Differential Resistance," *The journal of physical chemistry. B*, vol. 109, no. 8, pp. 3334–3339, 2005.

[207] J.-C. Li and X. Gong, "Diode rectification and negative differential resistance of dipyrimidinyl–diphenyl molecular junctions," *Organic electronics*, vol. 14, no. 10, pp. 2451–2458, 2013.

[208] E. D. Mentovich, I. Kalifa, A. Tsukernik, A. Caster, N. Rosenberg-Shraga, H. Marom, M. Gozin, and S. Richter, "Multipeak Negative-Differential-Resistance Molecular Device," *Small (Weinheim an der Bergstrasse, Germany)*, vol. 4, no. 1, pp. 55–58, 2008.

[209] Y. Chen, G.-Y. Jung, D. A. A. Ohlberg, X. Li, D. R. Stewart, J. O. Jeppesen, K. A. Nielsen, J. F. Stoddart, and R. S. Williams, "Nanoscale molecular-switch crossbar circuits," *Nanotechnology*, vol. 14, no. 4, pp. 462–468, 2003.

[210] Y. Liu, F. Han, F. Li, Y. Zhao, M. Chen, Z. Xu, X. Zheng, H. Hu, J. Yao, T. Guo, W. Lin, Y. Zheng, B. You, P. Liu, Y. Li, and L. Qian, "Inkjet-printed unclonable quantum dot fluorescent anti-counterfeiting labels with artificial intelligence authentication," *Nature Communications*, vol. 10, no. 1, pp. 2409–9, 2019.

[211] D.-I. Moon, A. Rukhin, R. P. Gandhiraman, B. Kim, S. Kim, M.-L. Seol, K. J. Yoon, D. Lee, J. Koehne, J.-W. Han, and M. Meyyappan, "Physically Unclonable Function by an All-Printed Carbon Nanotube Network," *ACS applied electronic materials*, vol. 1, no. 7, pp. 1162–1168, 2019.

[212] T. Zhang, D. Guérin, F. Alibart, D. Vuillaume, K. Lmimouni, S. Lenfant, A. Yassin, M. Oçafrain, P. Blanchard, and J. Roncali, "Negative Differential Resistance, Memory, and Reconfigurable Logic Functions Based on Monolayer Devices Derived from Gold Nanoparticles Functionalized with Electropolymerizable TEDOT Units," *Journal of physical chemistry. C*, vol. 121, no. 18, pp. 10131–10139, 2017.

[213] C. Nijhuis, W. Reus, and G. Whitesides, "Mechanism of Rectification in Tunneling Junctions Based on Molecules with Asymmetric Potential Drops," *Journal of the American Chemical Society*, vol. 132, no. 51, pp. 18386–18401, 2010.

[214] S. Fujii, M. Koike, T. Nishino, Y. Shoji, T. Suzuki, T. Fukushima, and M. Kiguchi, "Electric-Field-Controllable Conductance Switching of an Overcrowded

Ethylene Self-Assembled Monolayer," *Journal of the American Chemical Society*, vol. 141, no. 46, pp. 18544–18550, 2019.

[215] J. Soto J. R. Nechvatal M. E. Smid E. B. Barker S. D. Leigh M. Levenson M. Vangel D. L. Banks N. A. Heckert J. F. Dray A. L. Rukhin and S. Vo, "SP 800-22 Rev. 1a. A Statistical Test Suite for Random and Pseudorandom Number Generators for Cryptographic Applications," National Institute of Standards & Technology," *Gaithersburg, MD, USA,*, 2010.

[216] P. Slepicka, N. Slepickova Kasalkova, J. Siegel, Z. Kolska, and V. Svorcik, "Methods of Gold and Silver Nanoparticles Preparation," *Materials*, vol. 13, no. 1, p. 1.

[217] M. S. Khan, G. D. Vishakante, and S. H, "Gold nanoparticles: A paradigm shift in biomedical applications," vol. 199–200, pp. 44–58.

[218] D. Panda, P. P. Sahu, and T. Y. Tseng, "A Collective Study on Modeling and Simulation of Resistive Random Access Memory," vol. 13, no. 1, pp. 1–48.

[219] Y. Sakotsubo, T. Ohgi, D. Fujita, and Y. Ootuka, "Tunneling spectroscopy of isolated gold clusters grown on thiol/dithiol mixed self-assembled monolayers," *Physica. E, Low-dimensional systems & nanostructures*, vol. 29, no. 3, pp. 601–605, 2005.

[220] A. M. Jackson, Y. Hu, P. J. Silva, and F. Stellacci, "From Homoligand- to Mixed-Ligand- Monolayer-Protected Metal Nanoparticles: A Scanning Tunneling Microscopy Investigation," *Journal of the American Chemical Society*, vol. 128, no. 34, pp. 11135–11149, 2006.

[221] G. D. Kong, S. E. Byeon, S. Park, H. Song, S. Kim, and H. J. Yoon, "Mixed Molecular Electronics: Tunneling Behaviors and Applications of Mixed Self-Assembled Monolayers," *Advanced electronic materials*, vol. 6, no. 2, p. 1901157–n/a, 2020.

[222] J. Jin, G. D. Kong, and H. J. Yoon, "Deconvolution of Tunneling Current in Large-Area Junctions Formed with Mixed Self-Assembled Monolayers," vol. 9, no. 16, pp. 4578–4583.

[223] D. Su, M. Cortie, and G. Wang, "Fabrication of N-doped Graphene–Carbon Nanotube Hybrids from Prussian Blue for Lithium–Sulfur Batteries," *Advanced energy materials*, vol. 7, no. 8, p. 1602014–n/a, 2017.

[224] H. Jeong, D. M. Nguyen, M. S. Lee, H. G. Kim, S. C. Ko, and L. K. Kwac, "N-doped graphene-carbon nanotube hybrid networks attaching with gold nanoparticles for glucose non-enzymatic sensor," *Materials Science & Engineering C*, vol. 90, pp. 38–45, 2018.

[225] A. K. Feldman, M. L. Steigerwald, X. Guo, and C. Nuckolls, "Molecular Electronic Devices Based on Single-Walled Carbon Nanotube Electrodes," *Accounts of Chemical Research*, vol. 41, no. 12, pp. 1731–1741, 2008.

[226] X. Guo, J. P. Small, J. E. Klare, Y. Wang, M. S. Purewal, I. W. Tam, B. H. Hong, R. Caldwell, L. Huang, S. O'Brien, J. Yan, R. Breslow, S. J. Wind, J. Hone, P. Kim, and C. Nuckolls, "Covalently Bridging Gaps in Single-Walled Carbon Nanotubes with Conducting Molecules," *Science*, vol. 311, no. 5759, pp. 356–359, 2006.

[227] Z. Hu, J. M. M. L. Comeras, H. Park, J. Tang, A. Afzali, G. S. Tulevski, J. B. Hannon, M. Liehr, and S.-J. Han, "Physically unclonable cryptographic primitives

using self-assembled carbon nanotubes," *Nature nanotechnology*, vol. 11, no. 6, pp. 559–565, 2016.

[228] D. Son, J. H. Koo, J.-K. Song, J. Kim, M. Lee, H. J. Shim, M. Park, M. Lee, J. H. Kim, and D.-H. Kim, "Stretchable Carbon Nanotube Charge-Trap Floating-Gate Memory and Logic Devices for Wearable Electronics," *ACS nano*, vol. 9, no. 5, pp. 5585–5593, 2015.

[229] G. Sclauzero and A. Dal Corso, "Efficient DFT+U calculations of ballistic electron transport: Application to Au monatomic chains with a CO impurity," *Phys. Rev. B*, vol. 87, no. 8, 2013.

[230] K. K. Saha, W. Lu, J. Bernholc, and V. Meunier, "Electron transport in multi-terminal molecular device," 2009.

[231] H. Liu, H. Wang, J. Zhao, and M. Kiguchi, "Molecular rectification in triangularly shaped graphene nanoribbons," vol. 34, no. 5, pp. 360–365.

[232] M. J. Cyster, J. S. Smith, N. Vogt, G. Opletal, S. P. Russo, and J. H. Cole, "Simulating the fabrication of aluminium oxide tunnel junctions," *npj quantum information*, vol. 7, no. 1, pp. 1–12.

[233] C.-E. Kim, K. G. Ray, V. Lordi, and C. (United S. Livermore Lawrence Livermore National Lab. (LLNL), "A density-functional theory study of the Al/AlOx/Al tunnel junction," *Journal of applied physics*, vol. 128, no. 15, 2020.

[234] Y. Li, F. Demir, S. Kaneko, S. Fujii, T. Nishino, A. Saffarzadeh, G. Kirczenow, and M. Kiguchi, "Electrical conductance and structure of copper atomic junctions in the presence of water molecules," *Physical chemistry chemical physics : PCCP*, vol. 17, no. 48, pp. 32436–32442, 2015.

[235] R.-X. Huang, C.-J. Lu, and W.-C. Tian, "The Shell Structure Effect on the Vapor Selectivity of Monolayer-Protected Gold Nanoparticle Sensors," *Chemosensors*, vol. 2, no. 1, pp. 85–96, 2014.

[236] N. Kahn, O. Lavie, M. Paz, Y. Segev, and H. Haick, "Dynamic Nanoparticle-Based Flexible Sensors: Diagnosis of Ovarian Carcinoma from Exhaled Breath," *Nano Letters*, vol. 15, no. 10, pp. 7023–7028, 2015.

[237] V. T. Guse B Yasuda A Joseph Y, "Chemiresistor coatings from Pt- and Au-nanoparticle/nonanedithiol films: sensitivity to gases and solvent vapors," *Sensors & Actuators: B. Chemical, 98:188-195*, 2004.

[238] N. Kahn, O. Lavie, M. Paz, Y. Segev, and H. Haick, "Dynamic Nanoparticle-Based Flexible Sensors: Diagnosis of Ovarian Carcinoma from Exhaled Breath," *Nano Letters*, vol. 15, no. 10, pp. 7023–7028, 2015.

[239] J. M. Seminario, Y. Ma, and V. Tarigopula, "The Nanocell: A Chemically Assembled Molecular Electronic Circuit," vol. 6, no. 6, pp. 1614–1626.

[240] J. M. Tour, W. L. Van Zandt, C. P. Husband, S. M. Husband, L. S. Wilson, P. D. Franzon, and D. P. Nackashi, "Nanocell logic gates for molecular computing," vol. 1, no. 2, pp. 100–109.

[241] O. A. Yeshchenko, N. V. Kutsevol, and A. P. Naumenko, "Light-Induced Heating of Gold Nanoparticles in Colloidal Solution: Dependence on Detuning from Surface Plasmon Resonance," *Plasmonics (Norwell, Mass.)*, vol. 11, no. 1, pp. 345–350, 2016.

[242] K. Volk, J. P. S. Fitzgerald, and M. Karg, "In-Plane Surface Lattice and Higher Order Resonances in Self-Assembled Plasmonic Monolayers: From Substrate-

Supported to Free-Standing Thin Films," *ACS applied materials & interfaces*, vol. 11, no. 17, pp. 16096–16106, 2019.

[243] Z.-Z. J. Lim, J.-E. J. Li, C.-T. Ng, L.-Y. L. Yung, and B.-H. Bay, "Gold nanoparticles in cancer therapy," vol. 32, no. 8, pp. 983–990.

Appendix

Appendix A

Matlab Code for Plotting Energy Level Spectrum

```
figure;

plot([0 1],[energyLevelsOfBenzenedithiol; energyLevelsOfBenzenedithiol
],'k',[2   3],[energyLevelsOfAlCluster;   energyLevelsOfAlCluster],'k',[4
5],[energyLevelsOfJunction; energyLevelsOfJunction],'k')

ylabel('energy/eV')
title('benzenedithiol         Al cluster        dithiolbenzene
junction')
```

Appendix B

Matlab Code for Calculating Density of States (DMol^3)

```
ene=[energyLevelsOfJunction];
preden=gradient(ene);
den=preden.^-1;
figure;
plot(ene,den,[0],[250]);

title('dithiolbenzene 1-unit chain')
xlabel('Energy/eV')
ylabel('Density of states')
%dithiolbenzene junction
```

Appendix C

Python code for preprocessing DMol^3 output data

```
  import sys

  def main():
       path = r"FilePathofOutputData"
  str = path.split('\\')
    target = path.replace(str[-1], 'targettxt')
    file = open(path, 'rU')
    targetFile = open(target, 'w')
    lastValue = 0
    for line in file:
             cont = line.split()
    value = float(cont[5])
    if value >= -15 and value <= 0:
    if value != lastValue:
  targetFile.write(cont[5])
  targetFile.write(' ')
  lastValue = value
  print "target file created."
  file.close()
  sys.exit()

  if __name__ == '__main__':
main()
```

Appendix D

Python code for generating random set of resistance variables (random variable generator)

```
   import sys
   import random

   def main():
          i = 1
   while(i<=18):
                    nums = [1, 2, 3, 4, 5, 6, 7, 8, 9, 10, 11, 12, 13, 14, 15, 16, 17, 18, 19, 20, 21,
                    22, 23, 24, 25, 26, 27, 28, 29, 30, 31, 32, 33, 34, 35, 36]
   random.shuffle(nums)
   j = 0
print "random varialbes: " + str(18-i) + ":" + str(i) + " =============="
   var = " "
   cho = range(i*2)
   while(j<=(i*2-1)):
   cho[j] = nums[j]
   j=j+1
   cho.sort()
   j=0
   while(j<=(i*2-1)):
   var = var + str(cho[j]) + " "
   j=j+1
   print var
   print "\n"
   i=i+1
   sys.exit()

   if __name__ == '__main__':
main()
```

Appendix E

Bash script for calculating transmission using Quantum Espresso

```
#!/bin/bash
#SBATCH --job-name=Chain
#SBATCH --account=def-papadop
#SBATCH --time=0-7:20
#SBATCH --nodes=4
#SBATCH --ntasks-per-node=2
#SBATCH --mem=4G
module load quantumespresso/6.1
srun pw.x <Auwire.in> Auwire.out
srun pwcond.x <bands.in> bands.out
srun pw.x <Auwire1.in> Auwire1.out
srun pw.x <scat.in> scat.out
##srun pwcond.x <trans2.in> trans2.out
```

<<Sample input file for electrode region calculation>>

```
&CONTROL
      calculation='scf',
restart_mode = 'from_scratch',
  outdir='./SCRATCH',
  prefix='Auwire',
pseudo_dir ='./pseudo/',
/

&SYSTEM
      ibrav = 6,
    celldm(1) =15.0,
    celldm(3) =0.316,
    nat= 1,
    ntyp= 1,
    nspin = 1,
    ecutwfc = 25.0,
    ecutrho = 200.0,
    occupations='smearing',
    smearing='methfessel-paxton',
    degauss=0.01
input_dft='PW91'
/

&electrons
     conv_thr = 1.0d-8,
electron_maxstep = 500
mixing_beta = 0.6
mixing_mode = 'local-TF'
/

ATOMIC_SPECIES
  Au 196.966  Au.pz-rrkjus_aewfc.UPF
```

```
ATOMIC_POSITIONS {alat}
  Au   0.0  0.0  0.0

K_POINTS {automatic}
1 1 25 0 0 0
```

<<Sample input file for scattering region calculation>>

```
&CONTROL
calculation='scf'
restart_mode='from_scratch',
pseudo_dir ='./pseudo/',
outdir='./SCRATCH'
prefix ='scat',
tprnfor = .true.
/

&SYSTEM
ibrav=6,
celldm(1)=15.0000034699d0, celldm(3)=5.0123462078d0,
nat=35,
ntyp=4,
ecutwfc = 25.0,
ecutrho = 200.0
occupations = 'smearing',
smearing = 'methfessel-paxton',
degauss = 0.01
input_dft='PW91'
/

&electrons
conv_thr = 1.0d-8,
electron_maxstep = 500
mixing_beta = 0.6
mixing_mode = 'local-TF'
/
ATOMIC_SPECIES
Au 196.966  Au.pz-rrkjus_aewfc.UPF
C 12.0107  C.pz-rrkjus.UPF
H 1.007940d0 H.pz-rrkjus.UPF
S 32.065000d0 S.pz-n-rrkjus_psl.0.1.UPF

ATOMIC_POSITIONS {alat}
Au   0.0000000000d0   0.0000000000d0   0.0000000000d0
Au   0.0000000000d0   0.0000000000d0   0.3149542812d0
Au   0.0000000000d0   0.0000000000d0   0.6299085625d0
Au   0.0000000000d0   0.0000000000d0   4.3824376454d0
Au   0.0000000000d0   0.0000000000d0   4.6973919266d0
Au   0.0251013551d0  -0.2438657087d0   2.7276620569d0
Au   0.0241577512d0  -0.1148780734d0   2.3655994336d0
Au   0.0233697708d0   0.0021450893d0   2.0116538134d0
Au   0.0243404262d0   0.1191102774d0   2.6468788036d0
Au   0.0252802497d0   0.0021450728d0   3.0008408009d0
```

```
Au   0.0215203632d0   0.2481231158d0   2.2848413784d0
S    0.0000000000d0   0.0000000000d0   1.7228477964d0
S    0.0000000000d0   0.0000000000d0   4.0926797066d0
C    0.0000556965d0   0.0108879635d0   1.4988585249d0
C    0.0236943968d0   0.0128862277d0   3.8686956894d0
C    0.0008384995d0   0.1626453825d0   1.4089996319d0
C    0.0244772005d0   0.1646436469d0   3.7788367976d0
C    0.0008378848d0   0.1626452688d0   1.2335159239d0
C    0.0244765882d0   0.1646435345d0   3.6033530895d0
C    0.0000561985d0   0.0108876952d0   1.1436556040d0
C    0.0236949040d0   0.0128859616d0   3.5134927688d0
C   -0.0007274431d0  -0.1410599534d0   1.2336505587d0
C    0.0229112623d0  -0.1390616873d0   3.6034877225d0
C   -0.0007280581d0  -0.1410598364d0   1.4088634058d0
C    0.0229106448d0  -0.1390615711d0   3.7787005698d0
S    0.0000000000d0   0.0000000000d0   0.9196665012d0
S    0.0000000000d0   0.0000000000d0   3.2894958968d0
H    0.0014563757d0   0.2826570543d0   1.4756921608d0
H    0.0250950744d0   0.2846553189d0   3.8455293267d0
H    0.0014567586d0   0.2826571500d0   1.1668227944d0
H    0.0250954626d0   0.2846554161d0   3.5366599609d0
H   -0.0013440877d0  -0.2607995112d0   1.1664742579d0
H    0.0222946196d0  -0.2588012454d0   3.5363114243d0
H   -0.0013445481d0  -0.2607996010d0   1.4760403031d0
H    0.0222941532d0  -0.2588013351d0   3.8458774689d0

K_POINTS {automatic}
2 2 4 1 1 1
```

Appendix F

Bash script for running transmission and *I-V* calculations using SIESTA/TRANSIESTA.

```
#!/bin/bash
#SBATCH --time=4:55:00
#SBATCH --account=def-papadop
#SBATCH --mem=4G
#SBATCH --nodes=4
#SBATCH --ntasks-per-node=4
module load siesta/4.0
srun transiesta <elec1.fdf> elec1out.fdf


#!/bin/bash
#SBATCH --time=30:55:00
#SBATCH --account=def-papadop
#SBATCH --mem=16G
#SBATCH --nodes=4
#SBATCH --ntasks-per-node=4
module load siesta/4.0
srun transiesta <scat.fdf> scatout.fdf

#!/bin/bash
#SBATCH --time=55:30:00
#SBATCH --account=def-papadop
#SBATCH --mem-per-cpu=15G
module load siesta/4.0
srun tbtrans <scat.fdf> tran0.25V.fdf


<<Sample input file for electrode region calculation>>

# --------------------------------------------------------------------
---------
# Name and Label
# --------------------------------------------------------------------
---------

SystemName          right-Elec-Au
SystemLabel         right-Elec-Au

# --------------------------------------------------------------------
---------
# Lattice
# --------------------------------------------------------------------
---------

LatticeConstant             1.00 Ang
```

```
%block LatticeVectors
     4.444170      7.697520      0.000000
     8.888330      0.000000      0.000000
     0.000000      0.000000      7.257300
%endblock LatticeVectors

# K-points

%block kgrid_Monkhorst_Pack
1   0   0   0.0
0   1   0   0.0
0   0   10   0.5
%endblock kgrid_Monkhorst_Pack


# ------------------------------------------------------------------
---------
# Species and Atoms
# ------------------------------------------------------------------
---------

NumberOfSpecies        1
NumberOfAtoms         27

%block ChemicalSpeciesLabel
  1  79  Au
%endblock ChemicalSpeciesLabel

# ------------------------------------------------------------------
---------
# Atomic Coordinates
# ------------------------------------------------------------------
---------

AtomicCoordinatesFormat Ang

%block AtomicCoordinatesAndAtomicSpecies
      2.9627810      6.8422400      1.2095500     1
      1.4813930      4.2764000      1.2095500     1
      0.0000040      1.7105590      1.2095500     1
      5.9255590      6.8422400      1.2095500     1
      4.4441700      4.2764000      1.2095500     1
      2.9627810      1.7105590      1.2095500     1
      8.8883360      6.8422400      1.2095500     1
      7.4069480      4.2764000      1.2095500     1
      5.9255590      1.7105590      1.2095500     1
      4.4441700      5.9869600      3.6286500     1
      2.9627810      3.4211200      3.6286500     1
      1.4813930      0.8552790      3.6286500     1
      7.4069480      5.9869600      3.6286500     1
      5.9255590      3.4211200      3.6286500     1
      4.4441700      0.8552790      3.6286500     1
      8.8883360      3.4211200      3.6286500     1
```

```
      7.4069480      0.8552790      3.6286500     1
     10.3697300      5.9869600      3.6286500     1
      2.9627810      5.1316800      6.0477500     1
      1.4813930      2.5658400      6.0477500     1
      0.0000040     -0.0000010      6.0477500     1
      5.9255590      5.1316800      6.0477500     1
      4.4441700      2.5658400      6.0477500     1
      2.9627810     -0.0000010      6.0477500     1
      8.8883360      5.1316800      6.0477500     1
      7.4069480      2.5658400      6.0477500     1
      5.9255590     -0.0000010      6.0477500     1
%endblock AtomicCoordinatesAndAtomicSpecies

# Basis set variables
PAO.BasisType split
PAO.BasisSize DZP

# General variables

#NeglNonOverlapInt   True
ElectronicTemperature  25 meV
SolutionMethod    diagon
MeshCutoff           200. Ry
xc.functional         GGA          # Exchange-correlation functional
xc.authors            PBE
SpinPolarized false
          # Exchange-correlation version

# SCF variables

DM.MixSCF1   T
MaxSCFIterations      100          # Maximum number of SCF iter
DM.MixH              T
DM.MixingWeight      0.01         # New DM amount for next SCF cycle
DM.Tolerance         1.d-4         # Tolerance in maximum difference
DM.UseSaveDM          true         # to use continuation files
DM.NumberPulay         6

# MD variables

MD.FinalTimeStep 1
MD.TypeOfRun CG
MD.NumCGsteps     000
MD.UseSaveXV     .true.

# Output variables

WriteMullikenPop               1
WriteBands                    .false.
SaveRho                       .false.
SaveDeltaRho                  .false.
SaveHS                        .false.
SaveElectrostaticPotential    no
SaveTotalPotential            no
```

```
WriteCoorXmol                   .true.
WriteMDXmol                     .true.
WriteMDhistory                  .false.
WriteEigenvalues                no

# END OF VNL EXPORT
```

<<Sample input file for scattering region calculation>>

```
# ------------------------------------------------------------------
---------
# Name and Label
# ------------------------------------------------------------------
---------

SystemName          BDT-Au-1K
SystemLabel         BDT-Au-1K

# ------------------------------------------------------------------
---------
# Lattice
# ------------------------------------------------------------------
---------

LatticeConstant             1.00 Ang

%block LatticeVectors
     4.444170      7.697520      0.000000
     8.888330      0.000000      0.000000
     0.000000      0.000000     50.801640
%endblock LatticeVectors

# ------------------------------------------------------------------
---------
# Species and Atoms
# ------------------------------------------------------------------
---------

NumberOfSpecies        4
NumberOfAtoms        120

%block ChemicalSpeciesLabel
  1   1  H
  2   6  C
  3  16  S
  4  79  Au
%endblock ChemicalSpeciesLabel

# ------------------------------------------------------------------
---------
# Atomic Coordinates
```

```
# ----------------------------------------------------------------------
---------

AtomicCoordinatesFormat Ang

%block AtomicCoordinatesAndAtomicSpecies
      2.9627770       5.1316810       1.2095480      4
      1.4813890       2.5658410       1.2095480      4
      0.0000000       0.0000000       1.2095480      4
      5.9255550       5.1316810       1.2095480      4
      4.4441660       2.5658410       1.2095480      4
      2.9627770       0.0000000       1.2095480      4
      8.8883320       5.1316810       1.2095480      4
      7.4069440       2.5658410       1.2095480      4
      5.9255550       0.0000000       1.2095480      4
      4.4441660       5.9869610       3.6286460      4
      2.9627770       3.4211210       3.6286460      4
      1.4813890       0.8552800       3.6286460      4
      7.4069440       5.9869610       3.6286460      4
      5.9255550       3.4211210       3.6286460      4
      4.4441660       0.8552800       3.6286460      4
     10.3697200       5.9869610       3.6286460      4
      8.8883320       3.4211210       3.6286460      4
      7.4069440       0.8552800       3.6286460      4
      2.9627770       6.8422410       6.0477450      4
      1.4813890       4.2764010       6.0477450      4
     -0.0000000       1.7105600       6.0477450      4
      5.9255550       6.8422410       6.0477450      4
      4.4441660       4.2764010       6.0477450      4
      2.9627770       1.7105600       6.0477450      4
      8.8883320       6.8422410       6.0477450      4
      7.4069440       4.2764010       6.0477450      4
      5.9255550       1.7105600       6.0477450      4
      2.9627770       5.1316810       8.4668410      4
      1.4813890       2.5658410       8.4668410      4
      0.0000000       0.0000000       8.4668410      4
      5.9255550       5.1316810       8.4668410      4
      4.4441660       2.5658410       8.4668410      4
      2.9627770       0.0000000       8.4668410      4
      8.8883320       5.1316810       8.4668410      4
      7.4069440       2.5658410       8.4668410      4
      5.9255550       0.0000000       8.4668410      4
      4.4441660       5.9869610      10.8859400      4
      2.9627770       3.4211210      10.8859400      4
      1.4813890       0.8552800      10.8859400      4
      7.4069440       5.9869610      10.8859400      4
      5.9255550       3.4211210      10.8859400      4
      4.4441660       0.8552800      10.8859400      4
     10.3697200       5.9869610      10.8859400      4
      8.8883320       3.4211210      10.8859400      4
      7.4069440       0.8552800      10.8859400      4
      3.7034800       4.7040400      12.7615000      3
      3.7039253       4.7902424      14.5395900      2
      3.6928087       2.6334311      14.7209100      1
```

3.7150408	6.9472051	14.7236800	1
3.7101288	5.9945911	15.2530700	2
3.6977038	3.5838821	15.2539200	2
3.6976987	3.5838831	16.6449200	2
3.7101340	5.9946381	16.6459700	2
3.7150378	6.9472041	17.1753800	1
3.6928051	2.6334301	17.1781400	1
3.7039211	4.7901676	17.3593700	2
3.7034803	4.7040210	19.1372800	3
3.8889817	4.7210480	21.4297100	4
3.8743018	6.6735381	23.5981800	4
3.8952365	3.7921579	24.2392100	4
3.8966865	5.6494780	26.4719100	4
3.9027265	2.7682981	27.1131400	4
3.9041465	4.7210480	29.2815400	4
3.7044784	4.7063608	31.5578400	3
3.8915978	4.8169892	33.3248100	2
3.8804815	2.6601571	33.5060900	1
3.9027135	6.9739311	33.5088600	1
3.8853761	3.6106081	34.0391000	2
3.8977905	6.0192611	34.0419000	2
3.8853712	3.6106101	35.4301000	2
3.8977637	6.0143451	35.4353600	2
3.9026960	6.9711551	35.9590400	1
3.8804779	2.6601561	35.9633200	1
3.8905897	4.8126568	36.1516600	2
3.7036992	4.7117657	37.9189500	3
4.4441700	5.9869600	39.9157000	4
2.9627810	3.4211200	39.9157000	4
1.4813930	0.8552790	39.9157000	4
7.4069480	5.9869600	39.9157000	4
5.9255590	3.4211200	39.9157000	4
4.4441700	0.8552790	39.9157000	4
8.8883360	3.4211200	39.9157000	4
7.4069480	0.8552790	39.9157000	4
10.3697300	5.9869600	39.9157000	4
2.9627810	5.1316800	42.3347900	4
1.4813930	2.5658400	42.3347900	4
0.0000040	-0.0000010	42.3347900	4
5.9255590	5.1316800	42.3347900	4
4.4441700	2.5658400	42.3347900	4
2.9627810	-0.0000010	42.3347900	4
8.8883360	5.1316800	42.3347900	4
7.4069480	2.5658400	42.3347900	4
5.9255590	-0.0000010	42.3347900	4
2.9627810	6.8422400	44.7538900	4
1.4813930	4.2764000	44.7538900	4
0.0000040	1.7105590	44.7538900	4
5.9255590	6.8422400	44.7538900	4
4.4441700	4.2764000	44.7538900	4
2.9627810	1.7105590	44.7538900	4
8.8883360	6.8422400	44.7538900	4
7.4069480	4.2764000	44.7538900	4
5.9255590	1.7105590	44.7538900	4

```
      4.4441700      5.9869600     47.1729900     4
      2.9627810      3.4211200     47.1729900     4
      1.4813930      0.8552790     47.1729900     4
      7.4069480      5.9869600     47.1729900     4
      5.9255590      3.4211200     47.1729900     4
      4.4441700      0.8552790     47.1729900     4
      8.8883360      3.4211200     47.1729900     4
      7.4069480      0.8552790     47.1729900     4
     10.3697300      5.9869600     47.1729900     4
      2.9627810      5.1316800     49.5920900     4
      1.4813930      2.5658400     49.5920900     4
      0.0000040     -0.0000010     49.5920900     4
      5.9255590      5.1316800     49.5920900     4
      4.4441700      2.5658400     49.5920900     4
      2.9627810     -0.0000010     49.5920900     4
      8.8883360      5.1316800     49.5920900     4
      7.4069480      2.5658400     49.5920900     4
      5.9255590     -0.0000010     49.5920900     4
%endblock AtomicCoordinatesAndAtomicSpecies

# K-points

%block kgrid_Monkhorst_Pack
1   0   0   0.0
0   1   0   0.0
0   0   10   0.5
%endblock kgrid_Monkhorst_Pack


# Chemical species

NumberOfSpecies 4
%block ChemicalSpeciesLabel
  1  79 Au
  2   6  C
  3   1  H
  4  16  S
%endblock ChemicalSpeciesLabel

# Basis set variables
PAO.BasisType split
PAO.BasisSize    DZP

# General variables

#NeglNonOverlapInt   True
ElectronicTemperature  25 meV
SolutionMethod transiesta
MeshCutoff           200. Ry
xc.functional         GGA           # Exchange-correlation functional
xc.authors            PBE
SpinPolarized false
          # Exchange-correlation version
```

```
# SCF variables

DM.MixSCF1   T
MaxSCFIterations      100           # Maximum number of SCF iter
DM.MixH               T
DM.MixingWeight      0.01          # New DM amount for next SCF cycle
DM.Tolerance         1.d-4          # Tolerance in maximum difference
DM.UseSaveDM          true           # to use continuation files
DM.NumberPulay         6

# MD variables

MD.FinalTimeStep 1
MD.TypeOfRun CG
MD.NumCGsteps     000
#%block GeometryConstraints
#position from 1 to 36
#position from 41 to 85
#%endblock GeometryConstraints
MD.UseSaveXV     .true.

# Output variables

WriteMullikenPop                1
WriteBands                      .true.
SaveRho                         .false.
SaveDeltaRho                    .false.
SaveHS                          .true.
SaveElectrostaticPotential      no
SaveTotalPotential              no
WriteCoorXmol                   .true.
WriteMDXmol                     .true.
WriteMDhistory                  .false.
WriteEigenvalues                no

===================================================
===================================================

TS.TBT.Emin      -3.0 eV
TS.TBT.Emax       3.0 eV
TS.TBT.NPoints    2000

TS.TBT.NEigen              5

# Bias voltage
TS.Voltage 0.00 eV
TS.biasContour.NumPoints       20

# Transiesta: electrode definition:
# LEFT ELECTRODE

TS.HSFileLeft ./left-Elec-Au.TSHS
TS.ReplicateA1Left    1
TS.ReplicateA2Left    1
```

```
TS.NumUsedAtomsLeft   27
TS.BufferAtomsLeft    0

# RIGHT ELECTRODE
TS.HSFileRight ./right-Elec-Au.TSHS
TS.ReplicateA1Right   1
TS.ReplicateA2Right   1
TS.NumUsedAtomsRight  27
TS.BufferAtomsRight   0

==================================================
==================================================

Write.Denchar         true
WFS.Write.For.Bands  true
Denchar.TypeOfRun    3D
Denchar.PlotCharge   true

# END OF VNL EXPORT
# ------------------------------------------------------------------
---------
# ------------------------------------------------------------------
---------
```

Appendix G

Details of Hamming distance metric tests

To test the randomness of the generated keys, we chose the Hamming distance methodology, one of the commonly used testing metric for binary keys to test for randomness [98], [118]. By definition, the Hamming inter-distance between two strings of the same length is defined as the number of changes needed to go from one string to the other. It is a measure of how different two strings are [98]. In other words, the Hamming distance between arrays of two keys with the same length, is the total number of changes required in order to make the two keys equal. It is calculated by comparing bit-by-bit difference between the two keys. If the two keys are obtained from the same set of electrode pairs that are measured twice, we calculate the Hamming intra-distance value. On the other hand, we calculate the Hamming inter-distance value, if the keys are from different electrode pairs and/or from different samples. Measurements made on the same set of electrode pairs more than once showed good repeatability and stability, leading to very low intra-distances. Previous work in this field suggests that a inter-Hamming distance of 0.5 or closer indicates that the two keys are random, uncorrelated and unclonable [98], [119].

Example 1: 16-bit keys that were generated by comparing adjacent resistance data from electrical measurements done on two different samples:

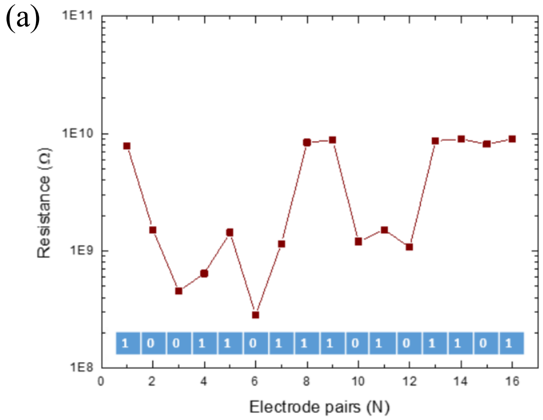

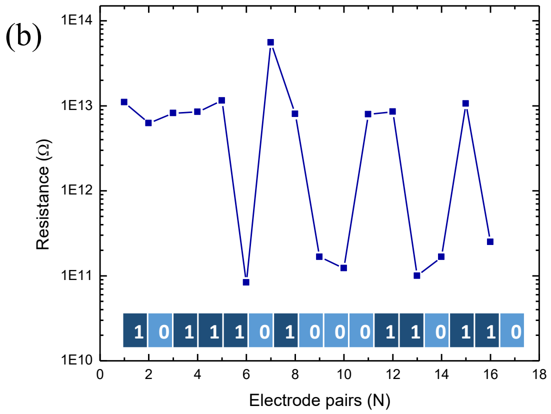

(c)

Key from sample A: N_{BDT}:N_{particle} ratio of 5:1 → 1001101110101101
Key from sample B: N_{NDT}:N_{particle} ratio of 5:1 →1011101000110110

The raw Hamming distance is therefore H_{raw} (key 1 – key 2) = 8

On comparing these two arrays of binary bits, the resulting Normalized Hamming distance is $H^{\mathrm{bin}}_{\mathrm{inter}}$ (key 1 – key 2) = 0.5.

Based on the values of the normalized Hamming distance; we can conclude that the generated keys are random, and unclonable.

<u>Details of NIST tests</u>

The generated arrays of bits also passed different randomness tests that are a part of NIST test suits [215]. According to the NIST test suit manual, the test statistic is used to calculate a ‘p-value’ that summarizes the strength of the evidence against the null hypothesis (the null hypothesis under test is that the sequence being tested is random). For all the tests, each p-value is the probability that a perfect random number generator would have produced a sequence less random than the test sequence. Some of the commonly used test suits are the frequency monobit and the cumulative sums test.

The focus of the frequency monobit test is to check the proportion of zeroes and ones for the entire sequence. The purpose of this test is to determine whether the number of ones and zeros in a sequence are approximately the same as would be expected for a truly random sequence. The test assesses the closeness of the fraction of ones to ½, that is, the number of ones and zeroes in a sequence should be about the same. On the other hand, the purpose of the cumulative sums test is to determine whether the cumulative sum of the partial sequences occurring in the tested sequence is too large or too small relative to the expected behavior of that cumulative sum for random sequences. On checking a binary key using the NIST test package, if the p-value is < 0.01, then we can conclude that the sequence is non-random. Otherwise, the sequence is random.

Example 1: Considering the 100-bit key that was generated by comparing adjacent resistance data from electrical measurements of 1:1 NDT samples:

Key:01110101101101011101010111000110011110110010101100100101100110111100

10111001010001111010101001010101

This key passed the frequency monobit and the cumulative sums test with a p-value > 0.01, indicating that the key is random (see table below).

p-values obtained for the 100-bit keys generated using circuit modeling.

	p-value		
Statistical Test Bit Stream (100 bits)	Frequency	Block Frequency	Cumulative Sums test-Forward
01110101101101011101 01011100011001111011	0.230139	0.904131	0.387010

001010110010010110011011110010111001010001111010101001010101			

Similar to the experimental results, the generated arrays of bits via circuit simulations also passed different randomness tests that are a part of NIST test suits (results shown below) and the Hamming algorithm-based randomness tests.

p-values obtained for the 100-bit keys generated using circuit modeling.

	p-value			
Statistical Test Bit Stream (27 bits)	Frequency	Block Frequency	Cumulative Sums test-Forward	Cumulative Sums test-Reverse
010101001010001010010101001	0.335924	0.670320	0.495894	0.664066
010111001010010010010101101	0.847390	0.818731	0.968556	0.968556
010101001101001010011001001	0.563703	0.818731	0.841231	0.968556
010101101010101011010101101	0.563703	0.818731	0.968556	0.841231
010111001010101011010101101	0.563703	0.818731	0.968556	0.841231
010101001101001010010001001	0.335924	0.818731	0.495894	0.664066
010101101010101011010001101	0.847390	0.818731	0.999692	0.999692
010101001010101010010101101	0.847390	0.818731	0.968556	0.999692
011101101101011010111001001	0.335924	0.367879	0.355810	0.495894
011111001010011110010001101	0.563703	0.670320	0.664066	0.841231
011010001010010101010001101	0.563703	0.818731	0.664066	0.841231
011111001110011110110011001	0.177932	0.201897	0.247312	0.247312
010101001010001010010101001	0.335924	0.670320	0.495894	0.664066
010111001010001010010101101	0.847390	0.818731	0.968556	0.968556
010101001101001010011001001	0.563703	0.818731	0.841231	0.968556